Université de Toulouse

THÈSE

En vue de l'obtention du

DOCTORAT DE L'UNIVERSITÉ DE TOULOUSE

Délivré par :
Institut National Polytechnique de Toulouse (INP Toulouse)

Discipline ou spécialité :

Dynamique des fluides

Présentée et soutenue par :
M. RENE LEDESMA ALONSO

le : mardi 3 décembre 2013

Titre :

STUDY OF THE INTERACTION BETWEEN A LIQUID FILM AND A LOCAL PROBE.

Ecole doctorale :
Mécanique, Energétique, Génie civil et Procédés (MEGeP)

Unité de recherche :
Institut de Mécanique des Fluides de Toulouse (I.M.F.T)

Directeur(s) de Thèse :
M. PHILIPPE TORDJEMAN
M. DOMINIQUE LEGENDRE

Rapporteurs :

M. JEAN-PIERRE AIME, UNIVERSITE BORDEAUX 1
M. JUAN JOSE SAENZ GUTIERREZ, UNIVERSIDAD AUTONOMA DE MADRID

Membre(s) du jury :
M. ELIE RAPHAEL, ESPCI PARIS, Président
M. DOMINIQUE LEGENDRE, INP TOULOUSE, Membre
M. PHILIPPE TORDJEMAN, INP TOULOUSE, Membre
M. THIERRY ONDARCUHU, CEMES TOULOUSE, Membre

Abstract

The static and dynamic interaction between a local probe and a liquid film provokes the deformation of the latter. This phenomenon has been described by means of analytical equations, which had been analyzed and numerically solved. Probe/liquid and liquid/substrate interaction potentials have been deduced from the integration of the dispersion forces. The pressure difference across the air/liquid interface has been calculated with a modified Young-Laplace equation, which takes into account the effects of gravity, surface tension, the liquid film/substrate and the probe/liquid interaction potentials. For the static case, the equilibrium modified Young-Laplace equation has been considered. The lubrication theory has been used to describe the liquid film evolution, in order to analyze the dynamic phenomenon. Numerical simulations of the equilibrium surface shape and the dynamic evolution of the film have been performed. Stable and unstable behaviors had been discerned, and results confirmed the existence of a threshold distance, for the static case, and a combination of oscillation parameters, for the dynamic situation, for which the jump of the liquid to contact the probe occurs. A theoretical analysis confirmed the existence of critical conditions separating the behavior regimes. This critical conditions indicate the role of the physical and geometric parameters in the system stability. For the dynamic case, preliminary results are reported and a qualitative interpretation of the phenomenon is formulated. In addition, AFM force and amplitude spectroscopy experiments had been performed and compared with the numerical results.

Résumé

L'interaction statique et dynamique entre une sonde locale et un film de liquide provoque la déformation de ce dernier. Ce phénomène a été décrit par des équations analytiques, qui ont été analysées et résolues numériquement. Les potentiels d'interaction sonde/liquide et liquide/substrat ont été déduits à partir de l'intégration des forces de dispersion. La différence de pression à travers l'interface air/liquide a été calculée avec une équation de Young-Laplace modifiée, qui prend en compte les effets de la gravité, de tension superficielle, ainsi que les potentiels d'interaction liquide/substrat et sonde/liquide. Pour le cas statique, l'équation modifiée de Young-Laplace en équilibre a été examinée. La théorie de la lubrification a été utilisé pour décrire l'évolution du film liquide, afin d'analyser le phénomène dynamique. Des simulations numériques de la forme de la surface d'équilibre et de l'évolution dynamique du film ont été réalisées. Des comportements stables et instables ont été discernés, et les résultats ont confirmé l'existence d'une distance de seuil, pour le cas statique, et d'une combinaison de paramètres d'oscillation, pour la situation dynamique, pour lesquelles le saut du liquide vers la sonde se produit. Une analyse théorique a confirmé l'existence de conditions critiques qui séparent les régimes de comportement. Ces conditions critiques indiquent le rôle des paramètres physiques et géométriques dans la stabilité du système. Pour le cas dynamique, les résultats préliminaires sont rapportés et une interprétation qualitative du phénomène est formulée. En outre, des expériences de spectroscopie AFM de force et amplitude ont été effectuées et comparées avec les résultats numériques.

Remerciements/Agradecimientos

Je veux remercier mes directeurs de thèse, Philippe et Dominique, pour leur connaissance, patience et amitié, mais surtout pour le choses qu'ils m'ont appris, non seulement dans le domain académique, mais aussi dans la vie. Aux membres des mon jury de thèse, Élie RAPHAËL, Thierry ONDARÇUHU, Juanjo SAENZ et Jean-Pierre AIMÉ, pour avoir pris le temps de lire mon manuscrit et de venir à ma soutenance, et aussi pour leurs critiques et commentaires sur mon travail. Aux experts de l'AFM, Richard ARINERO et Cédric CHARVILLAT, qui mon guidé dans des échelles où la longueur d'onde de la lumière ne nous aide pas.

Je veux remercier aux personnes appartenant au groupe INTERFACE (Patricia, Véronique, Catherine, Marie-Hélène, Julien, Frédéric, David, Sébastien, Wladimir, Jacques, Dominique et Philippe), car ils m'ont accueilli très chaleureusement, m'ont donné du courage et m'ont fait appartenir au troupe d'élite INTERFACE. Ils m'ont demontré, experimentalement et numeriquement, qu'on peut être intelligent, amical, modeste et joyeux en même temps. Aux personnes stupéfiantes qui sont devenues mes amis (Thomas, Fede, Marie, Benji, Lucia, Romain, Mathieu, Mika, Greg, Agathe, Mélanie, Yoan, Audrey, Élise, Jérôme, Jean-Lou, Martin, Nicolas, Joël, Auriane et Marine), et qui m'ont fait leur camarade au cours de cette traversée ondoyante qui est la thèse. Ils m'ont appris que la science, le divertissement, l'adrénaline, le bonheur et le bien-être se mélangent très bien dans le cocktail de la vie. A Arlette, car elle m'a offert son amitié et son soutien, mais surtout car elle est devenue un membre de ma famille et m'a fait appartenir à la sienne. Elle et sa famille (Robert, Anne-Marie, Nicole, Fabienne, Bertrand, etc ...) ont fait preuve que les êtres qui nous sont chers peuvent se trouver à l'autre côté du monde. Quiero agradecer a mi familia en México, Chabelita, Diana, Jacob y Ricardo, por su cariño y haberme dado las herramientas necesarias para hacer mi propio camino. Mi familia, estando tan lejos, siempre los sentí a mi lado, motivándome, guiándome, cuidándome y amándome. Y finalmente, quiero agradecer a Adri, mi hermosa novia, querida, compañera, amiga y musa, por haberme apoyado y estar a mi lado durante esta parte del trayecto. Ella, que además de haber compartido conmigo momentos de alegría, angustia, esfuerzo y satisfacción, ha aguantado mis tonterias y aún sigue brindándome su cariño y amor.

C'est grâce à eux, que j'ai eu le courage de continuer la course à pied. Ils sont tous des ingredients irremplaçables, sans lequelles mon guacamole n'aurait jamais eu son goût si spécial.

Contents

List of figures ix

List of tables xiii

Nomenclature xv

Introduction 1

I Static Deformation 7

1 Equation for the equilibrium shape 9
- 1.1 Overview . . . 9
  - 1.1.a Probe shape . . . 9
  - 1.1.b Probe/liquid system . . . 10
  - 1.1.c Liquid/substrate system . . . 12
- 1.2 Scope . . . 13
- 1.3 System description . . . 13
- 1.4 Interaction energies . . . 14
  - 1.4.a Spherical probe / differential volume of liquid . . . 14
  - 1.4.b Differential volume of liquid / substrate . . . 16
- 1.5 Pressure difference at the liquid surface . . . 17
- 1.6 Curvature decomposition . . . 20
- 1.7 Asymptotic analysis . . . 20
  - 1.7.a Far from the probe ($r^* \to \infty$) . . . 20
  - 1.7.b Close to the probe ($r^* \to 0$) . . . 22
- 1.8 Numerical method . . . 24
- 1.9 Concluding remarks . . . 25

2 Equilibrium behavior of a bulk liquid 27
- 2.1 The "jump-to-contact" phenomenon . . . 29
- 2.2 Surface apex behavior . . . 33
- 2.3 Characteristic length-scales . . . 36
- 2.4 Self-similarity . . . 38
- 2.5 Concluding remarks . . . 40

3 Dependence on the film thickness 43
- 3.1 Jump-to-contact . . . 46
- 3.2 Characteristic thicknesses . . . 48
- 3.3 Apex behavior in the small deformation regime . . . 50
- 3.4 Probe size effect . . . 51
- 3.5 Concluding remarks . . . 53

4 Mechanic analogy **55**
4.1 Spring-mass model . . . 55
4.2 Simplifications . . . 58
4.2.a Rigid Sample . . . 58
4.2.b Rigid Cantilever . . . 58
4.2.c Deformable sample and cantilever . . . 59
4.3 Some results . . . 60
4.4 Concluding remarks . . . 62

II Dynamic Deformation **63**

5 The dynamic behavior of a liquid sample **65**
5.1 Overview . . . 65
5.1.a Dynamic interaction . . . 65
5.1.b Surface waves . . . 67
5.1.c Thin films . . . 68
5.2 Scope . . . 69
5.3 Lubrication theory . . . 69
5.4 Quasi-linear thin-film equation . . . 72
5.5 Consequences of the probe oscillation . . . 72
5.6 Numerical scheme . . . 74
5.7 Concluding remarks . . . 76

6 Thin-film dynamics / static probe **77**
6.1 Numerical results . . . 77
6.2 Theoretical analysis of the thin-film transient behavior . . . 81
6.2.a Thin-film relaxation/diffusion . . . 82
6.2.b Thin-film excitation . . . 83
6.3 Concluding remarks . . . 87

7 Thin-film dynamics / oscillating probe **89**
7.1 Numerical results . . . 89
7.2 Thin-film stability . . . 93
7.3 Concluding remarks . . . 96

III AFM Experiments **99**

8 AFM spectroscopy experiments **101**
8.1 AFM overview . . . 101
8.2 AFM calibration . . . 102
8.2.a Scanner - Piezoelectric tube . . . 103
8.2.b Cantilever properties . . . 105
8.2.c Photodiode . . . 109
8.2.d Probe radius . . . 113
8.3 Liquid sample spectroscopy . . . 113
8.3.a Force/distance curves . . . 114
8.3.b Amplitude/distance curves . . . 118
8.4 Concluding remarks . . . 121

Conclusions and Perspectives 123

Bibliography 129

Appendices 135

A Numerical method / equilibrium 137

B Complete analysis on the static apex 139

C Pseudo-spectral method 141

D Math tools 145

E Publications 149

List of Figures

1.1 System and surface deformation . . . 13
1.2 Sphere-Molecule interaction . . . 14
1.3 Molecule (Differential Volume)-Substrate interaction . . . 16
1.4 Probe/Liquid film/Substrate interaction schema . . . 18
1.5 Modified capillary length vs film thickness . . . 20
1.6 Equilibrium typical solution and asymptotic approximations . . . 22

2.1 Dimensionless equilibrium profiles . . . 28
2.2 Bifurcation diagrams of the apex . . . 29
2.3 Derivative of the apex deformation . . . 30
2.4 Bifurcation diagrams of the peak curvature . . . 30
2.5 Minimum separation distance and maximum apex deformation . . . 31
2.6 Peak curvature . . . 33
2.7 Bulk proportionality constant . . . 34
2.8 Characteristic length-scales determination . . . 36
2.9 Radial position of the inflection point and the zero-curvature point . . . 37
2.10 Near-field self-similar mean curvature and interface deformation . . . 38
2.11 Near-field self-similar deformation profile . . . 39
2.12 Far-field self-similar deformation profile . . . 39

3.1 Dimensionless equilibrium thickness-dependent profiles . . . 44
3.2 Dimensionless equilibrium thickness-dependent local mean curvature . . . 45
3.3 Thickness-dependent apex position and mean curvature . . . 46
3.4 Thickness-dependent curves . . . 47
3.5 Dimensionless equilibrium critical profiles . . . 47
3.6 Thickness-dependent equation terms . . . 49
3.7 Maximum apex displacement and initial gap . . . 52

4.1 AFM schema and static mechanic analogy . . . 56
4.2 Mechanic analogy of the static probe/liquid/substrate system . . . 61

5.1 Lubrication assumption at the liquid film . . . 69

6.1 Dynamic evolution of the deformation profile. . . . 78
6.2 Dynamic evolution for a static probe . . . 79
6.3 Time decay coefficient . . . 82
6.4 Excited wavenumbers for film thickness and separation distance . . . 84
6.5 Time evolution of the excited wavenumbers . . . 85

7.1 Oscillating spatial and wavenumber profiles . . . 91
7.2 Oscillating surface phase diagrams . . . 94
7.3 Apex oscillation amplitude and phase shift . . . 95

8.1 AFM scheme . . . 102
8.2 AFM probe geometry . . . 103
8.3 AFM piezoelectric tube calibration . . . 105

8.4 AFM probe calibration curves . . . 106
8.5 Contact mode AFM deflection scheme and calibration curve . . . 110
8.6 Contact mode AFM force curve over rigid substrate . . . 111
8.7 Non-Contact mode AFM oscillation scheme and calibration curve . . . 112
8.8 Non-Contact mode AFM amplitude curve over rigid substrate . . . 113
8.9 Liquid sample and probes . . . 114
8.10 Force spectroscopy curve over liquid and PSD, B1-HDC probe . . . 115
8.11 Post-processed force spectroscopy curve over liquid, B1-HDC probe . . . 116
8.12 Force spectroscopy curve over liquid, ACT-02 probe . . . 117
8.13 Amplitude spectroscopy curves of a soft cantilever and over liquid . . . 119
8.14 Amplitude spectroscopy curves of a stiff cantilever and over liquid . . . 119
8.15 Amplitude spectroscopy curves of a stiffer cantilever and over liquid . . . 120

List of Tables

3.1 Parameters and characteristic film thickness 52

4.1 Force interaction coefficients and exponents. 55

5.1 Physical properties and dimensionless parameters for common liquids 74

6.1 Parameters dynamic liquid/static probe 78

7.1 Parameters dynamic liquid/oscillating probe 90

8.1 Probe properties and parameters 104

Nomenclature

Greek symbols

α	Interaction type exponent Real positive number
$\alpha\lambda^*_{CF}$	Cutoff wavelength (radial extent) for the discrete Hankel transform
α_0	Tip effect proportionality constant between $\eta_{0,max}$ and E
α_1	Tip effect constant in the relation between $\epsilon_{0,min}$ and E
β	Damping ratio
β_n, β_m	The nth or mth root of the Bessel function J_0
$\Delta\beta$	Separation between consecutive roots of the Bessel function J_0
ΔP	Pressure difference across the liquid/air interface
Δr	Radial position step size
Δt	Time step size
Δz	Probe displacement
δ	Probe deflection
$\Delta\rho$	Density difference across the liquid/air interface
ϵ_0	Equilibrium gap between the probe surface and the deformed interface at $r = 0$
η	Vertical interface position
η_0	Apex interface position, at $r = 0$
η_C	Interface position evaluated at $r = \lambda_C$
$\eta_{0,max}$	Maximum apex interface position
η_{guess}	Guess solution of the interface position at $r = 0$
γ	Liquid/air interfacial energy or surface tension
γ_{H_20}	Air/water surface tension
κ	Local mean curvature of the interface
κ_0	Peak curvature of the interface, at $r = 0$
κ_a, κ_m	Azimuthal and meridional curvatures of the interface
$\kappa_{0,crit}$	Critical peak curvature of the interface
Λ	Interaction type coefficient
λ	London-van der Waals constant
λ_C	Capillary length
λ_F	Film characteristic length
λ_H	Characteristic length given by the profile inflection point
λ_T	Transition length given by the zero-curvature position
λ_{CF}	Modified capillary length

μ	Dynamic viscosity of the liquid
ν	Time decay coefficient Time angular frequency Viscous damping coefficient
Ω	Temperature
ω_D	Angular frequency of the probe oscillation Driving frequency
$\omega_{c,0}$	Cantilever angular resonance frequency
ω_{PSD}	cantilever PSD peak frequency
$\omega_{vac,0}$	Cantilever resonance angular frequency in vacuum
ϕ	Liquid surface oscillation apex phase
ϕ_c	Cantilever response phase
$\phi_{c,free}$	Cantilever free oscillation phase
Φ_{ls}	Interaction energy between the substrate and a liquid differential volume
Φ_{ls}^{∞}	Interaction energy between the substrate and a liquid differential volume, placed at the undisturbed free surface, placed at $z = 0$
Φ_{pl}	Interaction energy between the probe and a differential volume
Φ_{pl}^{∞}	Interaction energy between the probe and a differential volume, for $D \to \infty$
Π_{ls}	Interaction potential between the liquid film and the substrate
Π_{pl}	Interaction potential between the probe and the liquid film
ρ_c	Cantilever material density
ρ_l	Molar density of the differential volume placed at L
ρ_p	Molar density of the probe
ρ_s	Molar density of the substrate
ρ_{air}, μ_{air}	Density and dynamic viscosity of air
σ	Numerical solution tolerance Truncation error
τ	Liquid film characteristic time scale
τ_c	Transitory settling time
Θ	Dimensionless coefficient of the polynomial used to find the critical apex conditions
θ	Azimuthal angle in the horizontal plane, measured from the horizontal axis, $0 \leq \theta \leq 2\pi$
Θ_s	Liquid sample diameter
Θ_{int}	The effective interaction diameter of the sample surface area
θ_{ls}	Liquid/substrate contact angle
Υ	Time integration variable
υ_p, υ_g	Phase and group velocity
υ_r, υ_z	Radial and axial components of the velocity field in the liquid film
φ	Polar angle, measured from the vertical axis, $0 \leq \varphi \leq \pi$
φ_0	Polar angle measured from the vertical axis to the circle passing through A and C
φ_L	Angle measured from the vertical axis to the line passing through L and the probe center
ϱ	Radial coordinate, the distance measured from the origin
ς	Spatial integration variable
ϑ	Cutoff wavenumber for the discrete Hankel transform

Ξ	Subset data point for the MA filter
ξ	Initial gap between the probe and the liquid surfaces at $r = 0$ Time-average gap between the probe surface and the $z = 0$ plane
ξ_{crit}	Critical initial gap
ζ	Spatial frequency, obtained from the separation distance as $1/D$
ζ_k	Discrete spatial frequency
ζ_{low}, ζ_{high}	Low and high cutoff spatial frequencies

Special symbols

$\bar{F}$	Smooth discrete force signal
$\Delta\mathcal{E}_\gamma$	Surface deformation energy change
$\hat{F}_k$	Discrete Fourier Transform of the force signal
$\mathbb{H}_0^{-1}$, $\mathbb{H}_v^{-1}$	Hankel inverse transform of order zero and of order v
$\mathbb{H}_0$, $\mathbb{H}_v$	Hankel transform of order zero and of order v
$\mathbf{b}$	Vector of boundary conditions
$\mathbf{F}$	Implicit vector valued function of $\mathbf{y}$
$\mathbf{f}$	Vector valued function of $\mathbf{y}$
$\mathbf{S}$	Vector of piecewise cubic polynomials to approximate $\mathbf{y}$
$\mathbf{Y}$	Vector of unknown functions
$\mathbf{y}$	Vector of unknown functions
$\mathcal{D}$	Lower position of the oscillating probe
$\mathcal{E}_p$	Interaction energy between the probe and a molecule, placed at a distance l
$\mathcal{E}_s$	Interaction energy between the substrate and a molecule, placed at a distance l
$\mathcal{E}_\gamma$	Surface deformation energy
$\mathcal{E}_\gamma^0$	Surface deformation energy of the undisturbed liquid
$\mathcal{M}$	Wavenumber-dependent function
$\mathcal{N}$	Zero order Hankel transform of the surface position η
$\mathcal{N}_H$, $\mathcal{N}_P$	The homogeneous and the particular solutions, components of $\mathcal{N}$
$\mathcal{P}$	Zero order Hankel transform of the pressure difference across the interface ΔP
$\mathcal{Q}$	Zero order Hankel transform of the probe/liquid interaction potential Π_{pl}
$\mathcal{T}$	Time period of the probe oscillation
$\mathcal{V}$	Probe characteristic speed
$\overline{F_p}$	Interaction force between the probe and a molecule, placed at a distance l
$\overline{F_s}$	Interaction force between the substrate and a molecule, placed at a distance l
$\overline{F_{ls}}$	Interaction force between the substrate and a differential volume
$\overline{F_{pl}}$	Interaction force between the probe and a differential volume
$\widehat{BP}$	Band-pass filter
$\widehat{l}$	Unit vector in the direction of the distance l
$\widehat{r}$, $\widehat{z}$	Unit vectors in the radial and axial directions of the cylindrical coordinates

General symbols

A	Hamaker constants ratio
B	Self-similar solution integration parameter

b	Self-similar solution fitting parameter
B_o^{eff}	Effective Bond number
B_o	Bond number
C_0, C_1	Coefficients of the solution of the linearized static equation
C_a	Capillary number
C_H	Frequency dependent coefficient obtained from the Hankel transform of the initial conditions $\eta(r, t = 0)$
C_n	The nth coefficient of the Fourier-Bessel series of $\mathcal{N}$
C_{lk}	Bulk proportionality constant
C_{lm}	Shallow film correction function
D	Separation distance between the probe center and the intially flat liquid surface
D_a	Probe/sample time-average separation distance
D_{min}	Minimum separation distance
E	Film thickness, measured from the substrate to the undisturbed free surface, placed at $z = 0$
E_c	Cantilever material Young's modulus
E_s	The sample elastic modulus
E_{bulk}	Bulk critical thickness
E_{puddle}, E_{cap}	Puddle and spherical cap assumptions of the sample thickness
$E_{shallow}$	Shallow film critical thickness
F	AFM measured force signal
f, G_a, G_b	Gaussian function and fitting parameters
f, L_a, L_b	Lorentzian function and fitting parameters
F_D	Driving force
F_j	Discrete force signal
F_γ	Surface deformation force
F_ρ	Gravity force (liquid weight)
$f_{c,0}$	Cantilever resonance frequency
F_{cap}	Capillary adhesion force
F_{int}	Probe/sample interaction force
F_{ls}	Magnitude of the liquid/substrate interaction force
F_{pl}	Magnitude of the probe/liquid interaction force
G	Asymptotic solution coefficient obtained from the static boundary conditions
g	Standard gravitational acceleration magnitude
G_m	The mth coefficient of the Fourier-Bessel series of η
H	Cantilever Hamiltonian
H_a	Modified Hamaker number
h_t	Tip height
H_{ls}	Hamaker constant of the liquid/substrate interaction
H_{pl}	Hamaker constant of the probe/liquid interaction
H_{ps}	Hamaker constant of the probe/sample interaction
i	Imaginary unit

I_c	Cantilever area moment of inertia
J_0, J_1	Zero and first order Bessel functions of the first kind
k	Angular wavenumber
K_0, K_1, K_2	Zero, first and second order modified Bessel functions of the second kind
k_B	Boltzmann constant
k_c	Cantilever stiffness or effective spring constant
k_s	Sample local stiffness or effective spring constant
K_{amp}	Photodiode amplitude calibration factor
K_{def}	Photodiode deflection calibration factor
K_{tube}	Piezoelectric tube calibration factor
l	The distance measured from the probe center to the point L The perpendicular distance from the substrate to L
$L(\rho, \theta, \varphi)$	A point outside the probe and temporary origin in the spherical coordinate system A point outside the probe, in the cylindrical coordinate system
l_c, w_c, t_c	Cantilever length, width and thickness
M	Parameter needed to determine Ξ
m_c	Cantilever equivalent mass
N	Total number of mesh points during spatial discretization Total number of acquired data points
P	Pressure field in the film
p	Cantilever momentum
P_{air}	Pressure at the air-side of the interface
P_{film}	Pressure at the liquid film-side of the interface
q	Wavenumber or spatial frequency
Q_c	Cantilever/media quality factor
R	Radius of the spherical probe
r	Radial coordinate, the perpendicular distance to the vertical axis
R_i	Specific value i of the probe radius, given in Table 3.1
Re_c	Cantilever Reynolds number
S	Space-bandwidth product
S_{ABC}	Spherical surface passing through the points A, B and C
t	Time
u	First derivative of the interface position η with respect to r
u_c	Reduced cantilever frequency
u_D	Reduced driving frequency
u_{PSD}	reduced PSD peak frequency
V	Piezoelectric or photodiode voltage
W	Liquid surface oscillation apex amplitude
W_c	Cantilever response amplitude
W_D	Amplitude of the probe oscillation Driving amplitude
$W_{c,0}$	Cantilever free resonance amplitude

$W_{c,free}$	Cantilever free oscillation amplitude
x	Final position of the probe surface after deflection
X_p	Generic term in eq.(2.1) or eq.(3.1)
Y_p	Generic term in eq.(1.23)
z	Axial coordinate, the perpendicular distance to the horizontal plane Probe position
z_j, z_m	Discrete jth or mth probe position
Z_q	Sinusoidal function, solution arising from $\mathcal{N}_H$

Subscripts

m	mth spatial frequency mesh point index during spatial discretization for a numerical method
n	nth space mesh point index during spatial discretization for a numerical method

Superscripts

$*$	Super-index denoting a dimensionless variable
j	jth iteration index or time index during temporal discretization for a numerical method

Derivatives

$\frac{\partial}{\partial r}$	Partial derivative with respect to the radial position
$\frac{\partial}{\partial t}$	Partial derivative with respect to time
$\frac{\partial}{\partial z}$	Partial derivative with respect to the axial position
$\frac{d}{dk}$	Angular wavenumber derivative
$\frac{d}{dr}$	Radial derivative
$\frac{D}{Dt}$	Material derivative or total derivative
∇_l	Directional derivative in the direction of l

Introduction

The purpose of this work

The Atomic Force Microscope (AFM) has proved to be a powerful tool to study the behavior of matter at the micro and nanoscopic scales. Its been almost 3 decades that this apparatus, which serves to image, manipulate and measure, has been conceived (Binnig and Quate, 1986). Over the years, the technological progress in the field has allowed the extraction and interpretation of quantitative and qualitative data from AFM measurements. AFM techniques are based on the measurement of the attractive interaction force, exerted between the AFM probe and the sample, which is the effect caused by the attractive London-van der Waals (L-vdW) forces between the molecules of the two bodies.

Recently, our research group (INTERFACE-group at the Institut des Mécanique des Fluides de Toulouse, IMFT) has become interested in employing this tool to study the properties of liquids. However, several constraints arise spontaneously when working with deformable samples. For instance, contact AFM techniques, commonly employed to obtain sample topographies, consist in pushing the AFM probe against the sample. These techniques are obviously not suitable for scanning liquid surfaces, because when probe/sample contact occurs the deformation of the liquid and its volume drainage toward the probe are fated. As well, the use of AFM techniques in vacuum, which increases the resolution and reduces the ambient noise, are not possible due to the inherent evaporation of the liquid. As a consequence, to analyze liquid samples, one must choose among the available non-contact AFM techniques in air. The methods are based on the tracking of the probe, which is forced to oscillate at a given amplitude and frequency. In fact, the behavior of the probe is distance-dependent, thus presenting a change in amplitude and a shift in frequency when the probe/sample distance (the so-called setpoint) is modified. Recording this oscillating parameters adjustment, over the entire sample surface, allows the reconstruction of the sample topography.

Over more than a decade, the imaging of liquid drops has been accomplished by means of non-contact AFM (Pompe et al. 1998; Fery et al. 1999; Pompe and Herminghaus 2000; Checco and Guenoun 2003; Checco et al. 2006; Berg et al. 2010). Even though the contact between probe and sample is not supposed to occur, either the local deformation or the oscillation of the liquid surface has been perceived, according to the scanning parameters (frequency, amplitude and setpoint), which may lead to the probe wetting in some cases. The importance of the sample deformation has been highlighted by several authors (Israelachvili 2011; Landman et al. 1990; Capella and Dietler 1999; Butt et al. 2005; Lenhard 2006; Checco et al. 2006; Bowen and Cheneler 2012), and it has been experimentally observed under varied conditions (Kuipers and Frenken 1993; Kuipers et al. 1995; Aimé et al. 1999b; Checco et al. 2006).

In general, to inhibit a significant perturbation of the sample, the equivalent spring constant of the cantilever should be smaller than the local intermolecular equivalent stiffness of the sample. In liquids, the intermolecular interaction, coming from L-vdW attractions or hydrogen bonds, is characterized by the surface tension, which is in the range $\left[10^{-2}, 10^{-1}\right]$ N/m. The probe stiffness is generally in the range $\left[10^{-2}, 10^{2}\right]$ N/m, often being greater than the liquid surface tension and occasionally in the same order of magnitude. As a consequence, the liquid surface shape is always modified by the approach of an AFM probe. But there is still more, if the probe/liquid distance is shorter than a threshold value, the probe/liquid attraction becomes unbounded and the intermolecular forces within the liquid are not capable anymore of maintaining the liquid molecules together at its surface. The liquid attains an unstable state, "jumps-to-contact" the probe and forms a capillary bridge.

Considering these facts, the evident reflex is to seek for a minimization of the surface deformation. Nevertheless, to keep the system interaction within the attractive regime, allowing the sample scanning, the probe/sample distance must remain small enough. Thence, the wisest reaction is to search for an optimization of the probe/liquid interaction. The probe oscillation conditions should be such to keep a high sensitivity, but without reaching the "jump-to-contact" state. As well, in order to reconstruct the liquid surface topography, the characterization of the entire deformation profile should be made.

However, we should keep in mind that non-contact AFM is a dynamic local probe technique, for which time is also an important variable. Taking into account the dynamic viscosity of common liquids, $\left[10^{-4}, 10^{0}\right]$ Pa s, and considering film thicknesses in the AFM length scale $\left[10^{-8}, 10^{-3}\right]$ m, the relaxation time of a liquid film can range in between $\left[10^{-12}, 10^{-7}\right]$ s. This scale corresponds to the time that the surface takes to attain an equilibrium position, when an instantaneous excitation is provoked. During the development of this thesis, we will give further details about the physical meaning of some significant dimensions (this time scale included), which determine the behavior of the probe/liquid system. At the present moment, a simple physical interpretation of the relaxation time is enough. Because of the

relatively small order of magnitude of this characteristic time scale compared to the common human time scales $\sim 10^{-3}$ s, an observer can pass by the transient relaxation phase, and consider that the corresponding equilibrium profile is reached instantaneously. As our first approach, a description of the equilibrium shape of the liquid is proposed and analyzed. This equilibrium approach is convenient to reveal the essential geometry of the problem and a first order stability criterion of the probe/liquid system.

On the other hand, when the probe shows a dynamic behavior, a monotonic displacement or an oscillating motion, which characteristic time scale (displacement time or oscillation period $\left[10^{-7}, 10^{-5}\right]$ s) is slightly larger than the liquid relaxation time, the dynamic response of the liquid sample should be taken into account. Even if the observer can not distinguish this phenomenon, the probe does undergo its dynamic effects. Therefore, our second strategy consists of the study of the dynamic evolution of a viscous thin film, which is perturbed by a local probe (either static or oscillating). This instantaneous approach depicts the characteristic dynamic scales of the problem (frequency, oscillation amplitude, spatial wavelength), and should help to discern a more precise stability criterion.

Based on the aforementioned approaches, the aim of this work is to provide significant advances in the determination of the optimal experimental parameters. A detailed description of the liquid surface deformation is meant to be obtained in relation to the physical and geometric conditions. Departing from an equilibrium analysis of the interaction of a liquid film with a static probe, the features of the sample behavior will be discerned. Afterwards, an analysis of the dynamic coupling between a probe and a thin-film is addressed.

It is important to say that, even though the study of microfluidic systems is an everyday task at the IMFT, it is the first time that the AFM probe/liquid system is the main point of a thesis made within the laboratory.

The structure of this thesis

This work is sectioned into three parts. I briefly describe them here.

Part I concerns the study of the interaction between a liquid film, a local probe and the underlying substrate. The aims of this part are:

- To describe the equilibrium shape of a liquid film in interaction with a probe.
- To forecast the critical conditions that provoke the probe wetting.

Besides, Part I is organized as follows. In Chapter 1, the equations describing the static shape of the liquid surface are derived. The dimensionless parameters and length scales that characterize the static phenomenon are deduced. In Chapter 2, the numerical results are presented, for the case of a film of infinite depth (bulk liquid). Physical interpretations based on theoretical approximations are considered. The results presented in this chapter, and its corresponding analysis, have led to two complementary publications, in Phys.Rev.Lett. (Ledesma-Alonso et al., 2012a) and Phys.Rev.E (Ledesma-Alonso et al., 2012b). In Chapter 3, the film thickness dependency is analyzed from the numerical results, obtained for a wide range of film thicknesses. Two asymptotic regimes are discerned, from the analysis of the involved characteristic length scales. The study developed in this chapter has generated another recent publication in Langmuir (Ledesma-Alonso et al., 2013). In Chapter 4, a mechanical analogy of the local probe/liquid film system, using equivalent masses and springs, is proposed and analyzed. Simple relationships between the geometric and physical parameters, which forecast the wetting critical conditions, are obtained.

Part II regards the dynamics of a viscous thin film in interaction with a probe and the underlying substrate. The purposes of this part are:

- To describe the shape evolution of a thin film in interaction with a static probe.
- To portray the dynamic interaction between a thin film and an oscillating probe.
- To figure out preliminary ideas of the critical dynamic conditions, in order to prevent the probe wetting.

Moreover, Part II is organized as follows. In Chapter 5, the equations describing the dynamic evolution of the surface of a viscous thin film are introduced. The dimensionless parameters, length and time scales that characterize the dynamic phenomenon are presented. In Chapter 6, the numerical results

concerning the interaction between a static probe and a thin film are studied. A theoretical analysis is developed in order to yield phenomenological interpretations. In Chapter 7, the dynamic response of a thin film interacting with an oscillating probe is set forth. Preliminary results are discussed and examined.

Part III pertains to performed AFM experiments. In Chapter 8, the calibration procedures and experimental techniques are detailed. The results obtained from force and amplitude AFM spectroscopy experiments are analyzed, from which physical parameters are deduced. In this instance, the procedure to estimate the probe/liquid Hamaker constant has been reported in the above-mentioned Phys.Rev.Lett. publication (Ledesma-Alonso et al., 2012a).

A brief general conclusion, including the current work and perspectives, is given to finalize this thesis.

Part I

Static Deformation (of a liquid film interacting with a probe)

Chapter 1

Equation for the equilibrium shape of a liquid sample interacting with a probe

1.1 Overview

Dispersion forces are responsible of the attraction between macroscopic dielectric bodies separated by microscopic distances. The magnitude of this forces depends on the nature of the interacting materials and their geometry. Their study is fundamental for the development of micro and nanotechnologies. Concerning solid materials, which shape is a priori known, such interaction forces have been largely studied. In contrast, for the case of deformable materials, only approximations have been made.

The Atomic Force Microscope (AFM) is capable of measuring this kind of forces. Indeed, some AFM techniques are based on this principle, and solid surfaces are usually analyzed in this way. The study of liquid materials by means of AFM has recently begun, therefore there are still open questions. For instance, even if the AFM does not touch the liquid sample, it provokes an intrusive effect on the surface shape, which must be quantified. In this chapter, the discussion starts with a brief summary on the current advances regarding the probe/liquid static interaction.

1.1.a Probe shape

According to the Hamaker theory (Hamaker, 1937), which explains the effect of van der Waals (vdW) forces between macroscopic objects, if the elements of a system are separated by short distances (in the range of $\left[10^{-9}, 10^{-7}\right]$ m), interaction forces appear between them. This is the basic principle of AFM, in which the force between a local probe and a sample is measured. Since the vdW forces act over a relatively short distance, in comparison with the size of the probe, which is commonly in the order of 10 μm, thus only its rounded extreme, the probe's tip, generates an effect on the sample, and the probe may be modeled as a sphere of equivalent radius R.

The consideration of a micrometer- or nanometer-sized spherical probe has been highly employed, due to the simplicity of the expressions describing the probe/sample interaction and capillary adhesion forces. The theoretical analysis of the interaction between an oscillating probe and a rigid sample (Aimé et al., 1999a; Nony et al., 1999; Zitzler et al., 2002; Couturier et al., 2003), the static interaction of the probe with a solid substrate with the formation of a capillary liquid bridge between them (Marmur, 1993; Lubarski et al., 2006; Sahagún et al., 2007), and some probe calibration models used to deduce the stiffness and tip radius (Hutter and J., 1993; Crassous et al., 1993; Santos et al., 2012), among many other studies, have been analyzed or developed under this consideration.

In contrast, correction factors have been introduced to account for the shape of a probe interacting with a flat rigid surface (Hartmann, 1991; Capella and Dietler, 1999; Butt et al., 2005; Sharpe, 2008), for which the interaction force is simply given by:

$$F_{int} = \frac{-H_{ps}\Lambda}{(D-R)^{\alpha}} \tag{1.1}$$

where H_{ps} is the probe/sample Hamaker constant, D the separation distance, R is the tip radius, α and Λ are a power-law index and a constant that depend on the probe geometry. For the case of a sphere $\Lambda = R/6$, where R is the sphere radius, for a paraboloid $\Lambda = (A_{xy})^2/12A_z$, where A_{xy} and A_z are the semi-axes of the paraboloid, and for a conical tip with a spherical apex $\Lambda = R\tan^2(\theta_c)$, where R and θ_c are the apex radius and the opening angle. For the three geometries, the power-law index takes the value $\alpha = 2$. Comparing these three probe shapes, one finds a geometry constant of $\Lambda = 0.1667R$ for a spherical probe, $\Lambda = 0.0833R$ for a paraboloid with $A_{xy} = A_z = R$ and $\Lambda = 0.1325R$ for a cone/sphere tip with an angle of $\theta = \pi/9$. As well, there are other works that employ a sphere-cone probe models to compute the interaction force with a flat rigid surface (Argento and French, 1996; Saint Jean et al., 1999). The resulting interaction force expressions include fancy correction factors, which employment remains a luxury for the physical understanding of non-contact AFM. The first conclusion is that the probe shape does not modify the spatial distribution of the force field, only its intensity. Thus, a spherical probe assumption should retain the physics of the phenomenon, despite the coarseness of its geometric description.

1.1.b Probe/liquid system

Whenever a probe approaches a soft sample, a "bump-like" deformation of the sample surface is expected to be observed. Notions of this phenomenon have been mentioned (Landman et al., 1990; Capella and Dietler, 1999; Butt et al., 2005; Lenhard, 2006; Checco et al., 2006; Bowen and Cheneler, 2012) and experimentally observed during temperature-dependent Scanning Tunneling Microscope (STM) measurements (Kuipers and Frenken, 1993; Kuipers et al., 1995). A "jump" of the surface to contact with the tip, which the authors attribute to the vdW attraction, is perceived when a Pb(110) sample surface melts at temperatures Ω slightly above the room temperature $\Omega > 320$ K. The measured probe/sample distance at which the jump-to-contact occurs was of at least 0.8 nm, for Pb surfaces slightly above room temperature $\Omega > 330$ K. For infinitely stiff systems, no jumps or instabilities are exhibited, which is the case of most solids at room temperature. In contrast, as it has been mentioned, for probe/soft samples systems, e.g. surface melting solids and liquid samples, the jump-to-contact phenomenon and instabilities are always present at short separation distances.

It is important to have in mind that the static probe/liquid interaction force has consequences over both, probe and liquid. Nevertheless, the stiffness of common AFM probes is significant enough, of the order of 10^1 N/m, to consider that the deflection of the cantilever is negligible in comparison with the expected deformation of the air/liquid interface, which is subject to a surface tension of around 10^{-2} N/m for common water-like liquids. Thence, a model considering a probe at a fixed position seems to be a good starting point.

Liquid films measured with an AFM generated greater thicknesses than the values obtained with ellipsometry (Mate et al., 1989; Forcada et al., 1991b). Qualitative descriptions of the surface deformation were presented, as well as the proposal of its quantitative determination via the pressure difference across the interface. The existence of a minimum probe/liquid separation distance, the "jump-to-contact" threshold, was revealed. An equivalent threshold distance between two liquid films has been experimentally observed and analytically calculated (Forcada, 1993; Christenson, 1994), and it was also discerned in a more recent study of the coalescence of two liquid films in a Surface Force Apparatus (SFA) experiment (Chen et al., 2004).

Experiments on hair conditioner films over human hair, performed with a AFM typical silicon probe, with a radius of 100 nm and a stiffness of 5 N/m, confirmed the truthfulness of surface deformation (Chen and Bhushan, 2005). In the above-mentioned reference, an effective spring constant of the liquid surface k_{liq} is used, which is taken as equal to the liquid surface tension γ. Based on the vdW interaction between a sphere and a flat surface, with a Hamaker constant H_{ps}, from a jump instability criterion (when the force gradient exceeds the system spring constant), the minimum distance between the stable liquid film and the AFM tip is:

$$D_{min} = \left(\frac{H_{ps}R}{3k_{liq}}\right)^{1/3}. \tag{1.2}$$

In the aforementioned reference (Chen and Bhushan, 2005), considering $\gamma = 0.02$ N/m for PDMS (as it is one of the main components of conditioner), a Hamaker constant of $H_{ps} = 10^{-20}$ J, and a film thickness of 3.5 nm, the estimated minimum distance was of $D_{min} \approx 2$ nm. In the SFA experiment (Chen et al., 2004), two PDMS films of thickness 25 nm deposited over two cylinders of radius $R = 20$ mm, one of

them mounted on a cantilever with a stiffness of 10^3 N/m, were approached at a velocity of 0.3 nm/s. In this case, considering $\gamma = 0.03$ N/m and $H_{ps} = 5 \times 10^{-20}$ J, the authors predicted a minimum distance of $D_{min} \approx 220$ nm, whereas the experimentally measured jump distance was around $D_{min} = 200$ nm.

The employment of the Young-Laplace equation to obtain the interface shape of a liquid body in interaction with a macroscopic solid has been widely used. For instance, it was employed to determinate the deformation of a surface undergoing an acoustic radiation pressure provoked by an acoustic transducer (Issenmann et al., 2006; Issenmann, 2007; Issenmann et al., 2008), or the equilibrium shape of a sessile drop over a substrate (Yi and Wong, 2007; Snoeijer and Andreotti, 2008).

The interaction between a charged/neutral particle and a liquid has been analyzed (Forcada et al., 1991a) in the past, which scope is more similar to the first objectives of this thesis. The approach lied in the minimization of the system potential energy, which led to a Young-Laplace equation close to the one presented herein. For an uncharged particle, with a purely vdW interaction, the problem linearization and the use of a particle/flat surface predicts a minimum distance, which is given by:

$$D_{min} = \frac{5}{4}\left[\frac{\lambda\rho_l}{C\gamma}\right]^{1/5},$$

where ρ_l is the density of atoms/molecules in the liquid, λ is the London-van der Waals (L-vdW) interaction constant of the particle and a liquid atom/molecule, γ is the surface tension and C is an adjustable parameter, which, according to the authors, depends on the magnitude of the gap between the particle and the liquid surface. In addition, for the case of purely non-retarded vdW interaction, a simple relation between the minimum separation distance D_{min} and the maximum stable surface deformation η_{max} was given $D_{min} \simeq 5\eta_{max}$, from observation of the numerical results. Nevertheless, results, which validate the two previous formulas and include values of the parameter C, are not shown for the uncharged particle case in the aforementioned publication.

Some other studies have been conducted regarding the interface deformation of a liquid due to its interaction with a second body. For example, the interaction between hydrophilic and hydrophobic micrometric glass probes with an air bubble in water was analyzed (Butt, 1994). The hydrophilic probe experiences a repulsive force when approaching the bubble, which is deformed to move away from the probe. When the probe reaches the water/air interface, if the applied force is below a threshold value, the bubble shows an hyperelastic solid behavior during the "indentation". In contrast, the hydrophobic probe experiences an attractive force and snaps into the bubble at a certain separation distance. Nevertheless, the bubble surface deformation is neither quantified nor described prior to the probe/bubble contact.

Research on the probe/droplet, droplet/droplet and solid/drop repulsive interaction in water or aqueous solutions has also been conducted. The repulsive nature of these phenomenon is attributed either to hydrophilic behaviors and addition of electrolytes and surfactants (Hartley et al., 1999; Nespolo et al., 2003), or to the hydrodynamic film drainage (Dagastine et al., 2006, 2010), or repulsive double-layer forces (Miklavcic et al., 1995; Horn et al., 1996).

Using a Derjaguin approximation, some numerical studies were performed to find the deformation provoked by a static parabolic probe over a liquid body (Cortat and Miklavcic, 2003, 2004; Wang et al., 2007). The Derjaguin approximation, which relates the energy per unit area Φ between two semi-infinite media, is given by:

$$\Phi = \frac{H_{ps}}{12D^2},$$

where H_{ps} is the Hamaker constant of the two media interaction and D the distance between a differential surface element of the first body and the equivalent of the second. This distance D is usually determined by locating the corresponding surface elements with the shortest separation distance. Then, for axisymmetric configurations, the force is approximated by:

$$F_{int} \approx 2\pi R\Phi.$$

The shape of the two bodies is arbitrary, but it is only valid for $D \ll R$, being R the effective radius of the interacting bodies. In the above-mentioned publications, the probe shape is given by the parametric equation:

$$z_p(r) = z_{p0} + \lambda r_p(r)^2$$

where z_{p0} is the probe apex, z_p and r_p are the coordinates of the probe point which is closest to a liquid surface point (r, z), and λ is the splay constant or parabolicity coefficient. This splay parameter

also corresponds to the tip apex curvature, which seem unrealistic in the case of AFM probes. The authors use $\lambda \in \left[10^{-2}, 10^{4}\right]$ m^{-1}, which corresponds to probes with an apex curvature of $\left[10^{-4}, 100\right]$ m. Notice that this inconsistencies lead to find deformations of an order between $z\,(r=0) \in [0.1, 1]$ μm, for a splay parameter of $\lambda = 0.1\text{m}^{-1}$ and a probe position of $z_{p0} = 3.55$ μm. Empirical and complicated relationships between the parameters are given to find the minimum probe position z_{p0}, to find a solution of the problem. In addition, the validity of Derjaguin-like approximations is questioned in cases of micro- and nanoscopic systems. Nevertheless, the authors present a mechanical analogy which gives a qualitative first approach of the problem, describing the existence of stable and unstable solutions from the energetic view point.

Finally, the deformation of a liquid surface in interaction with a spherical probe has been boarded simultaneously by another research group (Wang et al., 2011). Their numerical results generated similar surface deformation profiles to the ones we show in this work. Nevertheless, the proposed scope presented in this thesis, led into a parametric study, yielding simple relationships between the physical properties and several length scales, which characterize the system behavior.

The mutation of the sample position provokes an increase of the interaction strength, because the probe/sample distance shortens. The complexity of this coupling phenomenon avoids an analytical calculation of total probe/sample interaction force, because the sample deformation profile is unknown a priori. In conclusion, one should deal seriously with the surface deformation, mainly when one wants to maximize the probe sensitivity during liquid surfaces imaging. Therefore, in this work, an extensive analysis of the probe/liquid interaction is developed. One of the main objectives of this work is to yield precise relationships between the probe/liquid separation distance and the liquid surface deformation. Besides the probe/liquid interaction, in our study, we also consider the liquid/substrate interaction.

1.1.c Liquid/substrate system

Whenever a thin liquid film is deposited over a rigid substrate, interaction forces between the substrate and the liquid molecules should be considered. It has been suggested that the free energy of a thin film is different from that of an infinite liquid body (Deryaguin, 1993), as a consequence of the change in the thermodynamic properties. Consequently, the study of thin films systematically employs the liquid/substrate interaction energy Φ_{ls}:

$$\Phi_{ls} = \Phi_B - \frac{H_{ls}}{6\pi E^3}, \tag{1.3}$$

where H_{ls} is the liquid/substrate Hamaker (or Casimir-Lifshitz) interaction constant, E is the film thickness and Φ_B is the basal energy, the free energy of an hypothetical bulk phase. The quantity Φ_{ls} describes the attractive potential energy experienced by a liquid molecule placed at a distance E from the substrate, obtained from the integration of the pair potential energy between molecules over the substrate. A thermodynamic analysis to obtain and explain the nature of this energy per unit volume can be found elsewhere (Shedulko, 1972). It is important to note that E can not be smaller than a certain molecular length σ_0, in order to prevent the overlapping of molecules. This characteristic length scale is defined as (de Gennes, 1985; Israelachvili, 2011):

$$\sigma_0 = \sqrt{\frac{H_{ls}}{6\pi\gamma}} \tag{1.4}$$

where γ the liquid surface tension, H_{ls} the liquid/substrate Hamaker constant. This length scale is in the order of typical intermolecular distances, which is normally given by the addition of the vdW atomic/molecular radius of two adjacent particles. The liquid/substrate interaction energy has already been used to analyze the stability and rupture of thin liquid films (Ruckenstein and Jain, 1973; Forcada, 1993; Christenson, 1994; Reiter et al., 1999; Vaynblat et al., 2001; Ardekani and Joseph, 2009). To emphasize the importance of this potential energy, it has been shown that substrates of different thickness and chemical composition give rise to different interaction energies, which provoke the motion of nanodroplets positioned on top of this chemical step (Moosavi et al., 2008). Additionally, its impact has been observed on the friction force measured during contact AFM scanning (Lubarski et al., 2006).

The so-called disjoining pressure Π is the attractive interaction between the liquid film free surface

and the substrate surface. It is related to the liquid/substrate interaction energy as follow:

$$\Pi = \frac{1}{\mathcal{A}} \frac{d}{d\varepsilon} \left[\int_{\mathcal{V}} \Phi d\mathcal{V} \right], \tag{1.5}$$

where $\mathcal{A}$ and ε are the surface area and the separation distance between the interacting surfaces, and $\mathcal{V}$ is the film volume. In the case of a flat surface, it results that $\Pi = \Phi$. The determination of analytical expression for the disjoining pressure for films of non-uniform thickness has been the aim of some research (Yi and Wong, 2007; Dai and Leal, 2008), as well as the reconstruction of interaction energies from the AFM measurement of contact angles and dewetting patterns of thin polymer films over solid surfaces (Seemann et al., 2001).

The liquid/substrate interaction energy, or alternatively the disjoining pressure, and the Young-Laplace equation have been combined in order to find the equilibrium shape of sessile drops over solid substrates (de Gennes, 1985; Hocking, 1993a; Yi and Wong, 2007; Snoeijer and Andreotti, 2008; Diaz et al., 2010). The range of perturbation wavelengths for which instabilities occur (Ruckenstein and Jain, 1973), leading to the rupture of the film, its evolution and the rupture time (Ardekani and Joseph, 2009; Rubinstein and Leshansky, 2011) have been analyzed.

The local reduction of the film thickness provokes an increase of the interaction strength between liquid free surface and substrate. An analytical expression of the total liquid/substrate interaction force is not available, because the free surface deformation is unknown in advance. In brief, the deformation of the liquid, provoked by the approach of a probe, is modified by the thickness of the film. Thus, the liquid/substrate interaction is included in this analysis. Another objective is to understand the impact of the film thickness over the probe/liquid minimum separation distance and the maximum liquid free surface deformation.

1.2 Scope

As it has been already mentioned, the non-contact interaction between an AFM probe and a liquid film sample provokes the surface deformation of the latter. In the following sections of the present chapter, the system constituted by a spherical probe, a liquid film and a rigid substrate is described. The probe/liquid and liquid/substrate interaction potentials are deduced, from the integration of the pair potential energy between molecules. Both potentials are inserted in the modified Young-Laplace equation, which portrays the air/liquid interface position out of its pressure difference. The resulting non-linear ordinary differential equation is solved with the application of a numerical method, described at the end of the chapter. The analysis of the faraway surface position, which yields an asymptotic solution, produces some characteristic length scales. As well, symmetry conditions and the linearized equation are discussed in order to give an idea of the liquid response in the vicinity of the probe. The asymptotic solution and the symmetry conditions are incorporated to the numerical scheme. The results are reported in Chapter 2, for a bulk liquid, and in Chapter 2, for films with a finite thickness.

1.3 System description

Consider a flat horizontal solid substrate, over which a stable liquid film of thickness E is deposited. In addition, a spherical probe approaches from the top, and stops at a distance D from the liquid free surface. The space in between the film and the probe, being filled with air, is rarefied and taken as a non-constraining element, thus the air/liquid interface should be considered as a liquid free surface. It is expected that the interaction among the remaining elements creates an effect over the potential field at the film and the position of the free surface, as shown in Fig.1.1. In brief, the sphere/film interaction provokes a pressure difference across the interface and, as a consequence, an axisymmetric deformation of the free surface is induced. On the other hand, the film/substrate interaction and the hydrostatic pressure tend to bound the radial and axial extents of the deformation. The surface tension appears as a contractive force, which opposes the mutation of the free surface from its equilibrium flat shape.

In the following sections, the expressions used to describe the probe/liquid and liquid/substrate interaction potentials are obtained, in order to derive the equation that governs the liquid surface shape. This equation, which also includes surface tension and hydrostatic terms, is one of the foundations of the study to be reported in this thesis.

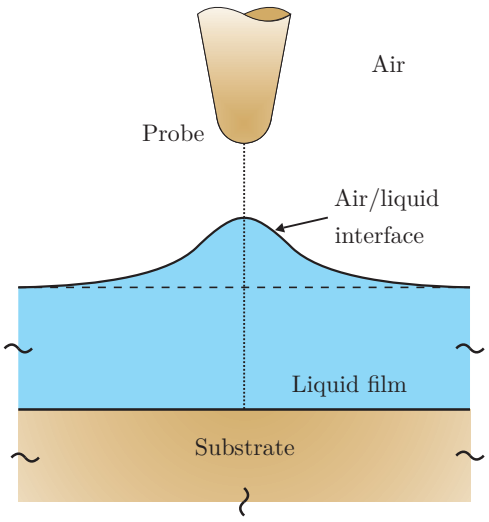


Figure 1.1: System and surface deformation.

1.4 Interaction energies

1.4.a Spherical probe / differential volume of liquid

Partially following the procedure stated in the literature(Hamaker, 1937) for the integration of the vdW forces of macroscopic spheres, a spherical coordinate system is used to obtain the interaction energy between a sphere and an external volume of liquid (see Fig.1.2). Afterwards, a geometric transformation is applied to write the interaction energy in a cylindrical coordinate system, in which the axisymmetric surface deformation problem is easily described.

Within a spherical coordinate system $(\varrho, \theta, \varphi)$, which origin is placed at the point L, the center of a spherical probe of radius R is placed at a distance l from L, as it is represented in Fig.1.2a. For a purely attractive case, the total interaction energy is obtained from the integration over the sphere of the vdW potential pair between each molecule in the sphere and a molecule at the point L. Hence, the interaction energy is given by:

$$\mathcal{E}_p = -\int_{l-R}^{l+R} \frac{\lambda \rho_p}{\varrho^6} S_{ABC} d\varrho,$$

where ρ_p is the density of molecules at the probe, λ is the London-van der Waals (L-vdW) constant, and the surface of the spherical cap S_{ABC} is:

$$S_{ABC} = \int_0^{2\pi} \int_0^{\varphi_0} \varrho^2 \sin(\varphi)\, d\varphi d\theta = 2\pi\varrho^2 \left[1 - \cos(\varphi_0)\right],$$

where φ_0 is the angle formed by the segments $\overline{AL}$ and $\overline{LB}$. Moreover, from the geometry, one knows that:

$$\cos(\varphi_0) = \frac{R^2 - \left(l^2 + \varrho^2\right)}{-2\varrho l}.$$

Therefore, the surface integral is:

$$S_{ABC} = \pi \frac{\varrho}{l} \left[R^2 - (l - \varrho)^2\right],$$

which leads, after integration, to an expression of the interaction energy:

$$\mathcal{E}_p = -\frac{4\pi\rho_p \lambda R^3}{3\left(l^2 - R^2\right)^3}.$$

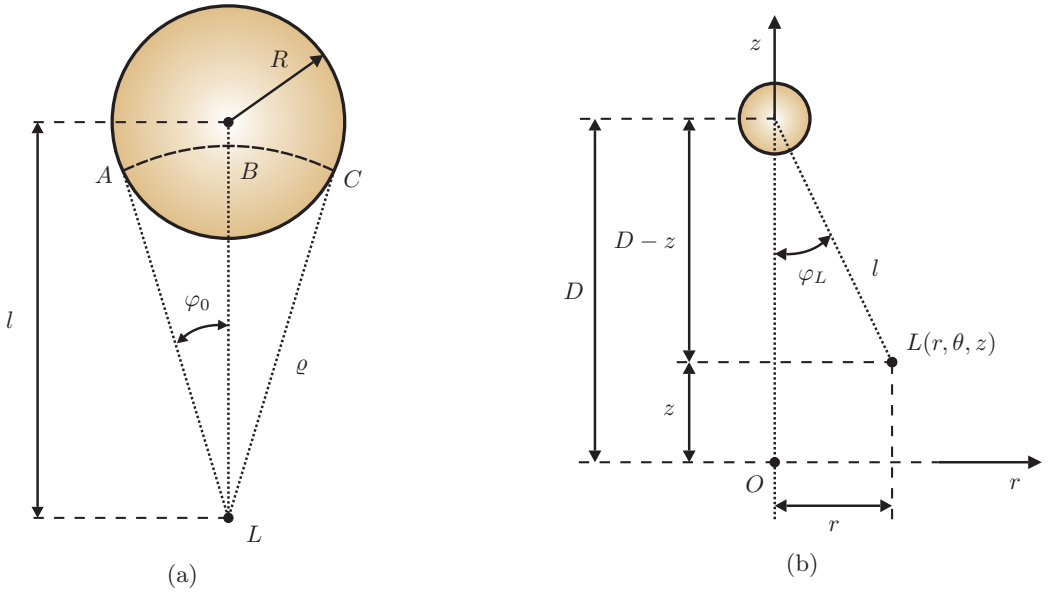


Figure 1.2: Interaction schema of a sphere and a molecule placed at L in (a) a spherical coordinate system and (b) a cylindrical coordinate system.

From the negative of the potential field gradient, the corresponding force is yielded:

$$\overline{F_p} = -\left(\nabla_l \mathcal{E}_p\right)\widehat{l} = -\frac{8\pi\rho_s\lambda R^3 l}{\left(l^2-R^2\right)^4}\widehat{l},$$

where $\widehat{l}$ is the unit vector of the line segment between L and the sphere center, and ∇_l is directional derivative in the direction of $\widehat{l}$. Then, $\overline{F_p}$ is the reciprocal attractive force between the spherical probe and a molecule placed at L. Replacing the molecule at L by a differential volume containing a molecule density, the interaction force is given by:

$$\overline{F_{pl}} = \rho_l \overline{F_p},$$

where ρ_l is the density of molecules at the differential volume. With the definition of the Hamaker constant probe/liquid interaction $H_{pl} = \lambda\pi^2\rho_p\rho_l$, the expression of the force field is written as:

$$\overline{F_{pl}} = -\frac{8H_{pl}R^3 l}{\pi\left(l^2-R^2\right)^4}\widehat{l}.$$

Therefore, $\overline{F_{pl}}$ denotes the reciprocal attractive force between the probe and the differential volume at L.

Now, consider a cylindrical coordinates system (r, θ, z) with its origin at the point O, which is located at a distance D from the center of the sphere, and a distance $\sqrt{r^2+z^2}$ from the point L, like the one shown in Fig.1.2b. The force field exerted by the sphere over the differential volume placed at L, and vice versa, is written in the new system of coordinates as:

$$\overline{F_{pl}} = \left|\overline{F_{pl}}\right|\left[-\sin\left(\varphi_L\right)\widehat{r} + \cos\left(\varphi_L\right)\widehat{z}\right],$$

where $\widehat{r}$ and $\widehat{z}$ are the unit vectors in the radial and axial directions, and φ_L is the angle between the segments connecting L, the sphere center and O, such that $\sin\left(\varphi_L\right) = r/l$ and $\cos\left(\varphi_L\right) = \left(D-z\right)/l$. One should take into account that the distance l is now given by the geometric relationship:

$$l = \sqrt{\left(D-z\right)^2 + r^2}.$$

Note that the force exerted by the sphere over a point at a distance l from its center does not depend on the azimuthal coordinate θ.

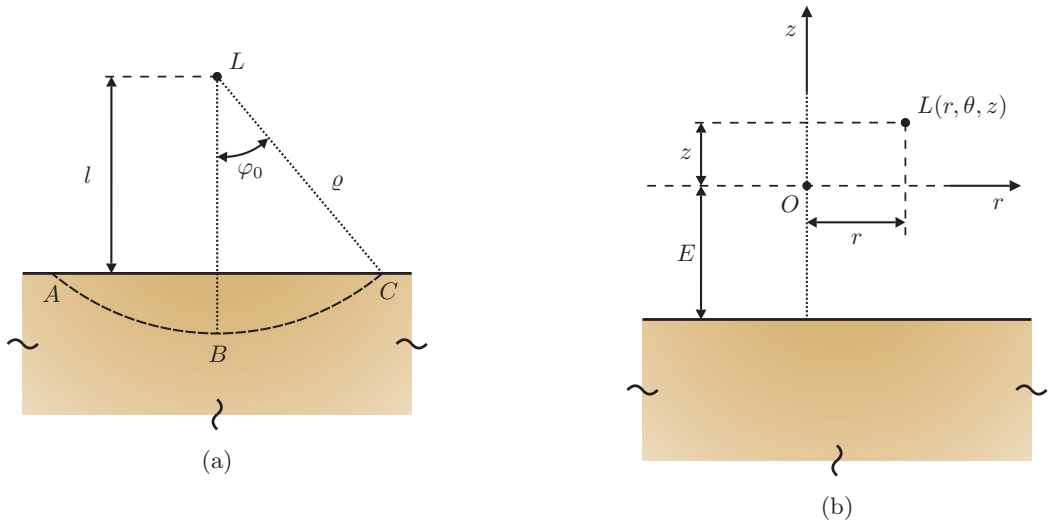


Figure 1.3: Molecule (Differential Volume)-Substrate interaction schema in (a) a spherical coordinate system and (b) a cylindrical coordinate system.

Additionally, one can express the force field as the gradient of a probe/liquid interaction energy:

$$\overline{F_{pl}} = \frac{\partial \Phi_{pl}}{\partial r}\widehat{r} + \frac{1}{r}\frac{\partial \Phi_{pl}}{\partial \theta}\widehat{\theta} + \frac{\partial \Phi_{pl}}{\partial z}\widehat{z},$$

thus, the attractive potential is given by:

$$\Phi_{pl} = \frac{4H_{pl}R^3}{3\pi}\frac{1}{\left[(D-z)^2 + r^2 - R^2\right]^3}. \tag{1.6}$$

This potential energy per unit volume corresponds to the pressure field that any differential volume, placed at the coordinates (r, θ, z) within the liquid film, undergoes due to the proximity of the spherical probe. As shown in the aforementioned expression, the pressure field within the liquid film is only a function of the radial and axial coordinates, r and z. When the probe is located at a relatively large vertical distance, $D \to \infty$, from the originally undeformed liquid surface, the probe/liquid interaction energy takes the value $\Phi_{pl}^{\infty} = 0$.

1.4.b Differential volume of liquid / substrate

Following the procedure stated in the literature(Ruckenstein and Jain, 1973; Yi and Wong, 2007; Dai and Leal, 2008) for the integration of the vdW forces of a semi-infinite solid, a spherical coordinate system is used to obtain the interaction energy between the substrate and an external volume of liquid (see Fig.1.3). Once again, a geometric transformation is applied to write the interaction energy in a cylindrical coordinate system.

Within a spherical coordinate system $(\varrho, \theta, \varphi)$, which origin is placed at the point L, the surface of a semi-infinite solid (substrate) is located at a perpendicular distance l from L, as depicted in Fig.1.3a. For a purely attractive case, the total interaction energy is obtained from the integration over the substrate of the vdW potential pair between each molecule in the substrate and a molecule at the point L. Hence, the interaction energy is given by:

$$\mathcal{E}_s = -\int_l^{\infty} \frac{\lambda \rho_s}{\varrho^6} S_{ABC} d\varrho,$$

where ρ_s is the density of molecules at the substrate, λ is the L-vdW constant, and the surface of the spherical cap S_{ABC} is:

$$S_{ABC} = \int_0^{2\pi}\int_0^{\varphi_0} \varrho^2 \sin(\varphi)\, d\varphi d\theta = 2\pi\varrho^2\left[1 - \cos(\varphi_0)\right],$$

where φ_0 is the angle formed by the segments $\overline{BL}$ and $\overline{LC}$. Moreover, from the geometry, one knows that:

$$\cos(\varphi_0) = \frac{l}{\varrho},$$

Therefore, the surface integral is:

$$S_{ABC} = 2\pi\varrho\left[\varrho - l\right],$$

which leads, after integration, to an expression of the interaction energy:

$$\mathcal{E}_s = -\frac{\pi\rho_s\lambda}{6l^3}.$$

From the negative of the potential field gradient, the corresponding force is yielded:

$$\overline{F_s} = -\left(\nabla_l\mathcal{E}_s\right)\widehat{l} = -\frac{\pi\rho_s\lambda}{2l^4}\widehat{l},$$

where $\widehat{l}$ is the unit vector of the line segment between L and B, perpendicular to the substrate surface, and ∇_l is directional derivative in the direction of $\widehat{l}$. Then, $\overline{F_s}$ is the reciprocal attractive force between the substrate and a molecule placed at L. Replacing the molecule at L by a differential volume containing a molecule density, the interaction force is given by:

$$\overline{F_{ls}} = \rho_l\overline{F_s},$$

where ρ_l is the density of molecules at the differential volume. With the definition of the Hamaker constant liquid/substrate interaction $H_{ls} = \lambda\pi^2\rho_l\rho_s$, the expression of the force field is written as:

$$\overline{F_{ls}} = -\frac{H_{ls}}{2\pi l^4}\widehat{l}.$$

Therefore, $\overline{F_{ls}}$ denotes the reciprocal attractive force between the differential volume placed at L and the substrate.

Now, consider a cylindrical coordinates system (r, θ, z) with its origin at the point O, which is located at a distance E perpendicular to the substrate surface, and a distance $\sqrt{r^2+z^2}$ from the point L, like the one shown in Fig.1.3b. The force field exerted by the substrate over the differential volume placed at L, and vice versa, is written in the new system of coordinates as:

$$\overline{F_{ls}} = -\left|\overline{F_{ls}}\right|\widehat{z},$$

where $\widehat{z}$ is the unit vector in the axial direction. One should take into account that the distance l i now given by the relationship $l = E + z$. Note that the force exerted by the substrate over a point at a distance l from its surface does not depend on the radial and azimuthal coordinates, r and θ.

Additionally, one can express the force field as the gradient of a liquid/substrate interaction energy:

$$\overline{F_{ls}} = \frac{\partial\Phi_{ls}}{\partial r}\widehat{r} + \frac{1}{r}\frac{\partial\Phi_{ls}}{\partial\theta}\widehat{\theta} + \frac{\partial\Phi_{ls}}{\partial z}\widehat{z},$$

thus, the attractive potential is given by:

$$\Phi_{ls} = -\frac{H_{ls}}{6\pi\left(E+z\right)^3}. \tag{1.7}$$

This potential energy per unit volume corresponds to the pressure field that any differential volume, placed at the coordinates (r, θ, z) within the liquid film, undergoes due to the proximity of the substrate. As shown in the aforementioned expression, the pressure field within the liquid film is only a function of the axial coordinate z. When the liquid film is unperturbed and the liquid surface remains at the equilibrium position $z = 0$, the liquid/substrate interaction energy takes the value $\Phi_{ls}^{\infty} = -H_{ls}/6\pi E^3$, at the free surface.

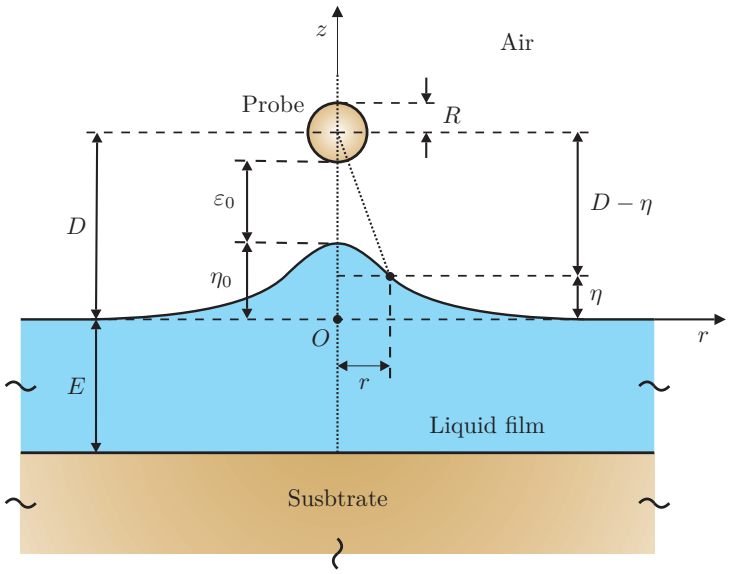


Figure 1.4: Probe/Liquid film/Substrate interaction schema.

1.5 Pressure difference at the liquid surface

Now, in a cylindrical system of coordinates (r, θ, z), consider the problem depicted in Fig.1.4. A liquid film is deposited over a flat solid substrate, at the axial position $z = -E$, and its free surface is located at the horizontal plane $z = 0$. The liquid film is unbounded in the radial direction, hence it is considered as an infinite reservoir in this direction and no constraint on the volume conservation is required. In addition, the center of a perfectly rigid sphere of radius R is lined up with the vertical axis $r = 0$, and placed at an axial distance $z = D$.

In this way, the pressure difference $\Delta P = P_{film} - P_{air}$ across the interface located at $z = \eta$, is described by the following modified Young-Laplace equation:

$$\Delta P = \Delta\rho g\eta + 2\gamma\kappa + \Pi_{pl} + \Pi_{ls}, \tag{1.8}$$

where $\Delta\rho = \rho_{film} - \rho_{air}$ is the liquid/air density difference, g is the acceleration of gravity, η is the local surface position, γ is the liquid/air surface tension, κ is the local mean curvature, Π_{pl} and Π_{ls} are the probe/liquid and the liquid/substrate interaction potentials, determined in the previous sections.

The local mean curvature, expressed in axisymmetric cylindrical coordinates, takes the form:

$$\kappa = -\frac{1}{2}\left(\frac{1}{r}\frac{\partial}{\partial r}\left[r\frac{\partial\eta}{\partial r}\left\{\left(\frac{\partial\eta}{\partial r}\right)^2 + 1\right\}^{-1/2}\right]\right). \tag{1.9}$$

Each interaction potential that contributes to the interface deformation corresponds to the potential energy difference between the perturbed state and the originally undisturbed state. At the liquid surface $z = \eta$, the interaction potential mutually exerted between the spherical probe and the liquid film is given by:

$$\Pi_{pl} = \left(\Phi_{pl} - \Phi_{pl}^{\infty}\right) = -\frac{4H_{pl}R^3}{3\pi}\frac{1}{\left[(D-\eta)^2 + r^2 - R^2\right]^3}, \tag{1.10}$$

where H_{pl} is the Hamaker constant of the probe/liquid interaction. In turn, the potential field created by the interaction between the substrate and the liquid film, at $z = \eta$, is described by:

$$\Pi_{ls} = \left(\Phi_{ls} - \Phi_{ls}^{\infty}\right) = -\frac{H_{ls}}{6\pi}\left[\frac{1}{(E+\eta)^3} - \frac{1}{(E)^3}\right], \tag{1.11}$$

where H_{ls} is the Hamaker constant of the liquid/substrate interaction.

Now, taking the probe radius R and the gap $D - R$ as the characteristic length scales, one finds several dimensionless quantities. The dimensionless film thickness and probe position are now defined as:

$$E^* = \frac{E}{R} \qquad\qquad D^* = \frac{D}{R}, \tag{1.12}$$

the dimensionless radial and axial coordinates are given by:

$$r^* = \frac{r}{R} \qquad\qquad z^* = \frac{z}{R}, \tag{1.13}$$

and the dimensionless free surface position and surface curvature are written as:

$$\eta^* = \frac{\eta}{D - R} \qquad\qquad \kappa^* = \kappa R. \tag{1.14}$$

A further inspection of Fig.1.4, leads to the appearance of other two important quantities, which will help to understand the interaction phenomenon. Imagine that the probe/liquid interaction can be turned on/off. Before starting our hypothetical experiment, the initial gap $\xi = D - R$ is defined as the space in between the sphere surface and the $z = 0$ plane, which corresponds to the position of the unperturbed liquid free surface. Once the interaction potential is switched on, the surface deformation is observed and the equilibrium gap ε_0 is defined as the separation distance between the sphere surface and the deformed liquid surface at $r = 0$. Finally, the dimensionless initial and equilibrium gaps are defined as:

$$\xi^* = \frac{D - R}{R} \qquad\qquad \varepsilon_0^* = \frac{\varepsilon_0}{D - R}. \tag{1.15}$$

Note that ξ^* corresponds to the ratio of the two characteristic length scales of the problem.

Therefore, with the use of these dimensionless quantities, eq.(1.8) can be rewritten as:

$$\Delta P^* = \frac{R}{\gamma \xi^*} \Delta P = B_o \eta^* + \frac{2}{\xi^*} \kappa^* + \frac{H_a}{\xi^*} \Pi_{pl}^* + \frac{A H_a}{8 \xi^* \left(E^*\right)^3} \Pi_{ls}^*, \tag{1.16}$$

where:

$$\kappa^* = -\frac{\xi^*}{2} \left(\frac{1}{r^*} \frac{\partial}{\partial r^*} \left[r^* \frac{\partial \eta^*}{\partial r^*} \left\{ \left(\xi^* \frac{\partial \eta^*}{\partial r^*} \right)^2 + 1 \right\}^{-1/2} \right] \right) \tag{1.17a}$$

$$\Pi_{pl}^* = \frac{-1}{\left[\left(D^* - \xi^* \eta^* \right)^2 + \left(r^* \right)^2 - 1 \right]^3} \tag{1.17b}$$

$$\Pi_{ls}^* = -\left[\left(1 + \frac{\xi^* \eta^*}{E^*} \right)^{-3} - 1 \right]. \tag{1.17c}$$

In eq.(1.16), we find the three dimensionless parameters that will be used to characterize the surface behavior. Among them, one finds the Bond number:

$$B_o = \frac{\Delta \rho g R^2}{\gamma}, \tag{1.18}$$

which compares the surface tension and gravity forces; a modified Hamaker number:

$$H_a = \frac{4 H_{pl}}{3 \pi \gamma R^2}, \tag{1.19}$$

which weighs probe/liquid interaction and surface tension forces; and the Hamaker constant ratio:

$$A = \frac{H_{ls}}{H_{pl}}, \tag{1.20}$$

which gives a relation between strength of probe/liquid and liquid/substrate interaction forces.

Orders of magnitude

The presented dimensionless analysis gives rise to an equation that is valid for a system involving a probe of arbitrary size. In addition, as it is clearly observed from the parameter definitions, H_a and B_o are coupled by R. Hence, their values only depend on the combination of physical properties, following the product:

$$H_a B_o = \frac{4}{3\pi}\left[\frac{H_{pl}\Delta\rho g}{\gamma^2}\right]. \tag{1.21}$$

For real systems (Israelachvili, 2011; Bergstrom, 1997; Visser, 1972; Mougin and H., 2003) , the probe/liquid Hamaker constant is $H_{pl} \in \left[10^{-21}, 10^{-19}\right]$ J and the liquid/substrate equivalent is in the same range $H_{pl} \sim H_{ls}$. In addition, typical room temperature liquids present a surface tension $\gamma \in \left[10^{-2}, 10^{-1}\right]$ N/m, a density difference $\Delta\rho \in \left[10^{2}, 10^{3}\right]$ kg/m^3 with respect to air, and a viscosity of $\mu \in \left[10^{-4}, 10^{0}\right]$ Pa s. Considering common AFM probes with a tip radius $R \simeq 10^{-8}$ m, the range of the dimensionless parameters defined in eqs.(1.18), (1.19) and (1.20) remains within $B_o \in \left[10^{-11}, 10^{-10}\right]$, $H_a \in \left[10^{-5}, 10^{-1}\right]$ and $A \in \left[10^{-2}, 10^{2}\right]$. For AFM probes, with $R \simeq 10^{-7}$ m, the range of the two first dimensionless parameters changes to $B_o \in \left[10^{-9}, 10^{-8}\right]$ and $H_a \in \left[10^{-6}, 10^{-3}\right]$.

1.6 Curvature decomposition

The assumption of small interface displacements, $\xi^*\left(d\eta^*/dr^*\right) \ll 1$, allows us to write the local mean curvature as a less complicated expression:

$$\kappa^* \simeq -\frac{\xi^*}{2}\left(\frac{1}{r^*}\frac{\partial}{\partial r^*}\left[r^*\frac{\partial \eta^*}{\partial r^*}\right]\right). \tag{1.22}$$

In this way, the dimensionless mean curvature κ^* is decomposed in two principal curvatures, as follows:

$$\kappa^* = \frac{1}{2}\left(\kappa_m^* + \kappa_a^*\right) \tag{1.23a}$$

$$\kappa_m^* = -\xi^*\left(\frac{d^2\eta^*}{dr^{*2}}\right) \qquad \kappa_a^* = -\xi^*\left(\frac{1}{r^*}\frac{d\eta^*}{dr^*}\right), \tag{1.23b}$$

where κ_m^* is the dimensionless meridional curvature, and κ_a^* is the dimensionless azimuthal curvature. The meridional component κ_m^* represents the axisymmetric curvature of the interface which determines the behavior of the profile at any axial plane, whereas the azimuthal curvature κ_a^* is the projection of the circle describing iso-deformation contour lines in the direction normal to the interface. This curvature decomposition will be used for describing the surface behavior and the involved physical mechanisms. Mainly at the inflection points, where a curvature component or both become equal to zero, particular surface features are observed.

1.7 Asymptotic analysis

1.7.a Far from the probe ($r^* \to \infty$)

An asymptotic behavior exists provided that the air/liquid interface rests in equilibrium, which is equal to set $\Delta P^* = 0$ in eq.(1.17b). Far from the vertical axis, where $r^* \gg 0$, the probe/liquid interaction potential is negligible $\Pi_{pl}^* \approx 0$. As a consequence, the surface is undisturbed and nearly flat $\xi^*\left(d\eta^*/dr^*\right) \ll 1$, and thence the local mean curvature can be approximated with eq.(1.22). As well, one can assume that the deformation-to-thickness ratio is small $\xi^*\eta^*/E^* \ll 1$, and that the liquid/substrate interaction potential can be approximated with a binomial expansion, as explained in Appendix D. The first-order approximation of eq.(1.17c) is given by:

$$\Pi_{ls}^* \simeq 3\frac{\xi^*\eta^*}{E^*}, \tag{1.24}$$

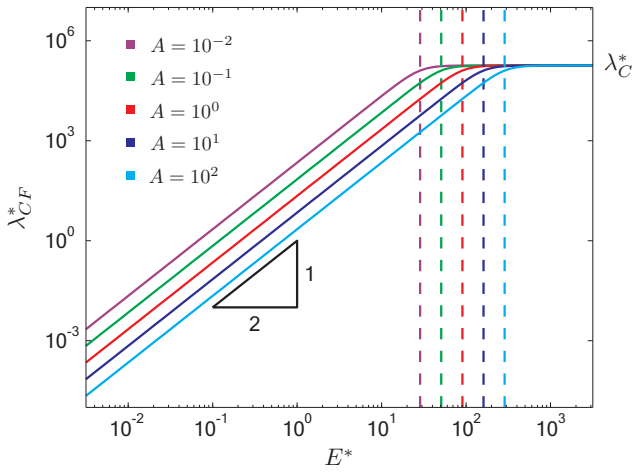


Figure 1.5: Modified capillary length λ^*_{CF} as a function of the film thickness E^*, for different values of the Hamaker ratio A and the dimensionless numbers $H_a = 5.48 \times 10^{-3}$ and $B_o = 3.07 \times 10^{-11}$. Continuous lines [——] indicate the behavior of λ^*_{CF}, whereas dashed lines [– – –] show the thickness at which $\lambda^*_{CF} = \lambda^*_C$.

Therefore, eq.(1.16) is simplified to the following linear differential equation:

$$\frac{1}{r^*}\frac{d}{dr^*}\left[r^*\frac{d\eta^*}{dr^*}\right] - \left[\frac{1}{(\lambda^*_C)^2} + \frac{1}{(\lambda^*_F)^2}\right]\eta^* = 0, \tag{1.25}$$

where λ_C is the conventional capillary length, given by:

$$\lambda_C = \sqrt{\frac{\gamma}{\Delta\rho g}}, \qquad \lambda^*_C = \frac{\lambda_C}{R} = \sqrt{\frac{1}{B_o}}, \tag{1.26}$$

and λ_F is a characteristic length of the film, given by:

$$\lambda_F = \sqrt{\frac{2\pi\gamma E^4}{H_{ls}}}, \qquad \lambda^*_F = \frac{\lambda_F}{R} = \sqrt{\frac{8\,(E^*)^4}{3AH_a}}, \tag{1.27}$$

which corresponds to the radial distance beyond which the liquid/substrate interaction contributes to the flattening of the liquid surface. Accordingly, the asymptotic behavior, depicted by the preceding equation, indicates that the leading effect of the film thickness shows up as a restriction to the radial extent of the deformation by means of a modified capillary length λ^*_{CF}, which is defined as:

$$\lambda_{CF} = \frac{\lambda_C\lambda_F}{\sqrt{(\lambda_C)^2 + (\lambda_F)^2}}, \qquad \lambda^*_{CF} = \frac{\lambda_{CF}}{R} = \frac{\lambda^*_C\lambda^*_F}{\sqrt{(\lambda^*_C)^2 + (\lambda^*_F)^2}}. \tag{1.28}$$

The dependency of λ^*_{CF} on the film thickness E^* and the Hamaker ratio A is shown in Fig.1.5. For thick films, $E^* \geq 10^3$, the film characteristic length is larger than the capillary length $\lambda^*_F \gg \lambda^*_C$, thus the modified capillary length is given by $\lambda^*_{CF} \approx \lambda^*_C$, being independent of the film thickness. A reduction of λ^*_F is provoked when E^* is decreased and, as it is explicit in eq.(1.28), λ^*_{CF} decays slowly. For very thin films, assuming that $\lambda^*_F \ll \lambda^*_C$, the modified capillary length tends to take the value of the characteristic film length, $\lambda^*_{CF} \to \lambda^*_F$. In this case, $\lambda^*_{CF} \sim \sqrt{E^*}$, in agreement with the shallow film behavior depicted in Fig.1.5. In addition, there exists a certain thickness at which $\lambda^*_F = \lambda^*_C$, corresponding to the transition between the two behaviors. Associated with this idea, the impact of A over the modified capillary length is easily deduced. A displacement of the transition toward a shorter E^* is observed when the value of A is lessened.

The comparison of both characteristic length scales, λ_C and λ_F, within the definition of λ^*_{CF}, indicates which one of the two mechanisms, gravity or liquid/substrate interaction, prevails and controls the radial extent of the surface deformation. The value of λ^*_{CF} determines the position beyond which the asymptotic

regime can be applied as a boundary condition. In the recent literature (Quinn et al., 2013), developed concurrent with our study, the inverse-square of λ^*_{CF} has been introduced as an effective Bond number B_o^{eff}, defined as:

$$B_o^{eff} = B_o + \frac{3AH_a}{8\left(E^*\right)^4}, \tag{1.29}$$

which indicates whether or not the effect of the substrate is negligible.

With the new length scale λ^*_{CF}, eq.(1.25) can be rewritten as:

$$\frac{1}{r^*}\frac{d}{dr^*}\left[r^*\frac{d\eta^*}{dr^*}\right] - \frac{\eta^*}{\left(\lambda^*_{CF}\right)^2} = 0, \tag{1.30}$$

which presents the exact solution:

$$\eta^* = GK_0\left(\frac{r^*}{\lambda^*_{CF}}\right), \tag{1.31}$$

where K_0 is a zero order modified Bessel function of the second kind, and G is a coefficient, to be obtained from the deformation at a radial position far from the vertical axis, e.g. $r^* = \alpha\lambda^*_{CF}$ being α a real positive number and customarily $\alpha > 1$. An example of this asymptotic solution is reported in Fig.1.6b.

Moreover, the properties of the modified Bessel functions allow us to find the slope of the asymptotic deformation profile, which is given by:

$$\frac{d\eta^*}{dr^*} = -\frac{G}{\lambda^*_{CF}}K_1\left(\frac{r^*}{\lambda^*_{CF}}\right),$$

where K_1 is a first order modified Bessel function of the second kind. Solving eq.(1.31) for G and substituting the outcome in the previous derivative, at $r^* = \alpha\lambda^*_{CF}$, generates the following relation:

$$\left.\frac{d\eta^*}{dr^*}\right|_{\alpha\lambda^*_{CF}} + \frac{K_1(\alpha)}{K_0(\alpha)}\left[\frac{\left.\eta^*\right|_{\alpha\lambda^*_{CF}}}{\lambda^*_{CF}}\right] = 0. \tag{1.32}$$

It is important to note that when the argument of the Bessel functions is $\alpha \gg 1$, their ratio is $K_1(\alpha)/K_0(\alpha) \to 1$. Unlike eq.(1.31), which requires the imposition of G to estimate η^* at $r^* = \alpha\lambda^*_{CF}$, eq.(1.32) has the advantage of being given only by the shape of the surface at $r^* = \alpha\lambda^*_{CF}$. Therefore, eq.(1.32) results to be a natural Robin boundary condition.

In brief, as a result of the previous asymptotic analysis, eq.(1.32) can be used as the boundary condition at the distant radial position $r^* = \alpha\lambda^*_{CF}$. It will be used to limit the radial domain, in the numerical solution of eq.(1.16).

1.7.b Close to the probe ($r^* \to 0$)

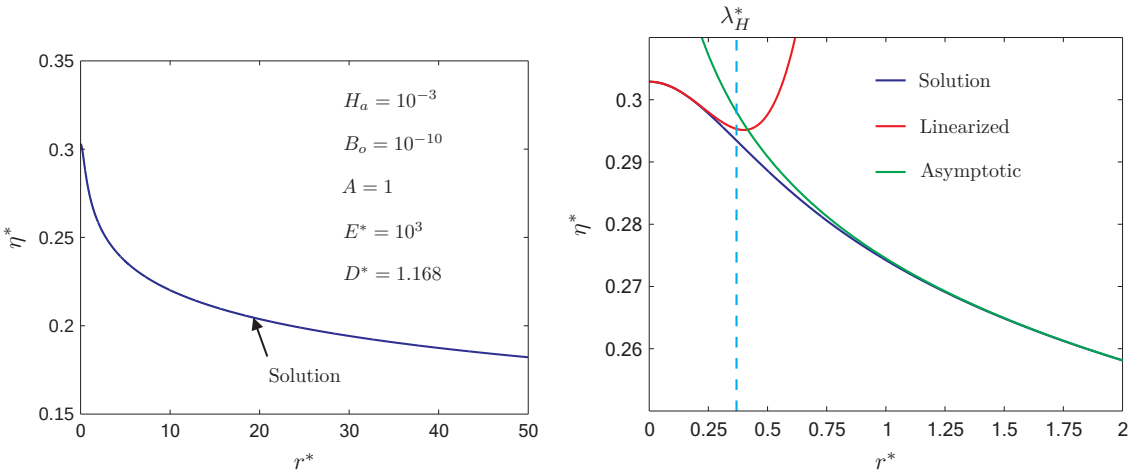
Once again, considering equilibrium conditions, i.e. $\Delta P^* = 0$, the highest position of the deformed liquid is found at its closest point to the probe surface, which, as one should expect, corresponds to the radial position $r^* = 0$. At this surface apex, one finds the apex deformation η_0^* and the peak curvature κ_0^*. Considering that the surface shows an axisymmetric profile, the symmetry condition is given by:

$$\left.\frac{d\eta^*}{dr^*}\right|_0 = 0, \tag{1.33}$$

which is to be applied as a boundary condition, in the solution of eq.(1.16).

Additionally, in the neighborhood of the vertical axis $r^* = 0$, the Taylor series of the first derivative of the deformation η^* with respect to the radial position r^* is, in dimensionless terms:

$$\frac{d\eta^*}{dr^*} \approx \left.\frac{d\eta^*}{dr^*}\right|_0 + \left.\frac{d^2\eta^*}{dr^{*2}}\right|_0 r^* + O\left\{r^{*2}\right\},$$



(a) (b)

Figure 1.6: (a) Exact solution of eq.(1.16) and (a) zoom of the central region, compared to the asymptotic approximations, given by eq.(1.31) with $G = 3.97 \times 10^{-3}$ and $\lambda^*_{CF} = \lambda^*_C = 10^5$, and eq.(1.38) with $\xi^* = 0.1682$, $\eta^*_0 = 0.3029$, $C_0 = -0.3886$ and $C_1 = 4.8670$, which corresponds to the values $\kappa^*_0 = 0.0326$, $\lambda^*_H = 0.3693$ and $b = 0.6247$.

which, after applying the above-mentioned symmetry boundary condition and dividing by r^*, is transformed into:

$$\frac{1}{r^*}\frac{d\eta^*}{dr^*} \approx \left.\frac{d^2\eta^*}{dr^{*2}}\right|_0 + O\left(r^*\right).$$

Now, taking into account the symmetry boundary condition, the local mean curvature at the vertical axis is inherently given by:

$$\kappa^*_0 = -\frac{\xi^*}{2}\left(\frac{1}{r^*}\frac{\partial}{\partial r^*}\left[r^*\frac{\partial\eta^*}{\partial r^*}\right]\Bigg|_0\right) = -\frac{\xi^*}{2}\left(\left.\frac{d^2\eta^*}{dr^{*2}}\right|_0 + \left[\frac{1}{r^*}\frac{d\eta^*}{dr^*}\right]\Bigg|_0\right),$$

which, with the employment of the previously developed of the Taylor expansion, turns into:

$$\kappa^*_0 = -\xi^*\left(\left.\frac{d^2\eta^*}{dr^{*2}}\right|_0\right). \tag{1.34}$$

This expression must be used to evaluate eq.(1.16) at $r^* = 0$, in order to obtain a numerical solution.

Linearizing eq.(1.16) in the vicinity of $r^* = 0$, and considering the small deformation approximation and a negligible B_o term at this radial position, gives the following simplified equation:

$$\frac{1}{r^*}\frac{d}{dr^*}\left[r^*\frac{d\eta^*}{dr^*}\right] - C_0 - C_1\left(r^*\right)^2 = 0, \tag{1.35}$$

where:

$$C_0 = \frac{H_a}{\xi^*}\Pi^*_{pl}\Big|_0 - \frac{AH_a}{8\xi^*\left(E^*\right)^3}\left[\Pi^*_{ls}\Big|_0 - 1\right]$$

$$C_1 = \frac{3H_a}{\xi^*}\left[\Pi^*_{pl}\Big|_0\right]^{4/3}\left[1 + \kappa^*_0\left(D - \xi^*\eta^*_0\right)\right] + \frac{3AH_a}{16\xi^*\left(E^*\right)^4}\kappa^*_0\left[\Pi^*_{ls}\Big|_0\right]^{4/3}.$$

The analytical solution of eq.(1.35), using the symmetry boundary condition at $r^* = 0$, is:

$$\eta^* \simeq \eta^*_0 + \frac{C_0}{4}\left(r^*\right)^2 + \frac{C_1}{16}\left(r^*\right)^4.$$

In this way, one notes that the surface deformation shows a parabolic shape around $r^* = 0$. An example of this surface shape approximation is displayed in Fig.1.6. As well, the second derivative of this solution

is:

$$\frac{d^2\eta^*}{dr^{*2}} \simeq \frac{C_0}{2} + \frac{3C_1}{4}\left(r^*\right)^2,$$

which, making use of eq.(1.34), yields the following expression of C_0 in terms of the peak curvature κ_0^*:

$$C_0 = \frac{-2\kappa_0^*}{\xi^*}.$$

As well, the second derivative of this approximative solution is used to estimate the radial position λ_H^* at which of the profile presents an inflection point, occurring when $\kappa_m^* = 0$. Therefore, from this reasoning and the definition of κ_m^* given in eq.(1.23), one has:

$$\lambda_H^* \sim \sqrt{\frac{-2C_0}{3C_1}}, \tag{1.36}$$

from which, one can deduce C_1 in terms of the inflection radial position λ_H^*:

$$C_1 = \frac{4\kappa_0^*}{3\xi^*\left(b\lambda_H^*\right)^2}, \tag{1.37}$$

where b is a correction factor that should be obtained from the comparison with the exact deformation profile. Thus, around $r^* = 0$, a similarity solution is found:

$$\frac{\xi^*\left(\eta^* - \eta_0^*\right)}{\kappa_0^*\left(\lambda_H^*\right)^2} \simeq -\frac{b^2}{2}\left[1 - \frac{1}{6}\left(\frac{r^*}{b\lambda_H^*}\right)^2\right]\left(\frac{r^*}{b\lambda_H^*}\right)^2, \tag{1.38}$$

which relates the reduced deformation profile $\xi^*\left(\eta^* - \eta_0^*\right)/\kappa_0^*\left(\lambda_H^*\right)^2$ and the reduced radial position r^*/λ_H^*.

The disadvantage of this approximative solution is that it requires the knowledge of the apex variables η_0^* and κ_0^*, and the surface inflection position λ_H^*, which are a priori unknown. Thus, despite the effort done to find an analytical approximation, we must solve eq.(1.16) by numerical means, in order to calculate the surface deformation. Nevertheless, once the numerical results are analyzed, if simple relationships are deduced to relate the variables η_0^*, κ_0^* and λ_H^* with the problem parameters H_a, A and B_o, then, eqs.(1.31) and (1.38) may be used to quickly describe the surface shape, as it is shown in Fig.1.6b.

1.8 Numerical method

When the sphere/liquid system is in equilibrium, the pressure difference across the air/liquid interface is $\Delta P^* = 0$. In these conditions, the Ordinary Differential Equation (ODE) given in eq.(1.16) describes a Boundary Value Problem (BVP), with separated Boundary Conditions (BCs). It shows a singularity at one of its endpoints, radial axis origin $r^* = 0$, and specifications in a semi-infinite range because $r^* \in [0, \infty[$.

The singularity problem is outreached with the employment of eq.(1.34). Therefore, eq.(3.1) is written as a system of non-linear ODEs, as follows:

$$\frac{d\eta^*}{dr^*} = u^* \tag{1.39a}$$

$$\frac{du^*}{dr^*} = \begin{cases} \dfrac{1}{2}\left[B_o\xi^*\eta^* + \dfrac{AH_a}{8\left(E^*\right)^3}\Pi_{ls}^* + H_a\Pi_{pl}^*\right] & \text{for } r^* = 0 \\ -\dfrac{u^*}{r^*}\left[\left(u^*\right)^2 + 1\right] + \left[B_o\xi^*\eta^* + \dfrac{AH_a}{8\left(E^*\right)^3}\Pi_{ls}^* + H_a\Pi_{pl}^*\right]\left[\left(u^*\right)^2 + 1\right]^{3/2} & \text{for } r^* > 0, \end{cases} \tag{1.39b}$$

where u^* is the first spatial derivative of the liquid surface position, and Π_{ls}^* and Π_{pl}^* are functions of r^* and η^*, as introduced in eqs.(1.17c) and (1.17b).

To deal with the semi-infinite range, we make use of eq.(1.32). Hence, the BCs are given by:

$$u^* = 0 \qquad \text{at } r^* = 0 \tag{1.40a}$$

$$u^* + \frac{K_1(\alpha)}{K_0(\alpha)}\left[\frac{\eta^*}{\lambda^*_{CF}}\right] = 0 \qquad \text{at } r^* = \alpha\lambda^*_{CF}, \tag{1.40b}$$

where α is a positive real number. The second BC must be given at a radial position greater than the modified capillary length, then $\alpha > 1$ should be chosen.

Due to the non-linearity of the system and the inherent behavior of BVPs, simultaneous solutions of eq.(1.39) exist. In order to find a solution of particular interest, an estimate of the solution, an "educated guess", is required. Based on the BCs, the educated guess for $r^* \in [0, \alpha\lambda^*_{CF}]$ can take the form:

$$u^* = -\frac{\eta^*_{guess}}{\alpha\lambda^*_{CF}}, \qquad \eta^* = \eta^*_{guess}\left(1 - \frac{r^*}{\alpha\lambda^*_{CF}}\right), \tag{1.41a}$$

where η^*_{guess} is the guess solution of the interface apex position. Depending on the proposed values of η^*_{guess}, different shapes of the interface profile are found.

The two-point BVP represented by eqs.(1.39) and (1.40) is worked out using a MATLAB routine. This tool includes the solver *bvp4c.m* (Kierzenka and Shampine, 2001), which uses a 3-stage Lobatto IIIa implicit Runge-Kutta formula (the so-called Simpson method (Shampine et al., 2003)) with a natural interpolant. Because of the smooth shape of the composing functions of the system expressed in eqs.(1.39), the solution is easily found with the proposed method (for further details see Appendix A).

In the present study, interface profiles were calculated with a radial extension up to three times the modified capillary length. The value $\alpha = 3$ was set to avoid the modification of the surface profile and minimize the approximation error. Solutions were obtained using $N = 6000$ logarithmically spaced mesh points and a tolerance on the residual of $\sigma_{Tol} = 10^{-4}$.

1.9 Concluding remarks

The modified Young-Laplace equation, that describes the surface deformation of a liquid film deposited over a rigid substrate and in interaction with a spherical probe, has been derived. The probe/liquid and liquid/substrate interactions were included in the modeling. An asymptotic solution and characteristic length scales defining the radial extent of the deformation profile were discussed. The apex deformation was analyzed, yielding some symmetry conditions and an analytical expression to evaluate the surface shape near the apex. Finally, a numerical method to solve the non-linear ODE was presented, along with the appropriate boundary conditions.

Chapter 2

Equilibrium behavior of a bulk liquid

When the air/liquid interface is in equilibrium, i.e. when the spherical probe is static and the evolution of the surface deformation has already reached a stationary regime, the pressure difference across the interface is $\Delta P^* = 0$. Considering a film with a large relative thickness $E^* \to \infty$, the liquid/substrate interaction becomes negligible at the liquid surface, and eq.(1.16) simplifies to:

$$B_o \xi^* \eta^* + 2\kappa^* + H_a \Pi_{pl}^* = 0, \tag{2.1}$$

where the local mean curvature κ^* and probe/liquid interaction Π_{pl}^*, are defined as:

$$\kappa^* = -\frac{\xi^*}{2}\left(\frac{1}{r^*}\frac{\partial}{\partial r^*}\left[r^* \frac{\partial \eta^*}{\partial r^*}\left\{\left(\xi^* \frac{\partial \eta^*}{\partial r^*}\right)^2 + 1\right\}^{-1/2}\right]\right)$$

$$\Pi_{pl}^* = \frac{-1}{\left[\left(D^* - \xi^* \eta^*\right)^2 + \left(r^*\right)^2 - 1\right]^3}.$$

This equation must be solved in order to find the surface shape of a very thick film, which shall be treated as a bulk liquid body.

The equivalent ODEs system given by eqs.(1.39) is numerically solved (see Section1.8), considering the appropriated weight of the liquid/substrate potential, i.e. $\Pi_{ls}^* = 0$. As well, $\lambda_{CF}^* = \lambda_C^*$ should be used in the BCs and the guess solution, expressed in eq.(1.40) and eq.(1.41), respectively.

For a given combination of dimensionless parameters, the modified Hamaker H_a and Bond B_o numbers, the interface position depends completely on the relative value of the separation distance D^*. If D^* is greater than a threshold value D_{min}^*, a "bump-like" equilibrium profile is attained. On the other hand, if D^* is smaller than D_{min}^*, the interface deformation grows until the liquid touches the sphere, developing the so-called "jump-to-contact" processes and the formation of a liquid capillary bridge (Orr et al., 1975). As a consequence, an equilibrium state is not obtained because, for a given combination of parameters, a numerical solution of eqs.(1.39) does not exist. Therefore, the equilibrium interface profile converges toward a solution only if $D^* \geq D_{min}^*$.

Examples of the typical equilibrium deformation profiles are shown in Fig.2.1, for different values of D^* and a single combination of parameters H_a and B_o. The provided guess solution is an initially flat surface placed at the horizontal plane, with $\eta_{guess}^* = 0$. As it is clearly depicted in the deformation profile shown in Fig.2.1a, the sphere pulls the interface towards itself only at a very reduced zone near the symmetry axis, also shown in Fig.2.1b which is a central region zoom. For $D^* \in [D_{min}^*, 1.2D_{min}^*]$, at $r^* \simeq 0$, the magnitude of the corresponding apex deformation provokes that $O\left\{\left(D^* - \xi^* \eta_0^*\right)^2 - 1\right\} \in \left[10^{-1}, 10^0\right]$, which in turn engenders a local interaction potential of the order $O\left\{\Pi_{pl}^*\right\} \in \left[10^0, 10^3\right]$. In the proximity of the vertical axis, due to the strength of the interaction, the surface shows a nearly parabolic shape. As well, at the same range $D^* \in [D_{min}^*, 1.5D_{min}^*]$, but for $r^* \gtrsim 10$, one finds that $O\left\{\left(D^* - \xi^* \eta_0^*\right)^2 - 1\right\} \in \left[10^{-1}, 10^0\right]$, being small compared to $O\left\{r^2\right\} \gtrsim 10^2$, which generates an interaction potential of $O\left\{\Pi_{pl}^*\right\} \lesssim 10^{-6}$. Therefore, from $r^* \simeq 10^2$ and beyond,

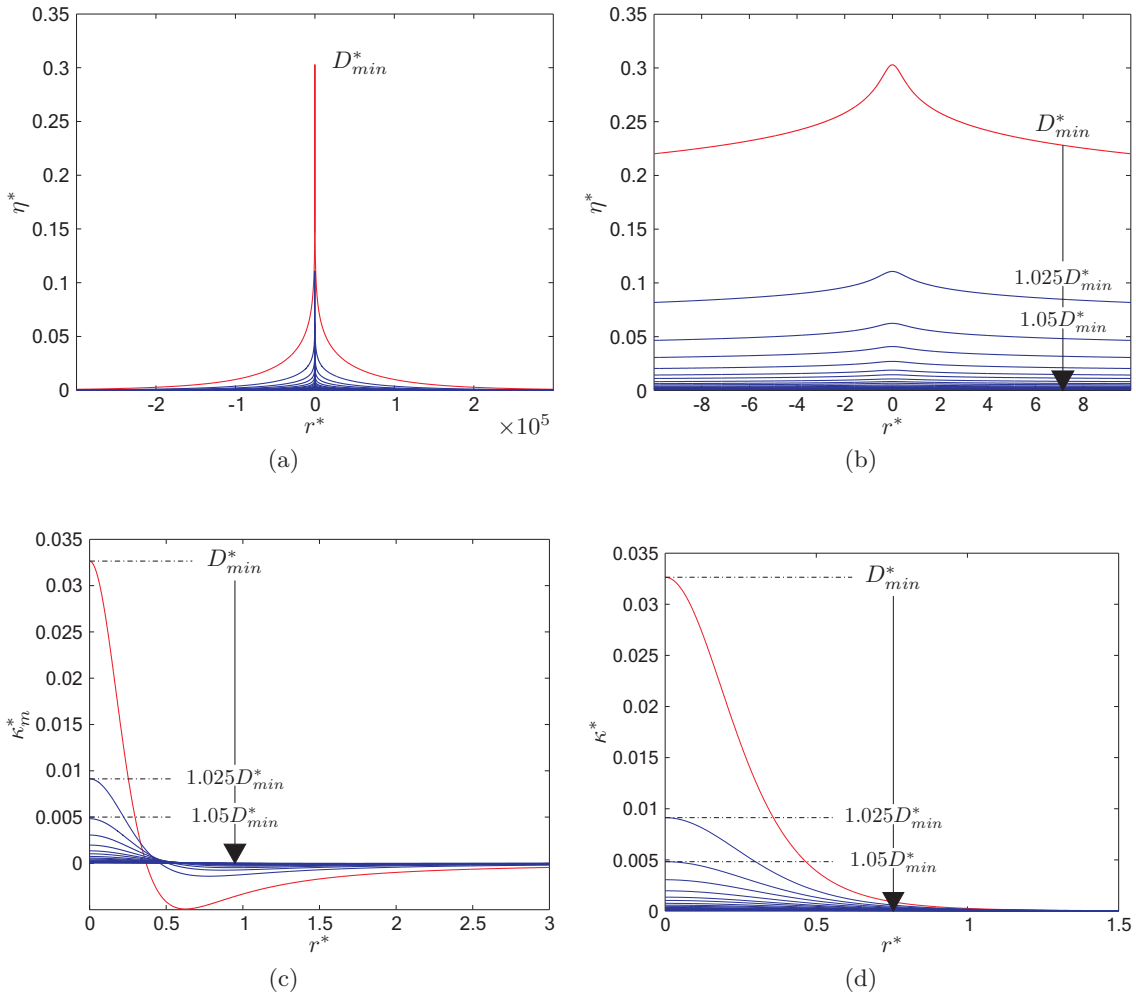


Figure 2.1: Dimensionless equilibrium (a) deformation profiles and zoom of the central region of (b) the deformation profiles, (c) the meridional curvature profiles and (d) the local mean curvature profiles obtained from solving eq.(2.1), for $H_a = 10^{-3}$, $B_o = 10^{-10}$, an initial guess $\eta^*_{guess} = 0$, and D^* with increments of $0.025D^*_{min}$ (from top to bottom). In this case, it was found that $D^*_{min} = 1.168$.

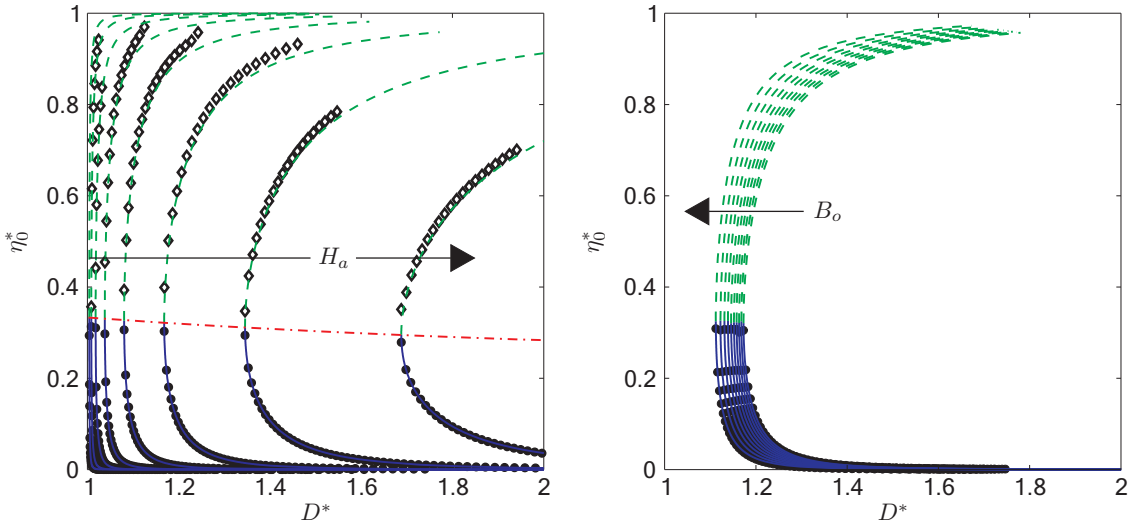


Figure 2.2: Bifurcation diagrams of the apex reduced deformation $\xi^*\eta_0^*$ as a function of D^* (a) for different values of $H_a \in \left[10^{-8}, 10^{-1}\right]$ and a fixed $B_o = 10^{-10}$, and (b) for different values of $B_o \in \left[10^{-11}, 10^{-2}\right]$ and a fixed $H_a = 10^{-3}$. Numerical solution of eq.(2.1) for [•] the stable and [◇] the unstable branches, and the analytical solution for [——] the stable and [– – –] the unstable branches given by eqs.(2.7) and (2.13). The position of the sphere surface [·] is also shown. [– · –] Critical apex deformation.

the asymptotic solution expressed in eq.(1.31) perfectly describes the declining capillary behavior of the deformation.

The corresponding curvature profiles, the meridional curvature κ_m^* and the mean curvature κ^*, as described in eq.(1.23), are displayed in Fig.2.1c and Fig.2.1d, respectively. There is a passage from positive to negative values of κ_m^*, which indicates a change in the sense of the surface tension force in the axial plane. This passage depends on the separation distance D^*, occurring at the radial position $r^* \simeq 0.37$ for $D^* = D^*_{min}$, and it is displaced to $r^* \simeq 1.08$ for $D^* = 1.5D^*_{min}$. On the contrary, κ^* remains always within positive values in the range depicted in Fig.2.1d $r^* \in [0, 1.5]$, showing a narrow logistic-like behavior, barely covering a projected probe radius. Nevertheless, κ^* also shows a passage from positive to a negative values at $r^* \simeq 25$ for $D^* = D^*_{min}$, moving to larger radial positions as D^* grows. In turn, this passage indicates the region at which the interaction potential has no effect and the capillarity completely determines the surface behavior.

In short, from the curves in Fig.2.1, reducing D^* provokes an increment in the magnitude of the attractive interaction force, leading to greater deformation and curvature states, as well as a slight variation of the radial extension of both.

2.1 The "jump-to-contact" phenomenon

In fact, for each combination of the parameters H_a and B_o, and for $D^* > D^*_{min}$, two solutions for the deformation profile arise depending on the value chosen for the apex guess solution: $\eta^*_{guess} = 0$ or $\eta^*_{guess} \approx 0.9$. By taking D^* and the two corresponding values of η_0^* as coordinate pairs, we obtain a bifurcation curve. Examples are shown in Fig.2.2: for a fixed value $B_o = 10^{-10}$ and illustrating the effect of H_a in Fig.2.2a, and for a fixed value $H_a = 10^{-3}$ and capturing the impact of B_o in Fig.2.2b. In spite of the different combination of parameters, all the bifurcation curves show similar trends and the apex position remains confined within the range $0 \leq \eta^*_{0,max} \leq 1$. When $D^* = D^*_{min}$, there is only one solution profile, corresponding to the maximum apex deformation $\eta^*_{0,max}$ and the minimum equilibrium gap $\varepsilon^*_{0,min}$ between the liquid surface and the sphere. For given H_a and B_o, there is no solution for the deformation profile further to the left than this critical point $\left(D^*_{min}, \eta^*_{0,max}\right)$, from which two branches emerge.

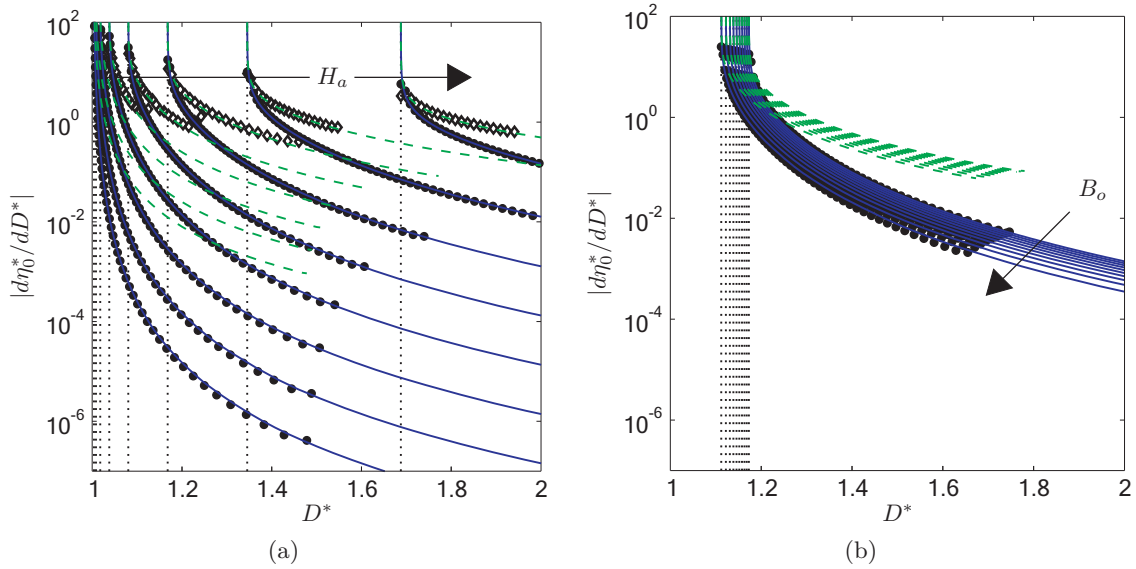


Figure 2.3: Derivative of the apex deformation with respect to the separation distance, multiplied by ξ^* and as a function of D^* (a) for different values of $H_a \in \left[10^{-8}, 10^{-1}\right]$ and a fixed $B_o = 10^{-10}$, and (b) for different values of $B_o \in \left[10^{-11}, 10^{-2}\right]$ and a fixed $H_a = 10^{-3}$. Numerical solution of eq.(2.1) for [•] the stable and [◇] the unstable branches, and the analytical solution for [—] the stable and [- -] the unstable branches, corresponding to the branches shown in Fig.2.2.

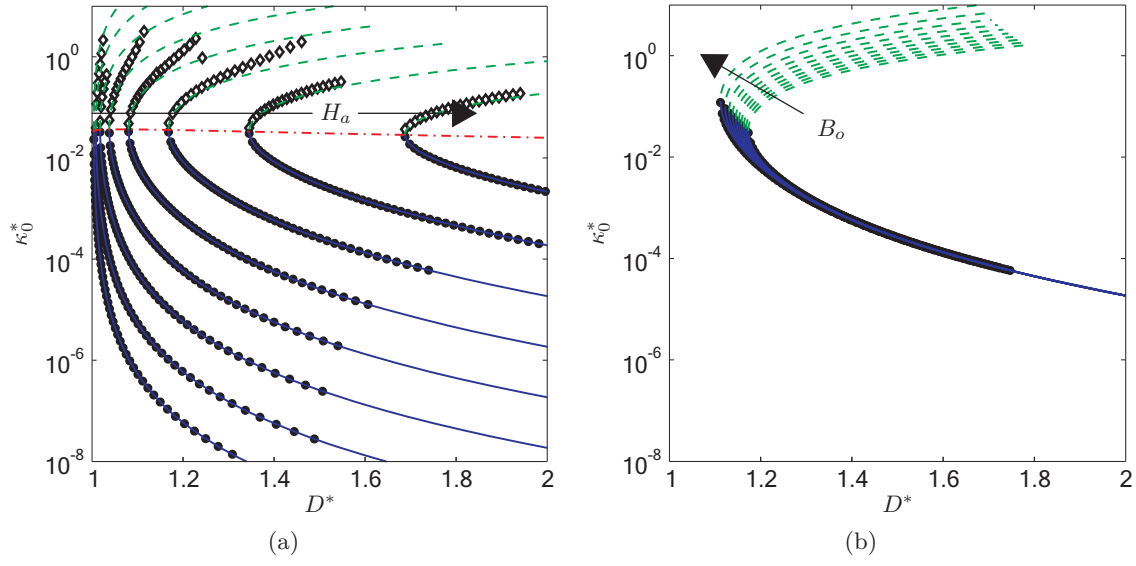


Figure 2.4: Bifurcation diagrams of the peak curvature as a function of D^* (a) for different values of $H_a \in \left[10^{-8}, 10^{-1}\right]$ and a fixed $B_o = 10^{-10}$, and (b) for different values of $B_o \in \left[10^{-11}, 10^{-2}\right]$ and a fixed $H_a = 10^{-3}$. Numerical solution of eq.(2.1) for [•] the stable and [◇] the unstable branches, and the analytical solution for [——] the stable and [– – –] the unstable branches, corresponding to the branches shown in Fig.2.2. [– · –] Critical peak curvature.

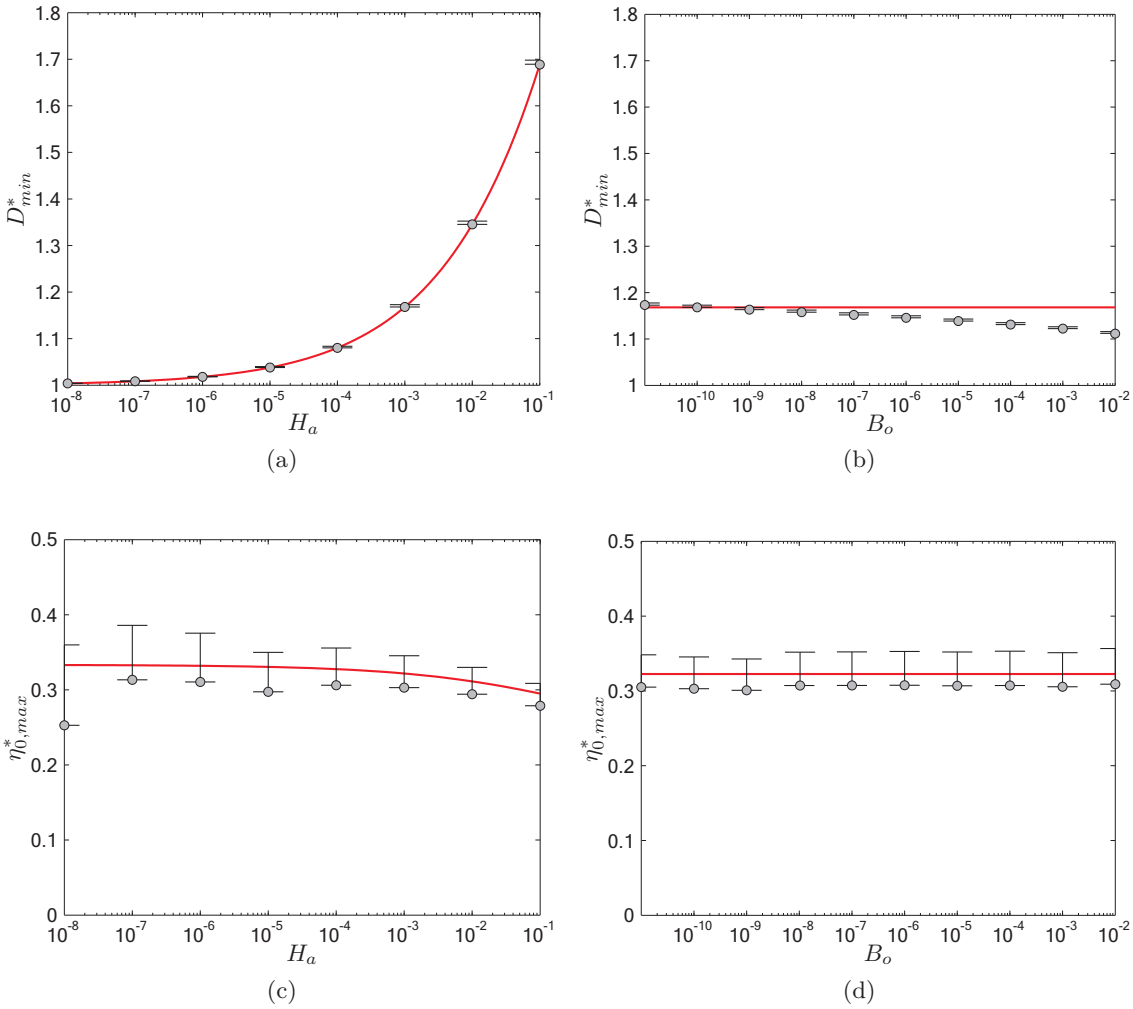


Figure 2.5: Minimum separation distance (a) as function of $H_a \in \left[10^{-8}, 10^{-1}\right]$ for a fixed $B_o = 10^{-10}$, and (b) as function of B_o for a fixed $H_a = 10^{-3}$. Maximum apex deformation (c) as function of $H_a \in$ for a fixed $B_o = 10^{-10}$, and (d) as function of B_o for a fixed $H_a = 10^{-3}$. [$\circ$] Numerical solution of eq.(2.1), and [——] tendency curve from the combination of eqs.(2.14), (2.13), (2.7) and (2.15). Note that the tendency curve is only function of H_a.

Consider the energy associated with the deformation profile $\mathcal{E}_\gamma$, defined as:

$$\mathcal{E}_\gamma = 2\pi\gamma R^2 \int_0^\infty r^* \sqrt{1 + \left(\xi^* \frac{d\eta^*}{dr^*}\right)^2}\, dr^*,$$

and the change in the deformation energy as:

$$\Delta\mathcal{E}_\gamma = \mathcal{E}_\gamma - \mathcal{E}_\gamma^0, \tag{2.3}$$

where $\mathcal{E}_\gamma^0$ is the energy associated with a flat undeformed interface. The stability of the solution, from an energetic point of view, is given by:

$$\frac{d\Delta\mathcal{E}_\gamma}{dD} < 0,$$

which indicates that, as the probe approaches the liquid surface, the surface deformation increases as well as the associated energy. The opposite case points out an unstable situation, as it is the case of a probe stuck to a sample while moving away. Herein, the first order approximation of the change in the deformation energy, given by:

$$\Delta\mathcal{E}_\gamma \sim \pi\gamma \left(R\xi^*\eta_0^*\right)^2,$$

is to be employed. One should have in mind that $\eta_0^* > 0$ for a purely attractive interaction. As well, from the definition of the initial gap $\xi^* = D^* - 1$, and due to the fact that the separation distance is always $D \geq R$, thus $D^* \geq 1$, it results that $\xi^* > 0$. Therefore, the stability criterion becomes:

$$\frac{d\eta_0^*}{dD^*} < -\frac{\eta_0^*}{\xi^*} \tag{2.4}$$

This coarse approximation of the stability criterion is enough to recognize a stable equilibrium surface deformation, in the vicinity of the critical point $\left(D_{min}^*, \eta_{0,max}^*\right)$.

As observed from Fig.2.2, the curve showing the highest apex deformation is an unstable branch from the energetic point of view. As well, the curve reporting the lowest apex position, associated to the minimum deformation energy, is a stable branch and, thus, describes the only meaningful interface profile. For the stable apex position, the dependency of η_0^* on D^* seems to take the form of a rectangular hyperbola, i.e. the deformation becomes larger as the distance between the probe and the undeformed surface is reduced. In Fig.2.3 and Fig.2.4, the absolute value of the derivative of η_0^* with respect to D^* and the mean curvature κ_0^* of both branches are shown, respectively. Shorter separation distances D^* yield steeper slopes for the derivative of η_0^* and larger peak curvatures for the stable branches. In both cases, D_{min}^* marks the location of a vertical asymptote, at which the stable branches come to a halt. The raised curvature of the unstable branches confirms their unstable nature, asserting their higher surface tension force.

In Fig.2.2, an increase of H_a generates a displacement of the bifurcation point $\left(D_{min}^*, \eta_{0,max}^*\right)$ toward larger values of D^* and slightly smaller values of η_0^*. For a very small H_a, the bifurcation curve tends to take the shape of the left side of a square. When H_a takes larger values, the curve suffers a vertical narrowing approaching an oval shape. Conversely, an increase of B_o, of several orders of magnitude, provokes a moderated decrease of D_{min}^* and a barely changing shape, negligible in comparison with that engendered by a modification of H_a.

Similarly, in Fig.2.3, a growth of H_a provokes a displacement of the vertical asymptote toward larger values of D^*, and as a consequence of the shape transformation of the deformation bifurcation curve, a decrease of the slope of the curve near D_{min}^*. In contrast, an increase of B_o moves gently the vertical asymptote to shorter values of D^*, as expected, and the shape of the curve remains unaffected.

As observed in Fig.2.4, the behavior and the shape of the mean curvature bifurcation diagrams is qualitatively similar to that of the deformation. The more significant difference is that κ_0^* is not constrained in a range of values. Steeper curves correspond to smaller values of H_a, whereas bifurcation point $\left(D_{min}^*, \kappa_{0,crit}^*\right)$ shifts to larger values of D^*, for larger values of H_a. The value of $\kappa_{0,crit}^*$ remains constant for any modification of H_a. On the other hand, a change in B_o hardly alters the shape of the curves. Nevertheless, an increase of B_o provokes a migration of $\kappa_{0,crit}^*$ toward larger values, and a weak displacement of D_{min}^* toward smaller dimensions.

In general, the impact of H_a is significant, while the effect of a change in B_o is irrelevant within the range of common liquids, as it is exposed in Fig.2.5. Increasing H_a provokes an important enlargement

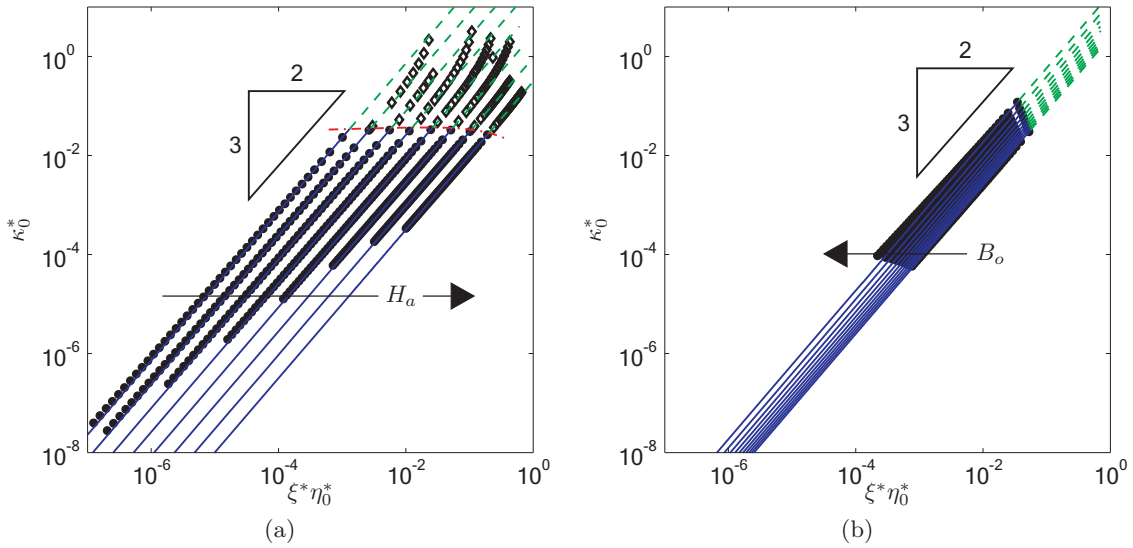


Figure 2.6: Peak curvature κ_0^* as a function of $\xi^*\eta_0^*$ obtained (a) for different modified Hamaker numbers in the range $H_a \in \left[10^{-8}, 10^{-1}\right]$ and a fixed Bond number of $B_o = 10^{-10}$, and (b) for different Bond numbers in the range $B_o \in \left[10^{-11}, 10^{-2}\right]$ and a fixed $H_a = 10^{-3}$. Numerical solution of eq.(2.1) for [•] the stable and [◇] the unstable branches, and the analytical solution for [——] the stable and [– – –] the unstable branches given by eqs.(2.7) and (2.13). [– · –] $\kappa_{0,crit}^*$ is obtained from the evaluation in eq.(2.13) with $\xi_{crit}^*\eta_{0,max}^*$, in turn obtained when solving eq.(2.14), and the values of C_{lk} shown in Fig.2.7. Arrows indicate the growth of the corresponding parameter.

of D_{min}^*, whereas enlarging B_o moves D_{min}^* slightly toward smaller values, as illustrated in Figs.2.5a and 2.5b, respectively. In order to find the bifurcation point, we have implemented a dichotomy method, which allows to control the trueness of the predicted value of D_{min}^*. In this study, D_{min}^* is forecast with an error smaller than 10^{-3}.

As shown in Fig.2.5c, the value of $\eta_{0,max}^*$ decreases slowly when increasing the magnitude of H_a, from an average value of $\eta_{0,min}^* \approx 0.315$ in the range $H_a \in \left[10^{-8}, 10^{-4}\right]$ toward a value slightly below $\eta_{0,min}^* \approx 0.3$ for $H_a = 10^{-1}$. In contrast, indicated in Fig.2.5d, $\eta_{0,max}^*$ remains constant for the tested values of B_o. It is important to mention that the employed methodology is based on a D_{min}^* accuracy control, giving, as a consequence, a bigger error in the calculation of $\eta_{0,max}^*$. Herein, the prediction of $\eta_{0,max}^*$ can present an error smaller than 7.3×10^{-2}, apart form the value obtained for $H_a = 10^{-8}$, which is of the order of 10^{-1}.

2.2 Surface apex behavior

When analyzing the apex behavior for a given combination of H_a and B_o, it is found that κ_0^* grows along with $\xi^*\eta_0^*$, which in turn becomes larger when D^* decreases, as observed in Fig.2.6. The peak curvature κ_0^*, specially when it approaches its critical value $\kappa_{0,crit}^*$, shows a remarkable simple dependency on the reduced deformation $\xi^*\eta_0^*$, which is given by:

$$\kappa_0^* \propto \left(\xi^*\eta_0^*\right)^{3/2}. \tag{2.5}$$

From fig.2.6, a horizontal logarithmic displacement is produced when modifying the dimensionless numbers: significantly toward larger values of $\xi^*\eta_0^*$ when H_a increases; slightly to smaller values of η_0^* when B_o grows. Whereas $\xi^*\eta_0^*$ approaches $\xi_{crit}^*\eta_{0,max}^*$, κ_0^* reaches its critical value $\kappa_{0,crit}^* \approx 3.5 \times 10^{-2}$, which stays nearly constant for small values of H_a. When increasing H_a, the critical curvature slowly decreases. For $H_a = 10^{-1}$, its value is slightly below $\kappa_{0,crit}^* \approx 2.9 \times 10^{-2}$. When increasing B_o, $\kappa_{0,crit}^*$ increases significantly, but barely reaching $\kappa_{0,crit}^* \approx 1.0 \times 10^{-1}$.

For the case of local probes, R is always much smaller than λ_C, and as a consequence $B_o \ll 1$. As a consequence, the hydrostatic term is negligible compared to that of the interaction terms near the symmetry axis, which implies that the surface deformation, and more precisely the apex deformation

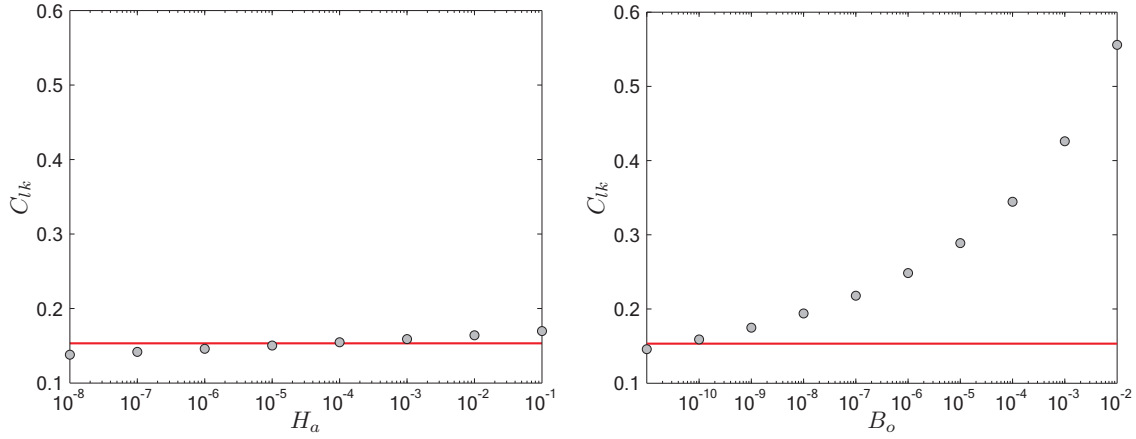


Figure 2.7: Bulk proportionality constant C_{lk} as a function (a) of the modified Hamaker number H_a for a fixed Bond number of $B_o = 10^{-10}$, and (b) of the Bond number B_o for a fixed $H_a = 10^{-3}$. The values of C_{lk} were obtained by fitting the data shown in Fig.2.6 in (2.13). [∘] Numerical solution and [——] the average value $C_{lk} \simeq 1.54 \times 10^{-1} \pm 1.58 \times 10^{-2}$.

η_0^*, is mostly controlled by the balance between the probe/liquid interaction potential and the capillary force. Thence, at $r^* = 0$, eq.(2.1) can be reduced to:

$$\Pi_{pl}^*\Big|_0 = -\frac{2\kappa_0^*}{H_a}, \tag{2.6}$$

Besides, the position of the sphere center can be written as a function of the apex product $\xi^*\eta_0^*$ and the peak curvature κ_0^*. Solving eq.(1.17b) for the dimensionless probe position D^* at $r^* = 0$, and using eq.(2.6), yields the following relationship:

$$D^* = \xi^*\eta_0^* + \sqrt{1 + \left[\frac{2\kappa_0^*}{H_a}\right]^{-1/3}}. \tag{2.7}$$

Also, from the geometry shown in Fig.1.4, an expression for D^* is inferred in terms of the the apex position η_0^*, the initial gap ξ^* and the reduced equilibrium gap ε_0^*:

$$D^* = 1 + \xi^*\eta_0^* + \xi^*\varepsilon_0^*, \tag{2.8}$$

which also leads to the relationship:

$$\varepsilon_0^* + \eta_0^* = 1,$$

which results from the dimensionless definition of the initial gap, $\xi^* = D^* - 1$. As a consequence, because $\eta^* \geq 0$ and $\varepsilon^* \geq 0$, the two variables are confined in the range $[0, 1]$.

A comparison between eq.(2.8) and the first-order approximation of eq.(2.7) (see Appendix D), gives the following expression of the peak curvature in terms of the initial and equilibrium reduced gaps:

$$\kappa_0^* = \frac{H_a}{16\left(\xi^*\varepsilon_0^*\right)^3}. \tag{2.9}$$

Following an equivalent approach, if we consider that the force due to the surface deformation can be taken as a linear function of the apex position:

$$F_\gamma \sim \pi\gamma\left(R\xi^*\eta_0^*\right), \tag{2.10}$$

and the force mutually exerted between the probe and the liquid surface can be approximated by the

force between a sphere and a flat surface (Israelachvili, 2011):

$$F_{pl} \sim \frac{H_{pl} R}{6 \left(R \xi^* \epsilon_0^*\right)^2}, \tag{2.11}$$

the equilibrium between these two forces, including a proportionality constant C_{lk}, allows to obtain a relationship between the apex position and the reduced gaps:

$$\eta_0^* = \frac{1}{C_{lk}} \frac{H_a}{8\xi^* \left(\xi^* \varepsilon_0^*\right)^2}, \tag{2.12}$$

which, in combination with eq.(2.9) gives a power law relationship between the apex variables:

$$\kappa_0^* = \left(C_{lk}\right)^{3/2} \sqrt{\frac{2}{H_a}} \left(\xi^* \eta_0^*\right)^{3/2}. \tag{2.13}$$

Eq.(2.13) is in agreement with the behavior observed in Fig.2.6, specifically near the critical conditions, and has been previously mentioned in eq.(2.5).

The proportionality constant C_{lk} is directly obtained by fitting the data shown in Fig.2.6 with eq.(2.13). As shown in Fig.2.7, the dependence of C_{lk} on H_a is negligible in comparison with its submission to the value of B_o. For any H_a, the proportionality constant shows an average value with a sparse deviation, $C_{lk} \simeq 1.54 \times 10^{-1} \pm 1.58 \times 10^{-2}$, whereas, it is undeniably a function that grows along with the magnitude of B_o.

Combining eqs.(2.7) and (2.13), gives the dependency of D^* on $\xi^* \eta_0^*$, leading to the bifurcation diagrams construction. The resulting relationship supplies the two physically possible solutions of eq.2.1, stable and unstable branches. Bifurcation curves obtained with this analytical approach are also shown in Fig.2.2a, for a fixed $B_o = 10^{-10}$ and a range $H_a \in \left[10^{-8}, 10^{-1}\right]$, and in Fig.2.2b, reckoned with $H_a = 10^{-3}$ and $B_o \in \left[10^{-11}, 10^{-2}\right]$. Furthermore, the corresponding derivative of η_0^* with respect to D^*, as well as the peak curvature κ_0^*, are compared to the numerical results in Fig.2.3 and Fig.2.4, respectively. In all cases, a very good accordance with the numerical solution is observed at the bifurcation points and the nearby region.

As it has already been mentioned, the value of D_{min}^* indicates the minimum axial position, at which the sphere can be located, to prevent the liquid from jumping to contact the sphere. This particular situation corresponds to an unbound magnitude of the probe/liquid interaction potential. In addition, this minimum distance D_{min}^* provokes the critical initial gap ξ_{crit}^*, the maximum apex deformation $\eta_{0,max}^*$ and the critical peak curvature $\kappa_{0,crit}^*$, which represent the critical stable conditions of the surface deformation. As well, as it is observed from the bifurcation diagrams, at D_{min}^* the apex position diverges $d\eta_0^*/dD^* \to \infty$ and, as a consequence, one can make the derivative $dD^*/d\eta_0^* = 0$.

It is well known that the system stability is deeply associated with the stationary points of the interaction potentials (Ruckenstein and Jain, 1973; Forcada, 1993; Christenson, 1994). Thus, consistent with the aforementioned hypothesis of the apex position divergence, differentiation of eq.(2.7), once again combined with eq.(2.13), gives rise to the polynomial equation:

$$\left(\xi_{crit}^* \eta_{0,max}^*\right)^3 + \Theta \left(\xi_{crit}^* \eta_{0,max}^*\right)^{5/2} - \left(\frac{\Theta}{4}\right)^2 = 0, \tag{2.14}$$

where $\Theta = \sqrt{H_a/2C_{lk}}$. The roots of this polynomial are meant to be found in order to estimate the critical apex product $\xi_{min}^* \eta_{0,max}^*$ of the maximum apex deformation and the critical initial gap. The acquired value is used in eq.(2.13) to determine the peak curvature. Afterwards, the minimum separation distance D_{min}^* is obtained when eq.(2.7) is evaluated. Then, the critical initial gap is given by:

$$\xi_{crit}^* = D_{min}^* - 1, \tag{2.15}$$

and the maximum apex position can be finally deduced. Both D_{min}^* and $\eta_{0,max}^*$ were analytically acquired for the range $H_a \in \left[10^{-8}, 10^{-1}\right]$ and shown in Fig.2.5. Since eq.(2.14) does not depends on B_o, the reference value for $H_a = 10^{-3}$ and $B_o = 10^{-10}$ is shown in the figure. Nevertheless, this constant value is close to the numerically calculated values of D_{min}^* and $\eta_{0,max}^*$, because their dependence on B_o is weak. In contrast, the curves obtained with the combination of eqs.(2.14), (2.13), (2.7) and (2.15),

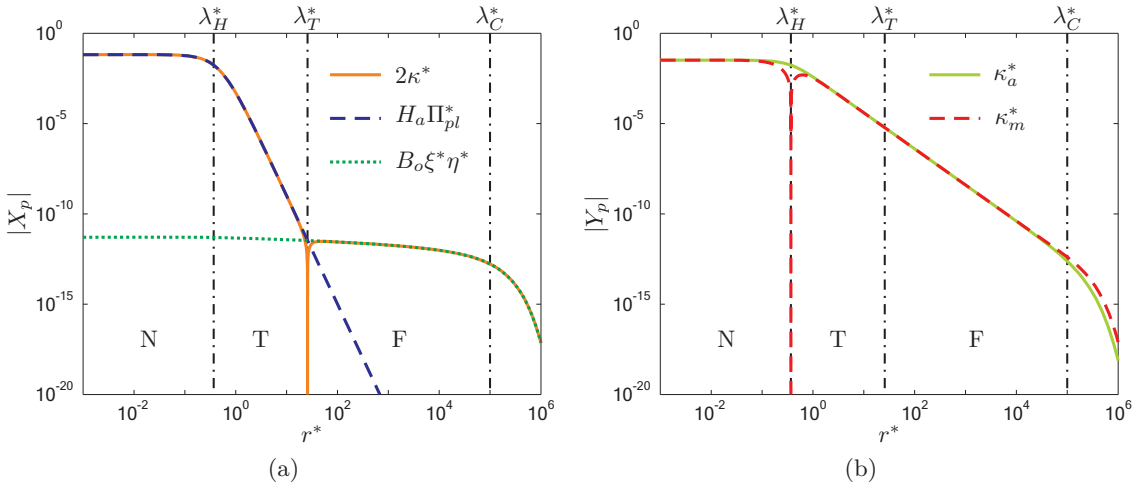


Figure 2.8: Characteristic length-scales determination. Different terms (a) X_p from eq.(2.1), for which $\sum X_p = 0$, and (b) Y_p from eq.(1.23), for which $\sum Y_p = 2\kappa^*$, as functions of r^*, for $H_a = 10^{-3}$, $B_o = 10^{-10}$ and $D^* = D^*_{min} = 1.168$. The upper-case letters N, T and F designate the near-field, transition and far-field zones, respectively, which extents are bounded by the characteristic length-scales λ_H^*, λ_T^* and λ_C^*.

depict the correct trend of D^*_{min} and $\eta^*_{0,max}$, in agreement with the numerical results. Further details on this analysis are given in Appendix B.

2.3 Characteristic length-scales

The absolute value of the terms appearing in eq.(2.1) and the curvature decomposition terms of eq.(1.23), which contribute to achieve an equilibrium state, are depicted in Fig.2.8. The existence of three important length-scales is emphasized.

Firstly, corresponding to the position for which $\kappa_m^* = 0$ (inflection point of the meridional profile), λ_H^* indicates the boundary of a near-field zone, in which the probe/liquid interaction plays a pivotal role, and the beginning of a transition zone, where all the variables and parameters contribute to the deformation. Then, at the radial extent for which $2\kappa^* = 0$ (zero-curvature point), λ_T^* marks the end of the transition region and the beginning of the far-field zone, which corresponds to a capillarity dominated decay. Finally, the dimensionless capillary length λ_C^* shows the extension at which the effect of all terms tend to disappear.

At $r^* \in [0, \lambda_H^*[$, the attractive term $H_a\Pi_{pl}^*$ (negative value) is mostly opposed by $2\kappa^*$ (positive), whereas the hydrostatic term $B_o\eta^*$ (positive) is negligible in comparison to the other terms. Characterized by H_a, the equilibrium profile in this near-field region is directly controlled by the balance between attractive potential and capillary pressure, both showing magnitudes that slowly decay when $r^* \to \lambda_H^*$. At $r^* = \lambda_H^*$, the meridional curvature κ_m^* changes from positive to negative values, whereas the azimuthal curvature κ_a^* keeps its positive value.

In the range $r^* \in]\lambda_H^*, \lambda_T^*[$, κ_a^* (positive) withstands both $H_a\Pi_{pl}^*$ (negative), which quickly losses its intensity, and κ_m^* (negative). In this region, κ_m^* and κ_a^*, the latter always showing a positive value, are the crucial antagonists. $B_o\eta^*$ remains nearly constant as it slowly gains weight while both $H_a\Pi_{pl}^*$ and $2\kappa^*$ decrease almost at the same rate. At $r^* = \lambda_T^*$, the magnitude of κ_m^* equals that of κ_a^* and, as a consequence, the curvature term $2\kappa^*$ goes to zero and changes from positive to negative values.

Within $r^* \in]\lambda_T^*, \lambda_C^*]$, $H_a\Pi_{pl}^*$ has become negligible whereas $2\kappa^*$ attains the order of magnitude of $B_o\eta^*$. In this zone, $B_o\eta^*$, which diminishes gradually, is opposed only by $2\kappa^*$, whereas κ_m^* and κ_a^* are still contending. The shape of the interface profile in this far-field zone is completely driven by B_o. Beyond the radial position $r^* = \lambda_C^*$, the interface returns to its unperturbed flat state.

In Fig.2.9, λ_H^* and λ_T^* are shown as functions of η_0^* for different values of H_a and B_o. Both radial positions follow similar trends. For a given combination of parameters, λ_H^* and λ_T^* decline as functions of η_0^*, following a rectangular hyperbola-like behavior. This tendency continues until the values of D^*_{min} and $\eta^*_{0,max}$ are reached, for which the limiting equilibrium profile and the minimum radial positions of λ_H^*

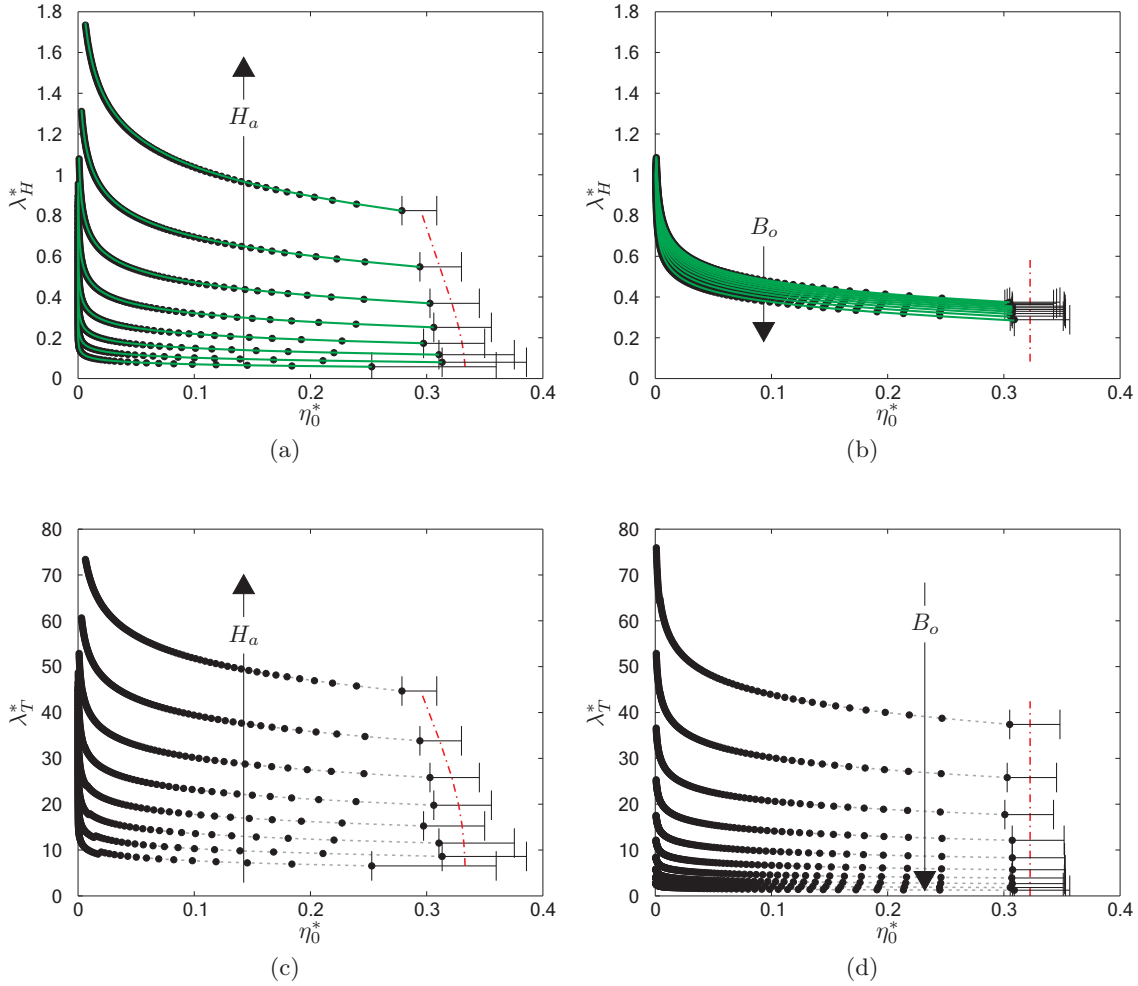
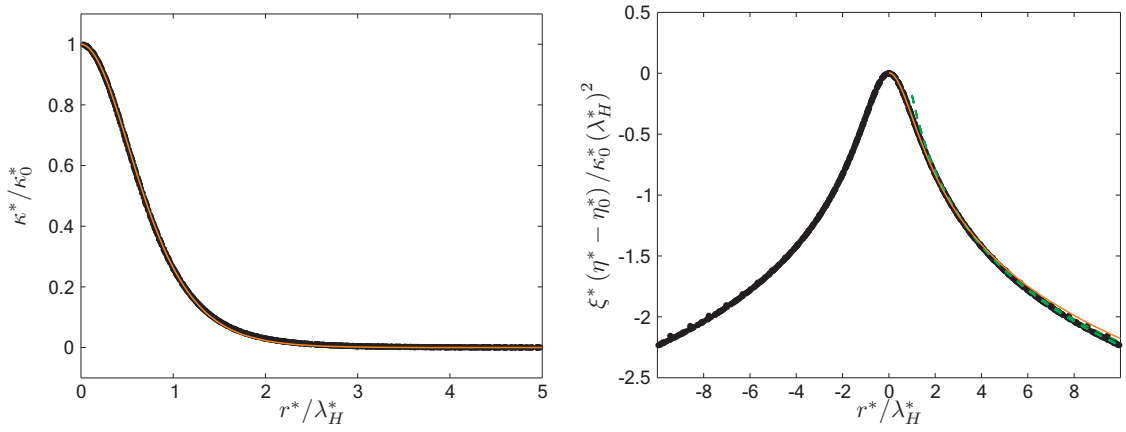


Figure 2.9: Radial position of the inflection point of the profile λ_H^* as a function of η_0^* obtained (a) for different modified Hamaker numbers in the range $H_a \in \left[10^{-8}, 10^{-1}\right]$ and a fixed$H_a\Pi_{pl}^*$ Bond number of $B_o = 10^{-10}$, and (b) for different Bond numbers in the range $B_o \in \left[10^{-11}, 10^{-2}\right]$ and a fixed $H_a = 10^{-3}$. Radial position of zero-curvature λ_T^* as a function of η_0^* obtained (c) for different modified Hamaker numbers in the range $H_a \in \left[10^{-8}, 10^{-1}\right]$ and a fixed$H_a\Pi_{pl}^*$ Bond number of $B_o = 10^{-10}$, and (d) for different Bond numbers in the range $B_o \in \left[10^{-11}, 10^{-2}\right]$ and a fixed $H_a = 10^{-3}$. [•] from the numerical solution of eq.(2.1), [——] eq.(2.16) with $b = 0.39$ and [– · –] from the critical conditions D_{min}^* and $\eta_{0,max}^*$. Arrows indicate the growth of the corresponding parameter.



(a) (b)

Figure 2.10: Near-field self-similar dimensionless (a) mean curvature and (b) interface deformation for $H_a \in \left[10^{-8}, 10^{-1}\right]$ and $B_o \in \left[10^{-11}, 10^{-2}\right]$. [•] Numerical solution of eq.(2.1) and approximations obtained from [——] eq.(2.17) and [– – –] eq.(2.19), for the curvature and the interface deformation, respectively.

and λ_T^* are attained. In Fig.2.9a, the numerical results indicate that λ_H^* shifts toward higher values when H_a increases in the range $H_a \in \left[10^{-8}, 10^{-1}\right]$ for a fixed B_o, at a given value of η_0^*. On the other hand, the impact of B_o on λ_H^*, within $B_o \in \left[10^{-11}, 10^{-2}\right]$ and for a fixed value of H_a, is relatively insignificant, as depicted in Fig.2.9b. Likewise, in Fig.2.9c, λ_T^* follows the same tendency as λ_H^* when H_a augments; however, an important decrease of λ_T^* is observed in Fig.2.9d, when B_o grows. The amount of change in λ_T^* when H_a increases is of the same order of magnitude as that observed when B_o decreases.

The curves in Fig.2.9 can also be analyzed as follows. For a given H_a, a decrease of D^* provokes the growth of Π_{pl}^* and η_0^*, leading to a decrease in both λ_H^* and λ_T^*, which is the action of the capillary pressure to restrain the radial extent of the deformation. From another viewpoint, for a given η_0^*, an increase of H_a generates an increment in both λ_H^* and λ_T^*, which indicates that the attractive potential spans over a larger zone. Because D^* and its induced η_0^* are not significantly affected by B_o, thus a change in this parameter has a faint effect over λ_H^*. On the other hand, an increase of B_o directly provokes a decrease of λ_T^*, which corresponds to enlarge the "heaviness" of the interface.

Recalling the linearization in the vicinity of $r^* = 0$, presented in Chapter1, from which λ_H^* can be estimated. Making $E^* \to \infty$ in eq.(1.36) gives:

$$\lambda_H^* = \frac{\sqrt{2}}{3b}\sqrt{\frac{\left(D^* - \xi^*\eta_0^*\right)^2 - 1}{1 + \kappa_0^*\left(D - \xi^*\eta_0^*\right)}}. \tag{2.16}$$

From the data shown in Figs.2.9a and 2.9b, $b = 0.39$ was found. An excellent agreement between the numerical results and eq.(2.16) is observed.

2.4 Self-similarity

Taking into account the length-scales, λ_H^* and λ_C^*, master curves that display the prevailing deformation profile (self-similarity) in the near- and far-field zones, respectively, are constructed. For $r^* \in [0, \lambda_H^*[$, the reduced variables κ^*/κ_0^* and r^*/λ_H^* allows us to find the dimensionless curvature presented in Fig.2.10a. This curve exhibits a logistic-like probability function shape:

$$\frac{\kappa^*}{\kappa_0^*} = \frac{4\exp\left(-\dfrac{r^*}{b\ \lambda_H^*}\right)}{\left[1 + \exp\left(-\dfrac{r^*}{b\ \lambda_H^*}\right)\right]^2}, \tag{2.17}$$

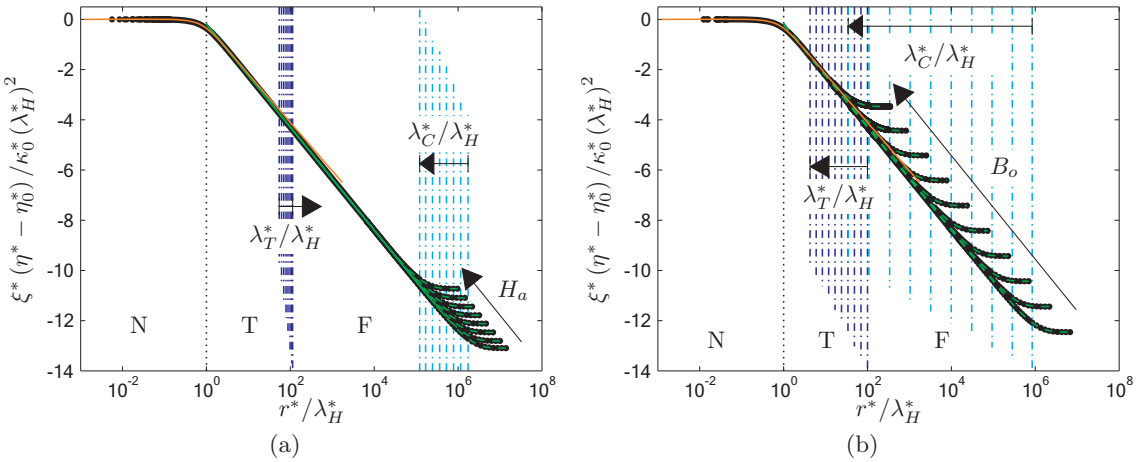


Figure 2.11: Near-field self-similar deformation profile obtained with the dimensionless variables in eq.(2.19): (a) for $H_a \in \left[10^{-8}, 10^{-1}\right]$ and a fixed $B_o = 10^{-10}$, and (b) for $B_o \in \left[10^{-11}, 10^{-2}\right]$ and a fixed $H_a = 10^{-3}$. [•] Numerical solution of eq.2.1 and approximations obtained from [——] eq.(2.19) and [– – –] eq.(2.20). The upper-case letters N, T and F designate the near-field, transition and far-field zones, respectively. Vertical lines indicate the positions of the reduced characteristic length-scales, while the sense of the arrows show its displacement when the corresponding dimensionless parameter grows.

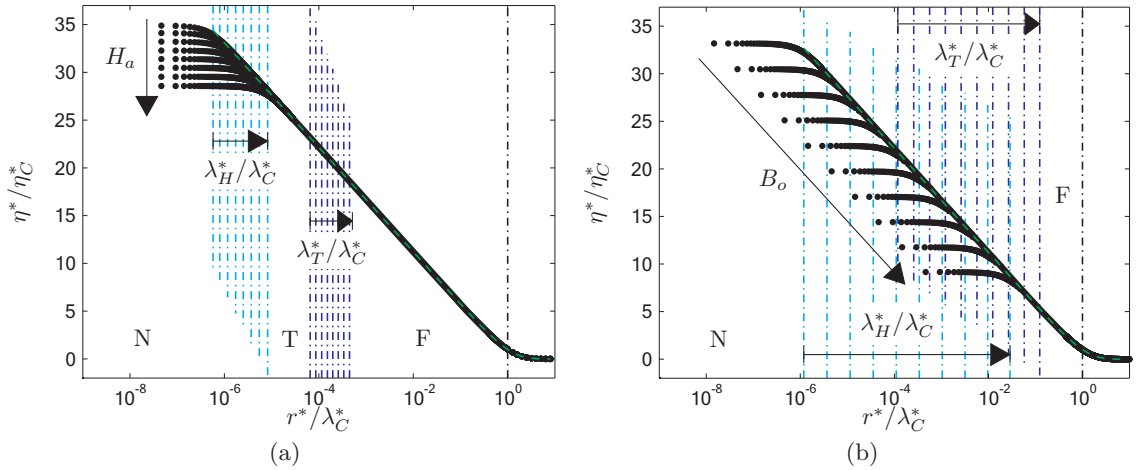


Figure 2.12: Far-field self-similar deformation profile obtained with the dimensionless variables in eq.(2.20): (a) for $H_a \in \left[10^{-8}, 10^{-1}\right]$ and a fixed $B_o = 10^{-10}$, and (b) for $B_o \in \left[10^{-11}, 10^{-2}\right]$ and a fixed $H_a = 10^{-3}$. [•] Numerical solution of eq.2.1 and [– – –] approximation obtained from eq.(2.20). The upper-case letters N, T and F designate the near-field, transition and far-field zones, respectively. Vertical lines indicate the positions of the reduced characteristic length-scales, while the sense of the arrows show its displacement when the corresponding dimensionless parameter grows.

where b is a fitting parameter, which is determined below. The relative error between the numerical solution of κ^*/κ_0^* and eq.(2.17) is 10^{-3}, for a radial position up to $r^* \leq 5\lambda_H^*$. In addition, the reduced curvature κ^*/κ_0^* is negligible for radial positions beyond $r^* \approx 10b\ \lambda_H^*$.

Matching eq.(2.17) with eq.(1.17a), for small displacements of the liquid surface, and integrating we find:

$$\xi^* \frac{1}{r^*} \frac{d\eta^*}{dr^*} = 8\kappa_0^* \left(\frac{b\ \lambda_H^*}{r^*} \right) \left\{ \frac{\exp\left(-\dfrac{r^*}{b\ \lambda_H^*} \right)}{1 + \exp\left(-\dfrac{r^*}{b\ \lambda_H^*} \right)} + \left(\frac{b\ \lambda_H^*}{r^*} \right) \left(\ln\left[1 + \exp\left(-\frac{r^*}{b\ \lambda_H^*} \right) \right] - \ln B \right) \right\}, \quad (2.18)$$

where, B is an integration constant. From the BC given by $[\eta^*]_0' = 0$ and the Taylor expansion of the logarithmic term in eq.(2.18) (as described in D), $B = 2$ is found. As well, evaluating eq.(2.18) and (2.17) at $r^* = \lambda_H^*$, where $2\kappa^* = \kappa_a^*$, a value of $b = 3.89 \times 10^{-1}$ is deduced. Afterward, performing a second integration of eq.(2.18), we obtain the expression of the dimensionless deformation profile:

$$\frac{\xi^* \left(\eta^* - \eta_0^* \right)}{\kappa_0^* \left(\lambda_H^* \right)^2} = 8b^2 \left\{ -\ln \frac{1}{2} \left[1 + \exp\left(-\frac{r^*}{b\ \lambda_H^*} \right) \right] + \int_0^{r^*/(b\ \lambda_H^*)} \ln \frac{1}{2} \left[1 + \exp\left(-\varsigma \right) \right] \frac{d\varsigma}{\varsigma} \right\}, \quad (2.19)$$

where ς is an integration variable. Once more, the relative error between the numerical solution and eq.(2.19) is of the order of 10^{-3}, also for a radial position up to $r^* \leq 5\lambda_H^*$. In Fig.2.10b, the surface shape given by eq.(2.19) is compared to the numerical results, showing a very good agreement within $0 \leq r^* \leq \lambda_H^*$, for $H_a \in \left[10^{-8}, 10^{-1} \right]$ and $B_o \in \left[10^{-11}, 10^{-2} \right]$. Therefore, it is proven that the reduced surface position $\xi^* \left(\eta^* - \eta_0^* \right) / \kappa_0^* \left(\lambda_H^* \right)^2$ and radial position r^*/λ_H^* are the dimensionless variables that characterize the self-similar behavior of the deformation profile in the near-field zone. The logarithmic plot of these variables, depicted in Fig.2.11, reveals that this unique behavior spans largely over the transition zone.

For $r^* \in]\lambda_T^*, \lambda_C^*]$, a couple of reduced variables based on the asymptotic solution given by eq.(1.31) indicates a unique far-field behavior. Considering that $\lambda_{CF}^* = \lambda_C^*$ and η_C^* being the surface position at the corresponding radial position $r^* = \lambda_C^*$, then it can be deduced that $\eta_C^* = GK_0(1)$. Therefore, the employment of the the reduced surface η^*/η_C^* and radial r^*/λ_C^* positions, leads to find the far-field self-similar deformation profile:

$$\frac{\eta^*}{\eta_C^*} = \frac{K_0\left(\dfrac{r^*}{\lambda_C^*} \right)}{K_0(1)}. \quad (2.20)$$

As shown in Fig.2.12, eq.(2.20) gives a quite good description of the far-field results within the range $\lambda_T^* < r^* \leq \lambda_C^*$, and even spanning over the whole transition zone. This far-field self-similarity describes a unique decaying behavior, observed from $r^* \simeq \lambda_H^*$ and beyond.

2.5 Concluding remarks

An extensive analysis of the deformation of a liquid surface, due to its interaction with a nano-probe, was presented. The phenomenon was portrayed by a strongly non-linear equation, and the effects of physical and geometric parameters over the system were considered. Mainly when the interaction within a nano-scale system is considered, our model generates a more accurate description of the interface deformation than previous works (Cortat and Miklavcic, 2004; Wang et al., 2007), which employ the Derjaguin approximation. Furthermore, the application of our results is possible at any scale, considering realistic situations, due to the performed dimensionless approach.

The interface profile evolution, whether the system attains equilibrium or not, depends on the relative magnitude of D^* with respect to the threshold distance D_{min}^*, which in turn is given by the combination of the remaining parameters, B_o and H_a. Bifurcation diagrams relating η_0^* and D^* are established, in which a zone with nonexistent equilibrium is uncovered and explained. This happens when $D^* < D_{min}^*$, which provokes the unbounded growth of the attractive force with no opposition of any other system mechanism.

On the other hand, steady state stable and unstable equilibrium profiles are obtained for $D^* \geq D_{min}^*$, thus the attractive force is thwarted mostly by the capillary pressure. In this case, D^* and its

corresponding deformation are located as points within the corresponding two branches of the bifurcation diagrams. D^*_{min} is also distinguished as the distance at which the two branches melt into a single maximum equilibrium deformation state.

Three different length-scales were obtained from the analysis of the steady state equilibrium profiles, all of them being function of H_a and/or B_o. They determine the existence of: a near-field zone, $r^* \in [0, \lambda^*_H[$, controlled by the attractive interaction/surface tension balance; a far-field zone, $r^* \in]\lambda^*_T, \lambda^*_C]$, dominated by the gravity/surface tension interplay; and a transition zone, $r^* \in]\lambda^*_H, \lambda^*_T[$, where all the variables take an important role. It was found that the two interior length-scales are affected by the size of the probe: $\lambda_H \lesssim R$ and $\lambda_T \gtrsim 10R$, while the capillary length remains fixed $\lambda_C \sim 10^{-3}$. These length-scales are responsible for the liquid surface self-similar deformation profile. The reduced variables, stemmed from eqs.(2.17)–(2.20), outline the self-similar profiles corresponding to the near- and far-field zones. $\xi^* \left(\eta^* - \eta^*_0\right) / \kappa^*_0 \left(\lambda^*_H\right)^2$ and r^*/λ^*_H entail a common profile, which describes precisely the liquid surface position in the near-field zone and quite beyond, for any combination of Ha, Bo and $D^* \geq D^*_{min}$. moreover, the far-field zone is also characterized by a self-similar behavior, which corresponds to an exponential-like decay, when employing η^*/η^*_C and r^*/λ^*_C.

The curvature of the stable profile is found to take a remarkable shape at its apex, $\kappa^*_0 \propto \left(\xi^* \eta^*_0\right)^{3/2}$. This fact and the problem geometry give rise to accurate simple formulas for computing the minimum separation distance D^*_{min}, its corresponding maximum deformation $\eta^*_{0,max}$ and minimum equilibrium gap $\epsilon^*_{0,min}$, when H_a and B_o are previously known from the literature (Israelachvili, 2011; Visser, 1972; Bergstrom, 1997) or experimentally obtained. In general, η_{max}, ϵ_{min} and, as a consequence, $D_{min} - R$ are always restricted to the range of the London-vdW interaction, which is of around $O(10\text{nm})$.

Chapter 3

Dependence on the film thickness

When the film E^* relative thickness takes finite values, the liquid/substrate interaction plays an important role in the deformation phenomenon of the liquid surface. As a consequence, the equilibrium shape of the film free surface is described by eq.(1.16), which, in equilibrium $\Delta P^* = 0$, is written as:

$$B_o \xi^* \eta^* + 2\kappa^* + H_a \Pi_{pl}^* + \frac{A H_a}{8\left(E^*\right)^3} \Pi_{ls}^* = 0, \tag{3.1}$$

where the local mean curvature κ^*, the probe/liquid Π_{pl}^* and the liquid/substrate Π_{ls}^* interaction potentials are defined as:

$$\kappa^* = -\frac{\xi^*}{2}\left(\frac{1}{r^*}\frac{\partial}{\partial r^*}\left[r^* \frac{\partial \eta^*}{\partial r^*}\left\{\left(\xi^* \frac{\partial \eta^*}{\partial r^*}\right)^2 + 1\right\}^{-1/2}\right]\right)$$

$$\Pi_{pl}^* = \frac{-1}{\left[\left(D^* - \xi^* \eta^*\right)^2 + \left(r^*\right)^2 - 1\right]^3}$$

$$\Pi_{ls}^* = -\left[\left(1 + \frac{\xi^* \eta^*}{E^*}\right)^{-3} - 1\right],$$

respectively.

Therefore, the unaltered system given by eqs.(1.39) is numerically solved (see Section1.8) in order to find the interface shape. In general, the modified capillary length is found in the range $\lambda_F^* \leq \lambda_{CF}^* \leq \lambda_C^*$, which should be used in the BCs expressed in eqs.(1.40) and the guess solution in eq.(1.41).

Some typical surface profiles obtained numerically are shown in Fig.3.1 for $H_a = 5.48 \times 10^{-3}$, $B_o = 3.07 \times 10^{-11}$ and $A = 1$, and a radial extension of about ten times the probe radius. Note that the presented window is much smaller than the capillary length $O\left\{\lambda_C^*\right\} \sim 10^5$, so that the entire interface deformation is not shown for a film with $E \to \infty$. In contrast, it is much larger than the film characteristic length of $O\left\{\lambda_F^*\right\} \sim 10^{-1}$ for a film with $E^* = 10^{-1}$, in which case, the entire deformation profile is depicted. As well, its corresponding local mean curvature is illustrated in Fig.3.2.

As it was found for the bulk behavior, there is a threshold separation distance D_{min}^* below which, no deformation profiles are found. The deformation profiles reported in Fig.3.1a were obtained for a single separation distance $D^* = 1.291$, which is equal to the threshold distance D_{min}^* for a bulk liquid with the same physical properties. The presented curves were obtained for different values of the relative thickness E^*, which varies over several orders of magnitude in the range $\left[10^{-1}, \infty\right[$. We observe that all the profiles exhibit a bump-like shape, roughly parabolic around $r^* = 0$, followed by an exponential-like decay. The profiles obtained for $E^* \geq 10^3$ are overlapped proving the existence of an asymptotic bulk regime. The vertical displacement of the surface weakens in magnitude and the deformation seems to be confined to a shorter radial extent as E^* is diminished. In addition, the curvature of the surface at $r^* = 0$ lowers when decreasing E^*. The local mean curvature of the aforementioned profiles is represented in Fig.3.2a, which shows a Lorentz distribution-like shape, barely covering a radial distance equal to a probe radius.

The deformation profiles corresponding to other separation distances, which are equal to the minimum separation distances D_{min}^* of different film thicknesses, $D^* = 1.289$ for $E^* = 10^{-2}$, $D^* = 1.256$ for

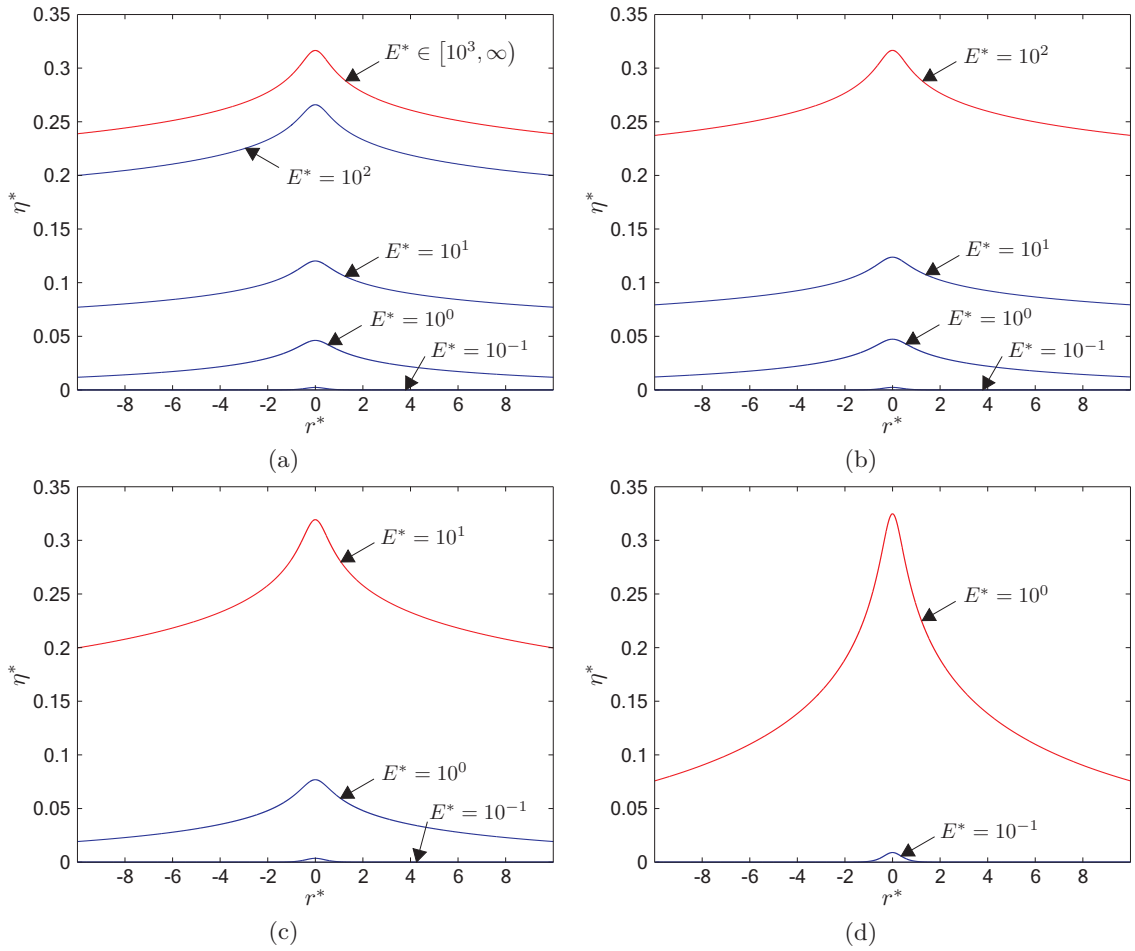


Figure 3.1: Dimensionless equilibrium thickness-dependent profiles, zoom of the central region obtained from solving eq.(3.1) for $H_a = 5.48 \times 10^{-3}$, $B_o = 3.07 \times 10^{-11}$ and $A = 1$, an initial guess $\eta^*_{guess} = 0$, and (a) $D^* = 1.291$ -corresponding to D^*_{min} for $E = 10^3$-, (b) $D^* = 1.289$ -corresponding to D^*_{min} for $E = 10^2$-, (c) $D^* = 1.256$ -corresponding to D^*_{min} for $E = 10^1$- and (d) $D^* = 1.202$ -corresponding to D^*_{min} for $E = 10^0$-.

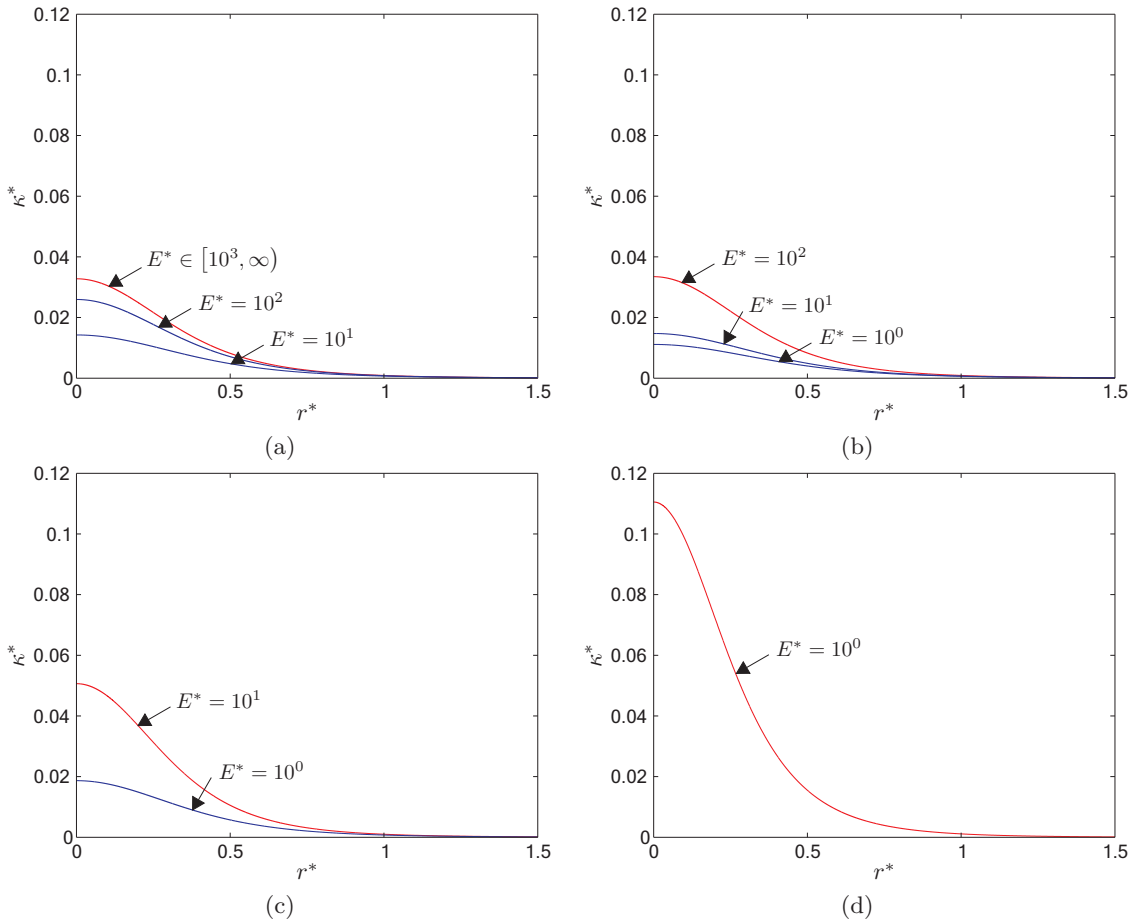
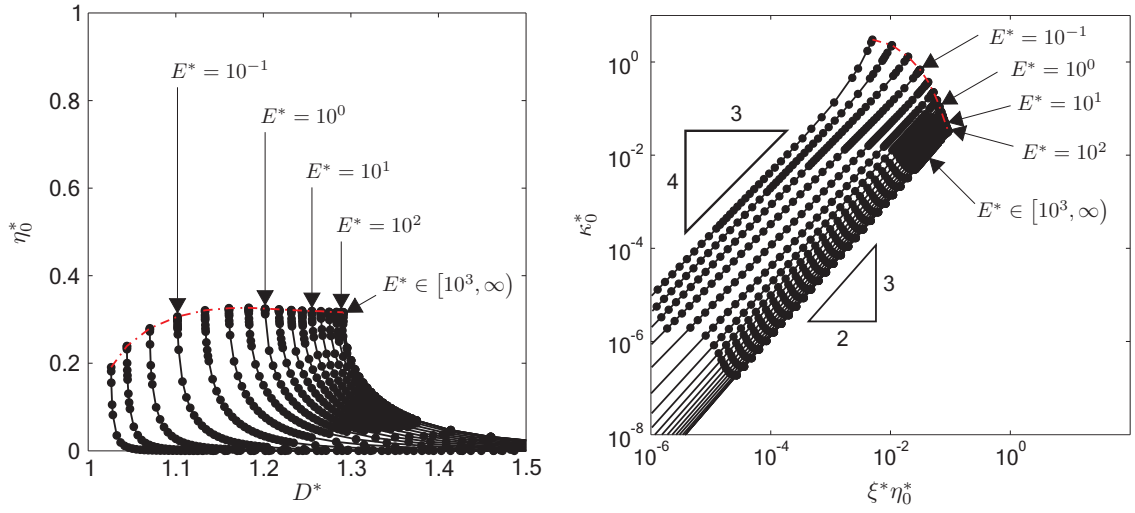


Figure 3.2: Dimensionless equilibrium thickness-dependent local mean curvature, zoom of the central region obtained from solving eq.(3.1) for with the same parameter values and variables as in Fig.3.1: (a) $D^* = 1.291$, (b) $D^* = 1.289$, (c) $D^* = 1.256$ and (d) $D^* = 1.202$.



(a) (b)

Figure 3.3: Thickness-dependent (a) apex reduced deformation $\xi^*\eta_0^*$ as a function of D^* and (b) peak curvature κ_0^* as a function of the apex position η_0^*, for $H_a = 5.48 \times 10^{-3}$, $B_o = 3.07 \times 10^{-11}$ and $A = 1$, an initial guess $\eta^*_{guess} = 0$. [○] numerical solution of eq.(3.1) and [– · –] extreme values $\kappa^*_{0,crit}$, D^*_{min} and $\eta^*_{0,max}$.

$E^* = 10^{-1}$ and $D^* = 1.202$ for $E^* = 10^0$, are shown in Figs.3.1b, 3.1c and 3.1d, respectively. As D^* decreases, the deformation profiles get narrower and sharper, and, as a consequence, their local mean curvature increase. The corresponding local mean curvature profiles are illustrated in Figs.3.2b, 3.2c and 3.2d, for $D^* = 1.289$, 1.256 and 1.202, respectively. it is important to notice that, for a given D^*, deformation profiles are not found for film thicknesses E^* larger than that for which the separation distance corresponds to D^*_{min}. From a common point of view, the threshold distance D^*_{min} behaves as a film thickness-dependent property.

3.1 Jump-to-contact

The corresponding behavior of the apex deformation η_0^* at $r^* = 0$ is shown in 3.3a, as a function of the separation distance D^*. As observed for an infinite film thickness, the obtained interface position for any film thickness depends on the guess solution. In 3.3a, we present the stable deformation, corresponding to the minimal free energy of the system, acquired by imposing $\eta^*_{guess} = 0$. Similar hyperbolic evolutions for η_0^* are observed for the different values of E^*. When sweeping from right to left, as the curve approaches the threshold distance D^*_{min}, the slope increases dramatically until a vertical asymptote is reached. At D^*_{min}, the maximum stable apex position $\eta^*_{0,max}$ is attained. For shorter separation distances, the probe/liquid attraction becomes unconstrained and the so-called "jump-to-contact" is observed, which provokes the wetting of the probe in a real experimental situation. Consistent with expectations on physical grounds, a decrease of E^* leads to a decrease of D^*_{min} along with a shrinkage of $\eta^*_{0,max}$, as the attractive liquid/substrate potential pulls the liquid film uniformly downward, therefore inhibiting its upward displacement. In other words, when the film thickness is lessened, the jump-to-contact condition is shifted to separation distances shorter than that observed for a bulk liquid. It is relevant to remark that a reduction of E provokes a similar effect as the one induced by an augmentation of B_o for a bulk behavior. In fact, the first order effect of a diminution in E^* is the increase of an effective Bond number, as it is stated in eq.(1.29), which justifies the previous idea.

The corresponding evolution of the peak curvature κ_0^* as a function of the apex reduced deformation $\xi^*\eta_0^*$ is shown in 3.3a for different values of the relative thickness E^*. As a general trend, for a given E^*, the peak curvature increases along with the associated deformation, showing a nearly constant slope in the presented logarithmic scale. The pattern of the curves in Fig.2.6b, when increasing the Bond number B_o, shows a important qualitative parallelism with the behavior of the curves in Fig.3.3b, when the film thickness E^* shrinks from 10^3 to 10^0. Nevertheless, mainly observed for the curves belonging to $E^* < 10^0$, the slope gradually becomes steeper as $\xi^*\eta_0^*$ increases and approaches the value of $\xi^*_{crit}\eta^*_{0,max}$.

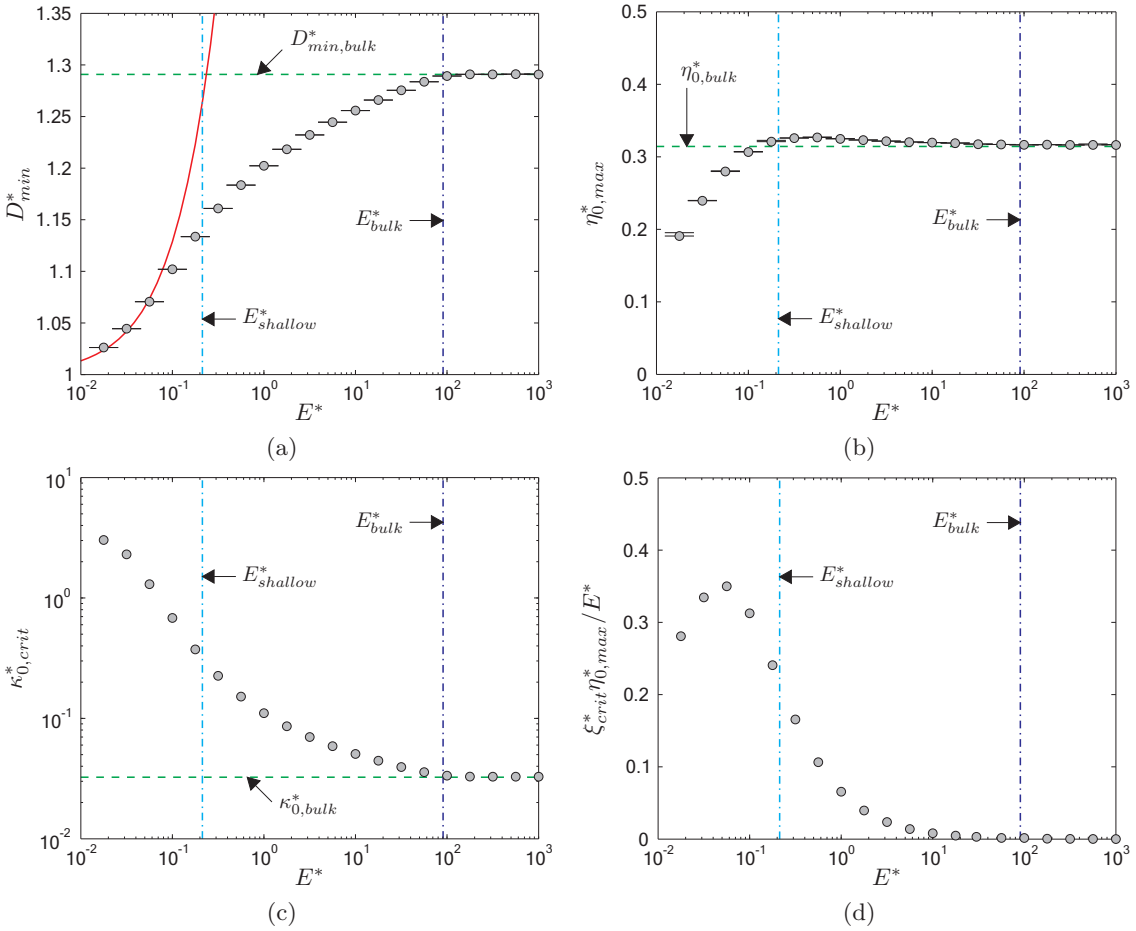


Figure 3.4: Thickness-dependent curves. (a) minimum separations distance D^*_{min}, (b) apex position η^*_0, (c) peak curvature κ^*_0 and (d) apex reduced product $\xi^*\eta^*_0/E^*$ as functions of E^*, for $H_a = 5.48 \times 10^{-3}$, $B_o = 3.07\times10^{-11}$ and $A = 1$. [$\circ$] numerical solution of eq.(3.1) and asymptotic approximations for [– – –] the bulk behavior $E^* > E^*_{bulk}$ and [——] the shallow film behavior $E^* < E^*_{shallow}$, with $E^*_{bulk} = 9.05\times10^{1}$ and $E^*_{shallow} = 2.13\times10^{-1}$. These approximations were obtained with eqs.(2.14), (2.13), (2.7) and (2.15) for bulk liquids, and eqs.(3.8) and (3.7) for shallow films, both cases also using eq.(B.1). The characteristic thicknesses, E^*_{bulk} and $E^*_{shallow}$, are defined in eqs.(3.3)) and (3.4), respectively.

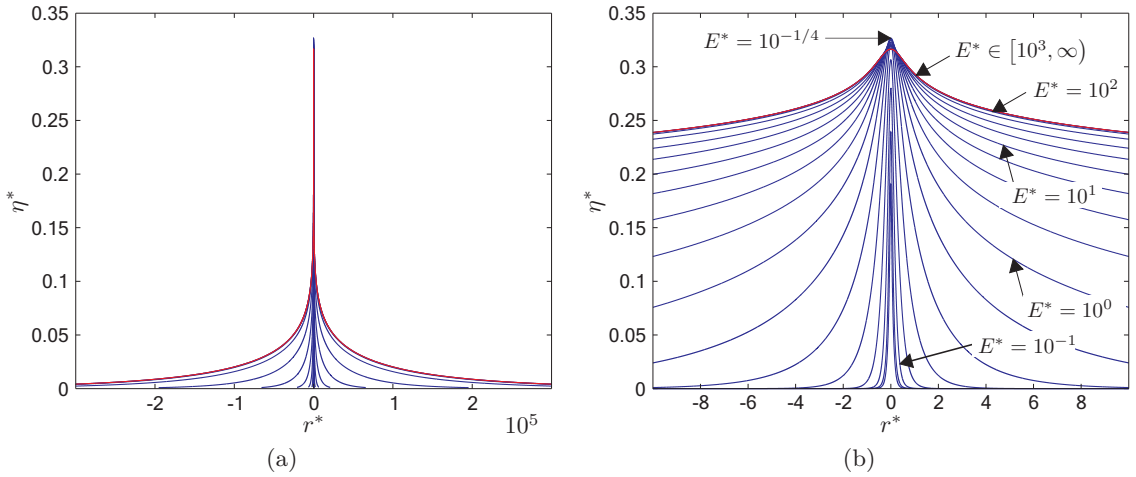


Figure 3.5: (a) Dimensionless equilibrium critical profiles and (b) zoom of the central region obtained from solving eq.(3.1), for $H_a = 5.48 \times 10^{-3}$, $B_o = 3.07 \times 10^{-11}$ and $A = 1$, at $D^* = D^*_{min}$ for different values of E^*.

In most of the cases, the behavior of each curve seems to be properly described by a power law. For relative thick films, an exponent of 3/2 has been found (Ledesma-Alonso et al., 2012a; Quinn et al., 2013), while for shallow films and small deformations, an exponent of 4/3, is discerned.

Fig. 3.4a reports the evolution of the minimum separation distance D^*_{min}, Fig.3.4b the maximum apex position $\eta^*_{0,max}$, and Fig. 3.4c the critical peak curvature, as function of the film relative thickness E^*. The bulk behavior is characterized by a plateau, which in the presented case takes the values $D^*_{min} \approx 1.29$, $\eta^*_{0,max} \approx 3.16 \times 10^{-1}$ and $\kappa^*_{0,crit} = 3.28 \times 10^{-2}$ for thicknesses $E^* \geq 10^2$. On the other hand, these variables tend toward the values $D^*_{min} \to 1$, $\eta^*_{0,max} \to 0$ and $\kappa^*_{0,crit} =\to 1/3$ when the limit of $E^* \to 0$ is approached. For intermediate thicknesses, typically varying from 10^{-1} to 10^2, D^*_{min} decreases, whereas $\kappa^*_{0,crit}$ increases, both shifting slowly but directly, in order to link the two asymptotic behaviors. In turn, $\eta^*_{0,max}$ goes through a dissimilar transition regime. The maximum apex position $\eta^*_{0,max}$ increases gradually when E^* decreases, attaining its maximum value $\eta^*_{0,max} = 3.27 \times 10^{-1}$ at $E^* \approx 5.6 \times 10^{-1}$. When E^* collapses, the value of $\eta^*_{0,max}$ decays abruptly toward zero. associated to noticeable variations due to the film thickness. It is interesting to note that for the dimensionless parameters considered here, the apex reduced deformation $\xi^*_{crit}\eta^*_{0,max}$ never exhibits larger values than that of the film relative thickness E^*, which makes $\xi^*_{crit}\eta^*_{0,max}/E^* < 1$. As it is shown in Fig.3.4d, the maximum value that the apex product takes is $\xi^*_{crit}\eta^*_{0,max}/E^* = 0.35$ for a film of thickness $E^* = 5.6 \times 10^{-2}$, whereas it is $\xi^*_{crit}\eta^*_{0,max}/E^* < 0.1$ in the range $E^* \in \left[10^0, \infty\right[$.

In Fig.3.5, the interface shape η^*, at $D^* = D^*_{min}$, is shown as a function of the radial position r^*, for different values of E^*. The surface position is shown in Fig.3.5a, up to a radial position equal to three times the capillary length of a bulk liquid. As previously discussed, the radial extent of the deformation diminish when E^* lowers. The surface profile sharpens, provoking the dilatation of the curvature at the surface apex. Indeed, as observed in 3.3b, for a fixed value of $\xi^*\eta^*_0$, the peak curvature κ^*_0 grows significantly in orders of magnitude when decreasing the film relative thickness E^*.

The evolution of the maximum apex position $\eta^*_{0,max}$ as a function of the film thickness E^* has already been discussed, when the analysis of the curve in Fig.3.4b was made. The augmentation of $\eta^*_{0,max}$, perceived during the initial decay of E^*, is also observed when comparing the profiles shown in Fig.3.5b. When E^* decreases from 10^3 to 10^{-1}, the surface sharpening is also a consequence of this apex position rising. Afterward, in spite of the abrupt abatement of $\eta^*_{0,max}$, occurring when E^* goes down, the surface profile continues to narrow because the rate at which the radial extension decreases is more important.

Based on these results, we can define two behaviors depending on the film thickness. For thin films, the amplitude of the surface deformation is restricted to a length scale significantly shorter than the capillary length, clearly indicating the appearance of a "localized tip effect". This phenomenon is characterized by a deformation profile of confined radial extent, specifically restricted to the near-field underneath the probe. In contrast, for thick films, the surface deformation is observed up to the capillary length. Hence, the tip effect is not observed for thicknesses above a characteristic value, which is found within $E^* \in \left[10^2, 10^3\right]$, and, as a consequence, the deformation corresponds to that of the bulk liquid.

3.2 Characteristic thicknesses

The characteristic radial length scales, introduced in the asymptotic analysis of the equilibrium interface profile, are now used to highlight the existence of two characteristic film thicknesses. When the capillary length λ_C is much smaller than the film characteristic length λ_F, a bulk liquid behavior is forecast. Nevertheless, when λ_C and λ_F are of the same order of magnitude, film thickness effects are expected to be observed. From $\lambda^*_F \sim \lambda^*_C$, a first critical film thickness E_{bulk} is obtained:

$$E_{bulk} \simeq \left(\frac{H_{ls}}{2\pi\Delta\rho g}\right)^{1/4} \quad , \quad E^*_{bulk} \simeq \left(\frac{3AH_a}{8B_o}\right)^{1/4}. \tag{3.3}$$

E_{bulk} is a constant for a given system, independent of the probe radius R, and $E^*_{bulk} = E_{bulk}/R$ depends on the dimensionless parameters A, H_a and B_o. The value of this critical thickness in common AFM setups is in the range $E_{bulk} \in [10^{-7}, 10^{-6}]$m, corresponding to $E^*_{bulk} \in [10^0, 10^3]$.

On the other hand, when the film characteristic length λ_F is of the order of the probe radius R, the probe/liquid attraction is only opposed by the liquid/substrate attraction. Hence, from $\lambda^*_F \sim 1$, we find

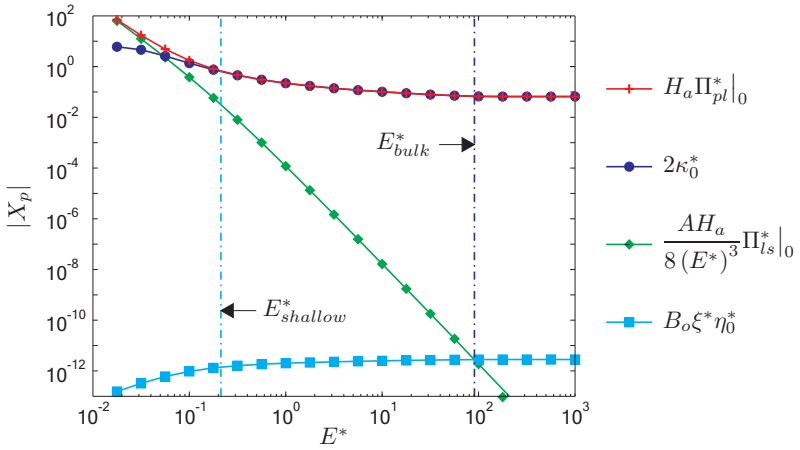


Figure 3.6: Absolute value of the different terms X_p from eq.(3.1) evaluated at $r^* = 0$, for which $\sum X_j = 0$, as functions of E^*, at $D^* = D^*_{min}$, and for $H_a = 5.48 \times 10^{-3}$, $B_o = 3.07 \times 10^{-11}$ and $A = 1$. The critical film thicknesses are $E^*_{shallow} = 2.13 \times 10^{-1}$ and $E^*_{bulk} = 9.05 \times 10^{1}$.

a second critical film thickness $E_{shallow}$, which is given by:

$$E_{shallow} \simeq \left(\frac{R^2 H_{ls}}{2\pi\gamma}\right)^{1/4} \quad , \quad E^*_{shallow} \simeq \left(\frac{3AH_a}{8}\right)^{1/4} . \tag{3.4}$$

$E_{shallow}$ is a function of the probe radius, scaling as $R^{1/2}$, and $E^*_{shallow} = E_{shallow}/R$ changes with the product of the parameters H_a and A. Within common AFM setups, this shallow critical thickness is in the order of $E_{shallow} \in [10^{-10}, 10^{-8}]$m, corresponding to $E^*_{shallow} \in [10^{-2}, 10^{0}]$.

It is expected to observe different behaviors depending on the film thickness, relative to the aforementioned critical values. They might be useful to mark the boundaries of the arising regimes, in which the involved mechanisms alternate their contribution.

In Fig.3.6, the terms in eq.(3.1) are shown as function of the film thickness E^* at the jump-to-contact condition D^*_{min}. The presented curves correspond to the reference case, for which $A = 1$, $H_a = 5.48 \times 10^{-3}$ and $B_o = 3.07 \times 10^{-11}$.

As it can be seen in the right-hand side of Fig.3.6, where $E^* > E^*_{bulk}$, the curvature and the probe/liquid interaction terms are nearly constants. Additionally, the hydrostatic term $B_o\eta^*$ exhibits a constant but smaller magnitude than to the two aforementioned terms. The presence of the substrate can be disregarded, because the liquid/substrate interaction term is utterly negligible. Consequently, the deformation of the liquid surface results from the equilibrium between the surface tension and the probe/liquid interaction, and, in dimensionless terms, it is only determined by the values of H_a and B_o. Moreover, the minimum separation distance D^*_{min} and the maximum apex position $\eta^*_{0,max}$ do not vary with the film relative thickness E^*, as depicted in Figs.3.4a and 3.4b. The surface deformation spreads to the effective capillary length, which is essentially given by the usual capillary length $\lambda^*_{CF} \approx \lambda^*_C$, because in this case $\lambda^*_F \gg \lambda^*_C$. We shall name this regime, the asymptotic "bulk" behavior.

For a film with an intermediate thickness $E^*_{shallow} < E^* < E^*_{bulk}$, though the magnitude of the liquid/substrate term exceeds that of the hydrostatic term, it is still negligible compared to the probe/liquid interaction and the curvature terms. Nonetheless, the latter two terms are not constant anymore, they increase slowly and simultaneously, remaining in balance, when reducing the film relative thickness E^*, as it can be discerned from Fig.3.6. In this case, the deformed surface shape stretches out to the effective capillary length λ^*_{CF}, which takes values between the capillary length λ^*_C and the film characteristic length λ^*_F. This constraint forces the surface to recover from its deformation, getting back to a flat profile at a radial distance shorter than the capillary length. The resulting restrained interface shape shows a curvature, in the zone nearby r^*_0, that is greater than that of the deformed bulk. Hence, the interface apex position results from the interplay of the three involved physical mechanisms: surface tension and probe/liquid interaction forces, directly, and liquid/substrate interaction force, by means of an implicit modification of the curvature.

In the left-hand side of Fig.3.6, where $E^* < E^*_{shallow}$, the curvature term seems to reach a saturated state. Meanwhile, the probe/liquid and the liquid/substrate attraction terms increase monotonically,

approaching each other in magnitude as E^* decreases from $E^*_{shallow}$ toward smaller values. Hence, the effect of the proximity of the substrate dominates over that of the surface tension, and the position of the film free surface is retrieved from the equilibrium of the probe/liquid and the liquid/substrate attractive interactions. D^*_{min} and $\eta^*_{0,max}$ change significantly with the film relative thickness E^*, as it is shown in Figs.3.4a and 3.4b, respectively. In this regime, the hydrostatic term tends to completely vanish. A direct effect of the substrate attraction is observed on the radial span of the surface deformation λ^*_{CF}. In this case, $\lambda^*_F \ll \lambda^*_C$, therefore the effective capillary length is mainly given by the film characteristic length $\lambda^*_{CF} \approx \lambda^*_F$. Therefore, the deformation profiles are sharp and they are restrained to a very narrow zone around $r^* = 0$. We name this regime, the asymptotic "shallow film" behavior, where the above-named localized tip effect is observed.

3.3 Apex behavior in the small deformation regime

We now focus on the particular evolution observed in Fig.3.3b for shallow films, $E^* < E^*_{shallow}$, and small deformations. Consequently, according to the relative contributions shown in Fig.3.6, the surface deformation results at first order from the balance between the probe/liquid and the liquid/substrate interactions. Therefore, eq.(3.1) becomes a straightforward balance:

$$\Pi^*_{pl} = -\frac{A}{8\left(E^*\right)^3}\Pi^*_{ls}, \tag{3.5}$$

which, under the small deformations consideration $\xi^*\eta^*/E^* \ll 1$ (see eq.(1.24)) and with the definition of the characteristic film length λ^*_F, is written as:

$$\Pi^*_{pl} = -\frac{\xi^*\eta^*}{H_a\left(\lambda^*_F\right)^2}. \tag{3.6}$$

As in Chapter 2, to analyze the apex behavior, we solve eq.(1.17b) for the dimensionless probe position D^* at $r^* = 0$, but now using eq.(3.6). Following this procedure, the following relationship is obtained:

$$D^* = \xi^*\eta^*_0 + \sqrt{1 + \left[\frac{\xi^*\eta^*_0}{H_a\left(\lambda^*_F\right)^2}\right]^{-1/3}}, \tag{3.7}$$

which gives the dependency of D^* on $\xi^*\eta^*_0$. Then, making $dD^*/d\eta^*_0 = 0$, leads to the following relationship:

$$\left(\xi^*_{crit}\eta^*_{0,max}\right)^{8/3} + \Theta\left(\xi^*_{crit}\eta^*_{0,max}\right)^{7/3} - \left(\frac{\Theta}{6}\right)^2 = 0, \tag{3.8}$$

where $\Theta = \sqrt[3]{8\left(E^*\right)^4/3A}$. This polynomial is meant to be solved in order to estimate the critical apex product $\xi^*_{crit}\eta^*_{0,max}$. The acquired value determines the minimum separation distance D^*_{min}, when it is used in eqs.(3.7). Afterwards, the critical initial gap ξ^*_{crit} and the maximum apex deformation $\eta^*_{0,max}$ can be deduced.

Furthermore, the geometric relationship $D^* = 1 + \xi^*\eta^*_0 + \xi^*\varepsilon^*_0$ (see Fig.1.4), along with the first order approximation of eq.(3.7), leads to an expression of the apex deformation in terms of the initial ξ^* and the equilibrium ε^*_0 gaps:

$$\eta^*_0 = \frac{H_a\left(\lambda^*_F\right)^2}{8\xi^*\left(\xi^*\varepsilon^*_0\right)^3}. \tag{3.9}$$

As well, equilibrium between the force due to the liquid/substrate interaction, which can be taken as:

$$F_{ls} \sim \frac{H_{ls}\eta^*_0}{R\left(E^*\right)^4}, \tag{3.10}$$

and the probe/liquid interaction force, given by eq.(2.11), including a proportional constant C_{lm}, yields

another relationship between the apex position and the reduced gaps:

$$\eta_0^* = \frac{(E^*)^4}{3\xi^* A C_{lm} \left(\xi^* \varepsilon_0^*\right)^2}, \tag{3.11}$$

Combining eqs.(3.9) and (3.11), and using the definition of λ_F^*, we find that

$$\eta_0^* = \frac{(E^*)^4}{3\xi^* A \left(C_{lm}\right)^3}, \tag{3.12}$$

which, with the knowledge of C_{lm}, gives an estimation of the apex position only in terms of the physical parameter A and the reduced dimension E^*.

From the combination of eqs.(3.6) and (3.1), we obtain an implicit relation between the problem parameters (E^*, D^*, A), the surface position and the radial coordinate:

$$\eta^* \left[(D^* - \xi^* \eta^*)^2 + (r^*)^2 - 1\right]^3 = \frac{8\,(E^*)^4}{3\xi^* A}. \tag{3.13}$$

Now, considering that $D^* \gg \xi^* \eta^*$ within the expression of the probe/liquid potential Π_{pl}^*, evaluated at $r^* = 0$, reduces the previous equation to:

$$\eta_0^* = \frac{8\,(E^*)^4}{3\xi^* A \left[(D^*)^2 - 1\right]^3}. \tag{3.14}$$

A comparison between eqs.(3.12) and (3.14) gives:

$$C_{lm} = \frac{1}{2}\left[(D^*)^2 - 1\right], \tag{3.15}$$

indicating that C_{lm}, which was originally considered as a constant, should be redefined as a correction function, dependent of the separation distance D^*.

Differentiating eq.3.13 twice and evaluating at $r^* = 0$, in order to obtain the peak curvature as described in eq.(1.34), gives:

$$\kappa_0^* = \frac{16\,(E^*)^4}{A\left[(D^*)^2 - 1\right]^4}. \tag{3.16}$$

Finally, the combination of eqs.(3.14) and (3.16), results in the power law:

$$\kappa_0^* = \sqrt[3]{A}\left(3\frac{\xi^* \eta_0^*}{E^*}\right)^{4/3}, \tag{3.17}$$

which is in agreement with the trend observed in Fig.3.3b for shallow films and small deformations. Within this regime, the minimum separation distance D_{min}^* and the maximum apex position $\eta_{0,max}^*$ are significantly modified by the film relative thickness E^*. Note also that in this regime, the deformation is dependent on the Hamaker constant ratio A, but not on the modified Hamaker and Bond numbers.

3.4 Probe size effect

With the purpose of determining the experimental parameters for AFM measurements, the probe size and the film thickness effects are quantitatively studied. Therefore, the dimensional jump-to-contact threshold is analyzed, considering constant physical properties of the system. The combined effect of H_a and E^* on the deformation, for a given value of $H_{ls} = H_{pl}$, is equivalent to study the effect of R and E on the free surface displacement. The dimensionless representation depicted in Fig.3.4b, corresponds to the evolution of $\eta_{0,max}^*$ in terms of E^* for a single value $H_a = 5.48 \times 10^{-3}$. As a consequence, it is possible to reconstruct the dimensional dependency of the maximum apex displacement $\eta_{0,max}$ on the film thickness E, but only for $R = R_3 = 10^{-8}$ m, with the parameters $\gamma = 3.1 \times 10^{-2}$ N/m and $H_{pl} = 4 \times 10^{-20}$ J. Additionally, considering the same physical parameters, eq.(3.1) was solved numerically for different

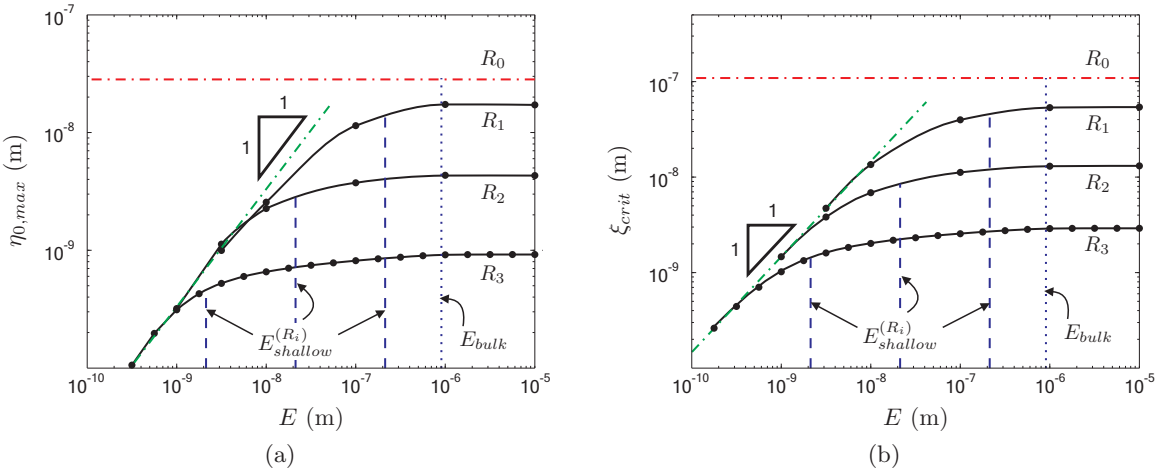


Figure 3.7: (b) Maximum apex displacement $\eta_{0,max}$ and (a) ξ_{crit} as functions of the film thickness E, for $H_{ls} = H_{pl} = 4 \times 10^{-20}$ J, $\gamma = 3.1 \times 10^{-2}$ N/m and different values of the probe radius R ($R_1 = 10^{-4}$ m, $R_2 = 10^{-6}$ m and $R_3 = 10^{-8}$ m). The values of $E_{shallow}$, corresponding to the different values of R are summarized in 3.1, as well as the value of E_{bulk}. The horizontal lines [– · –] are the solution of eqs.(2.14), (2.13), (2.7) and (2.15) for $\eta_{0,max}$ and ξ_{crit}, which corresponds to the thick film approximation, for $R_0 \gtrsim \lambda_C \sim 10^{-3}$m.

		$R_0 \sim \lambda_C$	R_1	R_2	R_3
R	[m]	10^{-3}	10^{-4}	10^{-6}	10^{-8}
H_a	[1]	5.48×10^{-13}	5.48×10^{-11}	5.48×10^{-7}	5.48×10^{-3}
B_o	[1]	3.07×10^{-1}	3.07×10^{-3}	3.07×10^{-7}	3.07×10^{-11}
E_{bulk}	[m]	9.05×10^{-7}			
$E_{shallow}^{R}$	[m]	6.73×10^{-7}	2.13×10^{-7}	2.13×10^{-8}	2.13×10^{-9}
$\eta_{0,max}$ (bulk)	[m]	2.83×10^{-8}	1.72×10^{-8}	4.31×10^{-9}	9.18×10^{-10}

Table 3.1: Values of the dimensionless parameters, the characteristic film thicknesses and the bulk apex displacement, for the different probe radii and for the given physical properties: $\gamma = 3.1 \times 10^{-2}$ N/m, $\Delta\rho = 9.7 \times 10^2$ kg/m^3 and $H_{pl} = H_{ls} = 4 \times 10^{-20}$ J.

values of E and for $R_2 = 10^{-6}$ m and $R_1 = 10^{-4}$ m. In Fig.3.7a, the maximum apex displacement $\eta_{0,max}$ is displayed as a function of the film thickness E, for the three probe radii. One notes that the evolution of $\eta_{0,max}(E)$ follows similar tendencies: for $E < E_{shallow}$, $\eta_{0,max}$ increases linearly with E; for $E_{shallow} < E < E_{bulk}$, $\eta_{0,max}$ grows monotonically as E increases with a slowly declining slope; and finally for $E > E_{bulk}$, $\eta_{0,max}$ reaches a plateau.

Fig.3.7a points out that, for a shallow film $E < E_{shallow}$, the maximum apex displacement $\eta_{0,max}$ is independent of the probe radius R. A linear dependency of the displacement on the thickness, $\eta_{0,max} = \alpha_0 E$ with $\alpha_0 \simeq 0.33$, is found. Since $E_{shallow}$ grows as $R^{1/2}$, the linear regime is extended to a larger range of E. Furthermore, the value of $\eta_{0,max}$ at the plateau, characteristic of the bulk behavior $E > E_{bulk}$, rises with the value of R. As depicted in eq.(3.3), E_{bulk} is constant for a given set of physical parameters, whatever the value of R. In 3.7a, the free surface displacement of a bulk liquid due to its interaction with a probe of millimetric size, $R_0 = 10^{-3}$m$\approx \lambda_C$, is also represented. In the theoretical case, in which $R = \lambda_C$, the two critical film thicknesses collapse into a single value, $E_{bulk} = E_{shallow}$. As a consequence, the value of $\eta_{0,max}$ obtained with $R = R_0$ in the bulk regime corresponds to the maximum displacement that the liquid surface can attain by increasing the probe radius, even for $R > \lambda_C$. Hence, for probes of larger radius, the system can be modeled as a film interacting with a flat solid surface, for which the maximum apex displacement is approximately the same as for $R \approx \lambda_C$, and completely independent of R. Table 3.1 reports the characteristic parameters computed for the different values of R.

The combined analysis of Figs.3.5 and 3.7a shows that the localized tip effect is only observed for shallow films for which $E < E_{shallow}$. As a consequence, when R increases, the localized tip effect is

observed at larger thicknesses due to the relation between $E_{shallow}$ and R. Within this regime, the linear dependency of $\eta_{0,max}$ on E can be understood by considering that the confined liquid behaves as a linearly elastic solid. This is in agreement with the linear relationship observed between the displacement and the thickness of confined materials undergoing a constant force test (Tordjeman et al., 2000). In conclusion, the localized tip effect is characterized by a constant reduced deformation:

$$\frac{\eta_{0,max}}{E} = \alpha_0, \tag{3.18}$$

which, in the particular case of $A = 1$, presents a value of $\alpha_0 \approx 0.33$.

A film of a very small thickness compared to the size of the probe ($R \gg E$) corresponds to $E < E_{shallow}$, so that the surface deformation at the jump-to-contact results from the balance between the probe/liquid and the liquid/substrate interactions. Considering the geometric decomposition, $D_{min} = R+\eta_{0,max}+\epsilon_{0,min}$, we can deduce from Fig.3.4 that the surface displacement and the equilibrium gap are comparable in magnitude, $\eta_{0,max} \sim \epsilon_{0,max}$. Thus, taking into account the dependency $\eta_{0,max} = \alpha_0 E$, it results that the equilibrium gap is much smaller than the probe radius, $\epsilon_{0,min} \ll R$. Therefore, eq.(1.10) can be condensed to:

$$\Pi_{pl} \simeq \frac{H_{pl}}{6\pi \left(\epsilon_{0,min}\right)^3}. \tag{3.19}$$

In addition, eq.(1.11) is also reduced into:

$$\Pi_{ls} \simeq \frac{\alpha_1 H_{ls}}{6\pi \left(E\right)^3}, \tag{3.20}$$

where $\alpha_1 = 1 - (1 + \alpha_0)^{-3}$. The balance between these two simplified potentials gives:

$$\epsilon_{0,min} \simeq \left[\alpha_1 A\right]^{-1/3} E. \tag{3.21}$$

Using this result, a linear evolution of the critical initial gap between the probe surface and the originally flat surface is yield:

$$\xi_{crit} \simeq \left\{\alpha_0 + \left[\alpha_1 A\right]^{-1/3}\right\} E. \tag{3.22}$$

In Fig.3.7b, the critical initial gap $\xi_{crit} = D_{min} - R$ is shown as a function of E for different values of R. ξ_{crit} behaves essentially the same way as $\eta_{0,max}$, shown in 3.7a. The only difference is that the magnitude of ξ_{crit} is slightly superior to that of $\eta_{0,max}$, for the same value of E. The linear dependency described by eq.(3.22), is verified in Fig.3.7b, for small values of E.

The value of the gap ξ_{crit} should be respected when performing AFM measurements, because it indicates the experimental setpoint needed to avoid the jump-to-contact and the wetting of the probe. For example, colloidal AFM probes, with a radius of $R = R_2 = 10^{-6}$ m, must be used at a distance $\xi_{crit} \gtrsim 10^{-8}$ m when scanning, while for common AFM probes with $R = R_3 = 10^{-8}$ m, we should respect $\xi_{crit} \gtrsim 10^{-9}$ m, which is one order of magnitude closer to the interface.

3.5 Concluding remarks

We have studied the interaction between an AFM probe and a liquid film deposited over a flat substrate. The competition between probe/liquid and liquid/substrate attraction determines the equilibrium position of the liquid surface. The radial extent of the deformation goes up to the effective capillary length λ_{CF}, which takes values between the capillary length λ_C, and the film characteristic length λ_F. When the deformation extends up to $\lambda_{CF} \sim \lambda_C$, gravity is responsible for the flattening of the surface. On the other hand, when $\lambda_{CF} \sim \lambda_F$, the liquid/substrate attraction is the mechanism that restrains the deformation.

From these two characteristic length scales, the existence of two characteristic film thicknesses, $E_{shallow}$ and E_{bulk}, is pointed out. $E_{shallow}$ depends on the liquid/substrate interaction constant and the liquid surface tension, and scales as $R^{1/2}$. In contrast, E_{bulk} is independent of the probe radius R, taking a constant value for a given set of physical properties of the system.

For shallow films, i.e. $E < E_{shallow}$, the maximum apex displacement varies linearly with the film thickness $\eta_{0,max} = \alpha_0(A)E$, and is independent of R. In addition, a localized tip effect is revealed, which

is characterized by a deformation of localized radial extent $\lambda_{CF} \sim \lambda_F$ and small amplitude. For thick films, i.e. $E > E_{bulk}$, no tip effect is observed, and $\eta_{0,max}$ takes a fixed value independent of the film thickness E, but given by the probe radius R.

From a practical point of view with the aim of performing AFM experiments, $E_{shallow}$ appears as the relevant characteristic thickness, which can be used to separate two regimes: a linear regime for $E < E_{shallow}$ where $\eta_{0,max}$ and D_{min} are controlled by the film thickness E; and a plateau regime for $E > E_{shallow}$ where $\eta_{0,max}$ and D_{min} are mainly determined by the probe radius R.

Chapter 4

Mechanic analogy of the static local probe / liquid system

4.1 Spring-mass model

In order to provide quick access to quantitative results, one may look for simple relationships to quantify the surface deformation. Since the apex position is representative of the utter surface deformation, one may try to understand the impact of the physical and geometric parameters on this relevant variable. In the previous chapters, our analysis has only treated the liquid surface deformation, ignoring the probe deflection. This is appropriated only for very stiff cantilevers, thus, in order to extrapolate the results, we should examine a more general situation.

Consider a probe placed above a liquid film, with an initial gap ξ between their surfaces, as shown in Fig.4.1a. Due to the probe/liquid interaction, both the cantilever and the liquid surface suffer a displacement from its initial position. The cantilever shows a deflection δ, whereas the liquid surface presents a deformation η_0 at its apex.

A simple way to describe the final equilibrium system lies in the modeling of its elements as spring-mass elements, as shown in Fig.4.1b. Herein, the initial gap is $\xi = D - R$, where D is the distance from the probe center to the initially flat liquid surface and R is the probe radius. The cantilever deflection is $\delta = \xi - x$, where x is the final lower position of the probe surface. The liquid surface deformation η_0 is the upper position of the liquid, which will be considered as flat element. Finally, the final gap between the surfaces is defined as $\varepsilon_0 = \xi - \eta_0$.

The system initial shape has been modified due to the probe/liquid interaction force. This force, which is given by a version of eq.(1.1) which includes the cantilever deflection and the liquid surface deformation, can be written as:

$$F_{int} = \frac{\Lambda H_{pl}}{(x - \eta_0)^{\alpha}},$$

where H_{pl} is the probe/liquid interaction constant (Hamaker constant), and Λ and α are interaction parameters that depend on the geometry of the interacting bodies. Table 4.1 summarizes the values of Λ and α reported in the literature (Israelachvili, 2011).

Geometry of the bodies	Λ	α
Two spheres of radius R	$R/12$	2
A sphere of radius R and a flat surface	$R/6$	2
Two flat surfaces with an interacting area of πR^2	$R^2/6$	3

Table 4.1: Interaction parameters of the van der Waals interaction force, given for two bodies of different geometries (Israelachvili, 2011).

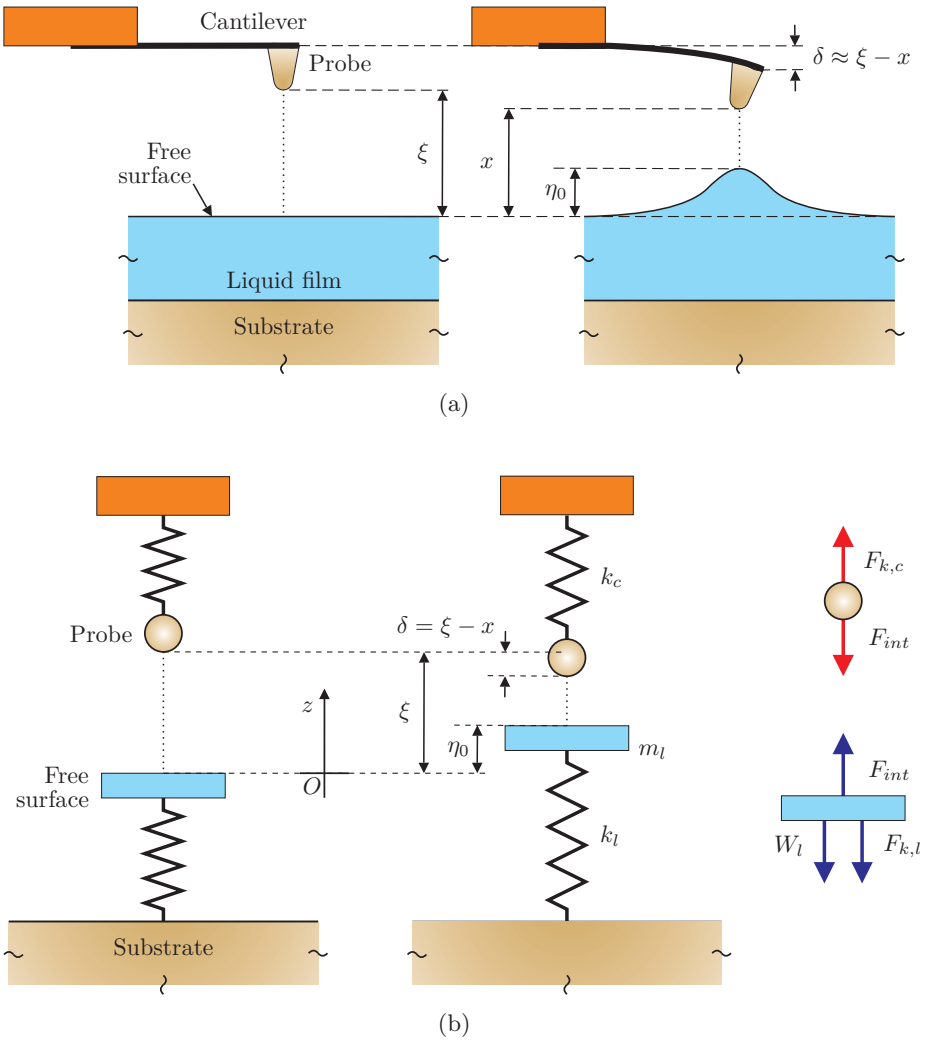


Figure 4.1: (a)Simple AFM schema, and (b) Spring-mass mechanic analogy and its corresponding free-body diagram.

The probe elastic restoring force is given by:

$$F_{k,c} = k_c \left(\xi - x\right),$$

where k_c is its equivalent spring constant.

In turn, the liquid restoring force is:

$$F_{k,l} = k_l \eta_0,$$

where k_l is the liquid effective spring constant, which for simplicity, will be linearly related to the liquid surface tension γ_l, i.e. $k_l \simeq C_{lk} \pi \gamma_l$.

The weight of the swifted amount of liquid is:

$$W_l = m_l g^*$$

where m_l is the mass of the liquid that has been swifted from its initial configuration, and g^* is a modified gravity constant, which is deduced from the definition of the effective Bond number B_o^{eff} (see eq.(1.29)), and is given by:

$$g^* = g + \frac{H_{ls}}{2\pi\rho_l E^4},$$

where H_{ls} is the liquid/substrate interaction constant (Hamaker constant), E is the liquid film thickness and ρ is the liquid density. As well, the involved liquid mass is defined as:

$$m_l \simeq C_{lm} \pi \rho_l R^2 \eta_0$$

where C_{lm} is a correction factor that depends on the initial gap ξ. A more precise definition will be given in the following.

From the free-body diagram of the probe, we find:

$$\begin{aligned} F_{k,c} - F_{int} &= 0 \\ k_c \left(\xi - x\right) - \frac{\Lambda H_{pl}}{\left(x - \eta_0\right)^{\alpha}} &= 0, \end{aligned}$$

whereas, for the liquid, we have:

$$\begin{aligned} F_{int} - W_l - F_{k,l} &= 0 \\ \frac{\Lambda H_{pl}}{\left(x - \eta_0\right)^{\alpha}} - m_l g^* - k_l \eta_0 &= 0. \end{aligned}$$

As a consequence, for a sphere in interaction with a flat surface, we have the system of equations:

$$k_c \left(\xi - x\right) - \frac{R H_{pl}}{6\left(x - \eta_0\right)^2} = 0 \tag{4.3a}$$

$$\frac{R^3 H_a}{8\left(x - \eta_0\right)^2} - \left[B_o^{eff} C_{lm} + C_{lk}\right] \eta_0 = 0 \tag{4.3b}$$

where:

$$H_a = \frac{4 H_{pl}}{3\pi\gamma_l R^2} \qquad B_o = \frac{\rho_l g R^2}{\gamma_l} \tag{4.4}$$

$$A = \frac{H_{ls}}{H_{pl}} \qquad B_o^{eff} = B_o + \frac{3 A H_a R^4}{8E^4}, \tag{4.5}$$

which describes the lower position of the probe x and the liquid surface position η_0. The dimensionless parameters H_a, A, B_o and B_o^{eff} have been already introduced in Chapter 1 (see eqs.(1.19), (1.20), (1.18) and (1.29)), which re-emergence indicates the consistency of the spring-mass model with our static liquid deformation model.

4.2 Simplifications

4.2.a Rigid Sample

By fixing $\eta_0 = 0$, a rigid sample is modeled instead of a liquid film , and we must only solve eq.(4.3a) to find the final probe position x. Hence,making $\eta_0 = 0$, the equation to be solved is rewritten as:

$$(\xi - x)\, x^2 = \frac{RH_{pl}}{6k_c}. \tag{4.6}$$

In the right column of Fig.4.2, the numerical solution of eq.(4.6) is shown for different cantilever stiffnesses.

Optimization of the function $\xi(x)$, leads to find the critical lower position of the probe surface:

$$x_{crit} = \sqrt[3]{\frac{RH_{pl}}{3k_c}}. \tag{4.7}$$

This expression has already been introduced (see eq.(1.2)). As well, this critical lower position is observed when the critical initial gap is given by the minimum distance:

$$\xi_{crit} = D_{min} - R = \frac{3}{2}x_{crit}, \tag{4.8}$$

where D_{min} is the minimum distance between the probe center and the initial liquid surface position. This provokes the critical deflection of the cantilever:

$$\delta_{crit} = \xi_{crit} - x_{crit} = \frac{1}{2}x_{crit}. \tag{4.9}$$

The analysis of this simplified case, has already been discussed in the literature(Hutter and J., 1993).

4.2.b Rigid Cantilever

By fixing $x = \xi$, thus $\delta = 0$, a rigid cantilever is modeled. Hence, only eq.(4.3b) should be solved, substituting $x = \xi$. It is important to have in mind that, for a deformable sample (bulk or liquid film) in the attractive regime $H_{pl} > 0$, the surface deformation usually shows positive values $\eta_0 > 0$. This assumption gives rise to a situation which is equivalent to the ones analyzed in Chapters 2 and 3.

Bulk Liquid

For the special case of a bulk (equivalent to Chapter 2), considering that the elastic force of the liquid is dominant over gravity and liquid/substrate interaction, we have:

$$\eta_0\,(\xi - \eta_0)^2 = \frac{R^3 H_a}{8C_{lk}}. \tag{4.10}$$

This equation is a dimensional equivalent of eq.(2.12), considering that $\varepsilon_0 = \xi - \eta_0$. As a result, the critical deformation of the liquid is:

$$\eta_{0,crit} = \frac{1}{2}R\sqrt[3]{\frac{Ha}{4C_{lk}}}, \tag{4.11}$$

which is found when the probe is placed at the minimal distance:

$$\xi_{crit} = D_{min} - R = 3\eta_{0,crit}, \tag{4.12}$$

which results from the optimization of eq.(4.10). The [——] curves in the left column of Fig.4.2, present an example of the numerical solution of eq.(4.10).

Shallow Film

On the other hand, for a shallow film (equivalent to Chapter 3), we can consider that the liquid/substrate interaction dominates over the elastic force and gravity. Thus, we have:

$$\eta_0 \left(\xi - \eta_0\right)^2 = \frac{E^4}{3C_{lm}AR}. \tag{4.13}$$

A comparison between eq.(4.13) and eq.(3.11) shows that the former is a dimensional equivalent of the latter, considering once more that $\varepsilon_0 = \xi - \eta_0$, and that $D = \xi + R$ As a consequence, the proportionality constant C_{lm} should be redefined as the correction function. This function, originally given in terms of D/R in eq.(3.15), is rewritten in terms of ξ and R, as follows:

$$C_{lm} = \frac{\xi\left(\xi + 2R\right)}{2R^2}. \tag{4.14}$$

Therefore, eq.(4.13) becomes:

$$\xi\left(\xi + 2R\right)\eta_0\left(\xi - \eta_0\right)^2 = \frac{2E^4R}{3A}. \tag{4.15}$$

The optimization of eq.(4.15) leads to:

$$\eta_{0,crit} \approx E\sqrt[4]{36A}, \tag{4.16}$$

which is found when the probe is placed at the minimal distance:

$$x_{crit} = \xi_{crit} = 3\eta_{0,crit}. \tag{4.17}$$

The [—] curves in the middle column of Fig.4.2, give the numerical solution of eq.(4.15).

4.2.c Deformable sample and cantilever

For a deformable liquid film and a common cantilever, showing deflection, the complete solution of the system presented in eqs.(4.3) is required.

Bulk Liquid

A bulk approximation is obtained when solving the following system of equations:

$$\left(\xi - x\right)\left(x - \eta_0\right)^2 = \frac{RH_{pl}}{6k_c} \tag{4.18a}$$

$$\eta_0\left(x - \eta_0\right)^2 = \frac{R^3H_a}{8C_{lk}}. \tag{4.18b}$$

Examples of the numerical solution of the system formed by eqs.(4.18), for three cantilevers of different stiffness, are illustrated by [– – –], [– · –] and [– · · –] curves in the left column subfigures of Fig.4.2.

From this situation, we can also conclude that the surface deformation is proportional to the cantilever deflection:

$$\eta_0 = \left(\frac{k_c}{\pi\gamma_l C_{lk}}\right)\delta. \tag{4.19}$$

Shallow Film

For the case of a shallow film, we have to solve:

$$\left(\xi - x\right)\left(x - \eta_0\right)^2 = \frac{RH_{pl}}{6k_c} \tag{4.20a}$$

$$x\left(x + 2R\right)\eta_0\left(x - \eta_0\right)^2 = \frac{2E^4R}{3A}. \tag{4.20b}$$

Examples of the numerical solution of the system formed by eqs.(4.20), for three cantilevers of different stiffness, are illustrated by the [– – –], [– · –] and [– · · –] curves in the middle column of Fig.4.2.

We can also conclude that the surface deformation is proportional to the cantilever deflection and inversely proportional to a function of the probe lower position:

$$\eta_0 = \left(\frac{4E^4 k_c}{H_{ls}}\right) \frac{\delta}{x\,(x+2R)}. \tag{4.21}$$

4.3 Some results

In Fig.4.2, several examples of the numerical solution of eq.(4.3), considering the interaction between a sphere and a flat surface, are shown. Each column corresponds to a different sample type, for which simplifications to eq.(4.3) were applied: a bulk liquid (left column), a shallow film of thickness $E = 1 \times 10^{-9}$ m (middle column) and a rigid sample (right column). As well, several stiffness levels were considered for the cantilever equivalent spring constant: [——] $k_c \to \infty$, [– – –] $k_c = 25$ N/m , [– · –] $k_c = 10^{-1}$N/m and [– · · –] $k_c = 10^{-2}$N/m.

The first row in Fig.4.2 shows the sample deformation as a function of the lower probe position ξ. Bifurcation diagrams are found, which differ according to the sort of sample. For the bulk liquid case, three branches appear. The ③ branch, presenting the highest values, corresponds to probe/liquid contact, whereas the ② branch (unstable), showing intermediate values and the ① branch (stable), presenting the lowest values, join in a bifurcation point, which indicates the critical conditions. In contrast, the shallow film presents only two branches, merging at the critical value of ξ. Equivalently, the ② branch, which shows a higher energy state, is unstable, and as a consequence the ① branch is lower in energy and stable. For the rigid sample case, as it is expected, no deformation is observed. From another viewpoint, considering the rigid sample case as the asymptotic limit $E \to 0$ of a shallow film, the two branches ① and ② collapse into a single curve $\eta_0 = 0$. No matter the nature of the sample, the bifurcation point for stiffer cantilevers is observed always at shorter values of ξ. Following the stable ① branch, the sample deformation increases monotonically when the value of ξ approaches the bifurcation point.

The second row in Fig.4.2 depicts the corresponding cantilever deflection, for the three aforementioned cases: bulk liquid, shallow film and rigid probe. For the bulk liquid, the three branches (① stable, ② unstable and ③ contact) exhibit larger deflections for the more flexible cantilevers than those observed for the stiffer probes. In the case of a rigid sample, as expected, the stable ① branches exhibit larger deflections for the more flexible cantilevers than those observed for the stiffer probes. The opposite situation is observed for the unstable ② branches, which confirms its unstable nature. Nevertheless, the ② branches of the different cantilevers seem to collapse in a single curve for large values of ξ. The shallow film case seems to present an hybrid behavior, between bulk and rigid sample, for the stable and unstable branches. For the three sample types, the cantilever deflection, following the stable ① branch, increases monotonically when the value of ξ approaches the bifurcation point.

The third row in Fig.4.2 presents the gap between the probe and the sample surfaces, for the three sample types. The vertical position of the branches is reversed from the order shown in the deformation bifurcation diagram. In other words, the highest values for the sample deformation correspond to the shortest gaps, and vice versa. For the bulk, the ③ branch exhibits negative values, which confirms that the probe/liquid contact has been attained. The ① stable and ② unstable branches expose similar features for the three types of samples. Following the stable branch, the gap decreases almost linearly when ξ diminishes from large values, and, as the bifurcation point gets closer, the gap reduction becomes abrupt. All the unstable branches approach a horizontal asymptote.

The fourth row in Fig.4.2 illustrates the interaction force between the probe and the different samples. For all the sample types, the magnitude of the force given by the ① stable branch is nearly zero for large values of ξ. As the ξ is reduced, the slope of the force curve becomes steeper, until an infinite slope is displayed, and the force diverges at the bifurcation point. In addition, the ② branches shows magnitudes which are significantly larger than those of the ① branches, ensuring their unstable nature. In the bulk case, the existing ③ contact branch appears as a continuous curve, showing magnitudes for probe positions to the left of the bifurcation point, which decrease monotonically while reducing ξ.

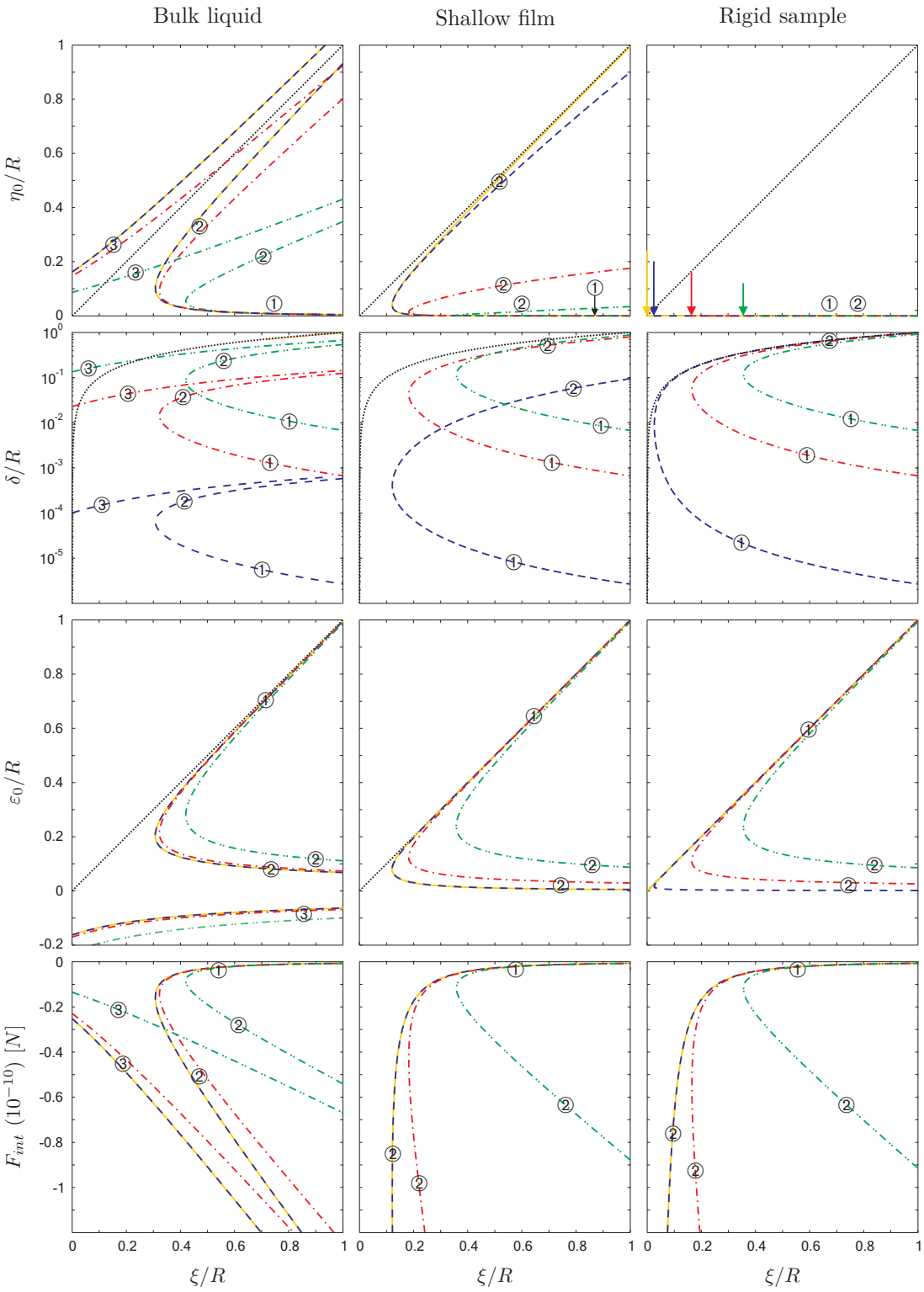


Figure 4.2: Mechanic analogy of the static probe/liquid/substrate system. (First row) sample surface deformation, (Second row) cantilever deflection $\delta = \xi - x$, (Third row) gap between surfaces $\varepsilon_0 = x - \eta_0$ and (Fourth row) interaction force, as functions of the initial gap $\xi = D - R$. $R = 10^{-8}m$ and $H_{pl} = 4 \times 10^{-20}$ Nm for different cantilever spring constant values: [——] $k_c \to \infty$, [– – –] $k_c = 25$ N/m, [– · –] $k_c = 10^{-1}$ N/m and [– · · –] $k_c = 10^{-2}$ N/m. Sample types: (Left column) bulk liquid with $Ha = 5.48 \times 10^{-3}$, and $C_{lk} = 0.1595$; (Middle column) shallow film with $E = 1 \times 10^{-9}$ m and $A = 1$; and (Right column) rigid sample. The ① stable, ② unstable and ③ contact branches are shown, if they exist for a particular case. [· · ·] Indicates the initial probe surface position.

4.4 Concluding remarks

Simple relationships have been given to determine the critical points, in particular the minimum probe/sample distance, according to the probe stiffness and the sample behavior. These expressions may be use to get quick access to experimental parameters, when performing AFM tests. Some numerical results have been presented, which are in good agreement with the results obtained with our static surface deformation model. They confirm the existence of stable and unstable behaviors. In the case of a bulk liquid sample, they reveal the existence of a probe/sample contact situation, which presents a higher energy state.

Part II

Dynamic Deformation (of a liquid film interacting with a probe)

Chapter 5

The dynamic behavior of a liquid sample interacting with a probe

5.1 Overview

Now that the static equilibrium interaction between a probe and a liquid sample has been presented, the study of the dynamic response of the liquid seems to be the natural sequel. Herein, we will derive the unsteady equations for the deformation of a liquid film in interaction with a probe. In this chapter, we will first consider the two following cases:

1. The transient regime of a viscous thin film, when it is subject to an attractive interaction due to the proximity of a static probe.

2. The global dynamic response of a viscous thin film, when it is subject to an attractive interaction due to an oscillating probe.

In the next chapters, the results concerning this two cases will be presented and analyzed.

The first problem, being purely academic, will provide a validation test for the methodology, which will be developed in this chapter. A comparison of the final thin-film state with the static equilibrium state, obtained from the previous chapters, will be made. The transmission of information from the proximity of the probe toward the modified capillary length should be done by means of wave propagation. Thence, from this case, we will recover some aspects of the natural response of liquid films, such as the dispersion relation and the phase velocity. In addition, the range of wavenumbers, that will be excited by the local probe, should arise from this analysis.

The second problem is our main objective, because the most commonly used AFM techniques are based on probe oscillation. In previous chapters, we have proven that, even if the probe does not touch the sample, the liquid surface is modified due to the probe proximity. Therefore, the probe non-contact periodic approach/retreat should provoke an intrusive effect over the liquid surface. In fact, it is expected to observe an oscillatory coupling phenomenon.

Keeping the aforementioned sketch in mind, we will proceed to lay the foundations for the study of both problems. In this chapter, the discussion starts with a brief summary on the current advances regarding the probe/liquid dynamic interaction, and some related phenomena, such as the generation of surface waves due to oscillatory coupling, and the evolution of viscous thin-films.

5.1.a Dynamic interaction

Nowadays, the determination of mechanical and rheological properties, from the sample interaction with an oscillating probe, is a common trend. The characterization of polymers from its deformation via force and amplitude spectroscopy, nano-indentation, and non-contact AFM imaging has been shown as a possibility (Magonov and Reneker, 1997). In the past, it has been proposed to study the change in liquid properties near a substrate, by means of non-contact AFM. By fitting the oscillation amplitude with a theoretical expression, the resulting parameters relate the damping and the liquid/substrate interfacial stiffness to the probe time-average position and to the oscillation amplitude and frequency (Lantz et al., 1999). The measured probe bending signal were compared to simulation results, obtained

with a modified driven harmonic oscillator equation accounting for the interface elasticity. More recently, the density layering of water in confined geometries and the change of viscosity, when an immersed AFM probe vibrates laterally at subnanometric separation distances from the supporting substrate, have been observed (Li et al., 2007). Some rheological properties of liquids have been deduced from this approach, for instance the viscoelastic modulus and the relaxation time of nanoconfined water and silicon oil (Li and Riedo, 2008). The film thickness and elastic modulus of metals and solid polymers were deduced from the shift of the vibration resonance modes of an AFM probe, in contact with the film surface (Crozier et al., 2000). Elastic properties of thin films, which are stressed and deformed due to the drainage of the viscous Newtonian fluid between the probe and the film (Leroy and Charlaix, 2011). Detection of a change in composition across polymeric nanocomposites and molecularly thick lubricated surfaces is viable by means of phase analysis during NC-mode AFM imaging (Bhushan and J., 2003; Scott and Bhushan, 2003).

However, the probe/sample dynamic interaction does not only concern the determination of physical properties, but also the analysis of the probe dynamic response. The exclusive situation in AFM experiments, in which the probe/sample interaction can be considered as quasi-static, is force/distance spectroscopy. General Intermittent Contact (IC) and Non-Contact (NC) mode AFM scanning conditions always entail a dynamic interaction, which requires a temporal analysis and modeling for understanding.

Even force spectroscopy has been analyzed as a dynamic phenomenon, when the probe vertical displacement is taken into account. For instance, in the literature, one can find a theoretical model of a non-oscillating probe interacting with a soft solid immersed in a liquid (Bowen and Cheneler, 2012). A classic mass-spring dynamic model including probe weight and inertia, had been adapted with the vdW attractive force, the fluid squeezing between the probe and the solid and a soft compliant substrate (elastohydrodynamic lubrication). Within the simulations of the probe approach, at constant vertical speed of the probe holder, the so-called snap-in phenomenon has been captured at a certain probe/sample distance. This fact consists of the sudden probe deflection that brings probe and sample into contact. Because the model had not taken into account for the sample deformation, the snap-in distance is underestimated, as the authors have also pointed out.

Concerning the probe oscillation near rigid samples, a long distance has been traveled (García and Pérez, 2002). Simulations of IC-mode AFM have been performed including vdW attractive, repulsive forces within the driven harmonic oscillator equations (García and San Paulo, 1999). Later, accounting for the capillary forces, the intermittent formation/rupture of a liquid bridge between probe and sample was observed from simulations and validated with experiments, in which the effects of relative humidity over hydrophobic and hydrophilic probes were also evaluated (Zitzler et al., 2002).

From a theoretical viewpoint, NC-AFM was the first to be analyzed in detail (Boisgard et al., 1998; Aimé et al., 1999a). The equation of a driven damped harmonic oscillator with a probe/sample interaction potential, approximated with sphere/plane formula, was proposed. It is given by:

$$\ddot{x} + \frac{\omega_{c,0}}{Q_c}\dot{x} + (\omega_{c,0})^2 (\xi - x) + \frac{H_{ps} R (\omega_{c,0})^2}{6 k_c x^2} = (\omega_{c,0})^2 W_D \cos(\omega_D t),$$

where x is the probe position in time t, ξ is time-average gap between the probe and the sample, $\omega_{c,0}$ is the probe resonance frequency, k_c is the cantilever stiffness, Q_c is the system quality factor, R is the probe radius, H_{ps} is the probe/sample Hamaker constant and W_D and ω_D are the driving amplitude and the driving frequency. This equation has been handled by considering a trial function with the form of an harmonic stationary motion:

$$x(t) = \xi + W_c \cos(\omega_D t + \phi_c),$$

where W_c and ϕ_c are the probe response amplitude and phase at the driving frequency ω_D. Using a variational method, the response amplitude and phase are obtained as functions of ω_D and ξ. In addition, the nonlinear behavior of the system revealed the simultaneous existence of three states, two stable and one unstable, when the probe oscillates with ω_D slightly below the free resonance frequency and the time-average gap is around $\xi \approx 10$ nm. Making some simplifications, these different behaviors are not observed neither when the ω_D is selected above the resonance frequency, nor when the following dimensionless parameter takes large values:

$$C^* = \frac{H_{ps} R}{k_c (W_{c,free})^3},$$

in which, $W_{c,free}$ corresponds to the free oscillation amplitude, when $\xi \to \infty$, at the resonance frequency $\omega_{c,0}$.

The precise stability condition has been published, as well as the set of equations, representing a closed loop NC-AFM virtual machine that keeps a constant amplitude (Couturier et al., 2003). IC-AFM has been studied by including a repulsion force with a linear elastic behavior (Nony et al., 1999; Aimé et al., 2001). Nevertheless, it has been observed that contact is achieved even without the employment of a repulsive interaction term. The use of driving frequencies below the free resonance frequency provoke an increase of the oscillation amplitude and the intermittent contact (Nony et al., 2001).

The probe/sample interaction phenomenon has been delved into with the addition of a Kelvin-Voigt viscoelastic material, as the sample in the NC-AFM model (Aimé et al., 1999b; Boisgard et al., 2002). Neglecting inertial effects, this sample deformation model was included as follows:

$$k_s \eta_0 + \nu_s \dot{\eta_0} = \frac{H_{ps} R}{6 \left(x - \eta_0\right)^2},$$

where η_0 is the sample displacement, $k_s = \Theta_{int} E_s$ is the sample local stiffness, Θ_{int} and E_s being the effective interaction diameter of the sample surface area and its elastic modulus, $\nu_s = \Theta_{int} \mu_s$ is the local friction coefficient, μ_s being the sample viscosity, and the relaxation time is defined as $\tau_s = \nu_s / k_s$. Explanations of the probe energy loss during oscillations were searched, suggesting that the local deformation of the sample should be the main source. Experiments with Polystyrene of low and high molecular weights were performed, validating the preceding assumption and showing a change of probe behavior depending on the sample mechanical properties, while keeping the tip/sample interaction constant. The probe displacement was decomposed using Fourier series, and the variational method led to find analytical approximations. For long relaxation times, only the first term in the Fourier series is considered, which approximates the probe motion to a rectangular periodic function, resulting in a displacement that varies as $1/\nu_s$ for highly viscous samples. In this case, the system instability arises when the gap between the probe and the sample is:

$$\xi - (W_D + \eta_0) = \frac{3}{2} \left(\frac{H_{ps} R}{6 k_s} \right)^{1/3}. \tag{5.1}$$

On the other hand, for short values of τ_s, the displacement of a almost purely elastic material is proportional to $1/k_s$, emerging from the use of the Fourier transform of a periodic pulse representing the probe motion. In this case, the system instability arises when the gap is:

$$\xi - (W_D + \eta_0) \simeq 2 \left(\frac{H_{ps} R}{6 k_s \sqrt{2 W_D}} \right)^{2/5}. \tag{5.2}$$

The model seems extremely useful notwithstanding the heuristic determination of the length Θ_{int}. It is important to have in mind that for the case of a liquid, or a noticeable fluid-like polymer, the sample behavior falls into the intermediate regime, for which no asymptotic solution can been obtained from the previous analysis. Besides, a Maxwell viscoelastic material should be more suitable to model a viscoelastic liquid.

As it has been experimentally observed, when imaging liquid droplets by means of NC-AFM(Checco et al., 2006), there exists a threshold setpoint (separation distance) D_{crit} for a given oscillation amplitude. As described by the author of the aforementioned publications, scanning with a D shorter than D_{crit} provokes the destabilization of the drop profile, and the drop can be dragged by the tip, whereas a further reduction of D spoils the sample. Notwithstanding, the correct procedure to image a liquid surface remains a recipe. One of the main objectives of this thesis is to determine relationships between the experimental NC-AFM parameters, which may yield good topographies of liquid surfaces.

5.1.b Surface waves

When a solid oscillates at the surface of a liquid sample, another phenomenon concerning the present study arises: the propagation of surface waves. The generation of surface waves due to its interaction with a moving body has been studied for more than half a century. The induced motion of the inviscid fluid of infinite depth, due to the small vertical oscillations of a half-immersed body, has been analyzed some

time ago (Havelock, 1955; Kim, 1965). As well, a theoretical analysis of the wave propagation generated by the vertical oscillation of a partially immersed plate, in inviscid (Hocking, 1987) and viscous (Miles, 1990) fluids of infinite depth, has been developed including the Young-Laplace equation, as well as a simple model accounting for the hysteresis and dynamic behavior of the contact angle. The linearized equations for inviscid fluid motion were solved, reporting the amplitude and the energy of the radiated wavetrain, among other results. These publications only consider inertial effects, which is very convenient for large length scales. Nevertheless, it is not the case of AFM situations, in which capillarity takes a main role.

More recently, regarding an inviscid fluid of infinite depth, the waves generated by an external pressure field that moves parallel to the liquid surface have been studied (Raphaël and de Gennes, 1996; Richard and Raphaël, 1999). From the linearized theory of capillary-gravity waves, the dispersion relation leads to the phase speed:

$$v_p = \frac{\nu}{k} = \left[\frac{g}{k} + \frac{k\gamma}{\rho}\right]^{1/2},$$

Finally, considering a sinusoidal probe motion, an impact assessment of the driving oscillation parameters on the thin-film response is made. The coupling of the film evolution and the probe dynamics, provoked by the time-varying probe/liquid interaction, is discussed. where ν is the time angular frequency, g the acceleration of gravity, k the wavenumber, γ the surface tension and ρ the liquid density. This relation implies a minimum phase speed:

$$v_{p,min} = \left[\frac{4g\gamma}{\rho}\right]^{1/4},$$

occurring at the minimum wavenumber $k_{min} = \sqrt{\rho g/\gamma}$. It has been observed that when the speed of the pressure field is greater than $v_{p,min}$, a withstanding force is generated as a surface tension effect. This force, which is named "wave resistance", opposes the motion of the body that generates the pressure field. Moreover, the capillary-gravity waves generated by an object moving at the air/water interface have been the object of subsequent investigations (Chepelianskii et al., 2008; Closa et al., 2010).

In conclusion, bodies, which induce a pressure field, moving near a liquid surface can create waves. Not only do these waves dissipate energy, but they provoke an effect over the moving object. Considering the usual AFM length scales, i.e. from micrometers to nanometers, capillarity effects should be considered, as well as the viscous damping. As well, the coupling of oscillatory behaviors, of the probe and the sample, may reveal information about the physical properties of both elements. For instance, the viscosity and surface tension of liquids can be obtained from the viscous dispersion of capillary-gravity waves. Recently, the non-contact electronic generation of waves, tracked via optical methods and analyzed employing the deep water approximation, has been achieved for polar liquids (Behroozi et al., 2001, 2010). Therefore, one should expect that the oscillatory response of a liquid surface due to its non-contact coupling with an oscillating probe, should provide a method to acquire the physical properties of liquid samples.

5.1.c Thin films

Remaining in the AFM context, the analysis of liquid samples is mostly limited to thin films. Within this framework, viscous effects are dominant, which makes the lubrication theory to be the most viable choice. Phenomena, such as film/substrate vdW interactions via the disjoining pressure, temperature-dependent liquid properties, drop spreading and sliding liquid bodies, have been analytically treated by this means (Oron et al., 1997). The use of intermolecular interaction forces within the coupled system of equations, given by the lubrication theory and the Young-Laplace equation, has been exploited to study the spreading of a sessile drop (Hocking, 1993b). Recent theoretical (Benzaquen et al., 2013) and numerical (Becker and Grün, 2005) advances, concerning the application of the lubrication approximation, encourage the employment of this theory. Despite its number of hypothesis, the thin-film equation usually produces results that depict the correct behavior and lead to satisfactory physical interpretations. In this way, its application has not been confined to the theory, but it has been largely spread to the analysis of experimental data. Up to date, a huge amount of experiments have been explained using the lubrication theory. For instance, the lubrication theory provided an estimation of the pressure and the gap size between approaching bodies immersed in viscous liquids (Davis et al., 1986; Zenit and Legendre, 2009). It has been employed to analyze the data from drainage experiments, performed with AFM (Dagastine et al., 2006) and laser interferometry (Davis et al., 1989; Klaseboer et al., 2000), during the approach and coalescence of droplets. As well, the coalescence of viscous drops itself, during its early

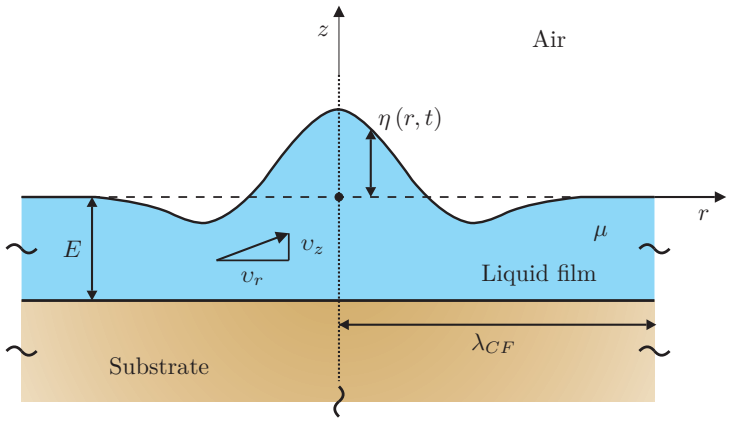


Figure 5.1: Lubrication assumption at the liquid film.

stages (Hernandez-Sanchez et al., 2012), and for miscible liquids (Borcia et al., 2011), has been treated by means of the lubrication theory. Finally, the self-similar evolution profile of an initially stepped polymer has been nicely described with the lubrication theory (Salez et al., 2012), being in excellent agreement with experiments even for a step of 0.1 times the film thickness, which highlights the robustness of the thin-film equation. This latter example also proves that the propagation of information, within viscous thin films, is well represented by means of the thin-film equation.

The application of the lubrication theory should provide us a tool for analyzing the liquid film deformation. It should provide a first approach to understand the probe/liquid dynamic interaction. This is the aim of the formulation presented in the following.

5.2 Scope

Considering a general case, in which the probe can either stay still or move, a liquid surface initially at rest exhibits a dynamic response. The surface evolution of the a liquid viscous thin-film is engendered as a consequence of the non-contact probe/liquid interaction. In the following sections of the present chapter, the thin-film equation, which describes the dynamic behavior of a viscous liquid film, is derived from the lubrication theory. The modified Young-Laplace equation, which was introduced in Chapter 1, is integrated to the analysis. Therefore, the dynamics of the liquid film is related to its surface shape, via the pressure difference across the surface. The resulting nonlinear thin-film equation is partially linearized, based on the small deformations hypothesis. As well, considering a sinusoidal probe motion, an impact assessment of the driving oscillation parameters on the thin-film response is made. The coupling of the film evolution and the probe dynamics, provoked by the time-varying probe/liquid interaction, is discussed. Afterwards, a pseudo-spectral numerical method, founded on the Hankel transform, is developed at the end of the chapter, in order to solve the quasi-linear equation.

5.3 Lubrication theory

Within a cylindrical axisymmetric coordinate system, consider the general motion of a liquid film, like the one displayed in Fig.5.1. Departing from the premise that a viscous dominated flow is developed within the thin film, the momentum and continuity equations reduce to the lubrication approximation equations:

$$\frac{\partial}{\partial z}\left(\upsilon_z\right) = -\frac{1}{r}\frac{\partial}{\partial r}\left(r\upsilon_r\right) \tag{5.3a}$$

$$\frac{\partial P}{\partial r} = \mu\frac{\partial^2}{\partial z^2}\left(\upsilon_r\right) \tag{5.3b}$$

$$\frac{\partial P}{\partial z} = -\Delta\rho g, \tag{5.3c}$$

where υ_r and υ_z are the radial and axial components of the velocity field, P is the pressure field within the liquid film and μ is the dynamic viscosity of the liquid.

From eq.(5.3c), it results that the pressure within the film increases with the depth below the surface:

$$P = P_{film}(r,t) - \Delta\rho g z. \tag{5.4}$$

Although, the pressure at the free surface P_{film} may change with the radial position and time. Assuming a no-slip BC at the substrate, $\upsilon_r = 0$ at $z = -E$, from eq.(5.3b), one finds the radial component of the velocity within the film:

$$\upsilon_r = \frac{1}{2\mu}\frac{\partial P_{film}}{\partial r}\left[z^2 + z(E-\eta) - E\eta\right] + \upsilon_r(\eta,t)\left[\frac{E+z}{E+\eta}\right]. \tag{5.5}$$

As well, one should consider a shear-free BC at the free surface:

$$\left.\frac{\partial \upsilon_r}{\partial z}\right|_{z=\eta} + \upsilon_r(\eta,t)\,\kappa = 0,$$

where κ is the curvature of the surface. Combining this BC with the derivative of eq.(5.5) with respect to z, after some math, one finds:

$$\upsilon_r(\eta,t) = -\frac{[E+\eta]^2}{2\mu}\frac{\partial P_{film}}{\partial r}\left[\frac{1}{1+\kappa(E+\eta)}\right]. \tag{5.6}$$

Integrating eq.(5.5) along the film thickness predicts the radial flux:

$$\int_{-E}^{\eta} \upsilon_r dz = -\frac{[E+\eta]^3}{12\mu}\frac{\partial P_{film}}{\partial r} + \frac{\upsilon_r(\eta,t)}{2}(E+\eta). \tag{5.7}$$

One should keep in mind that the surface position is a function of the radial position and time, i.e. $\eta(r,t)$.

Moreover, the integration of eq.(5.3a) over the film thickness, with the no-slip BC at the substrate, $\upsilon_z = 0$ at $z = -E$, yields the axial component of the velocity at the film surface:

$$\upsilon_z(\eta,t) = -\frac{1}{r}\int_{-E}^{\eta}\left[\frac{\partial}{\partial r}(r\upsilon_r)\right]dz.$$

Recalling the Leibniz integral rule:

$$\frac{\partial}{\partial r}\left[\int_{-E}^{\eta}(r\upsilon_r)\,dz\right] = \int_{-E}^{\eta}\left[\frac{\partial}{\partial r}(r\upsilon_r)\right]dz + r\upsilon_r(\eta,t)\frac{\partial \eta}{\partial r},$$

which, applied to the above-mentioned integral, gives the following relationship between the axial and radial velocity components, at $z = \eta$:

$$\upsilon_z(\eta,t) - \upsilon_r(\eta,t)\frac{\partial \eta}{\partial r} = -\frac{1}{r}\frac{\partial}{\partial r}\left[r\int_{-E}^{\eta}\upsilon_r dz\right]. \tag{5.8}$$

On the other hand, the kinematic condition at the liquid surface $z = \eta$ is given by:

$$\begin{aligned} 0 &= \frac{D}{Dt}[z-\eta] \\ &= \left[\frac{\partial z}{\partial t} - \frac{\partial \eta}{\partial t}\right] + \upsilon_r(\eta,t)\left[\frac{\partial z}{\partial r} - \frac{\partial \eta}{\partial r}\right] + \upsilon_z(\eta,t)\left[\frac{\partial z}{\partial z} - \frac{\partial \eta}{\partial z}\right], \end{aligned}$$

which reduces to:

$$\frac{\partial \eta}{\partial t} = \upsilon_z(\eta,t) - \upsilon_r(\eta,t)\frac{\partial \eta}{\partial r}, \tag{5.9}$$

after the assessment of the derivatives.

The substitution of eqs.(5.7) and (5.9) within eq.(5.8) yields a typical Reynolds lubrication equation:

$$\frac{\partial \eta}{\partial t} = \frac{1}{r}\frac{\partial}{\partial r}\left\{ r\left(\frac{[E+\eta]^3}{12\mu}\frac{\partial P_{film}}{\partial r} - \frac{[E+\eta]}{2}\upsilon_r(\eta,t)\right)\right\}, \tag{5.10}$$

which displays the behavior of the film surface in terms of the radial evolution of the pressure just below the interface, and the radial speed at the surface. If one makes the hypothesis of small deformations, which corresponds to small curvatures and $\kappa < (E+\eta)^{-1}$, thus, eq.(5.6) reduces to:

$$\upsilon_r(\eta,t) \approx -\frac{[E+\eta]^2}{2\mu}\frac{\partial P_{film}}{\partial r},$$

and eq.(5.10) becomes:

$$\frac{\partial \eta}{\partial t} = \frac{1}{r}\frac{\partial}{\partial r}\left\{ r\left(\frac{[E+\eta]^3}{3\mu}\frac{\partial P_{film}}{\partial r}\right)\right\}, \tag{5.11}$$

Considering the time τ as a characteristic time scale, then the dimensionless time variable is written as $t^* = t/\tau$, and employing the characteristic length scales and dimensionless variables described along the development of the dimensionless modified Young-Laplace equation, given by eq.(1.16) in Chapter 1, one is able to transform the preceding equation into:

$$\frac{\partial \eta^*}{\partial t^*} = \left(\frac{\tau\gamma E^3}{3\mu R^4}\right)\frac{1}{r^*}\frac{\partial}{\partial r^*}\left[r^*\left(1+\frac{\xi^*\eta^*}{E^*}\right)^3\frac{\partial P^*_{film}}{\partial r^*}\right],$$

from which, for the consistency of the dimensionalization process, the definition of the characteristic time scale results:

$$\tau = \frac{3\mu R^4}{\gamma E^3}. \tag{5.12}$$

A simple interpretation arises when one observes this definition: τ represents the time that the liquid film, with an effective viscosity $\mu(R/E)^2$, takes to undergo a deformation of magnitude R at its free surface, due to a shear stress equivalent to the Laplace pressure, which bends the free surface with a curvature of $1/3R$. This idea can be expressed as:

$$[\text{shear stress}] = [\text{viscosity}]\,[\text{shear rate}]$$
$$\left[\frac{\gamma}{3R}\right] = \left[\mu\left(\frac{R}{E}\right)^2\right]\left[\frac{R}{\tau E}\right].$$

In other words, this quantity indicates the time that the liquid film takes to react and move, when its surface is to be deformed. Therefore, depending on the liquid physical properties and the ratio of the film thickness to the probe size, with the use of eq.(5.12), one can infer the reaction time of the film. For constant physical properties, one can conclude that thick films are "fast", whereas thin films are relatively "slow". Values of this characteristic time scale, for different liquids are given in Table 5.1.

As well, using the definition of the dimensionless pressure difference across the air/liquid interface $\Delta P^* = P^*_{film} - P^*_{air}$ and considering a constant pressure at the air side of the interface, one is allowed to write the equivalence:

$$\frac{\partial P^*_{film}}{\partial r^*} = \frac{\partial \Delta P^*}{\partial r^*} \tag{5.13}$$

at the vicinity of the free surface $z = \eta$. Thus, we should recall the modified Young-Laplace equation, which relates the pressure difference with the probe/liquid Π^*_{pl} and the liquid/substrate Π^*_{ls} interaction potentials, the surface curvature κ^* and the hydrostatic pressure.

In consequence, the dimensionless lubrication equation that describes the dynamics of the liquid film

is given by:

$$\frac{\partial \eta^*}{\partial t^*} = \frac{1}{r^*}\frac{\partial}{\partial r^*}\left[r^*\left(1+\frac{\xi^*\eta^*}{E^*}\right)^3\frac{\partial \Delta P^*}{\partial r^*}\right] \tag{5.14a}$$

$$\Delta P^* = B_o\eta^* + \frac{2}{\xi^*}\kappa^* + \frac{H_a}{\xi^*}\Pi^*_{pl} + \frac{AH_a}{8\xi^*\left(E^*\right)^3}\Pi^*_{ls}. \tag{5.14b}$$

5.4 Quasi-linear thin-film equation

Since the air/liquid surface is perturbed by the proximity of the spherical probe, the surface deformation evolves in time, thus $\partial\eta^*/\partial t^* \neq 0$. In the absence of equilibrium, the pressure difference across the interface is not equal to zero, $\Delta P \neq 0$.

With the aim of facilitating the theoretical analysis and, if it is required, the obtaining of a faster numerical solution, we seek to simplify the thin-film equation, while keeping the physics, thus a first order approximation is pursued. Considering that the surface perturbation of the liquid surface will remain in the same order of magnitude as for the static case $\xi^*\eta^*/E^* \ll 1$, we may proceed to do some simplifications. According to this hypothesis, the dynamics of the film free surface is governed by a linearized lubrication equation. This partial differential equation includes the modified Young-Laplace equation, which can also be simplified with the assumption of small deformations $\xi^*\left(\partial\eta^*/\partial r^*\right) \ll 1$. Taking into account the above-mentioned considerations, the following Partial Differential Equation (PDE), which represents a quasi-linear thin-film equation, is deduced:

$$\frac{\partial \eta^*}{\partial t^*} = \frac{1}{r^*}\frac{\partial}{\partial r^*}\left[r^*\frac{\partial \Delta P^*}{\partial r^*}\right] \tag{5.15a}$$

$$\Delta P^* = -\frac{1}{r^*}\frac{\partial}{\partial r^*}\left[r^*\frac{\partial \eta^*}{\partial r^*}\right] + \frac{\eta^*}{\left(\lambda^*_{CF}\right)^2} + \frac{H_a}{\xi^*}\Pi^*_{pl}, \tag{5.15b}$$

where the modified capillary length λ^*_{CF} and the probe/liquid interaction term Π^*_{pl} are defined in eqs.(1.28) and (1.17b), respectively.

Despite the complexity reduction, this equation retains a nonlinear term, i.e. the probe/liquid interaction potential. It is important to recall that Π^*_{pl} is a function of the radial and probe center positions, $\Pi^*_{pl}\left(r^*, D^*\right)$, since the interface position η^* is a function of r^*. In addition, a general dynamic situation implies a time-varying separation distance $D^* = D^*\left(t^*\right)$, which, in turn, produces time-varying behavior of the interaction potential $\Pi^*_{pl} = \Pi^*_{pl}\left(r^*, t^*\right)$ and of the surface profile $\eta^* = \eta^*\left(r^*, t^*\right)$.

The behavior depicted by eq.(5.15), corresponds to the evolution of a viscous thin-film in interaction with a spherical probe. Since its derivation has been made considering a general probe motion, any driving function can be embedded, including a static position or a sinusoidal displacement. In the following, we will take advantage of these possibilities, in order to gain understanding of the thin-film behavior in AFM situations.

5.5 Consequences of the probe oscillation

Since a large number of AFM techniques are based on the probe oscillation, this situation requires special attention. In order to understand the role of the driving parameters in the probe/liquid dynamic interaction and the thin-film response, the probe motion is analyzed in detail. A comparison between the film characteristic time scale and the driving oscillation period is essential to achieve a good physical interpretation of the coupling phenomenon.

Consider a simple case, in which the axial position of the probe center can be decomposed as the linear combination of a time-average distance and a simple harmonic motion. Let's describe the probe position as:

$$D\left(t\right) = D_a + W_D\cos\left(\omega_D t\right), \tag{5.16}$$

where D_a is the time-average position, W_D the oscillation amplitude, $\omega_D = 2\pi/\mathcal{T}$ the oscillation angular frequency and $\mathcal{T}$ the oscillation period. Recalling the characteristic length scales defined in Chapter 1,

the probe radius R and the gap $D-R$, the dimensionless time-average position and oscillation amplitude are, respectively, given by:

$$D_a^* = \frac{D_a}{R} \qquad\qquad W_D^* = \frac{W_D}{D_a - R}. \tag{5.17}$$

As a consequence, the dimensionless time-average gap is defined as:

$$\xi^* = \frac{D_a - R}{R}. \tag{5.18}$$

Now, making use of the dimensionless time $t^* = t/\tau$, the probe motion is given by:

$$D^* = D_a^* + \xi^* W_D^* \cos\left(2\pi t^* \frac{Ca}{(E^*)^3}\right), \tag{5.19}$$

where Ca is the capillary number, defined as:

$$Ca = \frac{\mu \mathcal{V}}{\gamma}, \tag{5.20}$$

$\mathcal{V}$ being the probe characteristic speed, defined as:

$$\mathcal{V} = \frac{3R}{\mathcal{T}}. \tag{5.21}$$

The capillary number Ca compares the constraints provoked by the viscosity within the liquid film and the surface tension acting at the air/liquid interface.

In eq.(5.19), the ratio $(E^*)^3/Ca = \mathcal{T}/\tau$ also represents the dimensionless time period of oscillation $\mathcal{T}^* = \mathcal{T}/\tau$, which is a comparison of two characteristic time scales. If $\mathcal{T}^* \gg 1$, a quasi-static phenomenon should be observed, because the probe motion is so slow that the liquid film has enough time to arrive at its equilibrium configuration, almost instantaneously, and then to relax to the equilibrium configuration. Hence, the maximum deformation of the liquid free surface is in phase with the minimum position of the probe during an oscillation period, and the liquid dissipates the whole energy received from the probe. Under this conditions, the probe wetting depends only on the minimum separation distance $D_a^* - \xi^* W_D^*$. This is the case of films with $E^* \gtrsim 10^{-1}$ for low viscosity liquids, and of films with $E^* \gtrsim 10^{0}$ for high viscosity films, as it can be confirmed from the data in Table 4.1. If $\mathcal{T}^* \ll 1$, the probe moves so fast that the liquid film behaves as a rigid sample, because it can not follow the motion of the probe. Nevertheless, the liquid surface may not remain flat, but it should reach an equilibrium deformation profile. Once again, it is not absurd to anticipate that the probe wetting may only depend on $D_a^* - \xi^* W_D^*$. This corresponds to films with $E^* \lesssim 10^{-2}$ for low viscosity liquids, and of films with $E^* \lesssim 10^{-1}$ for high viscosity films. In contrast, when $\mathcal{T}^* \sim 1$, the liquid film is deformed due to the interaction with the probe, but the viscous dissipation provokes a phase shift of the film response with respect to the probe oscillation. In addition, because the oscillation period is shorter than the liquid relaxation time, the energy transferred from the probe is stocked in the liquid. In this case, the probe wetting can rely either on the separation distance $D_a^* - \xi^* W_D^*$ or on the time scale ratio $\mathcal{T}^* = \mathcal{T}/\tau$. This is the condition of films with $E^* \in \left[10^{-2}, 10^{-1}\right]$ for low viscosity liquids, and of films with $E^* \in \left[10^{-1}, 10^{0}\right]$ for high viscosity films.

Orders of magnitude

The presented dimensionless analysis, of the thin-film and probe equations, gives rise to a system of equations that is valid for a system involving a probe of arbitrary size. In addition, as it is clearly observed from the parameter definitions, Ca, H_a and B_o are coupled by the probe radius R. Hence,

		Ethanol	Acetone	PDMS	Glycerol	Water	Mercury
γ	$\times 10^{-3}$[N/m]	22.2	23.4	30.8	63.4	72.8	486.5
ρ	$\times 10^{3}$[kg/m^3]	0.789	0.791	0.966	1.260	1.002	13.579
μ	$\times 10^{-3}$[Pa s]	1.09	0.32	140.00	1000.00	1.00	1.55
λ_C	$\times 10^{-3}$[m]	1.694	1.736	1.803	2.265	2.721	1.911
$\tau\,(E/R)^3$	$\times 10^{-7}$[s]	0.015	0.004	1.364	4.732	0.004	0.001
H_a	$\times 10^{-3}$[1]	7.647	7.255	5.512	2.678	2.332	0.349
B_o	$\times 10^{-11}$[1]	3.486	3.317	3.075	1.950	1.350	2.738
C_a	$\times 10^{-3}$[1]	0.516	0.142	47.727	165.615	0.144	0.034

Table 5.1: Physical properties and dimensionless parameters for common liquids, also considering a probe radius of $R = 10^{-8}$ m, an oscillation period of $\mathcal{T} = 2.86 \times 10^{-6}$ s, the air density $\rho_{air} = 1.205$ kg/m^3 at room temperature and a probe/liquid Hamaker constant of $H_{pl} = 4 \times 10^{-20}$ J.

their values are restricted according to the products of physical properties given by:

$$H_a B_o = \frac{4}{3\pi}\left[\frac{H_{pl}\Delta\rho g}{\gamma^2}\right] \tag{5.22}$$

$$H_a\,(C_a)^2 = \frac{3}{\pi^3}\left[\frac{H_{pl}\,(\mu\omega_D)^2}{\gamma^3}\right] \tag{5.23}$$

$$\frac{(C_a)^2}{B_o} = \left[\frac{3}{2\pi}\right]^2\left[\frac{(\mu\omega_D)^2}{\Delta\rho g\gamma}\right] \tag{5.24}$$

We should keep in mind these products, because their are responsible of the ranges that the dimensionless parameters can take, for real probe/liquid/substrate systems. For common probe/liquid and liquid/substrate systems, the Hamaker constants $H_{pl} \sim H_{ls}$ are in the same range $H_{pl} \in \left[10^{-21}, 10^{-19}\right]$ J. Additionally, typical room temperature liquids present a surface tension $\gamma \in \left[10^{-2}, 10^{-1}\right]$ N/m, a density difference $\Delta\rho \in \left[10^{2}, 10^{3}\right]$ kg/m^3 with respect to air, and a viscosity of $\mu \in \left[10^{-4}, 10^{0}\right]$ Pa s. Then, for common AFM probes with a tip radius $R \simeq 10^{-8}$ m, the range of the dimensionless parameters defined in eqs.(1.18), (1.19), (1.20) remains within $B_o \in \left[10^{-11}, 10^{-10}\right]$, $H_a \in \left[10^{-5}, 10^{-1}\right]$ and $A \in \left[10^{-2}, 10^{2}\right]$. Considering films of a thickness within the range $E \in \left[10^{-10}, 10^{-6}\right]$ m and probes driving frequencies $\omega_D \in \left[10^{4}, 10^{7}\right]$ s^{-1}, the characteristic time, the characteristic speed and the capillary number defined in eqs.(5.12), (5.21) and (5.20) spread over $\tau \in \left[10^{-16}, 10^{-1}\right]$ s, $\mathcal{V} \in \left[10^{-5}, 10^{-2}\right]$ m/s and $Ca \in \left[10^{-7}, 10^{-1}\right]$. For AFM probes, with $R \simeq 10^{-7}$m, the extents of the dimensionless parameters change to $B_o \in \left[10^{-9}, 10^{-8}\right]$ and $H_a \in \left[10^{-6}, 10^{-3}\right]$, whereas the Hamaker ratio A is unaltered. If the driving frequency band is kept, the speed and the capillary number lie over $\mathcal{V} \in \left[10^{-4}, 10^{-1}\right]$ m/s and $Ca \in \left[10^{-6}, 10^{0}\right]$, preserving the same range widths. Furthermore, for the same film thickness, the span of the characteristic time is modified to $\tau \in \left[10^{-12}, 10^{3}\right]$ s.

Typical values for the problem physical and dimensionless parameters, for different liquids, are shown in Table 5.1. In the following chapters, the interaction between a spherical probe and a PDMS liquid sample, with the properties given in Table 5.1, will be considered.

5.6 Numerical scheme

The PDE, given by eq.(5.15), does not present an analytical solution. Nevertheless, it can be solved numerically using a pseudo-spectral method, described in Appendix C, which harness the Hankel transform of zero order (see Appendix D for the definition). The Hankel transform is an integral transform

equivalent to the two-dimensional Fourier transform for axisymmetric geometries. This interesting feature results very suitable for the present problem, because the Hankel transform will naturally reduce the complexity of the PDE.

With the application of the Hankel transform of zero order, the surface position and the pressure difference across the interface are transformed into the spatial frequency domain:

$$\mathcal{N}^* = \mathcal{N}^*\left(q^*, t^*\right) = \mathbb{H}_0\left\{\eta^*\left(r^*, t^*\right)\right\}$$
$$\mathcal{P}^* = \mathcal{P}^*\left(q^*, t^*\right) = \mathbb{H}_0\left\{\Delta P^*\left(r^*, t^*\right)\right\}.$$

where q^* is the wavenumber. As well, $\mathcal{N}^*$ is the wavenumber spectrum of the surface position η^*, i.e. the amplitude distribution of zero order Bessel functions $J_0\left(2\pi q^* r^*\right)$, whereas $\mathcal{P}^*$ is the equivalent for the pressure difference across the interface ΔP^*. Employing the Hankel properties given in Appendix D, the quasi-linear thin-film equation, transformed into the spatial frequency domain, is given by:

$$\frac{\partial \mathcal{N}^*}{\partial t^*} = -\left(k^*\right)^2 \mathcal{P}^*$$
$$\mathcal{P}^* = \left[\left(k^*\right)^2 + \frac{1}{\left(\lambda_{CF}^*\right)^2}\right]\mathcal{N}^* + \frac{H_a}{\xi^*}\mathcal{Q}^*,$$

where $k^* = 2\pi q^*$ is the angular wavenumber, and:

$$\mathcal{Q}^* = \mathcal{Q}^*\left(q^*, t^*\right) = \mathbb{H}_0\left\{\Pi_{pl}^*\left(r^*, t^*\right)\right\},$$

being $\mathcal{Q}^*$ the wavenumber spectrum of the probe/liquid interaction potential Π_{pl}^*.

Thereby, our thin-film equation is now written in a more simple way:

$$\frac{\partial \mathcal{N}^*}{\partial t^*} = -\nu^* \mathcal{N}^* - \frac{H_a}{\xi^*}\left(k^*\right)^2 \mathcal{Q}^*. \tag{5.26}$$

with:

$$\nu^* = \left(k^*\right)^2\left[\left(k^*\right)^2 + \left(\lambda_{CF}^*\right)^{-2}\right]. \tag{5.27}$$

A numerical method should be employed to solve Eq.5.26, because the transform $\mathcal{Q}^*$ of the probe/liquid interaction potential can not be obtained analytically.

First of all, we have to define the discrete domain, radial position and wavenumber, in which the solution will be found. The spatial mesh grid was constructed in such a way that $\eta^*\left(r^*, t^*\right)$ is distributed over the region $0 \leq r^* \leq \alpha\lambda_{CF}^*$, where $\alpha > 1$ is a positive integer. Thus, $\alpha\lambda_{CF}^*$ is the radial position whence the surface is expected to be unperturbed $\eta^*\left(r^* \geq \alpha\lambda_{CF}^*, t^*\right) = 0$. On the other hand, the wavenumber mesh grid was built in a similar way, therefore $\mathcal{N}^*\left(q^*, t^*\right)$ is distributed over the wavenumber band $0 \leq q^* \leq \vartheta$, where ϑ is the cutoff wavenumber whence $\mathcal{N}^*\left(q^* \geq \vartheta, t^*\right) = 0$. We should fix both α and ϑ, so the space-bandwidth product $S = 2\pi\alpha\lambda_{CF}^*\vartheta$ remains finite. Indeed, both values α and ϑ should be chosen according to the handled functions. For example, when applying the Hankel transform to Π_{pl}^*, which is nearly equal to zero $\Pi_{pl}^* \lesssim 10^{-12}$ for $r^* \geq 100$, leads to a value $\alpha \approx 5$ for a film of thickness $E^* = 1$, because $\lambda_{CF}^* \approx 22$. Nevertheless, the other terms in eq.(5.26) should also be considered. It is logic to suppose that the surface deformation η^* attains a radial extension around $r^* \sim \lambda_{CF}^*$, then $\alpha \approx 1$ is also proposed. As well, it is observed that $\mathcal{Q}^* < 1$ for $q^* \geq 2$, and its combination with the other variables and parameters in eq.(5.26) results even smaller. Therefore, it is also expected to observe $\mathcal{N}^* \simeq 0$ for $q^* \geq 2$. For the present study, considering $E^* = 1$, the values $\alpha = 5$ and $\vartheta = 2$, which yield a space-bandwidth product $S = 10\pi\lambda_{CF}^*$ and a total number of mesh points of $N \approx 10\lambda_{CF}^*$, for both spatial and wavenumber mesh grids. Further details on the selection of the cutoff distance and wavenumber, as well as the selection of the number of mesh points, is given in Appendix C.

The numerical method consists in performing iteration of the following routine:

1. The Hankel transforms of the surface position $\mathcal{N}^*$ and of the probe/liquid interaction potential $\mathcal{Q}^*$ are obtained.

2. Following the procedure described in the literature (Guizar-Sicairos and Gutierrez-Vega, 2004), the discrete Hankel transforms are obtained in terms of Fourier-Bessel series, with Bessel functions of the first kind and order zero $J_0\left(x\right)$.

3. Eq.(5.26) is discretized using a simple semi-implicit method, the combination of an explicit Euler method for the nonlinear term and an implicit Euler method for the linear term.

4. The discrete inverse Hankel transform is applied to find the surface position in the spatial domain. The apex position and speed, and its corresponding curvature are also obtained by the same procedure.

Once an iteration is done, the variables expressed in the spatial domain are once again transformed into the Hankel domain, and the process is repeated until the expected final time is reached. The details concerning this method are given in Appendix C.

At $t^* = 0$, a flat unperturbed free surface was considered, thus the initial conditions are $\eta^* = \mathcal{N}^* = 0$. The initial time step was fixed to $\Delta t^* = 10^{-5}$ for the static probe case, whereas for the oscillating probe it was given by $\Delta t^* = 10^{-5} \left(E^*\right)^3 / C_a$, 10^5 times smaller than the dimensionless oscillation period. Afterwards, based on the wave propagation distance, the successive values of the time step were numerically estimated (see Appendix C for details). For a given time step Δt^*, the local truncation error at each iteration is proportional to $O\left(\Delta t^*\right)$. The maximum time step, employed to observe the dynamic evolution of the surface, was unbounded for the case of a static probe, whereas, for the case of an oscillating probe, it was limited by the value $\Delta t^* = 10^{-2} \left(E^*\right)^3 / C_a$, a hundredth of the dimensionless oscillation period. Then, for the oscillating phenomenon, the truncation error is in the range $\sigma \in \left[O\left(10^{-4}/C_a\right), O\left(10^{-2}/C_a\right)\right]$. For the case of a static probe, the final time of the simulations was $t^* = 10^{12}$ and considering that an adaptive time step was employed, 250 time steps were calculated on average. For the case of a oscillating probe, the final time was chosen to be $t^* = 202\mathcal{T}^*$, in order to simulate 202 oscillation cycles. With an adaptive time step converging toward the imposed limit $\Delta t^* = 10^{-5} \left(E^*\right)^3 / C_a$, therefore, 20500 was the average number of time steps, for the oscillation case.

5.7 Concluding remarks

A thin-film equation, describing the dynamic surface deformation of a liquid film deposited over a rigid substrate and in interaction with a spherical probe, was constructed. The probe/liquid and liquid/substrate interactions were included in the modeling. The lubrication approximation is employed to relate the pressure difference and the motion of the free liquid surface. The resulting thin-film equation has been linearized, with the purpose of simplifying the equation and enabling a fast numerical solution. A pseudo-spectral numerical method was implemented to solve the presented thin-film nonlinear ODE.

As well, considering a sinusoidal probe motion, an impact assessment of the driving oscillation parameters on the thin-film response was made. Several behavior regimes were discussed. For thick films made of low viscosity liquids, a quasi-static behavior is forecast, whereas for thin films made of high viscosity liquids, a rigid sample behavior is expected. Our analysis foresees a phase shift between the probe oscillation and the sample response for the intermediate regime, which seems to be the most interesting case.

In Chapter 6, the derived equations will be numerically solved and analyzed, considering a thin-film in interaction with a static probe. In Chapter 7, the dynamic shape of a thin-film in interaction with a oscillating probe will be studied from the corresponding numerical results.

Chapter 6

Thin-film dynamics in response to a static probe

In this chapter, the behavior of a liquid film interacting with a static probe is reported. The numerical results of the thin-film dynamic response are presented and used as a test subject, in order to validate the methodology developed in the previous chapter. The final equilibrium position of the surface is compared with the static equilibrium solution obtained in Chapter 3. This matching only makes sense when the probe/liquid distance is equal or larger than the static threshold distance D^*_{min}. In addition, a theoretical analysis of the quasi-linear thin-film equation is performed. The aim of this analysis is to gain understanding of the dynamic response of a thin film, due to its interaction with a static probe.

6.1 Numerical results

When the liquid film is perturbed from its equilibrium shape $\eta^* = 0$, due to its interaction with a static probe, a transitory regime takes place before the liquid surface attains its equilibrium shape. The dynamic behavior of the film free surface is described by the quasi-linear thin-film equation, written as:

$$\frac{\partial \eta^*}{\partial t^*} = \frac{1}{r^*}\frac{\partial}{\partial r^*}\left[r^*\frac{\partial \Delta P^*}{\partial r^*}\right] \tag{6.1a}$$

$$\Delta P^* = -\frac{1}{r^*}\frac{\partial}{\partial r^*}\left[r^*\frac{\partial \eta^*}{\partial r^*}\right] + \frac{\eta^*}{\left(\lambda^*_{CF}\right)^2} + \frac{H_a}{\xi^*}\Pi^*_{pl}, \tag{6.1b}$$

where ΔP^* is the pressure difference across the air/liquid interface, λ^*_{CF} is the modified capillary length, ξ^* is the initial gap, H_a is the modified Hamaker number and Π^*_{pl} is the probe/liquid interaction term, which is given by the following expression:

$$\Pi^*_{pl} = \frac{-1}{\left[\left(D^* - \xi^*\eta^*\right)^2 + \left(r^*\right)^2 - 1\right]^3}. \tag{6.2}$$

These equations are solved with the numerical method presented in Chapter 5, for which D^* takes a constant value.

For a given combination of dimensionless parameters (the film thickness E^*, the Hamaker ratio A, the modified Hamaker H_a and Bond B_o numbers), the interface position depends completely on the relative value of the separation distance D^*, as it has been observed from the static analysis (see Chapter 3). In this way, the validation of the thin-film numerical model has been made by computing the final equilibrium surface shape, for a liquid film interacting with a static probe, and comparing it with the equivalent static equilibrium profile given in Chapter 3. Because the number of mesh points, according to the presented methodology, depends on the value of the modified capillary length λ^*_{CF}, we have decided to perform the model validation with a film of thickness $E^* = 1$, for which $\lambda^*_{CF} = 22.1$ with the parameters given in Table 6.1, in order to reduce the simulation time.

An example of the temporal surface evolution is shown in Fig.6.1, for a separation distance $D^* = 1.2017$ and the parameters given in Table 6.1. Considering a flat surface at $t^* = 0$, the instantaneous

Geometric and physical parameters			
Probe radius	R	[m]	10^{-8}
Film thickness	E	[m]	10^{-8}
Dimensionless parameters			
Dimensionless thickness	E^*		1
Dimensionless capillary length	λ_C^*		1.81×10^5
Film characteristic length	λ_F^*		2.21×10^1
Modified capillary length	λ_{CF}^*		2.21×10^1
Modified Hamaker number	H_a		5.48×10^{-3}
Hamaker ratio	A		1
Bond number	B_o		3.01×10^{-11}
Effective bond number	B_o^{eff}		2.05×10^{-3}
Simulation time step			
Initial time step	Δt^*		10^{-4}
Static critical conditions			
Minimum separation distance	D_{min}^*		1.2020
Maximum apex deformation	$\eta_{0,max}^*$		0.3247
Critical peak curvature	$\kappa_{0,crit}^*$		0.1105
Critical initial gap	ξ_{crit}^*		0.2020
Critical equilibrium gap	$\varepsilon_{0,min}^*$		0.6753

Table 6.1: Parameters used to obtain the dynamic response of the liquid film interacting with a static probe, corresponding to the physical properties of a PDMS thin film, given in Table 5.1.

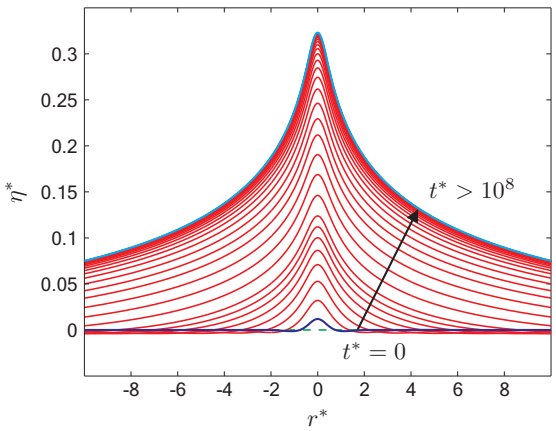


Figure 6.1: Dynamic evolution of the deformation profile for a static probe position $D^* = 1.2017$. [——] indicates the instantaneous surface shape from $t^* = 0$ to $t^* \to \infty$, following the sense of the arrow, [– – –] is the initially flat surface, and [——] and [——] represent the first time step and the equilibrium profile, respectively. Parameters are given in Table 6.1.

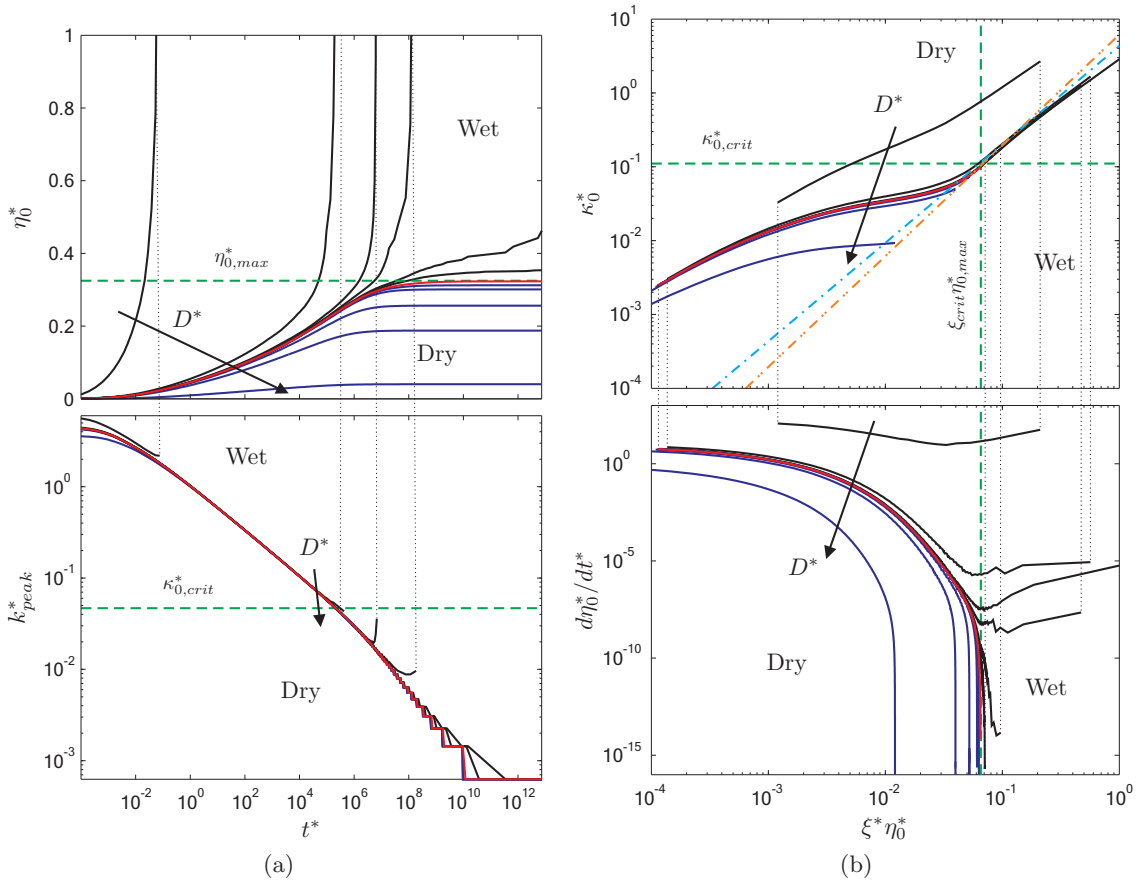


Figure 6.2: Dynamic evolution for a static probe: (a) apex deformation η_0^* (top) and peak angular wavenumber k_{peak}^* (bottom) as functions of t^* and (b) peak curvature κ_0^* (top) and apex speed $d\eta_0^*/dt^*$ (bottom) as functions of the apex position η_0^*, for $H_a = 5.48 \times 10^{-3}$, $B_o = 3.07 \times 10^{-11}$, $A = 1$ and a film thickness $E^* = 1$. Numerical solution of eq.(6.1) for different separation distances: [——] $D^* < D_{min}^*$, [——] $D^* \approx D_{min}^*$ and [——] $D^* < D_{min}^*$, where $D_{min}^* = 1.2017$ is the minimum separation distance obtained from the dynamic analysis. [– – –] indicates the values of $\eta_{0,max}^*$, $\kappa_{0,crit}^*$ and $\xi_{crit}^*\eta_{0,max}^*$ corresponding to the critical conditions, obtained from the static analysis (see Table 6.1). These values indicate the regions of probe wetting. The static [– · –] bulk and [– · –] shallow film approximations of the equilibrium peak curvature are shown. Parameters are given in Table 6.1.

application of the attractive force directly results into an acceleration of the air/liquid interface. Surface tension, viscosity and liquid/substrate interaction generate a restoring force, which acts to oppose the probe/liquid interaction and to constrain the interface deformation. At the initial stage, the liquid surface below the probe $r^* \in [0, 1)$ is sucked by the probe, creating a narrow bell-shaped bump. The bump volume has been gathered by draining the liquid from the vicinity, creating a trough at the zone $r^* \in (1, 2)$. As time goes by, more liquid is carried from the surroundings, increasing the size of the bump, narrowing its shape and displacing the liquid depression toward larger radial positions. The vertical size of the depression remains almost constant, whereas its radial width increases with time. At short times, the liquid surface undergoes a fast modification of its position. Around $t^* \gtrsim 10^5$, the rate of change, at which the bump volume increases and the trough displaces in the horizontal direction, slows down significantly. For $t^* \gtrsim 10^7$, the surface shape barely changes, reaching its final configuration at a time $t^* \approx 10^8$.

In addition, the temporal evolution of the surface apex position, its speed and curvature, as well as the peak of the angular wavenumber distribution corresponding to the Hankel transform of the surface profile, can be followed in Fig.6.2. In Fig.6.2 -top-, the apex follows different evolution paths depending on the value of the separation distance D^* relative to the threshold D^*_{min}. If $D^* < D^*_{min}$, the probe/liquid interaction becomes unbounded at a certain time, which also depends on D^*, and the apex position diverges. On the other hand, if $D^* \geq D^*_{min}$, the apex converges to a final equilibrium position, hedged by the maximum apex deformation η^*_0 obtained with D^*_{min}. In the displayed example, the estimated minimum separation distance is $D^*_{min} = 1.2017$, consequently giving a critical initial gap $\xi_{crit} = 0.2017$, which yields an equilibrium maximum apex deformation $\eta^*_{0,max} = 0.3230$ and a minimum equilibrium gap $\varepsilon^*_{0,min} = 0.6770$. For $D^*_{min} = 1.2017$, the equilibrium shape is attained at a settling time $t^* \gtrsim 10^8$, whereas for $D^* > D^*_{min}$ this time is significantly reduced as D^* increases.

Also, deduced from Fig.6.2 -bottom-, the wavenumber spectrum is shifted toward shorter frequencies, due to the energy dissipation in the film. This happens due to the creation of a deformation front, already mentioned during the description of Fig.6.1, which propagates at the group speed υ_g toward the modified capillary length λ^*_{CF}. The coarse behavior of the peak wavenumber at long times $t^* > 10^8$ is due to the minimum value employed for the wavenumber mesh grid. However, one expects to see this peak wavenumber k^*_{peak} dropping to zero as $t^* \to \infty$ for converging evolutions, as it will be discussed in the following section.

Recalling eq.(2.13), for an equilibrium deformation profile of a bulk liquid, the peak curvature is given by:

$$\kappa^*_0 = (C_{lk})^{3/2} \sqrt{(\frac{2}{Ha})} \, (\xi^* \eta^*_0)^{3/2} \, ,$$

in which, a bulk proportionality constant of $C_{lk} = 0.46$ is used, as estimated from the data in Fig.2.7 for the effective Bond number given in Table 6.1. As well, recalling eq.(3.17), the equilibrium deformation of a shallow film, the peak curvature is approximated with:

$$\kappa^*_0 = \sqrt[3]{A} \left(3 \frac{\xi^* \eta^*_0}{E^*} \right)^{4/3} .$$

Then, the final peak curvature should be found within the trends given by the aforementioned bulk and shallow film trends. Indeed, this is precisely observed for the converging evolutions, as shown in Fig.6.2b -top-. For $D^*_{min} = 1.2017$, and its corresponding apex product $\xi^*_{crit}\eta^* = 0.0651$, a critical peak curvature of $\kappa^*_{0,crit} = 0.1000$ was found.

In Fig.6.2b -bottom-, the apex speed is presented. Since the application of the probe/liquid interaction happens in an abrupt way at $t^* = 0$, which is equivalent to a Heaviside step function input, the surfaces acquires a relatively high speed. As the deformation increases, this speed decreases due to the viscous dissipation within the liquid phase. This trend is observed for $D^* \geq D^*_{min}$, until the speed drops to zero as the surface shape gets close to its equilibrium shape. In contrast, for the diverging cases $D^* < D^*_{min}$, the unbounded probe/liquid interaction provokes a re-acceleration of the vertical displacement.

Now, with the purpose of validating our method, we compare this results with the ones obtained from the static numerical resolution in Chapter3. As it is presented in Fig.3.4, for a film with $E^* = 1$, the static analysis yields a minimum separation distance $D^*_{min} = 1.2020$, a maximum apex deformation $\eta^*_{0,max} = 0.3247$ and a critical peak curvature $\kappa^*_{0,crit} = 0.1105$. Consequently, one finds a critical initial gap $\xi^*_{crit} = 0.2020$ and $\varepsilon^*_{0,min} = 0.6753$. With the values obtained with the dynamic model, the only significant accuracy loss is observed for the peak curvature, with a relative error of 9.5×10^{-2}, whereas

for the other quantities the relative error remains below 1×10^{-2}. Therefore, one can expect that the presented thin-film numerical model will provide a useful and precise tool to study the interaction between a liquid film and an oscillating probe.

6.2 Theoretical analysis of the thin-film transient behavior

As it is crucial to understand the natural response of the thin-film to any perturbation, a theoretical analysis is devised. The application of the Hankel transform of zero order turns the quasi-linear thin-film equation, given by the PDE in eq.(5.15), into the eq.(5.26), which is written as:

$$\frac{\partial \mathcal{N}^*}{\partial t^*} = -\nu^* \mathcal{N}^* - \frac{H_a}{\xi^*} \left(k^*\right)^2 \mathcal{Q}^*,$$

where:

$$\nu^* = \left(k^*\right)^2 \left[\left(k^*\right)^2 + \left(\lambda_{CF}^*\right)^{-2}\right],$$

whereas $\mathcal{N}^*$ and $\mathcal{Q}^*$ are the zero order Hankel transforms of the surface position η^* and the probe/liquid interaction potential Π_{pl}^*, respectively. In the Hankel domain, q^* is the spatial wavenumber and, as a consequence, $k^* = 2\pi q^*$ is the angular wavenumber.

Despite the reduction, this nonlinear ODE does not have an analytical solution, because Π_{pl}^* does not have an analytical Hankel transform. Nevertheless, if one considers a situation for which $D^* \gg \xi^* \eta^*$, the interaction potential becomes:

$$\Pi_{pl}^* \simeq \frac{-1}{\left[\left(D^*\right)^2 - 1 + \left(r^*\right)^2\right]^3},$$

which presents an analytic expression for its $\mathbb{H}_0$ transform, given in Appendix D. This fact reduces eq.(5.26) to:

$$\frac{\partial \mathcal{N}^*}{\partial t^*} = -\nu^* \mathcal{N}^* + \frac{\pi H_a}{4\xi^*} \left[\frac{\left(k^*\right)^4}{\left(D^*\right)^2 - 1}\right] K_2 \left\{k^* \sqrt{\left(D^*\right)^2 - 1}\right\}, \tag{6.3}$$

where K_2 is a second order modified Bessel function of the second kind.

The general solution, in the Hankel domain, of the linear non-homogeneous ODE given in eq.(6.3), is decomposed into:

$$\mathcal{N}^*\left(q^*, t^*\right) = \mathcal{N}_H^*\left(q^*, t^*\right) + \mathcal{N}_P^*\left(q^*, t^*\right) \tag{6.4}$$

where $\mathcal{N}_H^*$ and $\mathcal{N}_P^*$ are the homogeneous and the particular solutions, respectively. Both constituents are easily found, and they are expressed by the formulas:

$$\mathcal{N}_H^*\left(q^*, t^*\right) = C_H\left(q^*\right) \exp\left\{-\nu^* t^*\right\} \tag{6.5a}$$

$$\mathcal{N}_P^*\left(q^*, t^*\right) = \frac{\pi H_a \left(k^*\right)^4}{4\xi^*} \int_0^{t^*} \frac{\exp\left\{-\nu^*\left(t^* - \Upsilon\right)\right\}}{\left(D^*\right)^2 - 1} K_2 \left\{k^* \sqrt{\left(D^*\right)^2 - 1}\right\} d\Upsilon, \tag{6.5b}$$

where the probe position is temporarily given by $D^* = D^*\left(\Upsilon\right)$, Υ being the time integration variable The wavenumber dependent coefficient $C_H\left(q^*\right)$ should be obtained from the Hankel transform of the problem initial conditions:

$$C_H\left(q^*\right) = \mathbb{H}_0\left\{\eta^*\left(r^*, t^* = 0\right)\right\}.$$

Subsequently, from the definition of the inverse Hankel transform, the solution in the spatial domain is retrieved from:

$$\eta^*\left(r^*, t^*\right) = \eta_H^*\left(r^*, t^*\right) + \eta_P^*\left(r^*, t^*\right)$$

$$\eta_H^*\left(r^*, t^*\right) = \mathbb{H}_0^{-1}\left\{\mathcal{N}_H^*\left(q^*, t^*\right)\right\} = 2\pi \int_0^\infty \mathcal{N}_H^*\left(q^*, t^*\right) J_0\left(2\pi q^* r^*\right) q^* dq^*$$

$$\eta_P^*\left(r^*, t^*\right) = \mathbb{H}_0^{-1}\left\{\mathcal{N}_P^*\left(q^*, t^*\right)\right\} = 2\pi \int_0^\infty \mathcal{N}_P^*\left(q^*, t^*\right) J_0\left(2\pi q^* r^*\right) q^* dq^*.$$

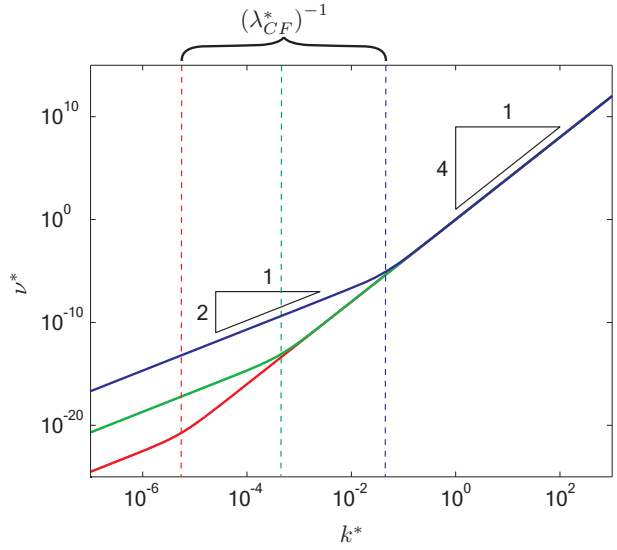


Figure 6.3: Time decay coefficient ν^* as a function of the angular wavenumber k^*, corresponding to thin films of thickness [——] $E^* = 1$, [——] $E^* = 10$, and [——] $E^* \geq 10^3$. The dashed vertical lines indicate the angular wavenumber given by λ^*_{CF}, obtained with $H_a = 5.48 \times 10^{-3}$, $B_o = 3.07 \times 10^{-11}$, $A = 1$ and the corresponding film thickness.

If one imagines a situation in which the liquid surface is initially undisturbed, suddenly a probe approaches and, after some time, it moves away, one can make some hypotheses. As soon as the probe approaches the liquid surface, the system state is excited and the interface deformation is acquired via the particular solution $\mathcal{N}^*_P$. Nevertheless, far from the probe, the liquid surface will suffer a deformation, not due to a direct probe stimulus but due to the diffusion of "elastic" energy over the film surface, depicted by the homogeneous solution $\mathcal{N}^*_H$. Thus, the probe provokes an excitation in the near-field, whereas there is a diffusion of surface tension energy toward the middle and far-fields. This solution evolves dynamically, in such a way that it should be computed until the last moment of probe/liquid interaction, until after the probe withdrawal. Once the system is let free, using the deformation profile given by the last computed $\mathcal{N}^*_P$ as a substitute for the initial condition, the thin film relaxation behavior is then portrayed by the homogeneous solution $\mathcal{N}^*_H$.

Indeed, relaxation and diffusion show similar features, as they both are portrayed by the homogeneous solution, thus we should consider them as a single occurrence. Therefore, the overall behavior of the thin-film can be decomposed into two main conceptions: relaxation/diffusion and excitation.

6.2.a Thin-film relaxation/diffusion

The relaxation/diffusion of the thin film is characterized by ν^*, which is now identified as a time decay coefficient. The trend of this wavenumber-dependent decay rate is displayed in Fig.6.3 for three different film thicknesses. From a comparison of the angular wavenumber k^* and the modified capillary length λ^*_{CF}, the time decay coefficient can be approximated by:

$$\nu^* = \begin{cases} \left(\dfrac{k^*}{\lambda^*_{CF}}\right)^2 & \text{for } k^* \ll (\lambda^*_{CF})^{-1} \\ (k^*)^4 & \text{for } k^* \gg (\lambda^*_{CF})^{-1}\,. \end{cases} \tag{6.6}$$

This power-laws indicate two different asymptotic behaviors: small wavenumbers (long wavelengths) are slowly weakened, whereas large wavenumbers (short wavelengths) are rapidly attenuated. As well, one should have in mind the classic definition of the group velocity (Lighthill, 1965), v_g is given by:

$$v_g = \frac{d\nu^*}{dk^*} = 2k^* \left[2\,(k^*)^2 + \frac{1}{(\lambda^*_{CF})^2}\right], \tag{6.7}$$

which represents the speed at which the envelope waveform travels and at which the energy propagates. It is natural to find that the group speed always decreases as the wavelength increases, because of the axisymmetric geometry. Therefore, the group velocity also shows two regimes:

$$\upsilon_g = \begin{cases} \dfrac{2k^*}{\left(\lambda^*_{CF}\right)^2} & \text{for } k^* \ll \left(\lambda^*_{CF}\right)^{-1} \\ 4\left(k^*\right)^3 & \text{for } k^* \gg \left(\lambda^*_{CF}\right)^{-1}. \end{cases} \tag{6.8}$$

Now, from this discrimination, one can understand why the early stages of the surface evolution, presented in Figs.6.1 and 6.2, evolve faster than the final stages. At first, the probe proximity excites relatively large angular wavenumbers $k^* > 1$, corresponding to short wavelengths of an order smaller than the probe radius. Due to the behavior in the short wavelength regime $k^* \gg \left(\lambda^*_{CF}\right)^{-1}$, the deformation is quickly disseminated with $\upsilon_g \sim \left(k^*\right)^3$. As it extends to larger radial positions, the speed of the deformation front decreases, attaining relatively smaller group velocities $\upsilon_g \sim k^*$ when the deformation reaches wavelengths that correspond to the regime $k^* \ll \left(\lambda^*_{CF}\right)^{-1}$. In conclusion, the decay coefficient ν^* is the leading factor associated in the surface energy diffusion at the thin-film.

We can go further with this analysis when pursuing an additional simplification in the homogeneous solution $\mathcal{N}^*_H$, given in eq.(6.5a). Considering that, for $x > 1$, one can approximate the zero order Bessel function with the following expression:

$$J_{\mathrm{v}}(x) \approx \sqrt{\frac{2}{\pi x}} \cos\left\{x - \frac{\pi}{2}\left(\mathrm{v} + \frac{1}{2}\right)\right\} = \Re\left[\sqrt{\frac{2}{\pi x}} \exp\left\{i\left(x - \frac{\pi}{2}\left(\mathrm{v} + \frac{1}{2}\right)\right)\right\}\right].$$

As a consequence, the homogeneous solution can be approximated with:

$$\eta^*_H\left(r^*, t^*\right) \approx \Re\left[\int_0^\infty Z_q\left(r^*, t^*\right) dq\right], \tag{6.9}$$

with:

$$Z_q\left(r^*, t^*\right) = 2C_H\left(q^*\right) \sqrt{\frac{q^*}{r^*}} \exp\left\{-\nu^* t^* + i\left(2\pi q^* r^* - \frac{\pi}{4}\right)\right\}. \tag{6.10}$$

This representation depicts the natural response of the liquid film to a perturbation, for $2\pi q^* r^* > 1$. It is important to observe that Z_q is a periodic spatial function, remaining fixed in space but with a magnitude that decreases in time. Therefore, the phase velocity of the waveform Z_q is zero $\upsilon_p = 0$, because an explicit dispersion relation does not arise, and the presented function is clearly identified as a sinusoidal standing wave.

According to eqs.(6.9) and (6.10), the addition of an infinite number of functions Z_q, each of them being a solution of the homogeneous equation, generates a complete estimate of the homogeneous solution η^*_H. A particular sinusoidal standing wave shows a wavenumber q^*, a wavelength $\left(q^*\right)^{-1}$, a permanent phase of $\pi/4$ and a wavenumber-dependent amplitude given by $2C_H\left(q^*\right)\sqrt{q^*}$. In addition, the hyperbolic spatial envelope $1/\sqrt{r^*}$ shows that the deformation profile is gradually reduced as r^* grows. And, as it has been already discussed, each waveform Z_q decays in time with a coefficient ν^*, determined by its own wavenumber q^*.

Despite the standing wave behavior of the waveforms Z_q, from the surface evolution displayed in Fig.6.1, one perceives the displacement of a deformation front. This is the distinctive effect of the wavenumber-dependent time decay coefficient ν^*. The amplitude of sinusoids with large wavenumbers q^* decays faster than those with small wavenumbers, thus the behavior of the liquid surface will be that of a deformation front propagating from $r^* = 0$ (large q^*) toward $r^* = \lambda^*_{CF}$ (small q^*). In other words, the surface shape will be determined by large wavenumbers q^* (short wavelengths) at short times, whereas at long times, the profile will be governed by small wavenumbers q^* (long wavelengths).

6.2.b Thin-film excitation

The excitation of the thin film, due to the probe interaction, is outlined only by the particular solution $\mathcal{N}^*_P$, given in eq.(6.5b). Especially, considering a static or quasi-static case, in which D^* changes slowly

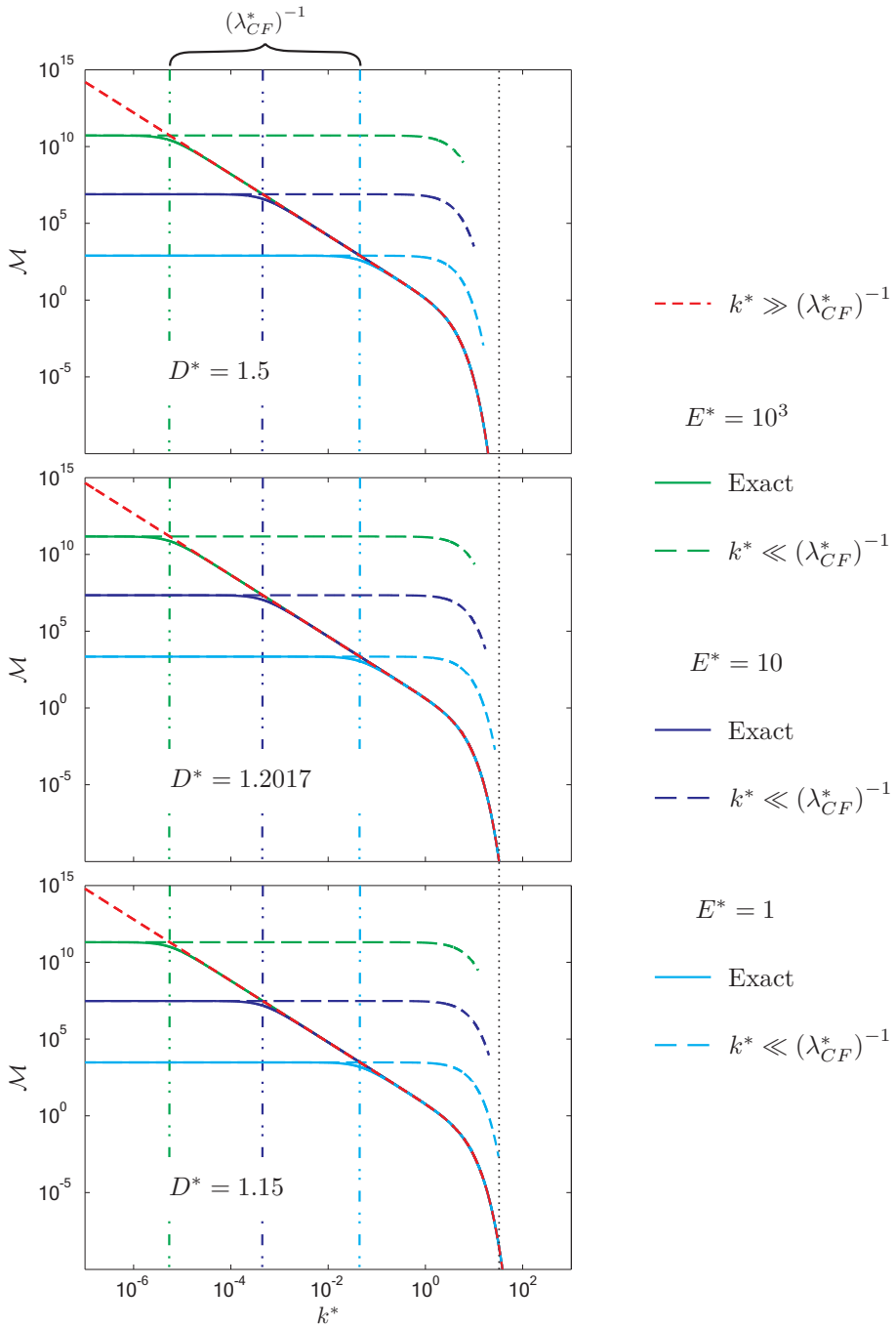


Figure 6.4: Dependence of the excited wavenumbers on the film thickness E^* and separation distance D^*. The function $\mathcal{M}$ (see eq.(6.12)) is plotted as a function of the wavenumber k^*, indicating the excited wavenumbers for different values of E^* and D^*. The curves correspond to the simplification for [– – –] $k^* \gg (\lambda^*_{CF})^{-1}$ and [– –, – –, – –] $k^* \ll (\lambda^*_{CF})^{-1}$. The [– · –, – · –, – · –] vertical lines indicate the wavenumbers given by λ^*_{CF}, corresponding to the different thicknesses. The curves were obtained with $H_a = 5.48 \times 10^{-3}$, $B_o = 3.07 \times 10^{-11}$, $A = 1$.

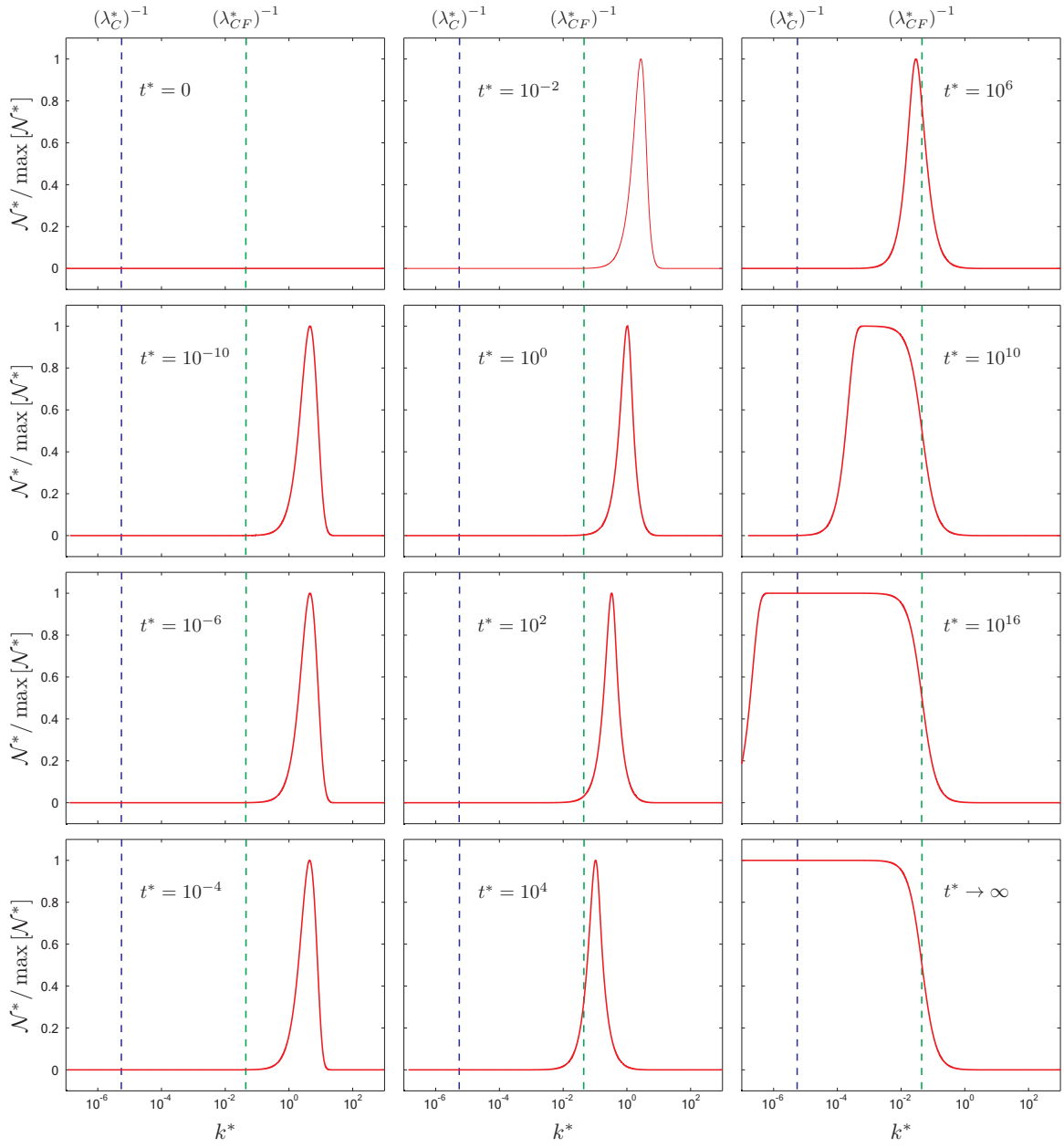


Figure 6.5: Time evolution of the excited wavenumbers for a film of thickness $E^* = 1$ and separation distance $D^* = 1.2017$. The quasi-static solution of $\mathcal{N}_P^*$, given by eq.(6.11), is plotted as a function of the wavenumber k^*, for which the liquid surface is initially flat at $t^* = 0$. $\mathcal{N}^*$ has been normalized with its maximum instantaneous value. The curves were obtained with $\xi^* = 0.2017$, and the parameters given in Table 6.1.

so that the system can be taken to be in equilibrium at all times, the particular solution reduces to:

$$\mathcal{N}_P^* = \frac{\pi H_a}{4\xi^*}\left[\frac{\mathcal{M}}{(D^*)^2-1}\right]\left[1-\exp\left\{-\nu^* t^*\right\}\right], \tag{6.11}$$

where $\mathcal{M}$ is a wavenumber-dependent function defined as:

$$\mathcal{M}(q^*) = \left[\frac{(k^*)^4}{\nu^*}\right] K_2\left\{k^*\sqrt{(D^*)^2-1}\right\}, \tag{6.12}$$

which indicates the range of wavenumbers that is excited for a given separation distance D^* and a film thickness E^*.

Since the time decay coefficient ν^* appears explicitly in the particular solution, its asymptotic behaviors, given in eq.(6.6), can also be applied. Therefore, the function $\mathcal{M}$, as well, shows the two following asymptotic behaviors:

$$\mathcal{M} = \begin{cases} \left[k^*\lambda_{CF}^*\right]^2 K_2\left\{k^*\sqrt{(D^*)^2-1}\right\} & \text{for } k^* \ll (\lambda_{CF}^*)^{-1} \\ K_2\left\{k^*\sqrt{(D^*)^2-1}\right\} & \text{for } k^* \gg (\lambda_{CF}^*)^{-1}. \end{cases} \tag{6.13}$$

The approximation for $k^* \gg (\lambda_{CF}^*)^{-1}$ depends only on the distance D^*, whereas for $k^* \ll (\lambda_{CF}^*)^{-1}$, $\mathcal{M}$ scales with the square of the modified capillary length.

As shown in Fig.6.4, the shape of the function $\mathcal{M}$ is well described by these approximations within the corresponding asymptotic regimes, whereas the transition region is relatively short. From the $\mathcal{M}$ curves, the more significant information that one can obtain is the range of excited wavenumbers, since the weight of each wavenumbers on the solution needs to be observed directly from $\mathcal{N}_P^*$. Therefore, the analysis of $\mathcal{M}$ will be mainly focused on the impact over the excited wavenumbers. Firstly, one notes that a variation of the film thickness E^* produces an obvious change in the modified capillary length λ_{CF}^*, displacing the junction between asymptotic regimes. However, for a given distance D^*, the broadness of the wavenumber band is not affected by an alteration of the film thickness E^*. For a given film thickness, following curves of the same color in Fig.6.4, as D^* decreases, the curve stretches to larger wavenumbers k^* and amplifies toward higher magnitudes of $\mathcal{M}$. The shape of all the $\mathcal{M}$ curves is similar and, for a given E^*, seems to follow a weak scaling, varying inversely with the separation distance D^*, i.e. smaller separation distances provoke the excitation of a wider wavenumber range.

Fig.6.5 displays a temporal evolution of the solution $\mathcal{N}_P^*$, which has been normalized with the instantaneous maximum value of $\mathcal{N}_P^*$. Note that the angular wavenumber axis is presented in a logarithmic scale. This example corresponds to the deformation of a liquid film, created by a static probe, which is placed at a separation distance $D^* = 1.2017$, for a film of thickness $E^* = 1$ and the dimensionless parameters given in Table 6.1. At small times $0 < t^* \leq 10^{-2}$, relatively large wavenumbers $k^* \in \left(10^0, 10^1\right)$ are excited. This indicates that the surface deformation is initially concentrated in a narrow zone near the vertical axis, $r^* \in \left[0, 10^0\right)$, which corresponds to the order of magnitude of the probe radius. During this stage, the wavenumber distribution $\mathcal{N}_P^*$ shows an asymmetric Lorentzian-like shape, which barely moves toward smaller values of k^* with time. The almost nonexistent displacement of the distribution indicates that this is the excitation phase of the phenomenon. The liquid film has taken its time to weigh up the impact of the probe attractive interaction. As time goes by within $10^{-2} < t^* \leq 10^2$, the distribution moves to the left with an increased speed, approaching the wavenumber given by $(\lambda_{CF}^*)^{-1}$. Thus, the deformation goes through a diffusion phase, transmitting the surface tension energy toward larger radial positions r^*, in the middle and far-fields, up to the modified capillary length λ_{CF}^*. When the peak of the distribution has already crossed the value $(\lambda_{CF}^*)^{-1}$, at a time in the range $10^4 < t^* < 10^6$, the distribution $\mathcal{N}_P^*$ shows a nice symmetric but still narrow bell-shape, within the horizontal logarithmic scale. Afterward, a behavior modification starts. The negative-slope side of the curve halts as it passes through $k^* = (\lambda_{CF}^*)^{-1}$, whereas the positive-slope side keeps on moving, expanding the distribution, increasing the broadness of the distribution in an asymmetric. This behavior denotes a relaxation phase, in which the thin-film reshapes to uniformly distribute the surface energy. Finally, as $t^* \to \infty$, the shape of $\mathcal{N}_P^*$ can be described as a sharp hyperbolic tangent-like shape in the logarithmic horizontal scale, which cor-

responds the final equilibrium surface deformation profile in Fig.6.1. The overall behavior corresponds exactly to the one described during the description of Figs.6.1 and 6.2, of the preceding section.

Even though this approximation provides a good qualitative description of the film evolution, one should keep in mind the disadvantages, inherent to the applied quasi-static simplification:

- The hypothesis $D^* \gg \xi^* \eta^*$ is not reliable near the critical separation distance D^*_{min}, where the probe/liquid interaction is maximized (Quinn et al., 2013).
- The quasi-static assumption implicitly denies the dynamic probe/surface interaction, because the interaction potential keeps a constant contribution to the deformation, whereas, indeed, it becomes stronger as η^* increases, which is also disregarded by the first hypothesis.

In conclusion, the presented analytical methodology provides a useful tool to understand the nature of the probe/liquid dynamic interaction. The different wavenumber-dependent regimes have been discerned and the role of the relaxation/diffusion and excitation stages has been described. However, in order to follow the precise metamorphosis of the liquid film, the numerical solution of eq.(5.15) must be calculated and analyzed.

6.3 Concluding remarks

The quasi-linear thin-film model, developed in Chapter 5, has been applied to the problem of a liquid surface instantaneously interacting with a static probe. Simulations were performed for different values of the probe/liquid film separation distance D^*, and the results were described in detail. We have verified that the final surface deformation agrees well enough with the static solution, obtained with the equilibrium modified Young-Laplace equation (introduced in Chapter 1 and numerically solved in Chapter 3). In addition, the dynamic evolution confirmed the divergence of the interface profile, entailing the dynamic "jump-to-contact" of the liquid over the probe and the subsequent wetting process, for $D^* < D^*_{min}$, where D^*_{min} is the threshold static separation distance. A good agreement between the dynamic and static approaches has been found, pertaining the critical conditions before wetting.

As well, when a further simplification is carried out (a quasi-static approximation), a compound solution is found in the wavenumber domain, by means of the Hankel transform. An interpretation of the role, that the different components of the solution take, is given and used to explain the qualitative behavior of the thin-film. Distinguishable relaxation/diffusion and excitation phases were revealed within the evolution of the thin-film, interacting with a static probe. A very good qualitative agreement between the theoretical analysis and the numerical results has been found. One expects to extrapolate the ideas, conceived in this chapter, to understand the thin-film behavior in response to a dynamic probe.

Chapter 7

Thin-film dynamics in response to an oscillating probe

In this chapter, the preliminary results on the dynamic response of a thin-film in interaction with an oscillating probe are reported. Different behaviors of the liquid surface are found according to the oscillation parameters. A description of these trends is given at the beginning of this chapter. The system stability is briefly addressed to conclude with this preliminary analysis.

7.1 Numerical results

When the liquid film is perturbed from its equilibrium shape $\eta^* = 0$, due to its interaction with an oscillating probe, a periodic response of the liquid surface is observed. The dynamic behavior of the film free surface is described by the quasi-linear thin-film equation, given by eq.(6.1). As well, the probe/liquid interaction term Π^*_{pl}, given by eq.(6.2), is now a time-dependent function because the probe motion is determined by the following expression:

$$D^* = D^*_a + \xi^* W^*_D \cos\left(2\pi t^* \frac{Ca}{(E^*)^3}\right), \tag{7.1}$$

where D^*_a is the time-average probe position, W^*_D is the oscillation amplitude, C_a is the capillary number and E^* is the film thickness. As well, we should remember that the time-average gap is defined as $\xi^* = D^*_a - 1$. The combination of eq.(6.1) and (6.2) is solved with the numerical method presented in Chapter 5, for which D^* takes the form given in eq.(7.1). Besides, we have chosen arbitrarily $n = 202$ as the maximum number of oscillation cycles for the simulations. Considering the parameters summarized in Table 7.1, simulations were performed with a fixed dimensional oscillation amplitude $W_D = R$. In addition, the time-average probe position was swept in the range $D_a \in [R + W_D, D_{min} + W_D]$, in order to analyze the impact of this parameter. Herein, we recall the static minimum separation distance $D_{min} = RD^*_{min}$, which indicates the wetting threshold distance for the interaction with a static probe. Considering the aforementioned parameters, the dimensionless time-average probe position was varied within the range $D^*_a \in [2, D^*_{min} + 1]$, where a value of $D^*_{min} = 1.2017$ was obtained in the previous chapter. Additionally, we define a useful parameter, which corresponds to the lower position of the probe:

$$\mathcal{D}^* = D^*_a - \xi^* W^*_D. \tag{7.2}$$

We will constantly make allusion to this parameter.

We will start discussing some features, discerned from the numerical results presented in this chapter, that may help in the description of the phenomenon. To start, three main different behaviors have been observed for the liquid films:

- Thin-films achieving a *permanent* regime, for which the surface motion shows well defined periodic motion, with constant apex oscillation amplitude and phase. We will call them Stable Oscillating Thin-Films (SOTF).

Geometric and physical parameters			
Probe radius	R	[m]	10^{-8}
Film thickness	E	[m]	10^{-8}
Oscillation parameters			
Oscillation amplitude	W_D	[m]	10^{-8}
Driving angular frequency	ω_D	$[s^{-1}]$	2.20×10^{6}
Period	$\mathcal{T}$	[s]	2.86×10^{-6}
Film time scale	τ	[s]	1.36×10^{-7}
Dimensionless parameters			
Dimensionless thickness	E^*		1
Dimensionless capillary length	λ_C^*		1.81×10^{5}
Film characteristic length	λ_F^*		2.21×10^{1}
Modified capillary length	λ_{CF}^*		2.21×10^{1}
Modified Hamaker number	H_a		5.48×10^{-3}
Hamaker ratio	A		1
Bond number	B_o		3.01×10^{-11}
Effective bond number	B_o^{eff}		2.05×10^{-3}
Dimensionless period	$\mathcal{T}^*$		2.1×10^{1}
Capillary number	Ca		4.74×10^{-2}
Simulation time step			
Initial time step	Δt^*		2×10^{-4}
Maximum time step	Δt^*		2×10^{-1}

Table 7.1: Parameters used to obtain the dynamic response of the liquid film interacting with an oscillating probe, corresponding to the physical properties of a PDMS thin film, given in Table 5.1.

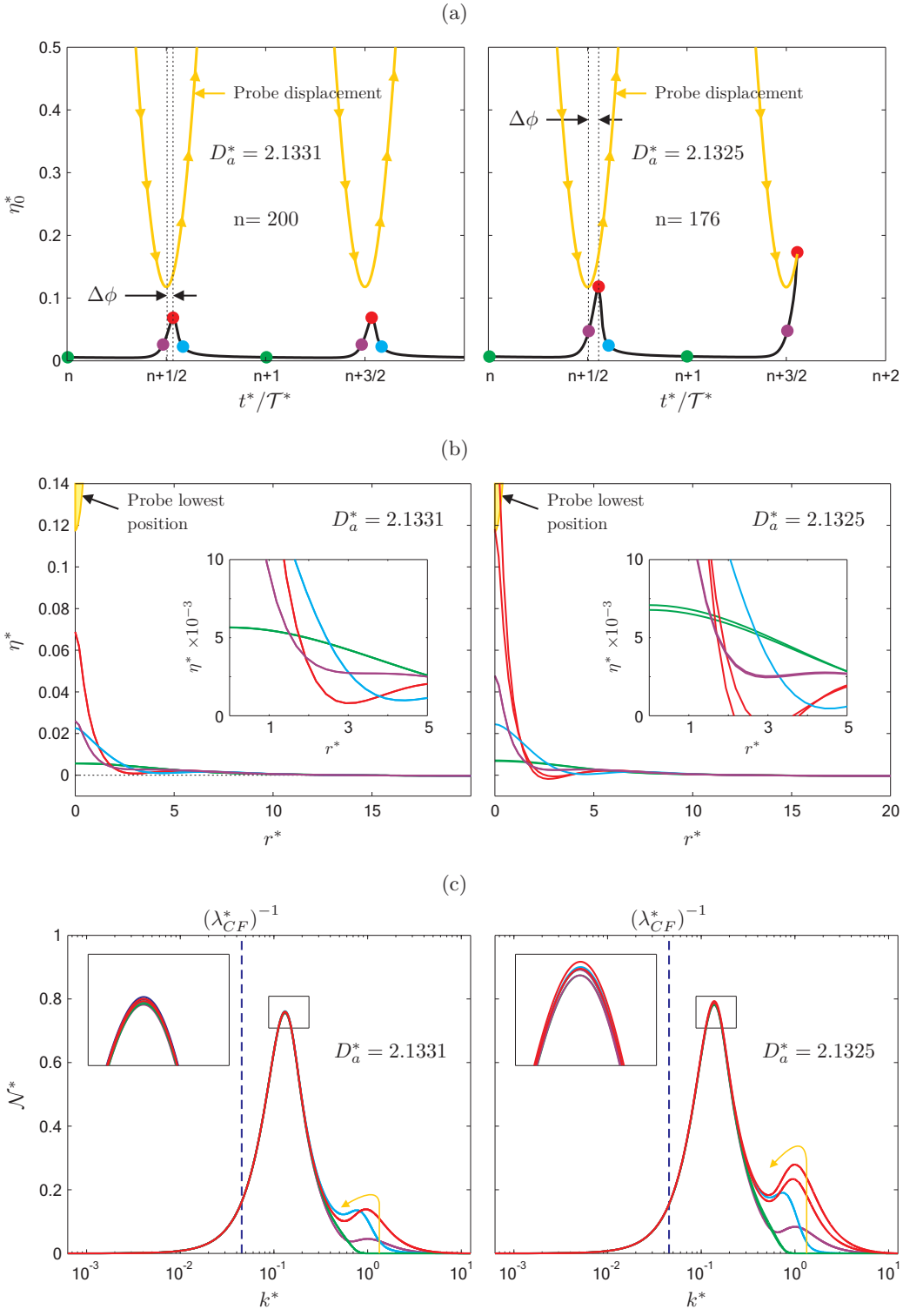


Figure 7.1: (a) Instantaneous position of [——] the surface apex η_0^* during two oscillating periods. [——] Indicates the instantaneous lower position of the probe. $\Delta\phi$ is the phase shift of the response apex oscillation with respect to the probe motion. (b) Surface position η^* and (c) instantaneous angular wavenumber spectrum $\mathcal{N}^*$ as functions of the radial position r^* and the angular wavenumber k^*, respectively. (Left column) curves obtained for a time-average probe position $D_a^* = 2.1331$ and (right column) for $D_a^* = 2.1325$. The color lines [——, ——, ——, ——] indicate the deformation profile and the wavenumber spectrum corresponding to the instants marked with [●,●,●,●] in the temporal chart (a). [→] indicates the sense of the probe excitation in the wavenumber domain during a cycle. Parameters are given in Table 7.1.

- Thin-films arriving to a *quasi-permanent* state, for which the surface motion shows a periodic motion, with slightly increasing oscillation amplitude and phase. We will call them Quasi-Stable Oscillating Thin-Films (QSOTF).

- Thin-films presenting a *diverging* behavior, at first they evolve quasi-periodically, showing an increase of amplitude and phase, until at a certain number of oscillations, the surface "jumps-to-contact" the probe. We will call them Unstable Oscillating Thin-Films (UOTF).

In fact, the QSOTF behavior exists only for the short-time simulations analyzed in this study. Performing long-time calculations should yield that the QSOTF cases either reach a permanent regime (being SOTF) or show a diverging behavior (being UOTF). Due to the behavior likeness, that QSOTF present with respect to SOTF, we will describe them as parts of the same group, which we will simply call Periodic Oscillating Thin-Films (POTF). Therefore, the qualitative description of the phenomenon is made only considering POTF and UOTF.

Some preliminary results are shown in Fig.7.1. In general, each time the probe approaches the liquid surface, a dynamic surface deformation is engendered, i.e. a liquid bump of changing size is observed below the probe. Indeed, the probe sucks the liquid within the region $r^* \in [0, 2[$, provoking the displacement of the same volume of the liquid from the zone $r^* \in]2, 5[$ and leaving a trough in its place. Fig.7.1a reports the evolution of the apex position, for (left column) a POTF case and (right column) a UOTF example. For the POTF case, obtained with a time-average probe position $D_a^* = 2.1331$, the apex follows a periodic displacement about a certain time-average value, slightly above the horizontal axis. Even though the time ratio $\mathcal{T}^* = \mathcal{T}/\tau$ is greater than 1, the liquid follows the probe motion with a phase $\phi \geq \pi$, i.e. the apex maximum position happens an instant after the probe reaches its lowest position. In the figure, the phase shift $\Delta\phi = \phi - \pi$ is illustrated instead. For the UOTF case, the apex motion oscillates as well, but around an increasing average trend. Consequently, after a certain number of cycles, the lowest probe position $\mathcal{D}^*$ is so small and the probe/liquid interaction so intense that a dynamic "jump-to-contact" phenomenon takes place. The jump of the liquid over the probe occurs at the beginning of the probe retreat motion. A phase shift $\Delta\phi$ is also observed, which for this case is slightly larger than that for the POTF case. As a consequence, one deduces that $\Delta\phi$ depends on the time-average distance D_a^*.

In both cases, before the liquid/probe contact happens, one clearly notes that the apex displacement is not symmetric with respect to the maximum attained value, indicating the footprints of a viscoelastic behavior. Indeed, at the left-hand side and at the summit, respectively tagged with bullets [•, •], the slope of the apex path and its magnitude are determined by D_a^*. Shorter values of D_a^*, induce larger values of η_0^* and, as a consequence, steeper slopes. When the probe moves away and probe wetting does not happen, now tagged with [•], the apex deformation suffers a fast and severe decrease, corresponding to an "elastic" recovery due to surface tension force. Afterward, a slow decrease in magnitude is observed due to the viscous relaxation, as the volume of liquid stocked below the probe gradually returns to its time-average position.

The surface profiles and angular wavenumber distributions, corresponding to the tagged instants in Fig.7.1a, are shown in Fig.7.1b and Fig.7.1c, respectively, with the same colors in order to distinguish the time sequence. We will start describing the POTF dynamic surface deformation, illustrated in the left column figures. Note that the curves of the same color, which correspond to the same instants of consecutive cycles, are indistinguishable in Figs.7.1b and 7.1c (also in the inlets). This fact is the main characteristic of POTF behaviors. Also, as it has been remarked, the surface shape seems to oscillate around the time-average profile, [——] profile, given at the half-period instant, tagged as [•] in Fig.7.1a. In an equivalent way, the surface shape in the wavenumber domain seems to fluctuate around an average bell-shaped distribution [——], centered slightly to the right of $k^* = 10^{-1}$, which corresponds to the time-average profile in the space domain, illustrated with the same color. As the probe approaches the liquid surface, the deformation profile grows below it, as shown by the profile [——]. The [——] wavenumber distribution indicates the appearance of a second bell-shaped form (right peak), centered at $k^* = 1$, which indicates an input energy injected by the probe approach. The [——] profiles, at the moment of larger deformation, tagged as [•] in Fig.7.1a, show the most intense mutation of shape during the oscillation cycle. This maximum surface profile [——] shows a Bessel function-like shape form, with a wavelength of around $r^* \approx 6$, in which a crest and a trough appear, swinging up and down the time-average profile [——]. The [——] wavenumber distribution indicates that the second bell, still centered at $k^* = 1$ and originally shown in [——], is growing as a consequence of the continuous injection of energy by the probe. When the probe is moving away, the [——] surface profile shows a severe reduction

of the apex deformation, as well as a displacement of liquid volume toward larger values of r^*. The corresponding wavenumber distribution [——] indicates the beginning of the thin-film relaxation phase, since the second bell displaces toward smaller wavenumbers k^*. Finally, as the energy has been dissipated over the entire liquid surface, the surface profile and wavenumber distribution recover their time-average shape [——].

Now, we will describe the UOTF dynamic surface deformation, illustrated in the right column figures. In this case, the curves of the same color, which correspond to the same instants of consecutive cycles, show different shapes. Therefore, the liquid surface does not recover a time-average profile from one cycle o the next one. As well, note that only one retreat profile [——] is shown, because at the retreat of the second oscillation cycle, the magnitude of the surface deformation indicates that the probe and the liquid have made contact. The thin-film has suffered a "jump-to-contact" the probe, which is the characteristic final stage of the UOTF behavior. The first oscillation cycle happens in the same way as the one described for the POTF, thus the second cycle will be described referring to the first one. The [——] profiles, given at the half-period instant and tagged as [•] in Fig.7.1a, do not overlay (see inlet). Similarly, the surface shape in the wavenumber domain mutates from a bell-shaped distribution, centered slightly to the right of $k^* = 10^{-1}$, to another with the same shape and position, but with a slightly larger magnitude, at the second oscillation cycle (the second [——] profile). The difference between the distribution curves [——] is clearly observed in the inlets of Figs.7.1b and 7.1c. As well, the [——] profiles, at the moment of larger deformation, tagged as [•] in Fig.7.1a, show very dissimilar forms for consecutive periods. The maximum surface profile [——], of the second cycle, presents a slight amplification of the peak-to-trough depth and a moderate narrowing of its wavelength, but a Bessel function-like shape shape is still observed around the [——] profile. The [——] wavenumber distribution indicates a small increase of the principal bell-shape (left peak), from one cycle to another. In contrast, the secondary bell-shape (right peak) curve centered at $k^* = 1$, exhibits a important magnitude growth from one cycle to another. Thus, each time the probe gets close to the surface, the amount of energy that it transfers to the liquid increases, for the UOTF case.

From the previous results and the corresponding analysis, we can make some hypotheses. Firstly, the energy transfered to the liquid film increases when the time-average distance D_a^* is reduced. One can deduce that there is a maximum amount of energy that the liquid film can dissipate during an oscillation cycle. If this threshold is overtaken, the liquid film stocks the excess, by increasing its curvature and the volume at the central bump. There is also a threshold value for the apex position and curvature, above which the liquid film can not continue to store the energy. Once, this values are surpassed, the surface oscillation is interrupted and the "jump-to-contact" dynamic phenomenon takes place at the next probe approach.

7.2 Thin-film stability

Now, phase portraits are used to understand the behavior of the thin-films during the entire simulation time. In Fig.7.2, the phase portraits of the apex variables and the probe position D^* are shown. The trajectories were obtained for the parameters given in Table 7.1, and for different values of D_a^*, departing for a initially flat liquid surface. The existence of a strange attractor, acting as a semi-stable limit cycle, is observed. From the behavior corresponding to $D_a^* \geq 2.1331$, one can easily discern a limit cycle. The $\langle \eta_0^* | D^* \rangle$ (apex position/probe position) diagram presents a *Jai alai* globe-shaped limit cycle, whereas the $\langle \kappa_0^* | D^* \rangle$ (peak curvature/ probe position) diagram shows an asymmetric boomerang-shaped limit cycle. The shape of both trajectories clearly indicates an hysteretic behavior, a consequence of the thin-film viscous nature. In the $\langle \eta_0^* | D^* \rangle$ and the $\langle \kappa_0^* | D^* \rangle$ diagrams, the trajectories coming from the bottom collapse into the limit cycle. In the $\langle d\eta_0^*/dt^* | D^* \rangle$ (apex speed/probe position) diagram, the limit cycle presents a twisted shape, for short values of D^*. It exhibits a lobe at the approach phase (positive values of the speed), and a wedge at the retreat phase (negative values). For the apex speed $d\eta_0^*/dt^*$, trajectories moving close to the zero speed line collapse into the limit cycle. When a perturbation, i.e. the injection of energy from the probe approach, takes the apex out of the limit cycle, toward larger values of η_0^*, κ_0^* and $d\eta_0^*/dt^*$, then the trajectory diverges from the limit cycle, triggering the dynamic "jump-to-contact" process and the probe wetting.

In Fig.7.2, one POTF and two UOTF behaviors, corresponding to $D_a^* \geq 2.1331$, $D_a^* \geq 2.1312$ and $D_a^* \geq 2.1268$, respectively, are shown. The three cases start with the same initial conditions, and the only difference is the value of D_a^*. The POTF and the first UOTF ($D_a^* \geq 2.1312$, center column in Fig.7.2)

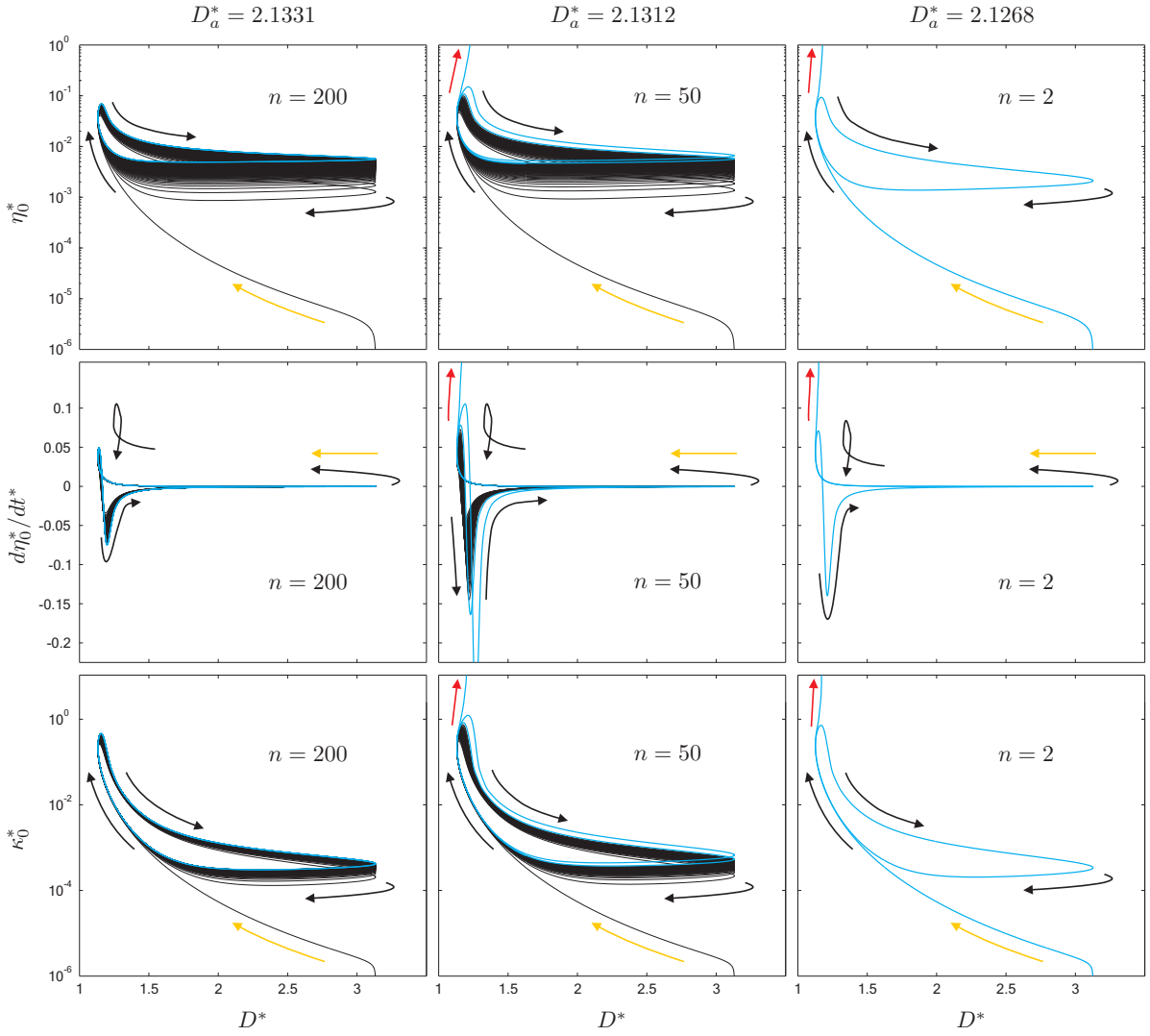


Figure 7.2: Phase diagrams of the oscillating liquid surface for different different time-average distances D_a^*. The phase diagrams represent: (First row) the apex deformation η_0^*, (Second row) the apex speed $d\eta_0^*/dt^*$ and (Third row) the peak curvature κ_0^*, as functions of the instantaneous sphere center position D^*. Each column corresponds to a different value of D_a^* decreasing from left to right. [——] represents the entire trajectory, whereas [——] shows the behavior of the two last calculated cycles. [→] indicates the starting stage, whereas [→] shows the sense of close-loops and [→] the diverging behaviors. Parameters are given in Table 7.1.

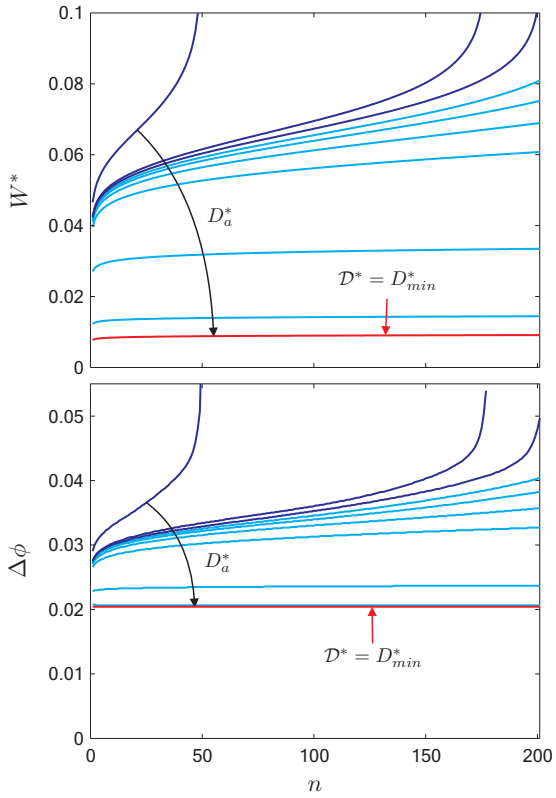


Figure 7.3: Apex (top) oscillation amplitude W^* and (bottom) phase shift $\Delta\phi$ as functions of the number of oscillation cycles n for different time-average distances D_a^*. Remember that $\mathcal{D}^* = D_a^* - \xi^* W_D^*$. [——] $\mathcal{D}^* \ll D_{min}^*$, [——] $\mathcal{D}^* < D_{min}^*$ and [——] $\mathcal{D}^* = D_{min}^*$, where $D_{min}^* = 1.2017$ is the minimum separation distance between a thin-film and a static probe. [➞] indicate the growth of D_a^*. Parameters are given in Table 7.1.

present initial stages that are quite similar, but only the POTF case seems to converge to the limit cycle, for $n = 202$ oscillations. The UOTF shows a chaotic behavior that starts at the early oscillation $n = 49$, diverging from the limit cycle at the next oscillation $n = 50$. As it can be observed in the phase portraits, at the $n = 49$ oscillation, the trajectory of the UOTF deviates from the limit cycle, mostly during the retreat phase, indicating an excessive energy stokage and provoking the divergence at the next oscillation. The remaining UOTF ($D_a^* \geq 2.1268$, right column in Fig.7.2), the injected energy since the first oscillation is too large that the limit cycle can not attract enough the system trajectory, ending with a rapid divergence at the $n = 2$ oscillation. It is confirmed in the phase portraits of Fig.7.2, that the maximum values of the apex deformation, speed and curvature, over a cycle, do not occur at the instant of lowest probe position $D^* = \mathcal{D}^*$. Moreover, one notes, mainly from the UOTF trajectories, that the phase ϕ is not only distance-dependent D_a^*, but it also increases at each oscillation.

Until now, stable and quasi-stable oscillating thin-films (SOTF and QSOTF) had follow the same POTF description, because their qualitative behavior during an oscillation cycle is very similar. However, since the system stability is about to be discussed, SOTF and QSOTF will be treated separately, because the analysis should encompass the long-term behavior.

In Fig.7.3, the apex oscillation amplitude W^* and the phase shift $\Delta\phi$ are reported as functions of the number of oscillation cycles n, for different values of the time-average probe position $D_a^* \in [2.2017, 2.1312]$. The $D_a^* = 2.1268$ case, presented in Fig.7.2, is not shown because the liquid surface oscillates only once before the dynamic "jump-to-contact" occurs. One should have in mind that the product $\xi^* W_D^*$, of the time-average gap and the probe oscillation amplitude, has been kept constant for all the results shown in this chapter.

For a quasi-static phenomenon, in which the liquid reacts instantaneously to follow the probe motion, we should observe a phase $\phi = \pi$. In this situation, when the probe reaches its lowest position, the liquid surface attains, simultaneously, its maximum deformation. Thus, for a quasi-static behavior, the phase shift is $\Delta\phi = 0$. As well, in this behavior limit, the apex oscillation amplitude is given by the difference between the static deformations corresponding to the farthest and the closest probe positions during an oscillation. For the cases studied in this chapter, even though $\mathcal{T}^* = \mathcal{T}/\tau > 1$, we have not found quasi-static responses, i.e. the phase shift is always greater than π, whereas the apex oscillation amplitude is smaller than the quasi-static equivalent.

SOTFs are observed for $\mathcal{D}^* \geq D_{min}^*$, where D_{min}^* is the minimum separation distance between a thin-film and a static probe. This behavior corresponds to the [——] curves in Fig.7.3. In this case, the surface oscillation is perfectly periodic, showing a well defined apex oscillation amplitude W^* and a phase $\Delta\phi \geq 0$, which are dependent on D_a^* but independent of the number of oscillations n.

QSOTF cases, correspond to the [——] curves. For this cases, there is a slight increase of W^* and $\Delta\phi$ at each oscillation cycle n, however their slope remains relatively moderated and, for the last simulated cycle $n = 202$, the liquid has not reached the probe surface. For QSOTF, the apex oscillation amplitude W^* and a phase $\Delta\phi \geq 0$ show a nearly linear behavior with respect to the number of cycles n (except for the first $n < 50$ cycles) with D_a^*-dependent slope and $W^*/\Delta\phi$-intercept.

UOTFs are easily identified as the [——] curves, because both variables W^* and $\Delta\phi$ diverge after a short number of oscillations $n < 202$. Their main feature is that the apex oscillation amplitude is unbounded, increasing at every cycle along with the peak probe/liquid interaction, until the latter becomes out of control. The phase shift follows the same trend. UOTFs are quickly detected for $\mathcal{D}^* \ll D_{min}^*$. For this case, the shape of the W^* and $\Delta\phi$ curves seems to be that of a third degree polynomial, with a steepness that increases as the distance D_a^* lessens.

A priori, when the apex oscillation amplitude attains a magnitude greater or equal to the lower probe position, $W^* \geq \mathcal{D}^* - 1$, only UOTF are observed. Nevertheless, as it is confirmed in Fig.7.3, for smaller values of W^*, the UOTF behavior is recognized. Therefore, for given oscillation amplitude $\xi^* W_D^*$ and sample thickness E^*, a threshold value of the lower probe position $\mathcal{D}_{min}^*$ should exist. Also, around this threshold value, the QSOTF behavior should occur within a transition range. Further analysis must be done in order to determine this transition regime.

7.3 Concluding remarks

The dynamic model, presented in Chapter 5, was used to simulate the evolution of a thin-film interacting with an oscillating probe. Preliminary results were presented, and the existence of stable, quasi-stable and unstable behaviors has been discussed. The impact of the time-average probe position D_a^*, on

the system behavior, has been qualitatively described. The apex oscillation amplitude W^* and phase shift $\Delta\phi$ have been proposed as representatives of the thin-film response. We have discerned that two variables that are directly related to the stability of the thin-film. The effect of D_a^* on W^* and $\Delta\phi$ has been portrayed. A parametric study of the other oscillation quantities, W_D^* and C_a, is currently in progress.

It has been revealed that, even for distances $D_a^* - \xi^* W_D^* < D_{min}^*$, distances at which a static probe approach is impossible, the probe/liquid dynamic interaction can be studied, at least for a certain number of oscillation cycles before the "jump-to-contact" and the probe wetting happen. This quasi-stable oscillation behavior is determined by the film thickness E^* and the oscillation parameters D_a^*, W_D^* and C_a, for a given combination of dimensionless parameters H_a, A and B_o. Further analysis is required in order to understand the mechanisms that provoke the existence of this quasi-stable regimes, as well as their lifespan. Experiments performed within these quasi-stable regimes present several advantages. For instance, they may reduce the probe/sample distance, increasing the probe sensitivity. Nevertheless, to avoid the probe/sample spoiling, the number of oscillation cycles before wetting should be known a priori.

In conclusion, a methodology has been established, leading to the acquirement of worthy information and understanding of the probe/film coupling. Notwithstanding, the dynamic thin-film response should be studied in depth, in order to yield analytical expression for the critical oscillation conditions. The subsequent analysis will provide the experimental parameters (setpoint, oscillation amplitude and frequency) to perform adequate AFM measurements over liquid samples.

Part III

AFM Experiments (on the surface of liquid samples)

Chapter 8

AFM force and amplitude spectroscopy experiments

In order to validate our models, AFM spectroscopy experiments have been conducted to characterize the strength of the interaction between the AFM probe and a liquid sample.

Two different methodologies were implemented. Force spectroscopy experiments, in contact AFM mode, were performed and confronted against our static deformation model. Amplitude spectroscopy tests, in non-contact AFM mode, were executed, yet its confrontation with our dynamic deformation model is currently in progress. A description of both AFM techniques will be given in the following, as well as in-depth portrayals of the calibration procedures and the performed experiments.

8.1 AFM overview

The Atomic Force Microscope (AFM) is based on the force interaction between a sample and a local probe. This probe consists of a cantilever, clamped to a piezoelectric actuator, as it is depicted in Fig.8.1. An AC voltage, a driving signal, provokes the periodic elongation of the actuator, and the consequent vibration of the cantilever. At the cantilever free end, a pyramidal tip is appended to the front-side. The sharp lower extreme of this tip is the element that directly senses the proximity to the sample, via the interaction forces. The sample is held by a magnetic core sample plate, which remains in a fixed position. As well, a laser beam is sent over the back-side of the cantilever, which reflection is captured by a four quadrant photodiode (optical lever technique). In turn, the piezoelectric actuator is attached to the scanner of the microscope, which is composed by an array of piezoelectric plates and a piezoelectric tube. A constant high voltage applied to the scanner plates provokes its elongation, allowing the lateral displacement of the probe, whereas the vertical displacement comes from the elongation of the scanner tube. This brief description corresponds to the actual framework of the Agilent Technologies®5500 Scanning Probe Microscope employed in this study. Among commercial apparatus, either similar variations or different microscope configurations can be found.

The AFM contact mode consists in using the probe as a stylus profiler, a permanent tip/sample contact provokes a soft touch (short range repulsive forces) and a consequent slight deflection of the cantilever. Then, a lateral scanning of the sample surface is performed. Changes in the deflection of the probe are used as a direct measurement of the local height of the sample. The cantilever deflection generates a voltage difference between the upper and the lower quadrants of the photodiode, whereas its torsion leads to a difference between lateral quadrants. In addition, the reconstruction of the sample topography can be executed by holding a constant value of either the cantilever deflection (Constant Force) or the probe/sample distance (Constant Height). The reconstruction of the sample topography is accomplished either by considering the vertical displacement of the probe or by deducting the local height from the cantilever deflection.

The AFM non-contact is based on the probe oscillation, generated by the vibration of the piezoelectric actuator at a frequency near the cantilever natural frequency. As the probe approaches the sample, the tip/sample interaction (long range attractive forces) engenders a modification of the cantilever oscillation amplitude and frequency, which are strongly dependent on the tip/sample separation distance. Therefore, when a lateral scanning of the sample is performed, a vertical displacement of the probe is carried out in

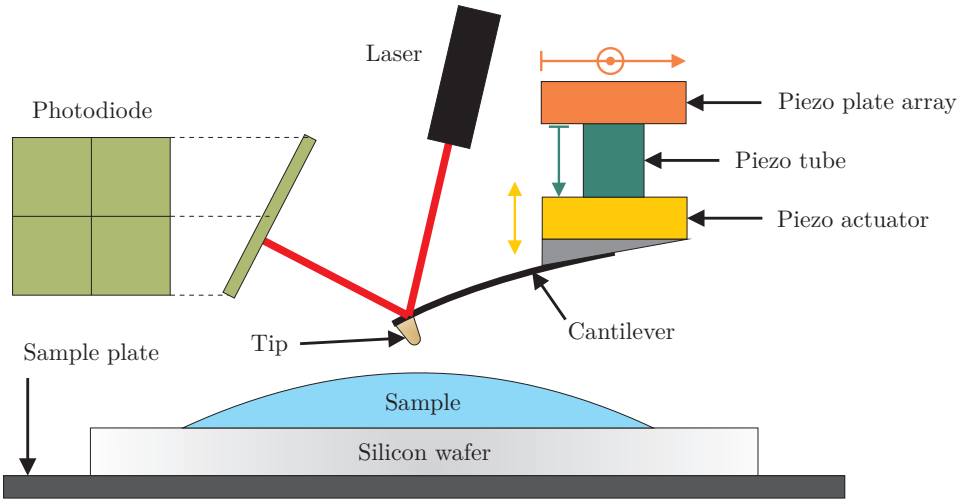


Figure 8.1: AFM scheme.

order to keep a constant value of either the oscillation amplitude (Amplitude Modulation - AM) or the frequency (Frequency Modulation - FM). This vertical displacement is an indirect measurement of the local height of the sample. As well, the cantilever vibration generates an oscillating voltage difference between the upper and the lower quadrants of the photodiode, from which the amplitude and phase are recovered. The reconstruction of the sample topography is accomplished either by considering the vertical displacement of the probe or by deducting the tip/sample distance from the cantilever oscillation amplitude and phase. Further details on the general functioning of both AFM modes can be found elsewhere(Binnig and Quate, 1986; Butt et al., 2005; Bhushan, 2004; Sharpe, 2008).

Herein, we were interested in performing spectroscopy tests. This kind of analysis allows the extraction of noteworthy data from ordinary AFM procedures. Nevertheless, an exhaustive inquiry of these data leads to the comprehension of the basic principles of the probe/sample interaction. Force spectroscopy consists in measuring the interaction force (voltage sensed by the photodiode) between the probe and the sample as a function of the probe displacement (voltage applied to the piezoelectric tube). Amplitude spectroscopy consists in recording the cantilever oscillation amplitude (amplitude of the voltage signal sensed by the photodiode) as a function of the probe displacement toward the sample (voltage applied to the piezoelectric tube). Despite the wide study of spectroscopy experiments over rigid samples, that one can find in the literature, there is a lack of information about the equivalent tests applied to largely deformable bodies, say liquids samples.

8.2 AFM calibration

In this study, several calibration factors must be found. Their knowledge is essential in order to transform the voltages measured by the detectors into the corresponding physical dimensions. This group comprises:

- The scanner piezoelectric tube calibration factor K_{tube}, which relates the applied high voltage and the axial elongation of the piezoelectric tube.
- The photodiode deflection calibration factor K_{def}, which relates the cantilever deflection to the voltage difference detected by the photodiode, for contact mode AFM.
- The photodiode amplitude calibration factor K_{amp}, which relates the cantilever oscillation amplitude to the amplitude of the oscillating voltage detected by the photodiode, for non-contact mode AFM.

In addition, other parameters are required to transform quantities or characterize one element and its interaction with the entire system. These experimental parameters are:

- The equivalent spring constant k_c of the cantilever, which is necessary to turn the measured cantilever deflection into a force.

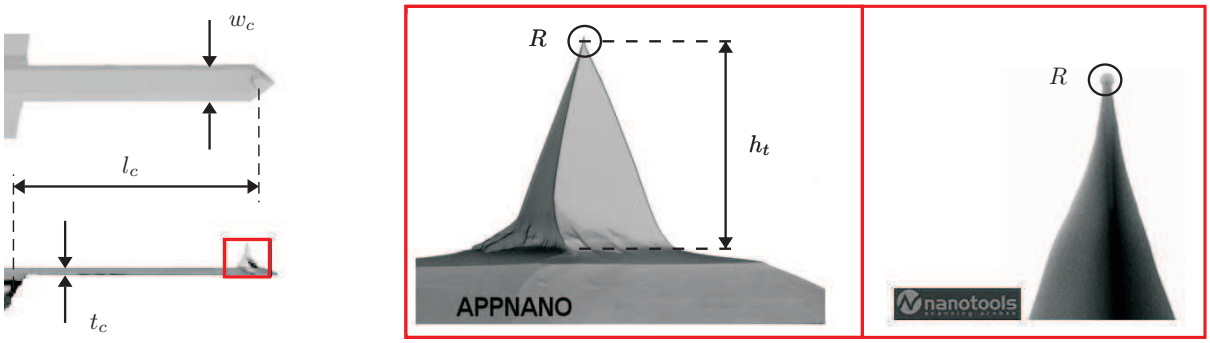


Figure 8.2: AFM probe geometry, of an Appnano ACT probe.

- The cantilever natural frequency $\omega_{c,0}$, which determines the behavior of the oscillating cantilever for given driving conditions of the piezoelectric actuator.
- The quality factor Q_c, which is representative of the energy dissipation mechanisms present in the cantilever and the surrounding media.

The calibration of the piezoelectric tube is performed regularly, to take into account the piezoelectric hysteresis effects, but it is not required every time that measurements are performed with the apparatus. On the other hand, the calibration of the other components should be performed each time a probe is mounted in the microscope, and before spectroscopy tests are performed over liquid samples. The suggested calibration procedure is the following:

1. Determination of the resonance frequency $\omega_{c,0}$ and quality factor Q_c.
2. Identification of the cantilever stiffness k_c.
3. Perform the specific photodiode calibration:
   - Deduction of the photodiode deflection factor K_{def} in force spectroscopy.
   - Ascertainment of the photodiode oscillation amplitude factor K_{amp} in amplitude spectroscopy.

In this section, a methodology is detailed for each calibration factor and experimental parameter. Examples considering a Nanotool®model B1-HDC probe, which is made up of a single-crystal silicon cantilever and a high density carbon spherical tip, and two Appnano®model ACT probes, which are made up of a single-crystal silicon cantilever and a silicon pyramidal tip, are described in order to explain the experimental procedure. The probe geometry is detailed in Fig.8.2, and the dimensions and properties of the tested probes is summarized in Table 8.1. The principal aim of this study is to set up an experimental procedure.

8.2.a Scanner - Piezoelectric tube

The vertical fine displacement Δz of the AFM probe is possible thanks to the employment of a piezoelectric tube. When a voltage difference ΔV is applied to this element, it experiences a mechanical stress (piezoelectric effect), which entails a size change in the axial direction, the vertical direction due to the physical setup of the apparatus. As a consequence, the probe, which is mechanically coupled to the tube, moves in the desired direction. A proper link between the applied voltage and the vertical displacement is required. The typical procedure consists in scanning a calibration grid in the AFM contact mode, as it is represented in Fig.8.3. The calibration grid presents a step-like topography, with a well-known step height. Then, the determination of the voltage difference, applied to the piezoelectric, needed to overcome the step is directly correlated to the physical size. The piezoelectric tube calibration was performed using a NT-MDT®silicon test grating TGX1, which presents a chessboard-like structure with a 0.6 μm step height. For the Agilent Technologies®5500 Scanning Probe Microscope (SPM) employed, the calibration procedure yielded a factor of $K_{tube} = 2.3 \times 10^{-8}$ m/V.

Cantilever dimensions		B1-HDC	ACT-01	ACT-02
Length, l_c	[μm]	450	125	
Width, w_c	[μm]	50	35	
Thickness, t_c	[μm]	2	4.5	
Tip dimensions		**B1-HDC**	**ACT-01**	**ACT-02**
Height, h_t	[μm]	-	14	
Radius, R	[nm]	20.36	6.78	36.78
Nominal radius	[nm]	20.00	<10.00	
Physical properties		**B1-HDC**	**ACT-01**	**ACT-02**
Natural frequency, $f_{c,0}$	[kHz]	15.06	270.25	354.91
Nominal frequency	[kHz]	13.00	200.00-400.00	
Natural angular frequency, $\omega_{c,0}$	$\times 10^4$[s^{-1}]	9.46	169.80	223.00
Stiffness, k_c	[N/m]	0.20	36.85	51.03
Nominal stiffness	[N/m]	0.20	25.00-75.00	
Q-factor, Q_c	[1]	130.50	1074.88	1084.70
Transitory settling time, τ_c	10^{-4}[s]	27.59	12.66	9.74
Damping ratio, β	$\times 10^2$[s^{-1}]	3.63	7.90	10.28
Viscous damping coefficient, ν	$\times 10^{-8}$[kg/s]	1.63	2.02	2.11
Equivalent mass, m_c	$\times 10^{-11}$[kg]	2.23	1.28	1.02
Calibration factors		**B1-HDC**	**ACT-01**	**ACT-02**
Deflection factor, K_{def}	[nm/V]	81.7	1.22	1.84
Amplitude factor, K_{amp}	[nm/V]	16.17	10.28	7.91
Oscillation parameters		**B1-HDC**	**ACT-01**	**ACT-02**
Free resonance amplitude, $W_{c,0}$	[nm]	30.25	49.65	17.42
Driving amplitude, W_D	[nm]	0.23	0.05	0.02
Driving force, F_D	$\times 10^{-11}$[N]	4.64	170.21	81.95
Driving frequency, ω_D	$\times 10^4$[s^{-1}]	9.53	169.87	223.06
Reynolds number, Re_c	[1]	3.93	34.31	45.06

Table 8.1: Cantilever geometry, physical properties of the probe, calibration factors and oscillation parameters of 1) a Nanotools B1-HDC probe and 2) two different Appnano ACT probes, tested in air with $\rho_{air} = 12.05 \times 10^{-1}$ kg/m^3 and $\mu_{air} = 18.27 \times 10^{-6}$ Pa$\cdot$s, and at a room temperature of $\Omega = 293.15$ K.

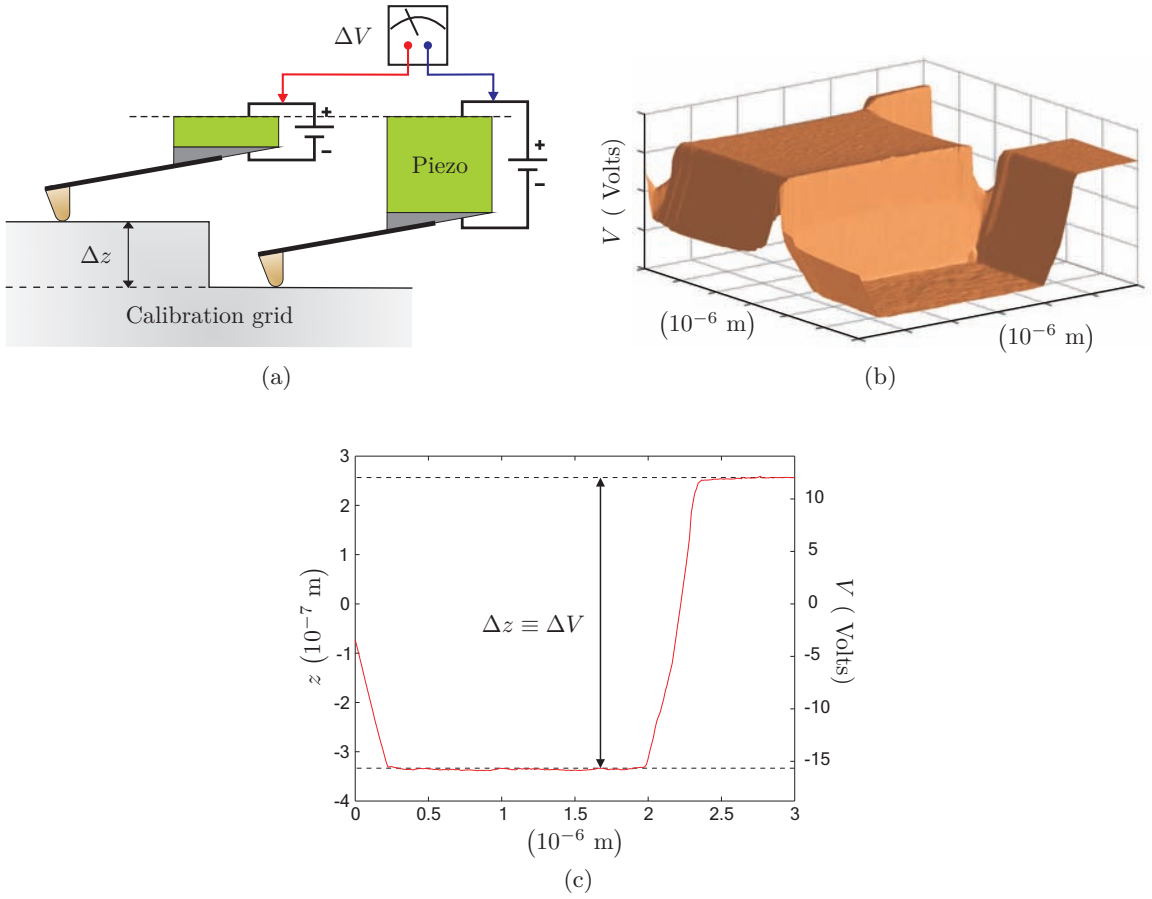


Figure 8.3: AFM piezoelectric tube (5500 SPM) calibration: (a) scheme describing the calibration procedure, (b) scanned topography in Volts, of the calibration grid TGX1, as function of the spatial position, and (c) transversal section of the calibration grid showing the voltage/vertical distance relation.

8.2.b Cantilever properties

The probe characterization is an unavoidable stage of the AFM usage. It is required to turn the acquired data into concrete results and to give them a physical meaning.

Depending on the physical properties of the sample and the wished type of analysis, a probe with the most suitable characteristics should be selected. Cantilevers with a very low spring constant k_c are crucial for a high vertical resolution (increased force sensitivity) in contact mode AFM. Nevertheless, instabilities are commonly observed when employing soft cantilevers, provoking an untimely contact between the probe and the sample. In the case of liquid samples, this early contact gives rise to the wetting of the probe and the formation of a capillary bridge, which is generally unwanted. A high resonance frequency is desired in order to reduce the effects of external vibrations in non-contact mode AFM. For liquid samples, a high resonance frequency reduces the magnitude of the liquid surface deformation, because the probe moves too fast for the fluid to react. A high Q-factor is important to reduce ambient noise, nevertheless a low Q-factor reduces the probe transitory settling time $\tau_c \approx 2Q_c/\omega_{c,0}$, in non-contact AFM.

One should consider that these cantilever properties are usually coupled. The main purpose is to maximize the benefits of all these parameters, and determine their optimal combination. Nevertheless, the probe selection is restrained by the commercial spectrum. In this study, a simple cantilever characterization was performed in order to understand the probe behavior when scanning over liquid samples.

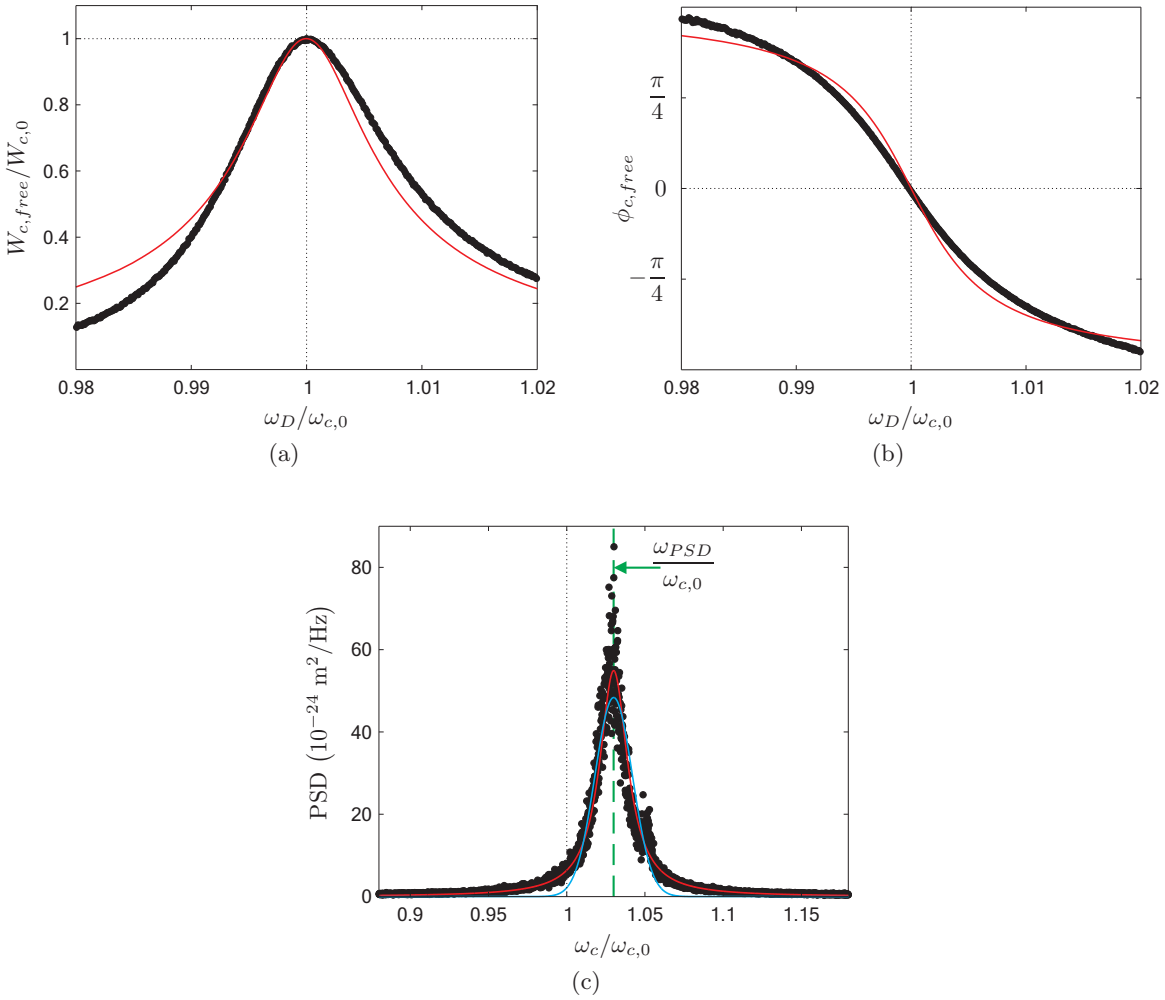


Figure 8.4: AFM probe calibration curves: (a) oscillation amplitude and (b) phase shift as functions of the reduced driving frequency, with [——] the fits given by eqs.(8.7a) and (8.7b). (c) power spectral distribution as function of the reduced cantilever frequency, compared to [——] Gaussian and [——] Lorentzian fits given by by eqs.(8.16) and (8.18), respectively. The presented experimental curves correspond to a Nanotools B1-HDC probe.

Resonance frequency

The eigenfrequency of an I-beam cantilever(Sharpe, 2008) in vacuum $\omega_{vac,0}$ can be estimated with:

$$\omega_{vac,0} \simeq 1.015 \frac{t_c}{(l_c)^2} \sqrt{\frac{E_c}{\rho_c}}, \tag{8.1}$$

where E_c is the Young's modulus and ρ_c is the density of the cantilever material, l_c is the cantilever length and t_c is the thickness. When the cantilever is immersed in a viscous media, the appropriate Reynolds number is defined as(Sader, 1998):

$$Re_c = \frac{\rho_{media} \omega_{c,0} (w_c)^2}{4\mu_{media}}, \tag{8.2}$$

where w_c is the cantilever width, and ρ_{media} and μ_{media} are the density and viscosity of the surrounding media. The cantilever natural frequency $\omega_{c,0}$, for $Re_c \to \infty$, is:

$$\omega_{c,0} = \omega_{vac,0}\left[1 + \frac{1}{2}\left(\frac{\nu}{m_c\omega_{vac,0}}\right)^2\right]^{-1/2}, \tag{8.3}$$

where ν is the viscous damping coefficient of the surrounding media and m_c is the cantilever equivalent mass, which is approximately $m_c \approx \rho_c l_c w_c t_c$. For intermediate values of Re_c, depending on the geometry of the cantilever, a correction factor should be added(Sader, 1998). In addition, the quality factor Q_c, which describes the coupling between the cantilever and the media, gives the ratio between the input and the output energy of the system. It is given by:

$$Q_c = \frac{m_c\omega_{c,0}}{\nu}. \tag{8.4}$$

Therefore, the ratio of natural frequencies is:

$$\frac{\omega_{c,0}}{\omega_{vac,0}} = \left[1 - \frac{1}{2}\left(Q_c\right)^{-2}\right]^{-1/2}. \tag{8.5}$$

Considering the B1-HDC probe geometry, with $l_c = 4.5 \times 10^{-4}$ m, $w_c = 5.0 \times 10^{-5}$ m and $t_c = 2.0 \times 10^{-6}$ m, a Young's modulus in the range $E_c = 130 - 185$ GPa for single-crystal silicon and a room temperature density of around $\rho_c = 2.33 \times 10^3$ kg/m^3, the natural frequency of the cantilever in vacuum may be in the range $\omega_{vac,0} \in [7.49, 8.91] \times 10^4$ s^{-1}, whereas, considering that in air $Q_c \in \left[10^1, 10^4\right]$ and $Re \in \left[10^0, 10^1\right]$, the range $\omega_{c,0}/\omega_{vac,0} \in [0.99, 1.00]$ is typically encountered in practice(Sader, 1998). As well, it has been observed a reduction of the Q-factor up to 1/2, when the surrounding media (air) is confinement between the probe and the sample(Leveque et al., 1997), which can reduce the ratio $\omega_{c,0}/\omega_{vac,0} \sim 0.95$.

When an oscillating force of constant amplitude is applied to the probe, the cantilever response strongly depends on the driving frequency. Enregistration of the probe resulting vibration leads to the construction of resonance curves, which show the cantilever oscillating amplitude and phase as functions of the driving frequency. The software employed to manipulate the microscope allows the acquisition of these curves. The resonance peak and phase curves of a tested AFM probe, Nanotools®model B1-HDC (single-crystal silicon cantilever and high density carbon spherical tip), are presented in Figs.8.4a and 8.4b, respectively.

In stationary regime, the position of a driven damped harmonic oscillator is given by:

$$x\left(t\right) = W_{c,free}\cos\left(\omega_D t + \phi_{c,free}\right), \tag{8.6}$$

where the oscillation amplitude $W_{c,free}$ and phase $\phi_{c,free}$ follow the relationships:

$$W_{c,free} = \frac{W_{c,0}}{\sqrt{\left(Q_c\right)^2\left(1 - u_D^2\right)^2 + u_D^2}} \tag{8.7a}$$

$$\phi_{c,free} = \arctan\left\{\frac{u_D}{Q_c\left(u_D^2 - 1\right)}\right\}, \tag{8.7b}$$

where $u_D = \omega_D/\omega_{c,0}$ is the reduced driving frequency, ω_D is the driving frequency, $\omega_{c,0}$ is the oscillator natural frequency, Q_c is the quality factor of the system and $W_{c,0}$ is the oscillation amplitude at the resonant frequency $u_D = 1$. For a driven damped harmonic oscillator, the resonance oscillation amplitude is given by:

$$W_{c,0} = W_D Q_c, \tag{8.8}$$

where W_D is the driving amplitude. Further details on the analysis that leads to this expression are given elsewhere (Bhushan, 2004; Sharpe, 2008).

Fitting a resonance curve with eq.(8.7a) leads to the determination of $\omega_{c,0}$ and Q_c. The application of this procedure to the experimental data in Fig.8.4a gives a resonance frequency of $\omega_{c,0} = 9.46 \times 10^4$ s^{-1}, a quality factor of $Q_c = 130.50$ and a transitory settling time $\tau_c \approx 2Q_c/\omega_{c,0} = 2.75 \times 10^{-3}$ s.

Herein, the experimental eigenfrequency is the precise value, which is close to the nominal value

provided by the manufacturer $\omega_{c,0} \approx 8.17 \times 10^4$ s^{-1}.

Stiffness

From linear theory of elasticity, the spring constant of an I-beam cantilever(Sharpe, 2008) is given by:

$$k_c = \frac{3E_c I_c}{(l_c)^3} \qquad \text{with} \qquad I_c = \frac{w_c (t_c)^3}{12}, \tag{8.9}$$

where E_c is the Young's modulus and I_c is the area moment of inertia of the cantilever cross section, whereas l_c, w_c and t_c are the length, width and thickness of the cantilever, respectively. Considering the B1-HDC probe geometry, with $l_c = 4.5 \times 10^{-4}$ m, $w_c = 5.0 \times 10^{-5}$ m and $t_c = 2.0 \times 10^{-6}$ m, and the Young's modulus range $E_c \in [130, 185]$ GPa for single-crystal silicon, the stiffness of the probe may be in the range $k_c \in [0.14, 0.2]$ N/m.

With an accuracy of 15−40%, the cantilever stiffness can be estimated from the deflection fluctuations, which result from the excitation due to random thermal forces. The vibration of an harmonic oscillator, which energy is associated with the cantilever natural frequency, is characterized by the Hamiltonian (Hutter and J., 1993; Capella and Dietler, 1999):

$$H = \frac{p^2}{2m_c} + \frac{1}{2} m_c (\omega_{c,0})^2 \delta^2, \tag{8.10}$$

where δ and p are the deflection and the momentum of the cantilever. The total energy of the system, H, is decomposed into a kinetic energy and a potential energy components and, as a consequence of the equipartition theorem, the average value of each one is equal to half the thermal energy. Hence:

$$\frac{1}{2} k_B \Omega = \left\langle \frac{1}{2} m_c (\omega_{c,0})^2 \delta^2 \right\rangle \tag{8.11}$$

where $k_B \approx 1.38 \times 10^{-23}$ J/K is the Boltzmann constant and Ω is the room temperature. Recalling that $(\omega_{c,0})^2 = k_c/m_c$, the equivalent spring constant calculated as:

$$k_c = \frac{k_B \Omega}{\langle \delta^2 \rangle}, \tag{8.12}$$

Nevertheless, when the cantilever deflection is measured with the optical lever technique (laser reflection), this relation becomes (Butt and M., 1995):

$$k_c = \frac{4 k_B \Omega}{3 \langle \delta^2 \rangle}. \tag{8.13}$$

Without the application of a driving force, the motion of the cantilever due to the thermal induced vibration is recorded. After the removal of ambient noise, the Power Spectral Density (PSD) is recovered as a function of the thermal induced cantilever frequency ω_c. The PSD of an harmonic oscillator is given by;

$$PSD(u_c) = \frac{1}{\omega_{c,0}} \left| \frac{d}{du_c} [W_{c,free}]^2 \right|, \tag{8.14}$$

where $u_c = \omega_c/\omega_{c,0}$ is the reduced cantilever frequency and $i = \sqrt{-1}$ is the imaginary unit. Once more, $W_{c,free}$ and $\phi_{c,free}$ are given by eqs.(8.7a) and (8.7b). The only difference is that, in the case of thermal vibrations, the resonance oscillation amplitude $W_{c,0}$ corresponds to the thermal random excitation amplitude, which is in the order of:

$$W_{c,0} \sim \sqrt{\frac{k_B \Omega Q_c}{2\pi m_c (\omega_{c,0})^2}}. \tag{8.15}$$

The PSD curve, which represents the manifold of states for a given total system energy, is easily acquired with a custom function of the microscope software. For soft cantilever, a peak is observed near its natural frequency, at the frequency ω_{PSD}, and the area under the curve represents the average deflection due to

thermal fluctuations $\langle \delta^2 \rangle$.

In order to simplify this procedure, the PSD is fitted with a Gaussian curve:

$$f(u_c) = G_a \exp\left[-\frac{(u_c - u_{PSD})^2}{2G_b^2}\right], \tag{8.16}$$

where $u_c = \omega_c/\omega_{c,0}$ is the reduced cantilever frequency, $u_{PSD} = \omega_{PSD}/\omega_{c,0}$ the reduced PSD peak frequency, and G_a and G_b are fitting parameters. Using the Gaussian integral, the average deflection is approximated with:

$$\langle \delta^2 \rangle \approx \omega_{c,0} \int_{-\infty}^{\infty} f(u_c)\, du_c = \omega_{c,0} G_a G_b \sqrt{2\pi}, \tag{8.17}$$

and the cantilever stiffness can be determined with eq.(8.13). The PSD can also be fitted with a Lorentzian function (distribution):

$$f(u_c) = \frac{L_a}{(u_c - u_{PSD})^2 + L_b^2}, \tag{8.18}$$

where u_c and u_{PSD} are defined as for the Gaussian function, and L_a and L_b are fitting parameters. The integral of the Lorentzian function, a cumulative distribution function described by an arctangent function, is easily evaluated, and the average deflection can be also approximated with:

$$\langle \delta^2 \rangle \approx \omega_{c,0} \int_{-\infty}^{\infty} f(u_c)\, du_c = \omega_{c,0} \frac{L_a}{L_b} \pi. \tag{8.19}$$

Both approaches give very similar results for the cantilever stiffness.

Applying the Gaussian fit to the data in Fig.8.4c, with a room temperature of $\Omega = 293.15$ K and a PSD peak at $\omega_{PSD} = 9.58 \times 10^4$ s^{-1}, an equivalent spring constant of $k_c = 0.26$ N/m is obtained, whereas the Lorentzian fit yields $k_c = 0.20$ N/m. Herein, the value obtained with the Lorentzian fit is retained, because it describes with a higher precision the experimental data. In addition, this value matches exactly the nominal value provided by the manufacturer $k_c \approx 0.2$ N/m.

With the knowledge of the resonance frequency $\omega_{c,0}$, the quality factor Q_c and the stiffness k_c, several physical properties of the probe are obtained. For example, the environment damping ratio and the equivalent viscous damping coefficient are given by $\beta = \omega_{c,0}/2Q_c$ and $\nu = 2m_c\beta$, respectively, whereas the cantilever equivalent mass by $m_c = k_c/(\omega_{c,0})^2$. For the B1-HDC probe tested in air, $\beta = 3.63 \times 10^2 \text{s}^{-1}$, $m_c = 2.23 \times 10^{-11}$ kg and $\nu = 1.62 \times 10^{-8}$ kg/s are found. The values obtained for the tested probes are given in Table 8.1.

It is important to keep in mind that this method is effective for soft cantilevers, which show large thermal induced amplitudes, within a controlled environment in which the small frequencies of ambient vibrations are easily filtered. This method is restricted by the deflection sensitivity of the photodiode, resulting in a less accurate estimate for stiffer probes. Nevertheless, the methodology was applied to the higher PSD peak registered in the range of thermal fluctuations $\omega_c \in \left[0, 6.3 \times 10^5\right]$ s^{-1} allowed by the 5500 AFM, which is probably a subharmonic vibration mode for stiff cantilevers.

8.2.c Photodiode

The photodiode calibration procedure should be performed each time a new probe is mounted. It depends on the geometry of the laser reflection setup(optical lever), which is strongly dependent of the probe dimensions and its relative positioning with respect to the photodiode.

Deflection

When a probe approaches and touches a rigid substrate, a deflection of the cantilever is provoked. The data recorded by the AFM is a voltage difference sensed between the two upper and the two lower quadrants of the photodiode, as it is illustrated in Fig.8.5a. In order to relate this voltage to the actual cantilever deflection, a force spectroscopy test is conducted on a rigid substrate, in this case a silicon wafer. From this test, a deflection calibration factor K_{def} is produced. An example of deflection spectroscopy is shown in Fig.8.5b, which consists in the acquisition of the photodiode voltage curve when the probe

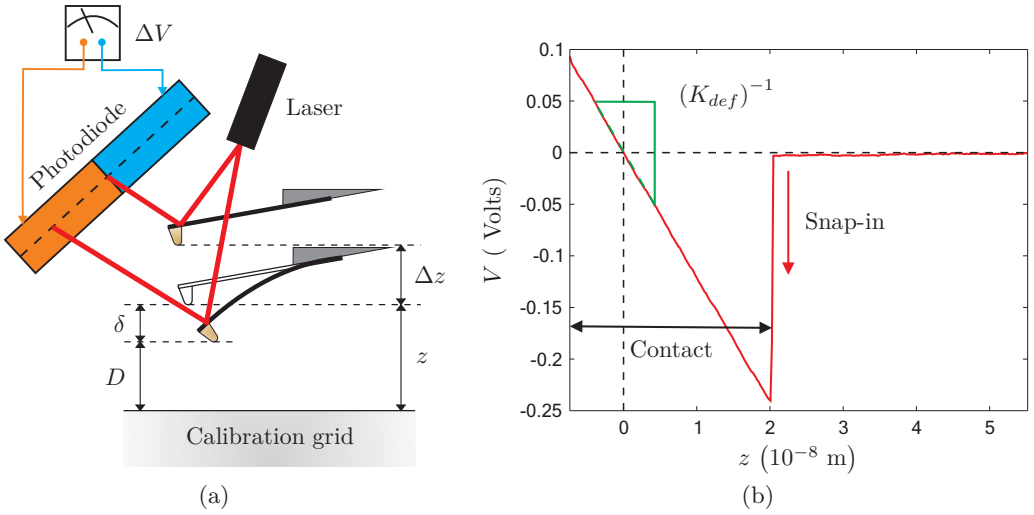


Figure 8.5: Contact mode AFM (a) deflection scheme and (b) typical calibration curve illustrating the photodiode measured voltage during the probe approach toward a rigid substrate, a silicon wafer, from which the photodiode calibration factor is obtained.

is displaced toward the substrate. The probe departs from a large separation distance z from the silicon wafer, recording an almost negligible voltage is. As the probe approaches the substrate, a small downward deflection δ with a weak increasing magnitude occurs, due to the attractive probe/substrate interaction force. At this point, the separation distance between the tip surface and the substrate is $D = z - \delta$. Nevertheless, at a certain distance, the cantilever becomes susceptible to a behavior deviation. A slight perturbation, either thermal fluctuations or ambient noise, triggers the so-called "snap-in" phenomenon, in which the cantilever leaps from a non-contact deflection to a probe/sample adhesion state, detecting the maximum approach deflection and force. The microscope continues to bring the probe closer to the substrate, gradually decreasing the deflection, until the probe reaches a key position, in which a zero force is registered. This state is usually taken as the $z = 0$ position because the probe stays in contact with the substrate, whereas the cantilever is undeformed. As the probe approach keeps on, the deflection of the cantilever is reversed to the upward direction, sensing a repulsive probe/substrate interaction force.

The $z = 0$ position marks the transition from the attractive to the repulsive force regime. Around this value, where small deflections of the cantilever are originated and the linear elastic regime prevails, the cantilever deflection is equivalent to the probe displacement. Therefore, the slope of this region in the voltage curve corresponds to the inverse of K_{def}, relating the recorded voltage with the cantilever deflection. For the data shown in Fig.8.5b, a deflection coefficient $K_{def} = 8.17 \times 10^{-8}$ m/V is found.

With the knowledge of this coefficient, reliable force/distance curves are retrieved. Using the piezoelectric tube calibration factor K_{tube}, the microscope enregisters the vertical displacement of the probe. As well, the cantilever deflection is recorded as a voltage, which is lately turned into the authentic deflection δ with the employment of K_{def}, and then into the interaction force $F_{int} = -k_c\delta$ with the use of the cantilever stiffness.

A typical force/displacement curve is obtained when performing an approach and a subsequent retreat of the probe from the sample. The corresponding force/distance curve is reconstructed by using $D = z - F_{int}/k_c$, to adapt the horizontal axis. Examples are shown in Fig.8.6. The probe approaches the substrate, detecting a small attractive force, the same behavior as described for the deflection in Fig.8.5b. The "snap-in" phenomenon, which is the sudden large deflection that brings the tip and the sample surface together, is observed. Contact is made and the deflection of the cantilever toward the substrate is preserved due to the attractive interaction force. Nevertheless, the magnitude of the force decreases, almost linearly proportional to z, as the probe gets closer to the substrate. At $z = 0$, where the force is zero, the substrate position is revealed. Afterwards, when $z < 0$ the probe experiences a repulsive force, which induces an upward deflection of the cantilever. The probe displacement stops and its withdrawal begins. As the probe displacement increases, the force comes back to the attractive regime, growing nearly proportional in magnitude with z, though the tip remains stuck to the substrate due to the capillary adhesion. At a certain distance near $z = 170$ nm, the detachment of the tip from the

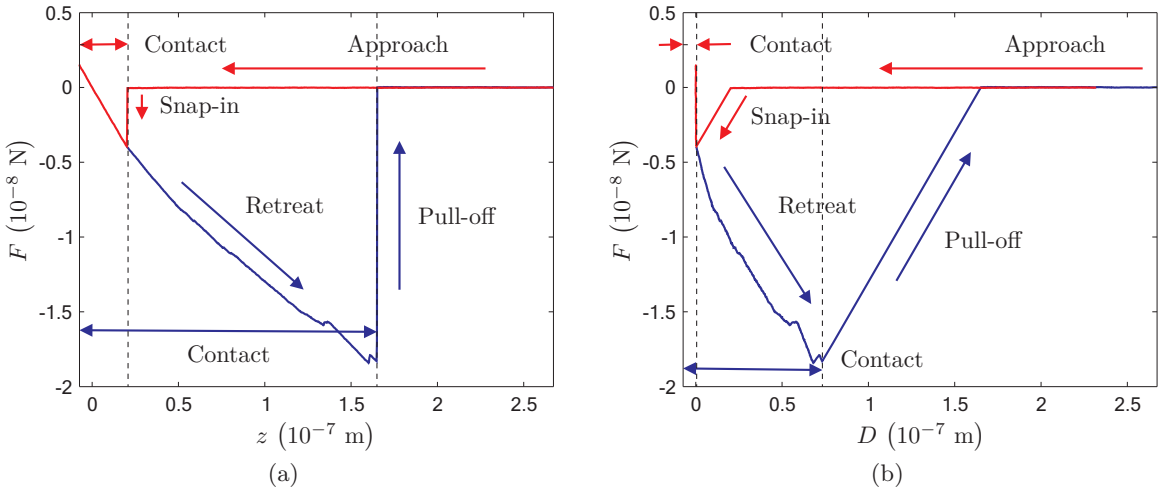


Figure 8.6: Contact mode AFM typical experimental force (—) approach and (—) retreat curves as functions of (a) the vertical displacement and (b) the surface separation distance, over a rigid substrate, a silicon wafer.

sample surface occurs. This "pull-off" phenomenon happens because the probe/substrate contact state becomes unstable for large values of z, and the cantilever comes back to its almost undeformed state. As the probe moves away, no force is sensed by the probe because the distance is enough to annihilate the probe/substrate interaction.

Nominal tests were performed for a cantilever vertical displacement of 2 μm and a duration of 400 s, using 2×10^5 data points. Taking into account that:

$$\text{Speed} = \frac{2 \times \text{Vertical displacement}}{\text{Duration}} \tag{8.20}$$

$$\text{Sample rate} = \frac{\text{Data points}}{2 \times \text{Vertical displacement}} \tag{8.21}$$

$$\text{Exposition time} = \frac{\text{Duration}}{\text{Data points}}, \tag{8.22}$$

Hence, force/distance curves were acquired with a cantilever vertical speed of 10 nm/s, a sample rate of 50 data points/nm and an exposition time of 2 ms/data point. Note that this exposition time is always longer than the transitory settling time of the tested probes, as it can be verified in Table 8.1.

Oscillation amplitude

When an oscillating probe approaches a rigid substrate, an alteration of the oscillation amplitude and phase are provoked. The data recorded by the AFM is an oscillating signal, coming from the instantaneous voltage difference between the two upper and the two lower quadrants of the photodiode. The amplitude of this periodic signal is recorded as a voltage, and it is presented as a function of the displacement of the probe average position, as it is illustrated in Fig.8.7a. In order to relate this voltage to the actual cantilever oscillation, an amplitude spectroscopy test is performed on a silicon wafer, from which an amplitude calibration factor K_{amp} is recovered. This kind of experiments was performed using a driving frequency ω_D with a slightly greater value than the cantilever resonance frequency $\omega_{c,0}$, in order to rest in the non-contact AFM regime (Aimé et al., 1999a; García and San Paulo, 1999), and a constant driving amplitude W_D. An example of amplitude spectroscopy is shown in Fig.8.7b, which corresponds to the amplitude of the photodiode periodic voltage signal when the oscillating probe is displaced toward the substrate.

At a large mean probe position D_a from the silicon wafer, the probe oscillates freely and the amplitude is recorded as a threshold voltage value. As the probe approaches the substrate, a gentle monotonic contraction of the cantilever oscillation amplitude W_c occurs, due to the combined effect of the driving force and attractive probe/substrate interaction force. As the distance is reduced, the amplitude reduction becomes more pronounced, until it reaches a linear regime with respect to the mean probe position.

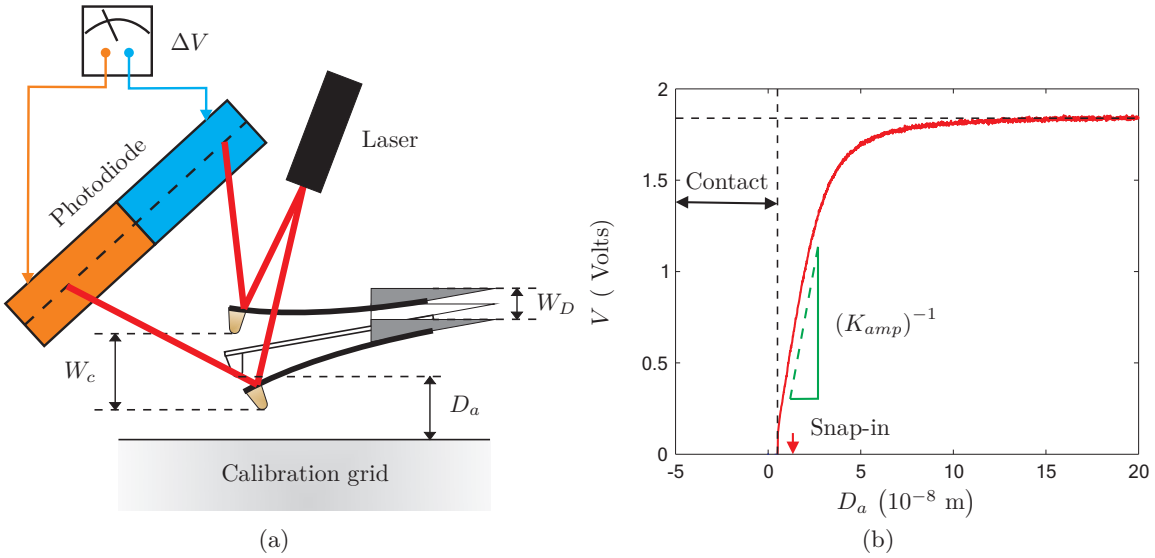


Figure 8.7: Contact mode AFM (a) oscillation scheme and (b) typical calibration curve illustrating the photodiode measured voltage during the probe oscillation approaching toward a rigid substrate, a silicon wafer, from which the photodiode calibration factor is obtained. The drive frequency was $\omega_D = \omega_{c,0} + 628.31$ s^{-1}.

The constant slope of this region in the voltage amplitude curve corresponds to the inverse of K_{amp}, relating the recorded amplitude of the voltage signal with the cantilever oscillation amplitude. For the data shown in Fig.8.7b, an amplitude coefficient $K_{amp} = 1.62 \times 10^{-8}$ m/V is found. It is important to notice that the probe/substrate interaction remains in the attractive regime. This behavior continues down to a mean distance at which the voltage amplitude is dramatically reduced to zero, indicating the "snap-in" phenomenon. The cantilever suffers a behavior deviation, leaping from the non-contact oscillatory state (attractive regime) to the probe/sample adhesion (attractive/repulsive regime). The microscope continues to bring the probe closer to the substrate, with an indiscernible response to the driving periodic force.

With the knowledge of the coefficient K_{amp}, authentic amplitude/distance curves are recovered. Using the piezoelectric tube calibration factor K_{tube}, the microscope enregisters the vertical displacement of the probe. As well, the cantilever oscillation is recorded as a voltage signal, from which an oscillation voltage amplitude is captured, and then turned into the authentic cantilever oscillation amplitude W_c with the employment of K_{amp}. Finally, the actual value of the driving amplitude $W_D = W_{c,0}/Q_c$ and the driving force $F_D = k_c W_D$ are retrieved. These results are summarized in Table 8.1.

Custom amplitude/distance curves are obtained when performing an approach and a subsequent retreat of the probe from the sample, with constant driving amplitude and frequency. An example is shown in Fig.8.8. The probe approaches the substrate, oscillating at its free amplitude and frequency. As the mean probe position D_a decreases, the oscillation amplitude is reduced as the attractive force increases in magnitude, the same behavior as described for the voltage amplitude in Fig.8.7b. After the amplitude/distance linear region is crossed, the oscillatory response is suddenly nullified and contact is made between the tip and the substrate, indicating the appearance of the "snap-in" phenomenon. The probe displacement stops at $D_a = -10$ nm and its withdrawal begins. The tip remains stuck to the substrate due to the adhesion/capillary adhesion, though the mean probe position increases. At a certain distance near $D_a = 25$ nm, the detachment of the tip from the sample surface occurs. This "pull-off" phenomenon allows the probe to recover its oscillatory behavior, also indicating the transition from the attractive to the repulsive force regime. Additionally, the oscillation amplitude at this point is greater than the one recorded in the approach curve at the same position D_a, revealing the position of the substrate. The amplitude corresponding to the "pull-off" distance is connected, by a line of unitary slope, to the position of the substrate, which is marked by the intersection at the probe position axis. As the probe moves away and D_a increase, the amplitude reduces until the cantilever returns to the behavior displayed by the approach curve.

Nominal tests were performed for a cantilever vertical displacement of 0.5 μm and a duration of 60

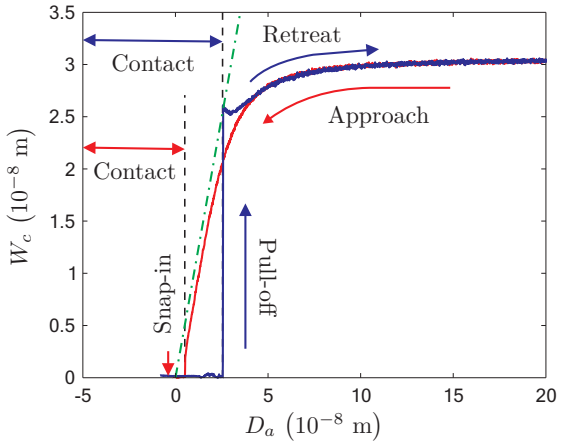


Figure 8.8: Non-Contact mode AFM typical experimental amplitude (——) approach and (——) retreat curves as functions of the vertical displacement over a rigid substrate, a silicon wafer.

s, using 1×10^4 data points. Considering the same definitions as for the force spectroscopy, given in eq.(8.22), amplitude/distance curves were acquired with a vertical speed of the mean probe position of 16.66 nm/s, a sample rate of 10 data points/nm and an exposition time of 6 ms/data point. Note that, for the amplitude spectroscopy, the ratio defined by:

$$\text{Cycles per point} = (\text{Exposition time})\,\omega_D, \tag{8.23}$$

indicates the number of oscillation cycles from which an amplitude measurement point is obtained. The test were conducted with 572 cycles/point for the B1-HDC probe, whereas for the ACT probes a minimum value of 10^4 cycles/point was used. From the transitory settling time of the tested probes, shown in Table 8.1, the minimum values of 262 cycles/point for the B1-HDC and 2125 cycles/point for the ACT probes are needed to surpass the cantilever transitory regime.

8.2.d Probe radius

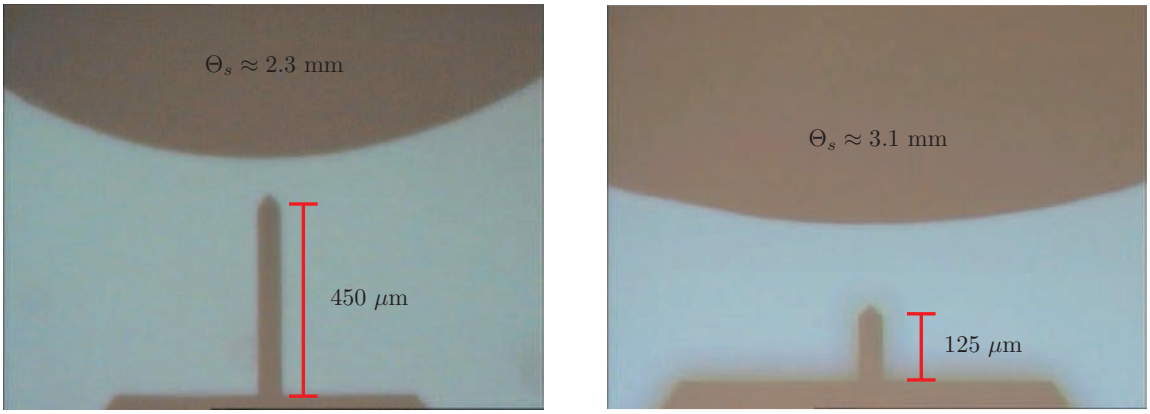
When the tip approaches the substrate, confinement and nucleation at the interstice provokes the condensation of ambient water, thus a capillary bridge and an adhesion capillary force F_{cap} are generated. The adhesion capillary force corresponds to the value measured during the probe retreat, at the "pull-off" distance D of the force/distance approach curve, as the one presented in Fig.8.6b. One can take advantage of this phenomenon to estimate the tip radius, assuming that condensed water films cover both surfaces, probe and substrate(Crassous et al., 1993, 2011). Hence, the tip radius is approximated by:

$$R \approx \frac{-F_{cap}}{4\pi\gamma_{H_20}}, \tag{8.24}$$

where γ_{H_20} is the air/water surface tension. Taking $\gamma_{H_20} = 7.2 \times 10^{-2}$ N/m, and the adhesion capillary force $F_{cap} = -1.85 \times 10^{-8}$ N observed in Fig.8.6, one finds a tip radius of $R = 20.5$ nm. As the ambient conditions were not strictly controlled during the test, the application of this technique is merely estimative. Nevertheless, a good agreement with the nominal value of the tip radius $R = [20 \pm 5]$ nm, provided by the manufacturer of the B1-HDC probe, is observed. In the following, a tip radius of $R = 20$ nm will be employed.

8.3 Liquid sample spectroscopy

PDMS (polydimethylsiloxane) $(C_2H_6OSi)_n$ drops, with a surface tension $\gamma = 3.1 \times 10^{-2}$ N/m, a density $\rho = 9.655 \times 10^2$ kg/m^3 and a viscosity $\mu = 1.4 \times 10^{-1}$ Pa·s, were deposited over a silicon wafer. The shape of the samples can be either a circular puddle or a spherical cap, depending on the volume of liquid. As this quantity is not precisely controlled, each sample thickness should be estimated. In the case of a circular puddle (considering a heavy drop analysis (de Gennes et al., 2003)), the thickness E is



(a) (b)

Figure 8.9: Liquid sample and probe (a) Nanotools model B1-HDC and (b) Appnano model ACT.

given by:

$$E_{puddle} = 2\lambda_C \sin\left(\frac{\theta_{ls}}{2}\right), \tag{8.25}$$

where λ_C is the capillary length and θ_{ls} the contact angle. Equivalently, for a spherical cap, one has:

$$E_{cap} = \frac{\Theta_s}{2}\sqrt{\frac{1-\cos(\theta_{ls})}{1+\cos(\theta_{ls})}}. \tag{8.26}$$

The sample diameter Θ_s was measured an hour after the sample was set in place, giving $\Theta_s \in [2,3]$ mm. According to the PDMS properties (see Table 5.1), the capillary length is around $\lambda_C = 1.8$ mm. As $O\{\lambda_C\} \sim O\{\Theta_s/2\}$, it is not obvious to determine whether gravity or surface tension will determine the shape of the sample. For the present instance, considering a contact angle in the range $\theta_{ls} \in [5°, 15°]$, the expected sample thicknesses may be either in the ranges $E_{puddle} \in [314.82, 934.88]$ μm and $E_{cap} \in [43.66, 131.65]$ μm, or in the interval between them. A posteriori estimation of the thickness, by means of a manual displacement of the AFM probe, yielded sample thicknesses in the range $E \in [175, 215]$ μm. Even though the sample thickness is roughly determined, it remains much greater than the order of magnitude of the tip radius $R \approx 10^{-8}$ m. Therefore, the relative thickness $E^* = E/R$ takes values $E^* \in \left[10^3, 10^5\right]$, which indicates that, a priori, the sample can be considered as a bulk. As a consequence, the experimental results must be compared to their equivalents obtained with the theoretical model for the bulk regime.

The difficulty of using a larger liquid volume is that other microscope components, not so far from the probe, may touch the sample before the tip, spoiling the experiments.

The 5500 AFM was employed in contact mode in order to obtain the force spectroscopy over the sample, whereas the non-contact mode was used to perform the amplitude spectroscopy. Experiments were made using the previously described B1-HDC probe and a Appnano®model ACT probe. Their characteristics are summarized in Table 8.1.

8.3.a Force/distance curves

The tip is placed near the liquid sample, and the calibration procedure is performed over the silicon wafer. Once the deflection calibration factor K_{def} and the stiffness k_c were calculated, the probe is retracted 250 μm and then placed above the center of the sample. Several scanning cycles, composed of an approach-withdrawal displacement of 2μm (motion of the piezoelectric tube) and a subsequent automatic approach of the same size (2 μm displacement with a step motor), were executed until the interface is reached. The last cycle is recorded, in which the tip approaches the minimum stable separation distance, and, simultaneously, the liquid jumps over the tip and the probe bends over dipping into the sample. The experiments were carried out taking 50 data points/nm, a vertical scan rate of 10 nm/s and an exposition time of 2 ms, which is enough to surpass the transitory regime of the tested probes.

An example of the force spectroscopy curves, for the B1-HDC probe, is shown in Fig.8.10a. As the

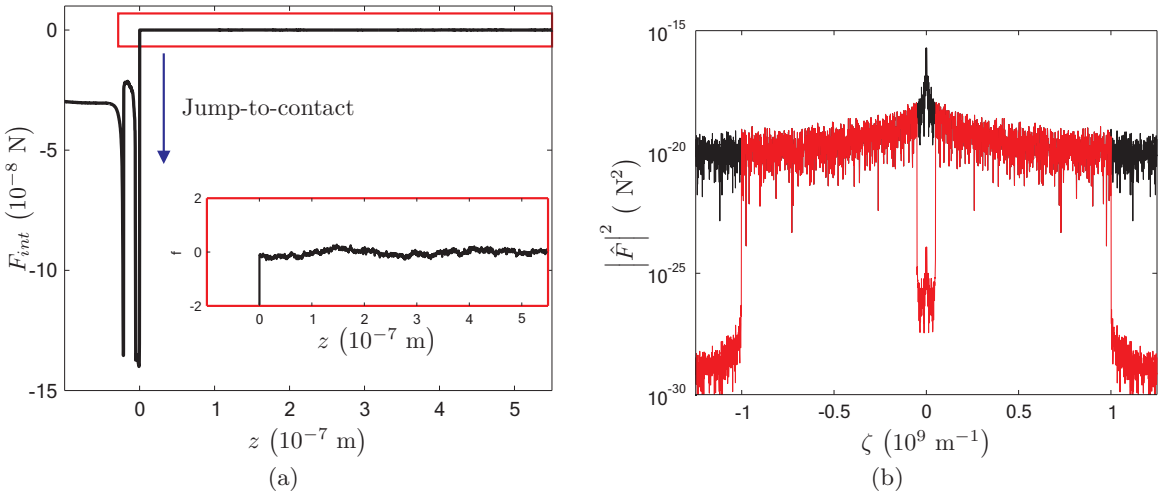


Figure 8.10: (a) Interaction force due to the cantilever deflection as a function of the vertical displacement over a deformable sample, B1-HDC probe over a PDMS puddle, and the corresponding (b) Power Spectral Density and filtered signal [——]as a function of the spatial frequency. B1-HDC probe.

probe approaches to the air/liquid interface, the measured force gradually increases, until at a threshold distance, the liquid "jumps" and wets the probe. The force due to the formation of a capillary bridge, hypothetically formed between the tip end and the sample, is expected to be around $O\{4\pi\gamma R\} \sim 10^{-8}$ N. Nevertheless, the registered contact force is greater than 10^{-7} N, indicating that the liquid mounts instantaneously over the probe. Complete and spontaneous wetting of PDMS over carbon nanotubes, implying a zero contact angle, has been observed (Barber et al., 2004). The increased cantilever deflection may be caused by to the weight of liquid over the probe and the liquid bridge covering partially or completely the tip pyramid. As well, the liquid mounting over the probe may provoke a deviation of the laser reflection and an faulty photodiode capture. As the probe continues its displacement toward negative values of z, the liquid wets the probe and an explanation of the left hand side of the curve is not possible. Although the dynamics of the wetting and spreading of the liquid over the probe is not under consideration, the "jump-to-contact" position has been revealed, and the reference position $z = 0$ is identified.

The microscope software does not count on the appropriated real-time signal processing to observed directly the probe/sample interaction regime. In addition, the common real-time resolution of an AFM is limited by the thermal noise, which takes values of around 10^{-12} N (Smith, 1995) at $\Omega = 293.15$ K. For these reasons, a procedure to "clean" the measured signal, which separates the interaction force from the ambient and thermal noise, as well as other scanning artifacts, was developed. This post-processing methodology consists of an spectral filtering and a smoothing of the force signal.

The first step is the application of the Discrete Fourier Transform (DFT) to the force signal $F(z)$, in order to obtain the spatial frequency response $\hat{F}(\zeta)$. This transform is computed as follows:

$$\hat{F}_k = \sum_{j}^{N} \left[F_j \exp\left\{ \frac{-2\pi i\,(j-1)\,(k-1)}{N} \right\} \right] \tag{8.27}$$

where F_j is the measured force at z_j for $1 \leq j \leq N$, $\hat{F}_k$ is the kth coefficient of the Fourier series corresponding to the wavenumber ζ_k for $1 \leq k \leq N$, $i = \sqrt{-1}$ is the imaginary unit and N is the number of acquired data points. As an example, the complex modulus of $\hat{F}$, is shown as in Fig.8.10b.

A band-pass filter $\widehat{BP}(\zeta)$ was implemented with the cutoff frequencies $\zeta_{low} = 4 \times 10^7$ m^{-1} and $\zeta_{high} = 10^9$ m^{-1}. These values indicate that only the wavelengths in the range 10^{-9} m $\leq (\zeta)^{-1} \leq 2.5 \times 10^{-8}$ m will take part in the reconstruction of the force signal. Lower frequencies than ζ_{low} are not a consequence of the van der Waals interaction potentials, and they usually represent the ambient noise. Higher frequencies than ζ_{high} are associated with the thermal noise. Therefore, the designed discrete

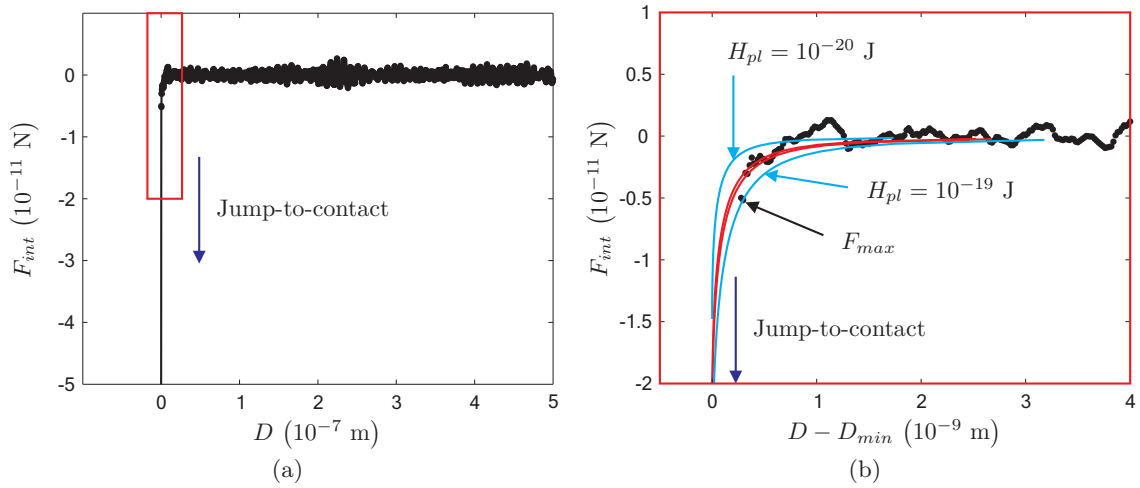


Figure 8.11: Post-processed force spectroscopy curve as a function of the probe position over a deformable sample, B1-HDC probe over a PDMS puddle. (a) complete curve in the attractive regime, (b) decay and fit with the model (——) for $H_{pl} \in \left[4 \times 10^{-20}, 5 \times 10^{-20}\right]$ J, and (——) for $H_{pl} = 10^{-20}$ J and $H_{pl} = 10^{-19}$ J.

filter is composed of the following linear combination of arctangent functions:

$$\widehat{BP}_k = \frac{1}{\pi}\left[\tan^{-1}\left(\zeta_k - \zeta_{low}\right) - \tan^{-1}\left(\zeta_k - \zeta_{high}\right)\right], \tag{8.28}$$

where $\widehat{BP}_k$ is the value of the filter at the wavelength ζ_k for $1 \leq k \leq N$. Afterwards, the filtered force $\tilde{F}(z)$ is reconstituted with the Inverse Discrete Fourier Transform (IDFT) of the filtered spectral signal:

$$\tilde{F}_j = \frac{1}{N}\sum_{k}^{N}\left[\left(\hat{F}_k \widehat{BP}_k\right)\exp\left\{\frac{2\pi i\left(j-1\right)\left(k-1\right)}{N}\right\}\right], \tag{8.29}$$

where $\tilde{F}_j$ is the value of the filtered force at z_j for $1 \leq j \leq N$, and i is once again the imaginary unit.

Despite the applied severe filter, the resulting signal still presents fine-scale structures, which are removed with the employment of a smoothing algorithm. A moving average (MA) filter with $2M+1 = \Xi$ points was applied to the force signal, where Ξ is the number of data points of the subsets, from which average values are obtained. The MA is defined as:

$$\bar{F}_m = \begin{cases} \dfrac{1}{2m-1}\displaystyle\sum_{j=1}^{2m-1}\tilde{F}_j & \text{for } 1 \leq m \leq M \\ \dfrac{1}{2M+1}\displaystyle\sum_{j=m-M}^{m+M}\tilde{F}_j & \text{for } M < m < N-(M+1) \\ \dfrac{1}{2\left(N-m\right)+1}\displaystyle\sum_{j=2m-N}^{N}\tilde{F}_j & \text{for } N-(M+1) \leq m \leq N. \end{cases} \tag{8.30}$$

where $\bar{F}_m$ is the value of the smoothed force at z_m for $1 \leq m \leq N$. The value of $\Xi = 29$ was observed to function properly. Nevertheless the number of points employed in the MA filter should rest in the range $\Xi \leq 50$, in order to be consistent with the sample rate (50 data points/nm) and do not eliminate information contained in wavelengths longer than 10^{-9} nm. The outcome is an average behavior, which successfully isolates the rise of the force magnitude, and the drop of the separation distance. An example of the resulting post-processed force curves is shown in Fig.8.11a.

Finally, the resulting force curve is compared to the theoretical model, as it is shown in Fig.8.12b. In equilibrium, the sphere/liquid interaction force F_{int} is equal to the addition of the deformation force F_γ

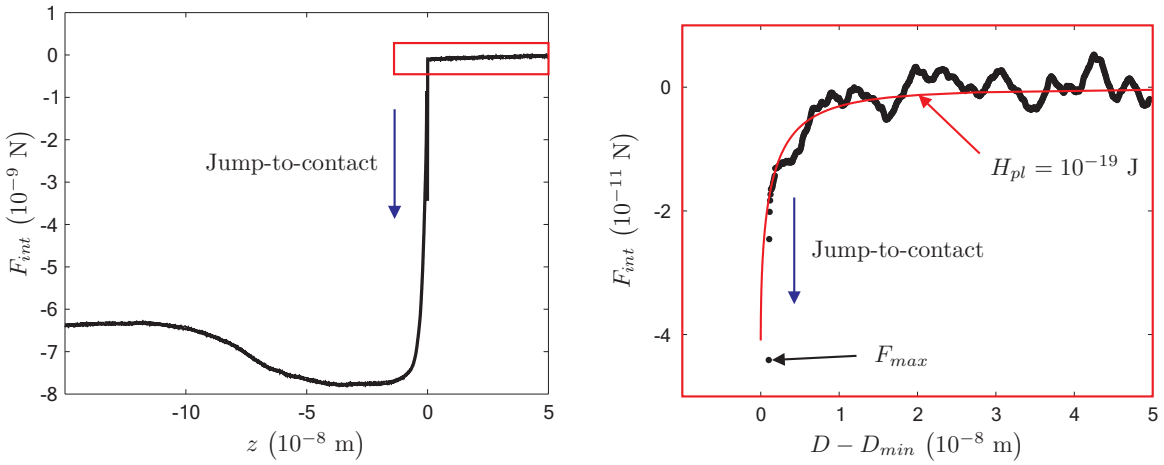


Figure 8.12: (a) Interaction force due to the cantilever deflection as a function of the vertical displacement over a deformable sample, ACT-02 probe over a PDMS puddle, and the corresponding (b) interaction force as a function of the probe position and fit with the model (——) for $H_{pl} = 1 \times 10^{-19}$ J.

and the gravity force F_ρ. In the first place, the change in the deformation energy η_0^* is computed as:

$$\Delta\mathcal{E}_\gamma = \mathcal{E}_\gamma - \mathcal{E}_\gamma^0, \tag{8.31}$$

where $\mathcal{E}_\gamma$ is the energy correlated to the equilibrium deformation shape $\eta(r)$, and $\mathcal{E}_\gamma^0$ is the energy associated with a flat undeformed interface $\eta = 0$. Both energy states are calculated from integrating the corresponding theoretical surface deformation, as follows:

$$\mathcal{E}_\gamma = 2\pi\gamma R^2 \int_0^{\lambda_C^*} r^* \sqrt{1 + \left(\xi^* \frac{d\eta^*}{dr^*}\right)^2}\, dr^*, \tag{8.32}$$

where λ_C^* is the dimensionless capillary length. Integrating for $\eta^* = 0$, the reference energy state results to be $\mathcal{E}_\gamma^0 = \pi\gamma\left(R\lambda_C^*\right)^2$. In turn, the deformation force is retrieved from the derivative of $\Delta\mathcal{E}_\gamma$, with respect to the apex position η_0, which is written as follows:

$$F_\gamma = -\frac{1}{\xi^* R}\frac{d}{d\eta_0^*}\left[\Delta\mathcal{E}_\gamma\right]. \tag{8.33}$$

On the other hand, the force due to gravity is given by:

$$F_\rho = -2\pi\Delta\rho g\xi R^3 \int_0^{\lambda_C^*} \eta^* r^* dr^*, \tag{8.34}$$

and the AFM measured force can be directly compared to the interaction force, which is obtained from the next addition:

$$F_{int} = F_\gamma + F_\rho. \tag{8.35}$$

The knowledge of the interface deformation $\eta(r)$ allows the quantification of the mutually exerted force of the probe and the liquid. For a given D^*, with the employment of eqs.(2.7), (2.13) and the coefficients $C_{lk} = 0.154$, the values of η_0^* and κ_0^* are obtained. The values of λ_H^* and λ_T^* are obtained from the interpolation of the curves in Fig.2.9. Together with η_0^* and κ_0^*, they are injected into the near-field self-similar deformation profile described in eq.(2.19), which is coupled at $r^* = \lambda_T^*$ with the far-field profile given by eq.(2.20). Subsequently, a force curve are computed with eqs.(8.32)-(8.35). These theoretical force curves are calculated using AFM parameters and the measured properties of the experimental liquid: a tip radius of $R = 2 \times 10^{-8}$ m, a gravitational acceleration constant of $g = 9.81$ m/s^2, and the physical properties of PDMS listed in Table 5.1, which leads to $\lambda = 1.8 \times 10^{-3}$ m and $B_o = 1.31 \times 10^{-10}$. Additionally, the expected range of the Hamaker constant $H \in \left[10^{-21}, 10^{-19}\right]$ N m, which conducts to the modified Hamaker number $H_a \in \left[3.5 \times 10^{-3}, 3.5 \times 10^{-5}\right]$, is swept for the

calculations. The position of the sphere is decreased from $D^* = 2.5D^*_{min}$ to $D^* = D^*_{min}$. The latter is calculated from solving eq.(2.14) for the product $\xi_{crit}\eta^*_{0,max}$, and then (B.1) for D^*_{min}.

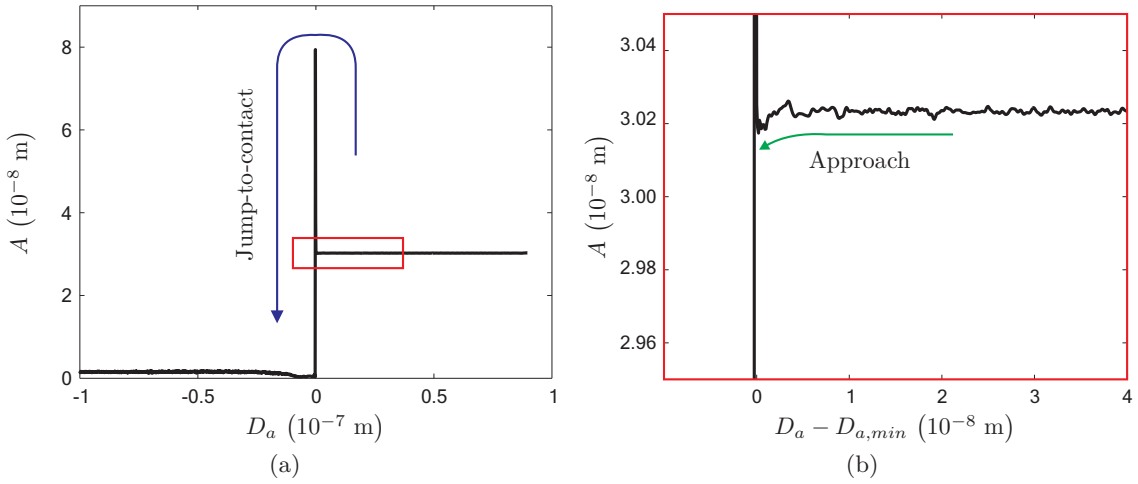
The interaction force F_{int} is negligible when the tip is placed far from the interface, as shown by the tendency of the theoretical curves in Fig.8.12b. When the sphere approaches the interface, the force grows monotonically in magnitude. As was expected and considered in eqs.(8.33)-(8.35), the attraction force shows negative values due to the orientation of the reference frame. Before reaching D_{min}, the force increases abruptly until it reaches a maximum value F_{max}, for which slope is indeterminate. Herein, D_{min} is identified as the horizontal position where the trajectory of each curve stops, indicating the appearance of the "jump-to-contact" phenomenon. An increase of H_a implies the displacement of D_{min} to greater values, as well as a directly proportional increasing scaling of the curve magnitude and F_{max}.

In Fig.8.12b, the AFM measured force curve is compared with the theoretical force curves obtained for different values of the Hamaker constant H_{pl}. Within the frame of reference employed, cantilever deflections toward the interface are considered as negative values and, thus, attraction forces as well. Theoretical and experimental force curves match up in orders of magnitude, and their behaviors are in very good agreement. Moreover, the quantitative behavior of the measured interaction force is encompassed by the tendencies exposed by the theoretical curves, specially when the probe/sample distance is short. When the nanoscopic tip is placed far from the sample, at a distance greater than $D = D_{min} + R$, the deflection of the cantilever is negligible. As it approaches the interface, from $D - D_{min} = R$ to $D - D_{min} = 0.5R$, the AFM measures a gradually increasing force. By reaching the position $D - D_{min} = 0.3 \times 10^{-9}$ m, the force increases abruptly, provoking a great deflection of the cantilever, which implies a magnitude of $F_{max} = 5 \times 10^{-12}$ N. At $D - D_{min} \approx 0$ m at which the force diverges, the liquid has jumped over the probe, and a capillary bridge is created.

Following the theoretical curves, the gap between the probe and the liquid surfaces arrives at its minimum value when reaching $D = D_{min}$. Hence, any separation distance smaller than D_{min} means imminent contact and the subsequent displacement of the liquid over the tip, which provokes an irreversible wetting process. Concretely, the rise of the force magnitude, in Fig.8.12b, is well described by the curves generated with $H_{pl} = 4 \times 10^{-20}$ J and 5×10^{-20} J, for which $H_a \in \left[1.37 \times 10^{-3}, 1.71 \times 10^{-3}\right]$, the Bond number being $B_o = 1.31 \times 10^{-10}$. The value $H_{pl} = 4.8 \times 10^{-20}$ J deduced from the literature (Israelachvili, 2011; Mougin and H., 2003; Visser, 1972) is enclosed in the range of H_{pl} deduced from our AFM measurements. As a consequence, from this comparison between experiments and theory, a minimum separation distance $D_{min} = [23.88 \pm 0.13] \times 10^{-9}$ m, at which the "jump-to-contact process happens", is forecast for the probe B1-HDC with $R = 20$ nm in interaction with the PDMS liquid sample.

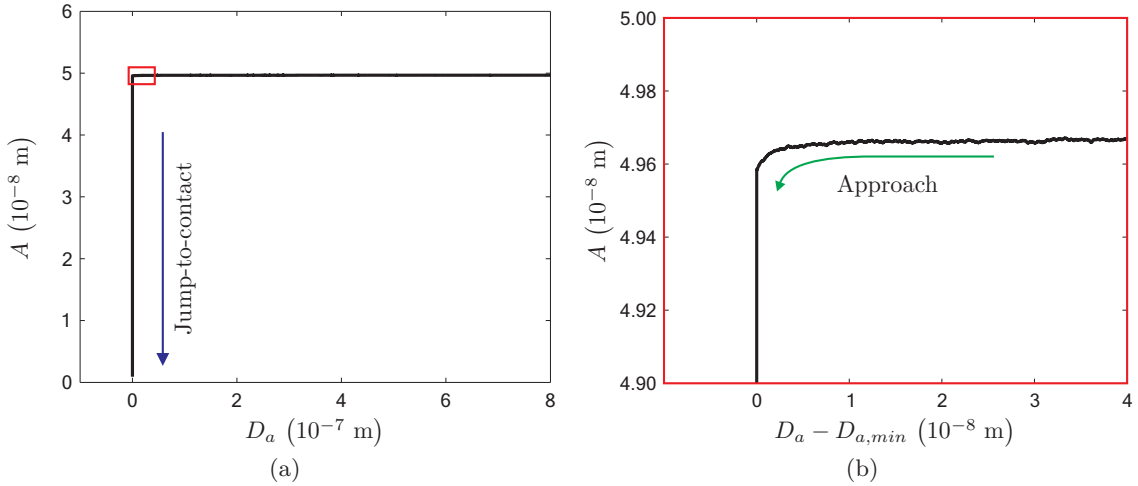
The results from the test performed to the probes ACT-02 are shown in Fig.8.12. The qualitative behavior is similar to that the soft cantilever case, before the "jump-to-contact" phenomenon occurs, even though the probe wetting shows a different appearance. In this case, the force due to the formation of a capillary bridge, between tip and sample, is expected to be around $O\{4\pi\gamma R\} \sim 10^{-8}$ N, which is close to the experimentally found value, as it can be confirmed in Fig.8.12a. As it is shown in Fig.8.12b, the post-processed data presents a good agreement with a fit of our model, given by the value of $H_{pl} = 1 \times 10^{-19}$ J. The cantilever becomes unstable at the position $D - D_{min} = 0.1 \times 10^{-9}$ m, revealing a maximum force of $F_{max} = 4.4 \times 10^{-11}$ N, proving the advantageous stability of stiff cantilevers. Indeed, using stiff levers allows to obtain force values at shorter distances, with respect to D_{min}, than when naturally unstable soft probes are employed. In the case, a minimum distance $D_{min} = 46.35 \times 10^{-9}$ m is found, for the probe ACT-02 with a radius of $R = 40$ nm. The force is one order of magnitude greater than the measured value for the B1-HDC probe, which is coherent with the assumption that the $F \sim R$. In conclusion, probes with soft cantilevers are recommended for force spectroscopy studies in order to benefit of a higher force sensitivity, whereas stiff cantilevers are advised to take advantage of a higher distance sensitivity. As well, the employment of tips with larger radius increase the magnitudes of the measured forces, as it is noticed when comparing the forces obtained in this study with their equivalents in the literature, acquired using probes with different radius(Crassous et al., 2011) and a Surface Force Apparatus (SFA)(Crassous et al., 1993).

The presented method, the Hamaker constant determination from force spectroscopy comparison, is based on a previously developed experimental technique (Eichenlaub et al., 2002), which has already been validated for the Hamaker constants of probe/rigid sample interactions.



(a) (b)

Figure 8.13: Amplitude spectroscopy curves illustrating the amplitude as a function of the vertical average position of the probe, of the B1-HDC probe with $k_c = 0.2$ N/m, over a deformable sample, a PDMS puddle. (a) complete view and (b) zoom of the region before the jump-to-contact.



(a) (b)

Figure 8.14: Amplitude spectroscopy curves illustrating the amplitude as a function of the vertical average position of the probe, of the ACT-01 probe with $k_c = 36.85$ N/m, over a deformable sample, a PDMS puddle. (a) complete view and (b) zoom of the region before the jump-to-contact.

8.3.b Amplitude/distance curves

The start-up of these experiments coincides with that of the force spectroscopy. The calibration procedure is accomplished over the silicon wafer, in the proximity of the liquid sample. After the calculation of the amplitude calibration factor K_{amp} and the cantilever stiffness k_c, the probe is retracted 250 μm and then placed above the center of the sample. While the probe is oscillating at the imposed frequency $W_{c,free}$, it is slowly approached to the sample, until the oscillation amplitude decreases up to a value within $W_c/W_{c,free} \in [0.96, 0.98]$. At this position, we expect that the mean distance, between the surfaces of the probe and the sample, is in the range $D_a - R \in (W_{c,free}, 2W_{c,free})$. A scanning cycle, made of an approach-withdrawal displacement of 1 μm (motion of the piezoelectric tube) of the mean probe position, is performed while the cantilever is stimulated by constant driving amplitude W_D and frequency ω_D. If contact between the probe and the liquid surface is not attained, a subsequent automatic approach of the same size (1 μm displacement with a step motor), is fulfilled. This two-step procedure is repeated until the probe/interface contact is accomplished, recording the last cycle. It is important to notice that, during the experiments, the photodiode output voltage is fixed for the peak amplitude of 5 V in the resonance curve. Therefore, the oscillation amplitude W_c can deviate significantly for the different types of probes. Experimental conditions include a driving frequency of $\omega_D = \omega_{c,0} + 628.31$ s^{-1}, which

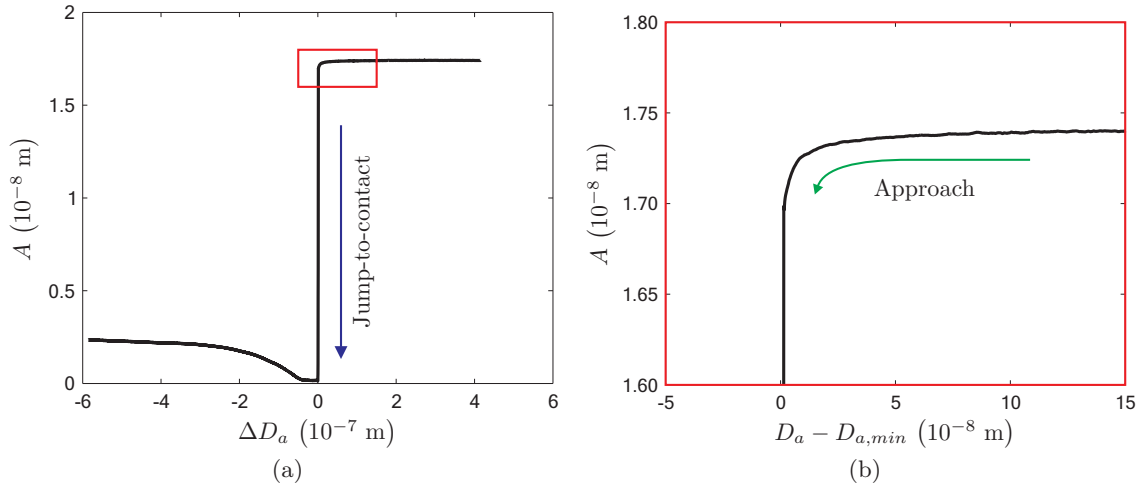


Figure 8.15: Amplitude spectroscopy curves illustrating the amplitude as a function of the vertical average position of the probe, of the ACT-02 probe with $k_c = 51.03$ N/m, over a deformable sample, a PDMS puddle. (a) complete view and (b) zoom of the region before the jump-to-contact.

are listed in Table 8.1 for the tested probes. As well, the amplitude spectroscopy curves were carried out taking 10 data points/nm and a vertical speed of 15 nm/s, which lead to an exposition time of 6.66 ms/data point. Recall that, dividing the exposition time by the oscillation period $(\omega_D)^{-1}$, one obtains the number of oscillation cycles from which an amplitude measurement is obtained. The amplitude measurements were acquired with 628 cycles/point for the B1-HDC probe, whereas for the ACT probes a minimum of 11313 cycles/point was used, which allows to surpass the transitory regime of the tested probes,

Some amplitude spectroscopy curves are shown in Figs.8.13a, 8.14a and 8.15a, for the B1-HDC and the two ACT probes, respectively. While the mean probe position is of the order of several times the free oscillating amplitude $W_{c,free}$, no perceptible change in the measured amplitude signal is registered. As the probe approaches the interface, ΔD_a going from $W_{c,free}$ to shorter values, the measured amplitude decreases until, at a new threshold distance, the probe/liquid contact occurs. At this critical stable mean distance D_a, a significant amplitude gradient is observed. Simultaneously, the liquid jumps over the tip and the probe bends over dipping into the sample, which leads to a "shut-off" of the probe oscillating behavior, thus the oscillation amplitude becomes $W_c = 0$. This "shut-off" looks different for each tested type of probe. For the B1-HDC probe, the amplitude suffers an important sudden increase and then goes down to zero, as shown in Fig.8.13a. For the ACT probes, the amplitude is directly switched off, as a violent drop depicted in Fig.8.14a, whereas the transition is much gentler in Fig.8.15a. Despite the existence of these particular evolutions, a general "jump-to-contact" phenomenon is revealed at a new critical mean distance $D_a = D_{a,min}$. After this first contact, the mean probe position continues to diminish as the probe stays still, but it regains a relatively small oscillatory motion after a displacement of several nanometers, as it is clearly observed in Figs.8.13a and 8.15a. The liquid mounting over the probe may provoke a deviation of the laser reflection and an faulty photodiode capture, which inhibits a proper interpretation of the curves at the region $D_a - D_{a,min} < 0$.

Since the oscillating driving force is $F_D \geq 10^{-10}$ N, which at 293.15 K is two orders of magnitude larger than the forces induced by Brownian motion (Smith, 1995), then the measured amplitude signal is considered be almost free of thermal noise. For these reasons, a spectral filtering is not needed, and the procedure to "clean" the measured amplitude signal becomes simple. The external vibrations and the residual noise appearing in the signal can be easily removed with the use of a signal smoothing. It consists only of a moving average (MA) filter with Ξ data points per subset. In this case, Ξ is selected according to the noise level in each experiment, without a straight restriction related to the sample rate.

After the application of this procedure on the signals, the amplitude "shut-off" is clearly observed when the probe approaches $D_{a,min}$. The evidence of a probe/sample attractive interaction regime is given by the curve tendency: a gradual diminution of the oscillation amplitude W_c as the distance D_a decreases, and the appearance of an unstable behavior that provokes the early probe/liquid contact. An extensive analysis of these curves is needed. The logical next step is the development of a theoretical model,

which will couple the dynamics of the liquid and the probe, and its comparison with the experimental results. In the literature, a model considering a Kelvin-Voigt viscoelastic material (Aimé et al., 1999b; Boisgard et al., 2002), has been presented and compared with experiments on polymers exhibiting solid-like behaviors. For our case, a Maxwell viscoelastic material seems more suitable to represent either a liquid or a polymer showing a liquid-like behavior. Therefore, the shape of the amplitude spectroscopy curves, just before the amplitude drop occurs, may allow the determination of the Hamaker constant H_{pl} of the probe/liquid interaction.

8.4 Concluding remarks

A combination of the force spectroscopy results and the numerical solution presented in Chapter1 yield interesting conclusions about the static probe/liquid interaction. The surface deformation η_{max}, the minimum separation distance D_{min} and the interaction force F_{int} increase in magnitude for larger values of the probe/liquid Hamaker constant H_{pl}. Likewise, an increase in the probe radius R provokes the enlargement of the maximum surface deformation η_{max} and maximum measured force F_{max}, nevertheless it causes a decrease of the minimum separation distance $D_{min} - R$ between the surfaces of the probe and the liquid. For very small tips, with a radius $R < 25$ nm, and considering $H_{pl} = 10^{-20}$ J, interaction forces of the order of $F_{max} = 10^{-12}$ N are generated, which is hardly measurable with a common apparatus. In contrast, we find a significantly quantifiable $F_{max} = 10^{-11}$ N for relatively large tips of $R > 30$ nm and the same H_{pl}, but strongly reducing the scanning resolution. Therefore, the resolution of AFM experiments rises when using probes with small tip radius, but their size is restricted by the minimum force measurable with an AFM. As well, cantilevers with low stiffness k_c slow down the arrival of the "jump-to-contact" phenomenon, nonetheless they increase the force sensitivity of the apparatus. In brief, the combination of probe properties should be optimized according to the apparatus limitations.

The employment of our probe/sample static interaction model is suggested to obtain quantitative data from local probe measurements of liquid surfaces. Whereas, a wide range of $H \in (10^{-19}, 10^{-21})$ J is commonly employed, our methodology allows us to estimate a more accurate value for a given probe/liquid system, when meticulous AFM measurements are performed. In addition, together with the estimation of the tip radius (Crassous et al., 1993), the minimum probe/liquid distance and its corresponding deformation are obtained. Our prediction of H_{pl} leads to find the minimum distance for scanning $D_{min} - R$, needed to keep an attractive interaction regime without wetting the probe.

Now, putting together the amplitude spectroscopy results and the preliminary numerical results introduced in Chapter5, several deductions are stated. The amplitude sensitivity of spectroscopy tests depends strongly on the driving amplitude W_D, the driving frequency ω_D and the cantilever stiffness k_c. An augmentation of ω_D reduces the transitory settling time and increases the resolution of the apparatus, leading to the acquisition of neat curves. An increase of the stiffness k_c or the reduction of the free oscillation amplitude W_D, delays the appearance of the "jump-to-contact" phenomenon, which is a consequence of the cantilever unstable behavior. In addition, the instantaneous behavior after the critical mean probe distance $D_{a,min}$ is attained, changes with both parameters W_D and k_c. In conclusion, the employment of stiffer cantilevers with higher resonance frequencies is advised for amplitude spectroscopy experiments, as well as for non-contact AFM scanning over liquid surfaces.

Conclusions and Perspectives

Conclusions

We have introduced a modified Young-Laplace equation that includes a probe/liquid interaction terms, resulting from purely attractive L-vdW forces. As well, the effect of the substrate over the liquid is considered, since there are also L-vdW attraction forces between the liquid and substrate molecules. Besides, the classic gravity and surface tension effects were also injected. Our methodology, based on these principles, leads us to an equilibrium modified Young-Laplace equation (zero pressure difference across the interface $\Delta P^* = 0$), which describes the equilibrium shape of the liquid surface. This resulting strongly non-linear equation has been analyzed and numerically solved. A dimensionless treatment was made in order to generalize the problem for probes of arbitrary size. Within this scope, all the equilibrium deformation profiles show a bump-like shape, highly curved at the apex and with an exponential-like decay. The magnitude and radial extent of the deformation is mainly determined by a combination of dimensionless parameters. This quantities, which arise naturally from the dimensionalization of the above-mentioned equation, are:

- The modified Hamaker number H_a, which compares the strength of the probe/liquid interaction with the surface tension.
- The Hamaker constant ratio A, which relates the probe/liquid and liquid/substrate interactions.
- The Bond number B_o, which weighs gravity and surface tension.

As well, several length scales, which value is clearly determined by the combination of H_a, A and B_o, are yielded:

- The capillary length λ_C, that indicates the radial position at which gravity flattens the surface.
- The characteristic film length λ_F, shows the radial extent whence the liquid/substrate interaction plays the same role as gravity.
- The modified capillary length λ_{CF}, which weighs the two previous regimes.
- The inflection point λ_H indicates the external boundary of a near-field zone, where probe/liquid interaction governs.
- The zero curvature point λ_T marks the beginning of the capillarity dominated decay, the far-field.

These length scales are important because they mark boundaries of the zones where different mechanisms dominate the surface behavior. In addition, some of them generate self-similar surface profiles. The near-field similarity profile is portrayed by the reduced variable $\xi^* \left(\eta^* - \eta_0^*\right) / \kappa_0^* \left(\lambda_H^*\right)^2$ and the reduced coordinate r^*/λ_H^*. The far-field similarity shape is given by the reduced deformation η^*/η_C^* (where η_C^* is the deformation at the capillary length) and the coordinate r^*/λ_C^*. Moreover, when λ_C and λ_F are compared, particular film thicknesses are obtained. E_{bulk}, coming from $\lambda_C \sim \lambda_F$, indicates the film thickness from which the bulk behavior is observed. $E_{shallow}$, coming from $\lambda_F \sim R$, indicates the film thickness below which the thin film behavior occurs.

A detailed analysis of the apex deformation η_0^*, the peak curvature κ_0^* and the initial gap ξ^{ast} has been reported. The surface shows a characteristic behavior depicted by the relations:

$$\kappa_0^* \sim \left(\xi^{*\eta_0^*}\right)^{3/2} \qquad \text{bulk liquid}$$

$$\kappa_0^* \sim \left(\frac{\xi^* \eta_0^*}{E^*}\right)^{4/3} \qquad \text{thin film.}$$

For the bulk case, the corresponding power-law is obtained from the balance of surface tension and probe/liquid interaction. For the thin film case, the balance between probe/liquid and liquid/substrate interactions yields the relationship, which clearly indicates the restraining effect of the film thickness E^* on the surface deformation.

Likewise, bifurcation diagrams of the interface deformation, as well as a capillarity region corresponding to the the probe/liquid wetting, have been identified. The bifurcation diagrams show stable

and unstable branches, depending on the criterion:

$$\frac{d\eta_0^*}{dD^*} < 0 \qquad \text{stable branch}$$
$$\frac{d\eta_0^*}{dD^*} > 0 \qquad \text{unstable branch.}$$

Both bifurcation branches are given, by the relations:

$$D^* = \xi^* \eta_0^* + \sqrt{1 + \left[\frac{2\kappa_0^*}{H_a}\right]^{-1/3}} \qquad \text{bulk liquid}$$
$$D^* = \xi^* \eta_0^* + \sqrt{1 + \left[\frac{\xi^* \eta_0^*}{H_a \left(\lambda_F^*\right)^2}\right]^{-1/3}} \qquad \text{thin film.}$$

In addition to the numerical results and the theoretical analysis, a simple model based on springs and masses has been presented. The adjustment of the spring constants and other coefficients, leads to a fair qualitative reproduction of the surface deformation. The probe deflection has been included, showing some examples for different cantilever stiffnesses. The main advantage of this model is its simplicity.

By performing AFM measurements on a standard liquid PDMS, the theoretical static results are compared to the force spectroscopy experiments. It has been shown that it is possible to predict the interface deformation, to obtain the critical distance before the capillary "jump-to-contact" and also to measure the Hamaker constant of a liquid.

As well, a dynamic model, corresponding to a viscous thin film, has been proposed. The thin film has been modeled using the lubrication equation coupled with the non-equilibrium Young-Laplace equation ($\Delta P^* \neq 0$). Some problem simplifications where proposed and applied, leading to a quasi-linear thin-film equation. The complexity reduction of this equation, by means of the Hankel transform, allowed the analysis of the first order trends of the thin-film, because a quasi-static analytical solution is available. A relaxation/diffusion behavior has been discerned as the natural response of the thin-film to external perturbations. It is the mechanism in which the surface relies on to distribute and dissipate the energy injected by the perturbations. A wavenumber-dependent time decay coefficient ν^* has been found. This parameters determines the phase velocity, at which the surface deformation is diffused over the surface. Two asymptotic regimes have been observed:

$$v_g = \frac{2k}{\left(\lambda_{CF}^*\right)^2} \qquad \text{for small wavenumbers } k^* \ll \left(\lambda_{CF}^*\right)^{-1}$$
$$v_g = 4\left(k^*\right)^3 \qquad \text{for large wavenumbers } k^* \gg \left(\lambda_{CF}^*\right)^{-1}.$$

When the probe approaches the surface, a typical response to the excitation has been observed. The wavenumber distribution that is excited shows a more significant dependence on the time-average probe position D_a^* than that on the film thickness. In general, this distribution shows a peak centered in the range $k^* \in \left[10^0, 10^1\right]$. This qualitative description provided understanding of the way the thin-film evolves when a probe approaches or moves away, even though the analysis is based on the hypothesis of quasi-static probe behavior.

However, a numerical solution of the quasi-linear equation was needed to study the film evolution. A pseudo-spectral method, also based on the Hankel transform, has been developed and tested. A validation of the models has been made when comparing the final dynamic state to the static results, finding a very good agreement. We have conclude that the response of the thin-film to its interaction with a static probe is characterized by the propagation of a deformation front, which displaces from the region below the probe toward the modified capillary length with a speed that decreases as the front reaches larger distances.

Preliminary results were presented, in which the effect of the time-average probe position has been analyzed, for fixed oscillation amplitude and frequency. Stable, quasi-stable and unstable dynamic regimes were observed for the liquid surface oscillation, according to the probe position. Nevertheless, qualitative descriptions of interesting variables, such as the liquid response amplitude and phase, have been developed. Stable dynamic regimes are depicted by a constant surface oscillation amplitude an phase, trajectories in the phase planes that are close to the limiting cycles. The main characteristic of

this kind of behaviors is the clear periodicity of all the variables, indicating the ability of the system to entirely dissipate the amount of energy injected by the probe approach. Unstable dynamic regimes present a "chaotic" behavior, diverging from the limiting cycles in the phase planes, and showing an oscillation amplitude and phase that increases abruptly in time. In this case, the amount of energy injected by the probe surpasses the threshold amount that the thin-film can dissipate during a cycle. Therefore, the stokage of energy, via an augmentation of the curvature and of the deformation volume, increases each cycle, until at a certain moment, the surface "jumps-to-contact" the probe. Quasi-stable regimes indicate that for the number of simulated cycles, neither the complete divergence nor the arrival to a permanent periodic state has been observed. In fact, this kind of behavior is merely indistinguishable for the simulation times. The transition between the stable and unstable types of evolutions should be determined by the probe oscillation parameters, W_D amplitude, D_a time-average distance and ω_D frequency. A parametric study of the phenomenon is currently in progress.

In brief, based on numerical and theoretical analysis, some understanding has been gain on the probe/liquid interaction regimes. The pursue of the adequate experimental conditions, required to perform local probe measurement on liquid interfaces has begun.

Perspectives

Our probe/liquid static interaction model was the first step toward the acquisition of quantitative data from local probe measurements over liquid surfaces. A first order stability criterion was yielded as a result. The development of a dynamic interaction model was the natural second step, in order to understand the effect of the oscillating probe over the liquid surface shape. This stage has not been accomplished in the present thesis. Only preliminary results have been reported. Nevertheless, the foundations for a physical understanding have been established, and a parametric study is currently in progress. Based on the presented results and the observed trends of the ongoing simulations, we expect to find a shorter transition zone between stable and unstable behaviors for larger probe oscillation amplitudes. The comparison of the phase shift versus the number of cycles will be the most interesting way to compare the results for different combination of parameters W_D^*, D_a^* and C_a. As well, simulations with a larger probe radius $R = 10^{-7}$ m, but the same film thickness $E = 10^{-8}$ m are running. These preliminary results and its corresponding analysis will be available in the next months, and we expect to publish them soon. Nevertheless, this result will only provide a second order stability criterion. In a real AFM situation, the deformation of the liquid surface may influence the amplitude and phase of the probe oscillation. Therefore, the third step of this work should concern the analysis of a real probe/liquid coupling.

In turn, when a surface imaging is performed, there exists a supplementary degree of freedom that we have not considered here. The lateral displacement of the probe should have consequences on the surface behavior, especially when the oscillation amplitude is small. Phenomena arising from this situation, like wave resistance or wave interference, should have an impact on the optimal lateral scanning speed.

Bibliography

J.P. Aimé, R. Boisgard, L. Nony, and G. Couturier. Nonlinear dynamic behavior of an oscillating tip-microlever system and contrast at the atomic scale. *Phys. Rev. Lett.*, 82(17):3388–3391, 1999a.

J.P. Aimé, D. Michel, R. Boisgard, and L. Nony. Growth kinetics of a nanoprotuberance under the action of an oscillating nanotip. *Phys. Rev. B*, 59(3):2407–2416, 1999b.

J.P. Aimé, R. Boisgard, L. Nony, and G. Couturier. Influence of noncontact dissipation in the tapping mode: Attempt to extract quantitative information on the surface properties with the local force probe method. *J. Chem. Phys.*, 114(11):4945–4954, 2001.

A.M. Ardekani and D.D. Joseph. Instability of stationary liquid sheets. *Proc. Natl. Acad. Sci.*, 106(13): 4992–4996, 2009.

C. Argento and R.H. French. Parametric tip model and force-distance relation for hamaker constant determination from atomic force microscopy. *J. Appl. Phys.*, 80(11):6081–6090, 1996.

A.H. Barber, S.R. Cohen, and H.D. Wagner. Static and dynamic wetting measurements of single carbon nanotubes. *Phys. Rev. Lett.*, 92:186103, 2004.

J. Becker and G. Grün. The thin-film equation: Recent advances and some new perspectives. *J. Phys.: Condens. Matter*, 17:S291–S307, 2005.

F. Behroozi, B. Lambert, and B. Buhrow. Direct measurement of the attenuation of capillary waves by laser interferometry: Noncontact determination of viscosity. *Appl. Phys. Lett.*, 78:2399, 2001.

F. Behroozi, J. Smith, and W. Even. Stokes' dream: Measurement of fluid viscosity from the attenuation of capillary waves. *Am. J. Phys.*, 78:1165–1169, 2010.

M. Benzaquen, T. Salez, and E. Raphaël. Intermediate asymptotics of the capillary-driven thin-film equation. *Eur. Phys. J. E*, 36:13082–3, 2013.

J.K. Berg, C.M. Weber, and H. Riegler. Impact of negative line tension on the shape of nanometer-size sessile droplets. *Phys. Rev. Lett.*, 105:076103, 2010.

L. Bergstrom. Hamaker constants of inorganic materials. *Adv. Colloid Interface Sci.*, 70:125–169, 1997.

B. Bhushan. *Handbook of nanotechnology*. Springer, 2004.

B. Bhushan and Qi J. Phase constrast imaging of nanocomposite and molecularly thick lubricant films in magnetic media. *Nanotechnology*, 14(8):886–895, 2003.

G. Binnig and C.F. Quate. Atomic force microscope. *Phys. Rev. Lett.*, 56(9):930–933, 1986.

R. Boisgard, D. Michel, and J.P. Aimé. Hysteresis generated by attractive interaction: Oscillating behavior of a vibrating tip-microlever system near a surface. *Surf. Sci.*, 401:199–205, 1998.

R. Boisgard, J.P. Aimé, and G. Couturier. Surface mechanical instabilities and dissipation under the action of an oscillating tip. *Surf. Sci.*, 511:171–182, 2002.

R. Borcia, S. Menzel, M. Bestehorn, S. Karpitschka, and H. Riegler. Delayed coalescence of droplets with miscible liquids: Lubrication and phase field theories. *Eur. Phys. J. E*, 34:11024–9, 2011.

J. Bowen and D. Cheneler. A dynamic model of the jump-to phenomenon during afm analysis. *Langmuir*, 28:17273–17286, 2012.

J.C. Butcher. *Numerical methods for odrinary differential equations.* John Wiley and Sons, second edition, 2008.

H.J. Butt. A technique for measuring the force between a colloidal particle in water and a bubble. *J. Colloid Interface Sci.*, 166:109–117, 1994.

H.J. Butt and Jaschke M. Calculation of thermal noise in atomic force microscopy. *Nanotechnology*, 6 (1):1–7, 1995.

H.J. Butt, B. Cappella, and M. Kappl. Force measurements with the atomic force microscope: Technique, interpretation and applications. *Surf. Sci. Rep.*, 59:1–152, 2005.

B. Capella and G. Dietler. Force-distance curves by atomic force microscopy. *Surf. Sci. Rep.*, 34:1–104, 1999.

A. Checco and P. Guenoun. Nonlinear dependence of the contact angle of nanodroplets on contact line curvature. *Phys. Rev. Lett.*, 91:186101, 2003.

A. Checco, H. Schollmeyer, J. Daillant, and P. Guenoun. Nanoscale wettability of self-assembled monolayers investigated by noncontact atomic force micrscopy. *Langmuir*, 22:116–126, 2006.

N. Chen and B. Bhushan. Atomic force microscopy studies of conditioner thickness distribution and binding interactions on the hair surface. *J. Microsc.*, 221:203–215, 2005.

N. Chen, T. Kuhl, R. Tadmor, Q. Lin, and J. Israelachvili. Large deformations during the coalescence of fluid interfaces. *Phys. Rev. Lett.*, 92(2):024501, 2004.

A.D. Chepelianskii, F. Chevy, and E. Raphaël. Capillary-gravity waves generated by a slow moving object. *Phys. Rev. Lett.*, 100:074504, 2008.

H.K. Christenson. Capillary condensation due to van der waals attraction in wet slits. *Phys. Rev. Lett.*, 73:1821–1824, 1994.

F. Closa, A.D. Chepelianskii, and E. Raphaël. Capillary-gravity waves generated by a sudden object motion. *Phys. Fluids*, 22:052107, 2010.

F.P.A. Cortat and S.J. Miklavcic. How closely can a solid approach an air-water surface without becoming wet? *Phys. Rev. E*, 68:052601, 2003.

F.P.A. Cortat and S.J. Miklavcic. Using stable and unstable profiles to deduce deformation limits of the air-water interface. *Langmuir*, 20:3208–3220, 2004.

G. Couturier, R. Boisgard, L. Nony, and J.P. Aimé. Noncontact atomic force microscopy: Stability criterion and dynamical responses of the shift of frequency and damping signal. *Rev. Sci. Instrum.*, 74(5):2726–2734, 2003.

J. Crassous, E. Charlaix, H. Gayvallet, and J. L. Loubet. Experimental study of a nanometric liquid bridge with a surface force apparatus. *Langmuir*, 9:1995–1998, 1993.

J. Crassous, M. Ciccotti, and E. Charlaix. Capillary force between wetted nanometric contacts and its application to atomic force microscopy. *Langmuir*, 27:3468–3473, 2011.

K.B. Crozier, G.G. Yaralioglu, F.L. Degertekin, J.D. Adams, and S.C. Minne. Thin film characterization by atomic force microscopy at ultrasonic frequencies. *Appl. Phys. Lett.*, 76:1950–1952, 2000.

R.R. Dagastine, R. Manica, S.L. Carnie, D.Y.C. Chan, G.W. Stevens, and F. Grieser. Dynamic forces between two deformable oil droplets in water. *Science*, 313:210–213, 2006.

R.R. Dagastine, G.B. Webber, R. Manica, G.W. Stevens, F. Grieser, and D.Y.C. Chan. Viscosity effects on hydrodynamic drainage force measurements involving deformable bodies. *Langmuir*, 26:11921–11927, 2010.

B. Dai and G. Leal. Disjoining pressure for nonuniform thin films. *Phys. Rev. E*, 78:061602, 2008.

R.H. Davis, J.-M. Serayssol, and E.J. Hinch. The elastohydrodynamic collision of two spheres. *J. Fluid Mech.*, 163:479–497, 1986.

R.H. Davis, J.A. Schonberg, and J.M. Rallison. The lubrication force between two viscous drops. *Phys. Fluids A*, 1(1):77–81, 1989.

P.-G. de Gennes. Wetting: Static and dynamics. *Rev. Mod. Phys.*, 57(3):827–863, 1985.

P.-G. de Gennes, F Brochard-Wyart, and D. Quere. *Capillarity and wetting phenomena: Drops, Bubbles, Pearls, Waves*. Springer, 2003.

B.V. Deryaguin. Effect of surface forces on the properties of boundary and thin layers of liquids and disperse systems. *Prog. Surf. Sci.*, 43:166–185, 1993.

M.E. Diaz, J. Fuentes, R.L. Cerro, and Savage M.D. An analytical solution for a partially wetting puddle and the location of the static contact angle. *J. Colloid Interface Sci.*, 348:232–239, 2010.

S. Eichenlaub, C. Chan, and S.P. Beaudoin. Hamaker constants in integrated circuit metalization. *J. Colloid Interface Sci.*, 248:389–397, 2002.

A. Fery, T. Pompe, and S. Herminghaus. Nanometer resolution of liquid surface topography by scanning force microscopy. *J. Adhesion Sci. Technol.*, 13(10):1071–1083, 1999.

M.L. Forcada. Instability in a system of two interacting liquid films: Formation of liquid bridges between solid surfaces. *J. Chem. Phys.*, 98(1):638–643, 1993.

M.L. Forcada, N.R. Arista, A. Gras-Marti, H.M. Urbassek, and Garcia-Molina R. Interaction between a charged or neutral particle and a semi-infinite nonpolar dielectris liquid. *Phys. Rev. B*, 44(15):052601, 1991a.

M.L. Forcada, M.M. Jakas, and A. Gras-Marti. On liquid-film thickness measurements with the atomic-force microscope. *J. Chem. Phys.*, 95(1):706–708, 1991b.

R. García and R. Pérez. Dynamic atomic force microscopy methods. *Surf. Sci. Rep.*, 47(6):197–301, 2002.

R. García and A. San Paulo. Attractive and repulsive tip-sample interaction regimes in tapping-mode atomic force microscopy. *Phys. Rev. B*, 60(7):4961–4967, 1999.

M. Guizar-Sicairos and J.C. Gutierrez-Vega. Computation of quasi-discrete hankel transforms of integer order for propagating optical wave fields. *J. Opt. Soc. Am. A*, 21(1):53–58, 2004.

H. C. Hamaker. The london-van der waals attraction between spherical particles. *Physica*, 4(10):1058–1072, 1937.

P.G. Hartley, F. Grieser, P. Mulvaney, and G.W. Stevens. Surface forces and deformation at the oil-water interface probed using afm force measurement. *Langmuir*, 15:7282–7289, 1999.

U. Hartmann. Van der waals interactions between sharp probes and flat sample surfaces. *Phys. Rev. B*, 43:2404–2407, 1991.

T. Havelock. Waves due to a floating sphere making periodic heaving oscillations. *Proc. R. Soc. A*, 231 (1184):1–7, 1955.

J.F. Hernandez-Sanchez, L.A. Lubbers, A. Eddi, and J.H. Snoeijer. Symmetric and asymmetric coalescence of drops on a substrate. *Phys. Rev. Lett.*, 109:184502, 2012.

L.M. Hocking. Waves produced by a vertically oscillating plate. *J. Fluid Mech.*, 179:267–281, 1987.

L.M. Hocking. The influence of intermolecular forces on thin fluid layers. *Phys. Fluids*, 5(4):793–799, 1993a.

L.M. Hocking. The spreading of drops with intermolecular forces. *Phys. Fluids*, 6(10):3224–3328, 1993b.

R.G. Horn, D.J. Bachmann, J.N. Connor, and S.J. Miklavcic. The effect of surface and hydrodynamic forces on the shape of a fluid drop approaching a solid surface. *J. Phys.: Condens. Matter*, 8:9483–9490, 1996.

J.L. Hutter and Bechhoefer J. Calibration of atomic-force microscope tips. *Rev. Sci. Instrum.*, 64(7): 1868–1873, 1993.

J. N. Israelachvili. *Intermolecular and surface forces*. Elsevier, 3rd edition, 2011.

B. Issenmann. *Deformations d'interfaces fluides par la pression de radiation acoustique*. PhD thesis, Université Bordeaux I, 2007.

B. Issenmann, R. Wunenburger, S. Manneville, and J.P. Delville. Bistability of a compliant cavity induced by acoustic radiation pressure. *Phys. Rev. Lett.*, 97:4, 2006.

B. Issenmann, A. Nicolas, R. Wunenburger, S. Manneville, and J.P. Delville. Deformation of acoustically transparent fluid interfaces by the acoustic radiation pressure. *Europhys. Lett.*, 83:6, 2008.

J. Kierzenka and L.F. Shampine. A bvp solver based on residual control and the matlab pse. *ACM Transactions on Mathematical Software (TOMS)*, 27(3):299–316, 2001.

W.D. Kim. On the hramonic oscillations of a rigid body on a free surface. *J. Fluid Mech.*, 21:427–451, 1965.

E. Klaseboer, J.Ph. Chevaillier, C. Gourdon, and O. Masbernat. Film drainage between colliding drops at constant approach velocity: Experiments and modeling. *J. Colloid Interface Sci.*, 229:274–285, 2000.

L. Kuipers and J.W.M. Frenken. Jump to contact, neck formation and surface melting in the scanning tunneling microscope. *Phys. Rev. Lett.*, 70(25):3907–3910, 1993.

L. Kuipers, M.S. Hoogeman, and J.W.M. Frenken. Jump to contact and neck formation between pb surfaces and a stm tip. *Surf. Sci.*, 340:231–244, 1995.

U. Landman, W.D. Luedtke, N.A. Burnham, and R.J. Colton. Atomistic mechanisms and dynamics of adhesion, nanoidentation, and fracture. *Science*, 248:454–461, 1990.

M. Lantz, Y.Z. Liu, X.D. Cui, H. Tokumoto, and S.M. Lindsay. Dynamic force microscopy in fluid. *Surf. Interface Anal.*, 27:354–360, 1999.

R. Ledesma-Alonso, D. Legendre, and P. Tordjeman. Nanoscale deformation of a liquid surface. *Phys. Rev. Lett.*, 108:106104, 2012a.

R. Ledesma-Alonso, P. Tordjeman, and D. Legendre. Multiscale deformation of a liquid surface in interaction with a nanoprobe. *Phys. Rev. E*, 85:061602, 2012b.

R. Ledesma-Alonso, D. Legendre, and P. Tordjeman. Afm tip effect on a thin liquid film. *Langmuir*, 29: 7749–7757, 2013.

J. Lenhard. Surprised by a nanowire: Simulation, control and understanding. *Phylosophy of Science*, 73:605–616, 2006.

S. Leroy and E. Charlaix. Hydrodynamic interactions for the measurement of thin film elastic properties. *J. Fluid Mech.*, 674:389–407, 2011.

G. Leveque, P. Girard, S. Belaidi, and G. Cohen-Solal. Effects of air damping in noncontact resonant force microscopy. *Rev. Sci. Instrum.*, 68(11):4137–4144, 1997.

T.-D. Li and E. Riedo. Nonlinear viscoelastic dynamics of nanoconfined wetting liquids. *Phys. Rev. Lett.*, 100:106102, 2008.

T.-D. Li, J. Gao, R. Szoszkiewicz, U. Landman, and E. Riedo. Structured and viscous water in sub-nanometer gaps. *Phys. Rev. B*, 75:115415, 2007.

M.J. Lighthill. Group velocity. *IMA J. Appl. Math.*, 1(1):1–28, 1965.

G.V. Lubarski, M.R. Davidson, and R.H. Bradley. Particle-surface capillary forces with disjoining pressure. *Phys. Chem. Chem. Phys.*, 8:2525–2530, 2006.

S. N. Magonov and D. H. Reneker. Characterization of polymer surfaces with atomic force microscopy. *Annu. Rev. Mater. Sci.*, 27:175–222, 1997.

A. Marmur. Tip-surface capillary interactions. *Langmuir*, 9:1922–1926, 1993.

C.M. Mate, M.R. Lorenz, and V.J. Novotny. Atomic force microscopy of polymeric liquid films. *J. Chem. Phys.*, 90(12):7550–7555, 1989.

S.J. Miklavcic, R.G. Horn, and D.J. Bachmann. Colloidal interaction between a rigid solid and a fluid drop. *J. Chem. Phys.*, 99:16357–16364, 1995.

J. Miles. Capillary-viscous forcing of surface waves. *J. Fluid Mech.*, 219:635–646, 1990.

A. Moosavi, M. Rauscher, and S. Dietrich. Size dependent motion of nanodroplets on chemical steps. *J. Chem. Phys.*, 129(4):044706, 2008.

K. Mougin and Haidara H. Wetting of liquid films at nanoscale heterogeneous surfaces. *Europhys. Lett.*, 61(5):660–666, 2003.

S.A. Nespolo, D.Y.C. Chan, F. Grieser, P.G. Hartley, and G.W. Stevens. Forces between a rigid probe particle and a liquid interface: Comparison between experiments and theory. *Langmuir*, 19:2124–2133, 2003.

L. Nony, R. Boisgard, and J.P. Aimé. Nonlinear dynamical properties of an oscillating tip-cantilever system in tapping mode. *J. Chem. Phys.*, 111(4):1615–1627, 1999.

L. Nony, R. Boisgard, and J.P. Aimé. Stability criterions of an oscillating tip-cantilever system in dynamic force microscopy. *Eur. Phys. J. B*, 24:221–229, 2001.

A. Oron, S.H. Davis, and S.G. Bankoff. Long-scale evolution of thin liquid films. *Rev. Mod. Phys.*, 69 (3):931–980, 1997.

F. M. Orr, L. E. Scriven, and A. P. Rivas. Pendular rings between solids: Meniscus properties and capillary force. *J. Fluid Mech.*, 67:723–742, 1975.

T. Pompe and S. Herminghaus. Three-phase contact line energetics from nanoscale liquid surface topographies. *Phys. Rev. Lett.*, 85:1930–1933, 2000.

T. Pompe, A. Fery, and S. Herminghaus. Imaging liquid structures on inhomogeneous surfaces by scanning force microscopy. *Langmuir*, 14:2585–2588, 1998.

D.B. Quinn, J. Feng, and H.A. Stone. Analytical model for the deformation of a fluid-fluid interface beneath an afm probe. *Langmuir*, 29:1427–1434, 2013.

E. Raphaël and P.-G. de Gennes. Capillary gravity waves caused by a moving disturbance: Wave resistance. *Phys. Rev. E*, 53:3448–3455, 1996.

G. Reiter, A. Sharma, A. Casoli, M.-O. David, R. Khanna, and P. Auroy. Thin film instability induced by long-range forces. *Langmuir*, 15:2551–2558, 1999.

D. Richard and E. Raphaël. Capillary-gravity waves: The effect of viscosity on the wave resistance. *Europhys. Lett.*, 48(1):49–52, 1999.

B.Y. Rubinstein and A.M. Leshansky. Rupture of thin liquid films: Generalization of weakly nonlinear theory. *Phys. Rev. E*, 83:031603, 2011.

E. Ruckenstein and R.K. Jain. Spontaneous rupture of thin liquid films. *J. Chem. Soc. Faraday Trans.*, 70:132–146, 1973.

J.E. Sader. Frequency response of cantilever beams immersed in viscous fluids with applications to the atomic force microscope. *J. Appl. Phys.*, 84(1):64–76, 1998.

E. Sahagún, P. García-Mochales, G.M. Sacha, and J.J. Sáenz. Energy dissipation due to capillary interactions: Hydrophobicity maps in force microscopy. *Phys. Rev. Lett.*, 98(17):4, 2007.

M. Saint Jean, S. Hudlet, C. Guthmann, and Berger J. Van der waals and capacitive forces in atomic force microscopies. *J. Appl. Phys.*, 86(9):5245–5248, 1999.

T. Salez, J.D. McGraw, O. Bäumchen, K. Dalnoki-Veress, and E. Raphaël. Capillary-driven flow induced by a stepped perturbation atop a viscous film. *Phys. Fluids*, 24(10):102111, 2012.

S. Santos, L. Guang, T. Souier, K. Gadelrab, M. Chiesa, and N.H. Thomson. A method to provide rapid in situ determination of tip radius in dynamic atomic force microscopy. *Rev. Sci. Instrum.*, 83:043707, 2012.

W.W. Scott and B. Bhushan. Use of phase imaging in atomic force microscopy for measurement of viscoelastic contrast in polymer nanocomposites and molecularly thick lubricant films. *Ultramicroscopy*, 97:151–169, 2003.

R. Seemann, S. Herminghaus, and K. Jacobs. Dewetting patterns and molecular forces: A reconciliation. *Phys. Rev. Lett.*, 86(24):5534–5537, 2001.

L.F. Shampine, I. Gladwell, and S. Thompson. *Solving ODEs with MATLAB*. Cambridge University Press, 2003.

J. N. Sharpe. *Handbook of experimental solid mechanics*. Springer, 2008.

A. Shedulko. Thin liquid films. *Advan. Colloid Interface Sci.*, 1:391–464, 1972.

D.P.E. Smith. Limits of force microscopy. *Rev. Sci. Instrum.*, 66(5):3191–3195, 1995.

J.H. Snoeijer and B. Andreotti. A microscopic view on contact angle selection. *Phys. Fluids*, 20:057101, 2008.

P. Tordjeman, E. Papon, and J.J. Villenave. Squeeze elastic deformation and contact area of a rubber adhesive. *J. Chem. Phys.*, 113(23):712–716, 2000.

D. Vaynblat, J.R. Lister, and T.P. Witelski. Rupture of thin viscous films by van de walls forces: Evolution and self-similarity. *Phys. Fluids*, 13:1130–1140, 2001.

J. Visser. On hamaker constants: A comparison between hamaker constants and lifshitz-van der waals constants. *Advan. Colloid Interface Sci.*, 3:331–363, 1972.

Y.Z. Wang, D. Wu, X.M. Xiong, and J.X. Zhang. Universal and scaling behavior at the proximity of the solid to the deformable air-water interface. *Langmuir*, 23:12119–12124, 2007.

Y.Z. Wang, B. Wang, X.M. Xiong, and J.X. Zhang. Spherical solid model system: Exact evaluation of the van der waals interaction between a microscopic or submacroscopic spherical solid and a deformable fluid interface. *Surf. Sci.*, 605:528–538, 2011.

T. Yi and H. Wong. Theory of slope-dependent disjoining pressure with application to lennard-jones liquid films. *J. Colloid Interface Sci.*, 313:579–591, 2007.

R. Zenit and D. Legendre. The coefficient of restitution for air bubbles colliding against solid walls in viscous liquids. *Phys. Fluids*, 21(8):083306, 2009.

L. Zitzler, S. Herminghaus, and F. Mugele. Capillary forces in tapping mode atomic force microscopy. *Phys. Rev. B*, 66:155436, 2002.

Appendix

Appendix A

Numerical method for the equilibrium modified Young-Laplace equation

The non-linear ODEs system, given by eqs.(1.39), can be represented as:

$$\mathbf{y}' = \frac{d\mathbf{y}}{dr^*} = \mathbf{f}\left(r^*, \mathbf{y}\right), \qquad 0 \leq r^* \leq \alpha\lambda^*_{CF}, \tag{A.1}$$

where:

$$\mathbf{y} = \begin{bmatrix} \eta^* \\ u^* \end{bmatrix} \qquad\qquad \mathbf{f} = \begin{bmatrix} u^* \\ \dfrac{du^*}{dr^*} \end{bmatrix}$$

and:

$$\frac{du^*}{dr^*} = \begin{cases} \dfrac{1}{2}\left[B_o\xi\eta^* + \dfrac{AH_a}{8\left(E^*\right)^3}\Pi^*_{ls} + H_a\Pi^*_{pl}\right] & \text{for } r^* = 0 \\ -\dfrac{u^*}{r^*}\left[\left(u^*\right)^2 + 1\right] + \left[B_o\xi\eta^* + \dfrac{AH_a}{8\left(E^*\right)^3}\Pi^*_{ls} + H_a\Pi^*_{pl}\right]\left[\left(u^*\right)^2 + 1\right]^{3/2} & \text{for } r^* > 0. \end{cases} \tag{A.2}$$

The system is subject to the two-point BCs, stated in eqs.(1.40), which are now represented as:

$$\mathbf{b}\left(\mathbf{y}\left(0\right), \mathbf{y}\left(\alpha\lambda^*_{CF}\right)\right) = 0. \tag{A.3}$$

The spatial domain is divided in $N-1$ subintervals $\left[r^*_n, r^*_{n+1}\right]$ with $n = 1, 2, \ldots, N$, being N the number of mesh points. In addition, the function $\mathbf{S}\left(r^*\right)$ is introduced, corresponding to a piecewise cubic polynomial that collocates at the ends of each subinterval and at the midpoint, within the mesh $0 = r^*_1 < r^*_2 < \cdots < r^*_N = \alpha\lambda^*_{CF}$. Explicitly, one has $\mathbf{y}_n = \mathbf{S}\left(r^*_n\right) \approx \mathbf{y}\left(r^*_n\right)$, which also shows first derivative continuity at the endpoints, $\mathbf{y}'_n = \mathbf{S}'\left(r^*_n\right)$.

With the distance between mesh points defined as $\Delta r^*_n = r^*_{n+1} - r^*_n$, the Simpson formula using analytical condensation (Butcher, 2008) is written as:

$$\begin{aligned} \tilde{\mathbf{y}} &= \frac{1}{2}\left[\mathbf{y}_{n+1} + \mathbf{y}_n\right] - \frac{\Delta r^*_n}{8}\left[\mathbf{f}\left(r^*_{n+1}, \mathbf{y}_{n+1}\right) - \mathbf{f}\left(r^*_n, \mathbf{y}_n\right)\right] \\ \tilde{r} &= r^*_n + \frac{\Delta r^*_n}{2} \\ \tilde{\mathbf{f}} &= \mathbf{f}\left(\tilde{r}, \tilde{\mathbf{y}}\right) \\ \mathbf{y}_{n+1} &= \mathbf{y}_n + \frac{\Delta r^*_n}{6}\left[\mathbf{f}\left(r^*_n, \mathbf{y}_n\right) + 4\tilde{\mathbf{f}} + \mathbf{f}\left(r^*_{n+1}, \mathbf{y}_{n+1}\right)\right]. \end{aligned} \tag{A.4}$$

If $\Delta r^* = max\left\{\Delta r_n^*\right\}$, the mesh is bounded above $\Delta r^*/\Delta r_n^* \leq 1$, and the Simpson's formula is uniformly $O\left\{\left(\Delta r^*\right)^5\right\}$ accurate at all the collocation points.

The application of the condensed Simpson method leads to the system of algebraic equations:

$$\mathbf{F}\left(X, \mathbf{Y}\right) = 0, \tag{A.5}$$

where:

$$\begin{aligned} X &= \left[r_0^*, r_1^*, \ldots, r_N^*\right]^T \\ \mathbf{Y} &= \left[\mathbf{y}_0, \mathbf{y}_1, \ldots, \mathbf{y}_N\right]^T \\ F_0\left(X, \mathbf{Y}\right) &= \mathbf{b}\left(\mathbf{y}_0, \mathbf{y}_N\right) \\ F_n\left(X, \mathbf{Y}\right) &= \mathbf{y}_n - \mathbf{y}_{n-1} - \frac{\Delta r_{n-1}^*}{6}\left[\mathbf{f}_{n-1} + 4\mathbf{f}_{n-1/2} + \mathbf{f}_n\right], \end{aligned} \tag{A.6}$$

for $n = 1, 2, \ldots, N$, and:

$$\begin{aligned} \mathbf{f}_n &= \mathbf{f}\left(r_n^*, \mathbf{y}_n\right) \\ \mathbf{f}_{n-1/2} &= \mathbf{f}\left(r_{n-1}^* + \frac{\Delta r_{n-1}^*}{2}, \frac{\mathbf{y}_n + \mathbf{y}_{n-1}}{2} - \frac{\Delta r_{n-1}^*}{8}\left[\mathbf{f}\left(r_n^*, \mathbf{y}_n\right) - \mathbf{f}\left(r_{n-1}^*, \mathbf{y}_{n-1}\right)\right]\right). \end{aligned} \tag{A.7}$$

The system of $2N$ equations given by eqs.(A.6) is solved at each iteration with a classic Newton's method:

$$\mathbf{Y}^{j+1} = \mathbf{Y}^j - \left[\left.\frac{\partial \mathbf{F}}{\partial \mathbf{Y}}\right|^j\right]^{-1} \mathbf{F}^j, \tag{A.8}$$

using finite differences to approximate the Jacobian $\partial\mathbf{F}/\partial\mathbf{Y}$ at the jth iteration, in order to find successively the solution vector $\mathbf{Y}^{j+1}$. The educated guess given in eqs.(1.41) is employed as the first vector guess $\mathbf{Y}^0$.

As well, the function $\mathbf{S}\left(r^*\right)$ is the natural continuous extension of the Simpson formula because, at both end points and the midpoint of each subinterval, one has:

$$\begin{aligned} \mathbf{S}'\left(r_n^*\right) &= \mathbf{f}\left(r_n^*, \mathbf{S}\left(r_n^*\right)\right) \\ \mathbf{S}'\left(r_{n+1/2}^*\right) &= \mathbf{f}\left(r_n^* + \frac{\Delta r_n^*}{2}, \mathbf{S}\left(r_n^* + \frac{\Delta r_n^*}{2}\right)\right) \\ \mathbf{S}'\left(r_{n+1}^*\right) &= \mathbf{f}\left(r_{n+1}^*, \mathbf{S}\left(r_{n+1}^*\right)\right). \end{aligned} \tag{A.9}$$

Then the coefficients of the cubic polynomial are easily computed and, at each iteration, the solution can be interpolated anywhere within the range $r^* \in [0, \alpha\lambda_{CF}^*]$.

The accuracy of the approximation, obtained with the solver *bvp4c.m*, results from an algorithm on the control of residuals. The residual of the polynomial solution is given by:

$$\sigma\left(r^*\right) = \mathbf{S}'\left(r^*\right) - \mathbf{f}\left(r^*, \mathbf{S}\left(r^*\right)\right), \qquad 0 \leq r^* \leq \alpha\lambda_{CF}^*, \tag{A.10}$$

and $\sigma_{BC} = \mathbf{b}\left(\mathbf{S}\left(0\right), \mathbf{S}\left(\alpha\lambda_{CF}^*\right)\right)$ in the boundaries. Then:

$$\sigma\left(r^*\right) = \mathbf{S}'\left(r^*\right) - y'\left(r^*\right) + O\left\{\left(\Delta r^*\right)^4\right\}, \tag{A.11}$$

and on each subinterval $\left[r_n^*, r_{n+1}^*\right]$, the residual estimation is calculated as:

$$\left\|\sigma\left(r^*\right)\right\|_n = \int_{r_n^*}^{r_{n+1}^*} \left\|\sigma\left(r^*\right)\right\|^2 dr^*. \tag{A.12}$$

When running the MATLAB routine, iterations are made until the desired tolerance on the residual is obtained, $\max\left\{\left\|\sigma\left(r^*\right)\right\|_n\right\} \leq \sigma_{Tol}$.

Appendix B

Complete analysis on the static apex

At the vertical axis $r^* = 0$, the position of the sphere center can be written as a function of the apex product $\xi\eta_0^*$ and the peak curvature κ_0^*. Solving eq.(1.17b), for the dimensionless probe position D^*, yields the relationship:

$$D^* = \xi\eta_0^* + \sqrt{1 + \left[f\left(\xi\eta_0^*, \kappa_0^*\right)\right]^{-1/3}}, \tag{B.1}$$

in which the involved function corresponds to the evaluation of the probe/liquid interaction potential at the apex position:

$$f\left(\xi\eta_0^*, \kappa_0^*\right) = \Pi_{pl}^*\Big|_0.$$

As a consequence, from eq.(1.16) and for $\Delta P^* = 0$, the formal definition of this function is:

$$f\left(\xi\eta_0^*, \kappa_0^*\right) = \frac{1}{H_a}\left[2\kappa_0^* + B_o\xi\eta_0^* + \frac{AH_a}{8\left(E^*\right)^3}\Pi_{ls}^*\Big|_0\right]. \tag{B.2}$$

Moreover, when the deformation-to-thickness ratio is small $\xi\eta^*/E^* \ll 1$, the liquid/substrate interaction at the apex position $\Pi_{ls}^*\Big|_0$ is approximated with the first-order expansion introduced in eq.(1.24). Therefore, eq.(B.2) takes the approximate form:

$$f\left(\xi\eta_0^*, \kappa_0^*\right) \simeq \frac{1}{H_a}\left[2\kappa_0^* + \frac{\xi\eta_0^*}{\left(\lambda_{CF}^*\right)^2}\right]. \tag{B.3}$$

As it can be deduced from eq.(B.3), the film thickness impact is not restricted to reduce the modified capillary length λ_{CF}^*. It provokes indirect consequences on the apex product $\xi\eta_0^*$ and the peak curvature κ_0^*, and, by means of eq.(B.1), on the separation distance D^*. In addition, when $B_o \ll 1$, the term containing this parameter is negligible in comparison with the other elements of eq.(B.2), and $\lambda_{CF}^* \approx \lambda_F^*$ should be treated in eq.(B.3).

A comparison between eq.(2.8) and the binomial expansion (see Appendix D) of eq.(B.1) gives:

$$\varepsilon_0^* = \frac{1}{2\xi}\left[f\left(\xi\eta_0^*, \kappa_0^*\right)\right]^{-1/3} - \frac{1}{8\xi}\left[f\left(\xi\eta_0^*, \kappa_0^*\right)\right]^{-2/3} + O\left\{\frac{1}{\xi}\left[f\left(\xi\eta_0^*, \kappa_0^*\right)\right]^{-1}\right\} \tag{B.4}$$

which allows to calculate the reduced equilibrium gap, if the function $f\left(\xi\eta_0^*, \kappa_0^*\right)$ can be deduced. It is also possible to find a relationship between $\xi\eta_0^*$ and κ_0^*, which means that the function can be written only in terms of one variable, usually as $f\left(\xi\eta_0^*\right)$.

In this work, it has been confirmed that no solution of the problem can be found for shorter separation distances D^* than a threshold distance D_{min}^*. Additionally, at D_{min}^*, the apex position diverges $d\eta_0^*/dD^* \to \infty$ and, as a consequence, the derivative $dD^*/d\eta_0^* = 0$. Also, considering that:

$$\frac{d\left(\xi\eta_0^*\right)}{d\eta_0^*} = \xi + \eta_0^*\frac{d\xi}{d\eta_0^*},$$

and also knowing that, from the definition of the initial gap ξ, one has:

$$\frac{d\xi}{d\eta_0^*} = \frac{dD^*}{d\eta_0^*}.$$

Thus, differentiation of the function $f(\xi\eta_0^*)$ gives:

$$\frac{d\left[f\left(\xi\eta_0^*\right)\right]}{d\eta_0^*} = \left\{\frac{d\left(\xi\eta_0^*\right)}{d\left(\eta_0^*\right)}\right\}\frac{d\left[f\left(\xi\eta_0^*\right)\right]}{d\left(\xi\eta_0^*\right)},$$

which, calculated at $D^* = D^*_{min}$ yields:

$$\left.\frac{d\left[f\left(\xi\eta_0^*\right)\right]}{d\eta_0^*}\right|_{\xi_{crit},\eta^*_{0,max}} = \xi_{crit}\left.\frac{d\left[f\left(\xi\eta_0^*\right)\right]}{d\left(\xi\eta_0^*\right)}\right|_{\xi_{crit},\eta^*_{0,max}}.$$

To unearth the critical stable conditions D^*_{min}, ξ_{crit} and $\eta^*_{0,max}$, the minimum of eq.(B.1) is ascertained analytically . Consequently, making $dD^*/d\eta_0^* = 0$ yields the following equation:

$$\left[f'\left(\xi_{crit}\eta^*_{0,max}\right)\right]^2 = 36\xi^2_{crit}\left[f\left(\xi_{crit}\eta^*_{0,max}\right)\right]^{8/3}\left\{1+\left[f\left(\xi_{crit}\eta^*_{0,max}\right)\right]^{-1/3}\right\}, \tag{B.5}$$

where:

$$f'\left(\xi\eta_0^*\right) = \frac{d\left[f\left(\xi\eta_0^*\right)\right]}{d\left(\xi\eta_0^*\right)}.$$

Thus, with the knowledge of the function $f(\xi\eta_0^*)$, eq.(B.5) must be solved numerically to find the critical apex product $\xi_{crit}\eta^*_{0,max}$. Afterward, eq.(B.1) is once again used to determine the value of the threshold distance D^*_{min}, from which the critical initial gap $\xi_{crit} = D^*_{min} - 1$ is deduced and, finally, the maximum apex deformation $\eta^*_{0,max}$ is obtained.

Appendix C

Pseudo-spectral method for the thin-film equation

The first step of the proposed pseudo-spectral method consists in computing the Hankel transform of order zero of the involved functions. Therefore, a mesh in the spatial domain and another in the wavenumber domain should be generated. Consider the integer $\alpha > 1$, $\alpha\lambda^*_{CF}$ is the radial position whence the surface is expected to be unperturbed $\eta^*\left(r^* \geq \alpha\lambda^*_{CF}, t^*\right) = 0$, and ϑ is the cutoff wavenumber whence $\mathcal{N}^*\left(q \geq \vartheta, t^*\right) = 0$. In other words, $\eta^*\left(r^*, t^*\right)$ is distributed over the region $0 \leq r^* \leq \alpha\lambda^*_{CF}$, whereas $\mathcal{N}^*\left(q^*, t^*\right)$ is distributed over the wavenumber band $0 \leq q \leq \vartheta$. We should fix both α and ϑ, so the space-bandwidth product $S = 2\pi\alpha\lambda^*_{CF}\vartheta$ remains finite.

Following the procedure described in the literature (Guizar-Sicairos and Gutierrez-Vega, 2004), the discrete Hankel transform is obtained in terms of Fourier-Bessel series, being $J_0\left(x\right)$ the Bessel function of the first kind and order zero. The discretization of the spatial domain is given by the radial mesh point $r^*_n = \beta_n / \left(2\pi\vartheta\right)$, where $n = 1, 2, ..., N$ is a natural number, N is the total number of mesh points and β_n is the nth root of $J_0\left(x\right) = 0$. Similarly, the transform $\mathbb{H}_0$ is obtained at the spatial frequency mesh point $q_n = \beta_n / \left(2\pi\alpha\lambda^*_{CF}\right)$.

The expansion of $\mathcal{N}^*$ in terms of Bessel functions of the first kind and order zero, the Fourier-Bessel series, is given by:

$$\mathcal{N}^*\left(q^*, t^*\right) = \sum_{n=1}^{\infty} C_n J_0\left(\beta_n \frac{q}{\vartheta}\right), \tag{C.1}$$

where the coefficients of the series are given by:

$$C_n = \frac{2}{\vartheta^2\left[J_1\left(\beta_n\right)\right]^2} \int_0^{\vartheta} \mathcal{N}^*\left(q^*, t^*\right) J_0\left(\beta_n \frac{q}{\vartheta}\right) q^* dq^*, \tag{C.2}$$

which, using the definition of the inverse Hankel transform given in eq.(D.7), are approximated by:

$$C_n \simeq \frac{2}{\vartheta^2\left[J_1\left(\beta_n\right)\right]^2} \left\{\frac{1}{2\pi}\eta^*\left(\frac{\beta_n}{2\pi\vartheta}\right)\right\}. \tag{C.3}$$

Therefore, the discrete Hankel transform of $\eta*$ is given by:

$$\mathcal{N}^*\left(\frac{\beta_m}{2\pi\alpha\lambda^*_{CF}}, t^*\right) \simeq \frac{1}{\pi\vartheta^2} \sum_{n=1}^{N} \left\{\frac{J_0\left(\dfrac{\beta_m\beta_n}{S}\right)}{\left[J_1\left(\beta_n\right)\right]^2} \eta^*\left(\frac{\beta_n}{2\pi\vartheta}, t^*\right)\right\}, \tag{C.4}$$

and equivalently, the transform of the probe/liquid interaction is:

$$\mathcal{Q}^*\left(\frac{\beta_m}{2\pi\alpha\lambda^*_{CF}}, t^*\right) \simeq \frac{1}{\pi\vartheta^2} \sum_{n=1}^{N} \left\{\frac{J_0\left(\dfrac{\beta_m\beta_n}{S}\right)}{\left[J_1\left(\beta_n\right)\right]^2} \Pi^*_{pl}\left(\frac{\beta_n}{2\pi\vartheta}, t^*\right)\right\}. \tag{C.5}$$

Similarly, the Fourier-Bessel series of η^* in terms of Bessel functions of the first kind and order zero is:

$$\eta^*\left(r^*,t^*\right)=\sum_{m=1}^{\infty}G_m J_0\left(\beta_m\frac{r^*}{\alpha\lambda_{CF}^*}\right), \tag{C.6}$$

where β_m is the mth root of $J_0\left(x\right)=0$, and the coefficients are given by:

$$G_m=\frac{2}{\left(\alpha\lambda_{CF}^*\right)^2\left[J_1\left(\beta_m\right)\right]^2}\int_0^{\alpha\lambda_{CF}^*}\eta^*\left(r^*,t^*\right)J_0\left(\beta_m\frac{r^*}{\alpha\lambda_{CF}^*}\right)r^*dr^*, \tag{C.7}$$

which, using the definition of the Hankel transform given in eq.(D.6), are approximated by:

$$G_m\simeq\frac{2}{\left(\alpha\lambda_{CF}^*\right)^2\left[J_1\left(\beta_m\right)\right]^2}\left\{\frac{1}{2\pi}\mathcal{N}^*\left(\frac{\beta_m}{2\pi\alpha\lambda_{CF}^*},t^*\right)\right\}. \tag{C.8}$$

Therefore, the discrete inverse Hankel transform of $\mathcal{N}^*$ is obtained with:

$$\eta^*\left(\frac{\beta_n}{2\pi\vartheta},t^*\right)\simeq\frac{1}{\pi\left(\alpha\lambda_{CF}^*\right)^2}\sum_{m=1}^{N}\left\{\frac{J_0\left(\dfrac{\beta_n\beta_m}{S}\right)}{\left[J_1\left(\beta_m\right)\right]^2}\mathcal{N}^*\left(\frac{\beta_m}{2\pi\alpha\lambda_{CF}^*},t^*\right)\right\}. \tag{C.9}$$

Thence, recalling that $J_0\left(0\right)=1$, the surface apex position η_0^* is:

$$\eta_0^*\left(t^*\right)\simeq\frac{1}{\pi\left(\alpha\lambda_{CF}^*\right)^2}\sum_{m=1}^{N}\left\{\frac{1}{\left[J_1\left(\beta_m\right)\right]^2}\mathcal{N}^*\left(\frac{\beta_m}{2\pi\alpha\lambda_{CF}^*},t^*\right)\right\}, \tag{C.10}$$

the peak curvature is:

$$\kappa_0^*\left(t^*\right)\simeq\frac{\xi}{2\pi\left(\alpha\lambda_{CF}^*\right)^2}\sum_{m=1}^{N}\left\{\frac{\left(k_m^*\right)^2}{\left[J_1\left(\beta_m\right)\right]^2}\mathcal{N}^*\left(\frac{\beta_m}{2\pi\alpha\lambda_{CF}^*},t^*\right)\right\}, \tag{C.11}$$

and, using eq.(5.26), the temporal first derivative of the apex position is:

$$\frac{\partial\eta_0^*}{\partial t^*}\simeq\frac{-1}{\pi\left(\alpha\lambda_{CF}^*\right)^2}\sum_{m=1}^{N}\left\{\frac{1}{\left[J_1\left(\beta_m\right)\right]^2}\left[\nu_m^*\mathcal{N}^*\left(\frac{\beta_m}{2\pi\alpha\lambda_{CF}^*},t^*\right)+\frac{H_a}{\xi}\left(k_m^*\right)^2\mathcal{Q}^*\left(\frac{\beta_m}{2\pi\alpha\lambda_{CF}^*},t^*\right)\right]\right\}. \tag{C.12}$$

where:

$$k_m^*=\frac{\beta_m}{\alpha\lambda_{CF}^*} \tag{C.13}$$

$$\nu_m^*=\left(k_m^*\right)^2\left[\left(k_m^*\right)^2+\left(\lambda_{CF}^*\right)^{-2}\right]. \tag{C.14}$$

The separation between consecutive roots of $J_0\left(x\right)$, when $x\to\infty$, is approximately $\Delta\beta=\beta_n-\beta_{n-1}\approx\pi$. As a consequence, the separation between radial mesh points is $\Delta r_n^*\approx 1/\left(2\vartheta\right)$, the cutoff radial position is roughly given by $\alpha\lambda_{CF}^*\approx N\Delta r_n^*$. Therefore, the space-bandwidth product is $S\approx N\pi$ and the number of mesh point should be $N\geq 2\vartheta\alpha\lambda_{CF}^*$.

Both values α and ϑ are chosen according to the handled functions. For example, when applying the Hankel transform to Π_{pl}^*, which is nearly equal to zero $\Pi_{pl}^*\lesssim 10^{-12}$ for $r^*\geq 100$, leads to a value $\alpha\approx 5$ for a film of thickness $E^*=1$, because $\lambda_{CF}^*\approx 22$. Nevertheless, the other terms in eq.(5.26) should also be considered. It is logic to suppose that the surface deformation η^* attains a radial extension around $r^*\sim\lambda_{CF}^*$, then $\alpha=5$ is proposed. As well, it is observed that $\mathcal{Q}^*<1$ for $q\geq 2$, and its combination with the other variables and parameters in eq.(5.26) results even smaller. Therefore, it is also expected to observe $\mathcal{N}^*\simeq 0$ for $q\geq 2$. As a consequence, $\vartheta=2$, $S=10\pi\lambda_{CF}^*$ and $N\geq 10\lambda_{CF}^*$ are advised.

Summarizing, the Hankel transforms are calculated as follows:

$$\mathcal{N}_m^*\big|^j = \frac{1}{\pi\vartheta^2}\sum_{n=1}^{\infty}\left\{\frac{J_0\left(\frac{\beta_m\beta_n}{S}\right)}{\left[J_1\left(\beta_n\right)\right]^2}\eta_n^*\big|^j\right\} \tag{C.15}$$

$$\mathcal{Q}_m^*\big|^j = \frac{1}{\pi\vartheta^2}\sum_{n=1}^{\infty}\left\{\frac{J_0\left(\frac{\beta_m\beta_n}{S}\right)}{\left[J_1\left(\beta_n\right)\right]^2}\Pi_{pl,n}^*\big|^j\right\} \tag{C.16}$$

$$\Pi_{pl,n}^*\big|^j = \frac{-1}{\left[\left\{D^*\big|^{j+1} - \xi\eta_n^*\big|^j\right\}^2 + \left(r_n^*\right)^2 - 1\right]^3}, \tag{C.17}$$

where jth time step defined as $\Delta t^*\big|^{j+1} = t^*\big|^{j+1} - t^*\big|^j$. One should keep in mind that:

$$r_n^* = \beta_n/\left(2\pi\vartheta\right), \qquad q_m^* = \beta_m/\left(2\pi\alpha\lambda_{CF}^*\right), \tag{C.18}$$

$$k_m^* = 2\pi q_m^*, \qquad \nu_m^* = \left(k_m^*\right)^2\left[\left(k_m^*\right)^2 + \left(\lambda_{CF}^*\right)^{-2}\right]. \tag{C.19}$$

For the case of a static probe, the separation distance is obviously $D^*\big|^{j+1} = D_a^*$, whereas for an oscillating probe, it is given by:

$$D^*\big|^{j+1} = D_a^* + \xi W_D^*\cos\left(2\pi t^*\big|^{j+1}\frac{Ca}{\left(E^*\right)^3}\right), \tag{C.20}$$

with $t^*\big|^{j+1} = t^*\big|^j + \Delta t^*\big|^{j+1}$.

Once the Hankel transforms are known, one deals with the thin-film equation in the wavenumber domain. Eq.(5.26) is solved using a simple semi-implicit method, the combination of an explicit Euler method for the nonlinear term and an implicit Euler method for the linear term. The discretization by means of this approach gives the following expression:

$$\mathcal{N}_m^*\big|^{j+1} = \left[\frac{1}{1+\Delta t^*\big|^{j+1}\nu_m^*}\right]\mathcal{N}_m^*\big|^j - \left[\frac{H_a\Delta t^*\big|^{j+1}\left(k_m^*\right)^2}{\xi\left(1+\Delta t^*\big|^{j+1}\nu_m^*\right)}\right]\mathcal{Q}_m^*\big|^j, \tag{C.21}$$

where $n = 1, 2, ..., N$ is a natural number, N is the total number of mesh points in the wavenumber domain, j is the index denoting the evaluation of the variables at jth iteration, and $\Delta t^*\big|^j$ is the corresponding time step. The local truncation error at each iteration is proportional to the iteration time step, $O\left(\Delta t^*\big|^j\right)$.

After the iteration is performed, $\mathcal{N}^*\Big|^{j+1}$ is employed to calculate the apex speed:

$$\frac{\partial\eta_0^*}{\partial t^*}\Big|^{j+1} = \frac{-1}{\pi\left(\alpha\lambda_{CF}^*\right)^2}\sum_{m=1}^{N}\left\{\frac{1}{\left[J_1\left(\beta_m\right)\right]^2}\left[\nu_m^*\mathcal{N}_m^*\big|^{j+1} + \frac{H_a}{\xi}\left(k_m^*\right)^2\mathcal{Q}_m^*\big|^{j+1}\right]\right\}. \tag{C.22}$$

And finally, the inverse Hankel transform is applied to find the surface position, the apex position

and the peak curvature, as follows:

$$\eta_n^*\big|^{j+1} = \frac{1}{\pi\left(\alpha\lambda_{CF}^*\right)^2}\sum_{m=1}^{\infty}\left\{J_0\left(\frac{\beta_n\beta_m}{S}\right)\frac{\mathcal{N}_m^*\big|^{j+1}}{\left[J_1\left(\beta_m\right)\right]^2}\right\} \tag{C.23}$$

$$\eta_0^*\big|^{j+1} = \frac{1}{\pi\left(\alpha\lambda_{CF}^*\right)^2}\sum_{m=1}^{N}\left\{\frac{\mathcal{N}_m^*\big|^{j+1}}{\left[J_1\left(\beta_m\right)\right]^2}\right\} \tag{C.24}$$

$$\kappa_0\big|^{j+1} = \frac{\xi}{2\pi\left(\alpha\lambda_{CF}^*\right)^2}\sum_{m=1}^{N}\left\{\left(k_m^*\right)^2\frac{\mathcal{N}_m^*\big|^{j+1}}{\left[J_1\left(\beta_m\right)\right]^2}\right\}. \tag{C.25}$$

At $t^*\big|^0 = 0$, a flat unperturbed free surface was considered, thus the initial conditions are $\eta_n^*\big|^0 = \mathcal{N}_m^*\big|^0 = 0$, for any r_n^* and q_m^*. In addition, the initial time step was fixed to $\Delta t^* = 10^{-5}$ for the static probe case, whereas for the oscillating probe it was given by $\Delta t^* = 10^{-5}\left(E^*\right)^3/C_a$, 10^5 times smaller than the dimensionless oscillation period. Afterwards, based on the wave propagation distance, the successive time steps were numerically estimated with:

$$\Delta t^*\big|^{j+1} = \left[\frac{min\left(\eta^*\big|^{i-1}\right) - min\left(\eta^*\big|^{i-2}\right)}{min\left(\eta^*\big|^{j}\right) - min\left(\eta^*\big|^{i-1}\right)}\right]\Delta t^*\big|^{j}. \tag{C.26}$$

The maximum time step, employed to observe the dynamic evolution of the surface, was unbounded for the case of a static probe, whereas, for the case of an oscillating probe, it was limited by the value $\Delta t^* = 10^{-2}\left(E^*\right)^3/C_a$, a hundredth of the dimensionless oscillation period. Then, for the oscillating phenomenon, the truncation error is in the range $\sigma \in \left[O\left(10^{-4}/Ca\right), O\left(10^{-2}/Ca\right)\right]$.

Appendix D

Math tools

Binomial expansions

For any value of n, the binomial $1+x$ can be expanded, in the proximity of $x = x_0$, as

$$(1+x)^n = (1+x_0)^n \left[1 + n\left(\frac{x-x_0}{1+x_0}\right) + \frac{n(n-1)}{2}\left(\frac{x-x_0}{1+x_0}\right)^2 + \frac{n(n-1)(n-2)}{6}\left(\frac{x-x_0}{1+x_0}\right)^3 + \dots\right], \tag{D.1}$$

Then, for $n = 1/2$ and $x_0 = 0$, we have

$$\sqrt{1+x} = 1 + \frac{x}{2} - \frac{x^2}{8} + \frac{x^3}{16} + O\left\{x^4\right\}, \tag{D.2}$$

and, for $n = -3$ and $x_0 = 0$, we have

$$\frac{1}{(1+x)^3} = 1 - 3x + 6x^2 - 10x^3 + O\left\{x^4\right\}. \tag{D.3}$$

Taylor Expansion

The Taylor series expansion of the following logarithmic expression around $x = 0$ is given by:

$$\ln\left[1+\exp(-x)\right] \approx \ln[2] - x\frac{\exp(-x)}{[1+\exp(-x)]} + \frac{x^2}{2}\frac{\exp(-x)}{[1+\exp(-x)]^2} + O\left\{x^3\right\}, \tag{D.4}$$

therefore, multiplying the whole expansion by $1/x$, we have that:

$$\frac{1}{x}\ln\left[1+\exp(-x)\right] \approx \frac{1}{x}\ln[2] - \frac{\exp(-x)}{[1+\exp(-x)]} + x\left(\frac{1}{2}\frac{\exp(-x)}{[1+\exp(-x)]^2} + O\{x\}\right). \tag{D.5}$$

Hankel transform

Being q the spatial frequency or wavelength, the Hankel transform of order v is given by:

$$g(q) = \mathbb{H}_v\{f(r)\} = 2\pi\int_0^\infty f(r)\, J_v(2\pi qr)\, r dr, \tag{D.6}$$

while the inverse transform is given by:

$$f(r) = \mathbb{H}_v^{-1}\{g(q)\} = 2\pi\int_0^\infty g(q)\, J_v(2\pi qr)\, q dq, \tag{D.7}$$

where $J_v(x)$ is a v order Bessel function of the first kind.

For any $F = F(r,t)$, the Hankel transform $r \to q$ of F is given by:

$$\mathbb{H}_v\left\{\frac{\partial F}{\partial t}\right\} = \frac{\partial}{\partial t}\mathbb{H}_v\left\{F\right\}. \tag{D.8}$$

In addition, for any $f = f(r)$, one has the Hankel transform of the particular operator:

$$\mathbb{H}_v\left\{\frac{1}{r}\frac{d}{dr}\left[r\frac{df}{dr}\right]\right\} = -\left(2\pi q\right)^2\mathbb{H}_v\left\{f\right\} + v^2\mathbb{H}_v\left\{\frac{f}{r^2}\right\}. \tag{D.9}$$

As well, the Hankel transform of the derivative is:

$$\begin{aligned}\mathbb{H}_v\left\{\frac{\partial f}{\partial r}\right\} &= -\left(1-v\right)\mathbb{H}_v\left\{\frac{f}{r}\right\} - 2\pi q\mathbb{H}_{v-1}\left\{f\right\}\\ &= -\left(1-v\right)\mathbb{H}_v\left\{\frac{f}{r}\right\} + \left(-1\right)^v 2\pi q\mathbb{H}_{1-v}\left\{f\right\}.\end{aligned} \tag{D.10}$$

Considering the function $\mathcal{D} \neq \mathcal{D}(r)$, one has the following useful transform:

$$\mathbb{H}_v\left\{\frac{r^v}{\left[\mathcal{D}^2 + r^2\right]^{\delta+1}}\right\} = \left(2\pi\right)^{2\delta+1-v}\frac{\left(2\pi\mathcal{D}\right)^{v-\delta}q^\delta}{2^\delta\Gamma\left(\delta+1\right)}K_{v-\delta}\left(2\pi q\mathcal{D}\right) \tag{D.11}$$

where $\Gamma\left(\delta+1\right)$ is the Gamma function, which for $\delta \in \mathbb{N}$ is given by $\Gamma\left(\delta+1\right) = \delta!$, and $K_\alpha\left(x\right)$ is the αth order modified Bessel function of the second kind. With the well-know property of the Bessel functions of the second kind $K_{-\alpha}\left(x\right) = K_\alpha\left(x\right)$.

Another frequently used transform is:

$$\mathbb{H}_v\left\{r^v H\left[\varsigma - r\right]\right\} = \frac{\varsigma^{v+1}}{2\pi q}J_{v+1}\left(2\pi q\varsigma\right) \quad \text{for } \varsigma > 0, \text{ and } v > -\frac{1}{2} \tag{D.12}$$

where H is a Heaviside step function defined as:

$$H\left[\varsigma - r\right] = \begin{cases}1 & \text{for } r \leq \varsigma\\ 0 & \text{for } r > \varsigma,\end{cases} \tag{D.13}$$

and, ς is a real positive number.

Finally, for a Gaussian function, we have:

$$\mathbb{H}_v\left\{\exp\left(-\pi r^2\right)\right\} = \exp\left(-\pi q^2\right). \tag{D.14}$$

Gaussian function

The Gaussian function is a bell shape-like function, a probability density function commonly used in statistics. It is defined by the expression:

$$P\left(x\right) = \frac{1}{\sigma\sqrt{2\pi}}\exp\left[\frac{-\left(x-x_0\right)^2}{2\sigma^2}\right], \tag{D.15}$$

where x_0 is the peak maximum position and σ is standard deviation of the density function. This function is normalized so that:

$$\int_{-\infty}^{\infty} P\left(x\right)dx = 1. \tag{D.16}$$

The Gaussian integral is defined as:

$$\int_{-\infty}^{\infty}\exp\left[-x^2\right]dx = \sqrt{\pi}. \tag{D.17}$$

Lorentzian function

The Lorentzian function is a bell shape-like function, usually employed to describe resonance behaviors and singly peaked distributions. It is defined by the expression:

$$L\left(x\right)=\frac{1}{\pi}\frac{\frac{1}{2}\Gamma}{\left(x-x_0\right)^2+\left(\frac{1}{2}\Gamma\right)^2}, \tag{D.18}$$

where x_0 is the peak maximum position and Γ is a parameters that specifies the width of the distribution. This function is normalized so that:

$$\int_{-\infty}^{\infty}L\left(x\right)dx=1. \tag{D.19}$$

The integral of the Lorentzian function can also be written as:

$$\int_{-\infty}^{\infty}\frac{b}{x^2+b^2}dx=\pi. \tag{D.20}$$

Fast Fourier Transform

Consider a signal $x(t)$ and its Fourier transform of $\hat{x}(\omega)$. The discrete signals x_j at the time t_j and $\hat{x}_k$ at the frequency ω_k are related via the Fast Fourier Transform, which is defined as:

$$\hat{x}_k=\sum_j^N\left[x_j\exp\left\{\frac{-2\pi i\left(j-1\right)\left(k-1\right)}{N}\right\}\right], \tag{D.21}$$

and the Inverse Fast Fourier Transform:

$$x_j=\frac{1}{N}\sum_k^N\left[\hat{x}_k\exp\left\{\frac{2\pi i\left(j-1\right)\left(k-1\right)}{N}\right\}\right], \tag{D.22}$$

where N is the number of acquired data points.

Appendix E

Publications

- R. Ledesma-Alonso, D. Legendre, and P. Tordjeman. Nanoscale deformation of a liquid surface. Phys. Rev. Lett., 108:106104, 2012.

- R. Ledesma-Alonso, P. Tordjeman, and D. Legendre. Multiscale deformation of a liquid surface in interaction with a nanoprobe. Phys. Rev. E, 85:061602, 2012.

- R. Ledesma-Alonso, D. Legendre, and P. Tordjeman. AFM tip effect on a thin liquid film. Langmuir, 29:7749–7757, 2013.

Nanoscale Deformation of a Liquid Surface

Rene Ledesma-Alonso, Dominique Legendre, and Philippe Tordjeman
Université de Toulouse, INPT, UPS, CNRS, IMFT (Institut de Mécanique des Fluides de Toulouse), Allée Camille Soula, F-31400 Toulouse, France
(Received 23 November 2011; published 8 March 2012)

We study the interaction between a solid particle and a liquid interface. A semianalytical solution of the nonlinear equation that describes the interface deformation points out the existence of a bifurcation behavior for the apex deformation as a function of the distance. We show that the apex curvature obeys a simple power-law dependency on the deformation. Relationships between physical parameters disclose the threshold distance at which the particle can approach the liquid before capillarity provokes a ''jump to contact.'' A prediction of the interface original position before deformation takes place, as well as the attraction force measured by an approaching probe, are produced. The results of our analysis agree with the force curves obtained from atomic force microscopy experiments over a liquid puddle.

DOI: 10.1103/PhysRevLett.108.106104 PACS numbers: 68.03.−g, 68.37.Ps

In nature and manmade systems, lying on a vast domain of physics from micro- and nanofluidics, tribology, biophysics, etc., to atomic force microscopy (AFM) experiments, we often encounter situations where liquids undergo deformations due to the interaction with solid objects. Despite a significant range of object sizes, the deformation occurs at a nanoscopic scale induced by van der Waals (vdW) molecular interactions [1]. This deformation grows as the gap decreases, just before a critical distance at which the system suffers an irreversible ''jump-to-contact'' process and forms a capillary bridge [1,2]. Nowadays, the study of liquid properties at the nanoscale [3] based on near-field technique experiments is still a great challenge. Imaging liquids and quantifying their properties at this length scale require one to model the interaction force between liquids and nanoprobes, to determine the near-field liquid deformation, and to predict the critical distance before capillary contact. The aim of this Letter is to address all these points.

By employing an augmented Young-Laplace equation, the interface deformation due to a quasistatic approach of a particle is studied. An exact expression of the pressure field created by the vdW interaction between a sphere and a deformable surface is employed. The resulting strongly nonlinear interface equation, which includes an exact expression of the vdW volume attractive potential, is analyzed. A dimensionless treatment is made in order to generalize the problem whatever the length scale of the sphere radius. Likewise, a bifurcation diagram of the interface deformation, as well as a capillarity region corresponding to the particle-liquid wetting development, is clearly identified. Finally, by performing AFM measurements on a standard liquid polydimethylsiloxane, we validate our theoretical results and show that it is possible to predict the interface deformation, to obtain the critical distance before the capillary jump, and also to measure the Hamaker constant of a liquid with an accurate resolution up to 20 nm, which completely determines the near-field tip force.

We start by modeling the tip as a sphere of radius R, which provokes the deformation of a liquid surface originally placed at $z = 0$ (Fig. 1). The pressure difference across the interface is described by

$$2\kappa\gamma = -\Delta\rho g\eta + \Pi, \tag{1}$$

where κ is the local mean curvature, γ is the surface tension, $\Delta\rho$ is the density difference between the liquid phase and air, g is the acceleration due to gravity, and η is the interface vertical coordinate. Π is the pressure field at the interface resulting from the vdW attractive potential exerted by the whole sphere over the liquid:

$$\Pi = \frac{4HR^3}{3\pi}[(D-\eta)^2 + r^2 - R^2]^{-3}, \tag{2}$$

where H is the Hamaker constant and D is the distance from the center of the sphere to the original position of the interface. Here no assumption is made for this expression, which is obtained directly from the Hamaker theory [4]. In previous studies, the potential was approximated by

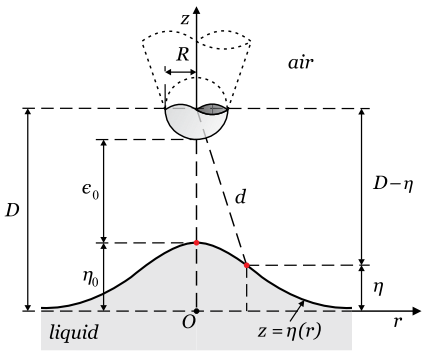


FIG. 1 (color online). Geometry of the sphere-air-liquid system.

 © 2012 American Physical Society

considering a paraboloidlike microscopic tip with a local two-parallel-plate interaction [5] and a local sphere-plan interaction [6].

Taking R as the characteristic length scale of the system, we define the distance $D^* = D/R$, the horizontal $r^* = r/R$ and vertical $z^* = z/R$ coordinates, the deformation $\eta^* = \eta/R$, and the curvature $\kappa^* = \kappa R$; we also introduce the modified Hamaker number $H_a = 4H/(3\pi\gamma R^2)$ and, by using the capillary length $\lambda = \sqrt{\gamma/(\Delta\rho g)}$, the Bond number $B_0 = (R/\lambda)^2$. Typically, for ordinary AFM experiments in air, the values taken by these numbers range mostly over $H_a \in [10^{-7}, 10^{-2}]$ and $B_0 \in [10^{-11}, 10^{-8}]$. For small deformations of the interface, merging Eqs. (1) and (2) gives the dimensionless expression

$$\frac{1}{r^*}\frac{d}{dr^*}\left[\frac{r^*\frac{d\eta^*}{dr^*}}{(\frac{d\eta^*}{dr^*})^2+1}\right] = B_0\eta^* - \frac{H_a}{[(D^*-\eta^*)^2 + r^{*2} - 1]^3}. \tag{3}$$

Note that the same relation can be obtained by minimizing the total energy functional with respect to η [7].

Equation (3) is strongly nonlinear mainly due to the nature of the interaction term. A symmetry boundary condition $[\eta^*]' = 0$ is considered at $r^* = 0$. Far from the axis, at $r^*_\infty \gg 0$, where the vdW potential is negligible ($\Pi \approx 0$) and the profile is nearly flat ($[\eta^*]'_\infty \ll 1$), the boundary condition is given by the asymptotic solution of Eq. (3):

$$[\eta^*]'_\infty + \sqrt{B_0}\frac{K_1(r^*_\infty\sqrt{B_0})}{K_0(r^*_\infty\sqrt{B_0})}\eta^*_\infty = 0, \tag{4}$$

where K_0 and K_1 are zero- and first-order modified Bessel functions of the second kind.

A numerical method implemented within a MATLAB routine was used to solve Eq. (3). In Fig. 2, an example of the interface shape at equilibrium for different separating distances D^* is shown, where a "bumplike" deformation is clearly observed. The inner zone is dominated by the interaction term; hence, it is restricted to the region where the attractive influence of the sphere is significant, approximately up to $r^* = 1$. As a consequence, the external region spans from this boundary to a distance near the dimensionless capillary length $\lambda^* = 1/\sqrt{B_0}$, where the asymptotic solution perfectly describes the declining capillary behavior of the deformation. The radial extension of both regions is barely modified when increasing D^*, while, as it is reduced, the height of the profile undergoes a significant and monotonic growth. Note that the results show that $[\eta^*]' \leq 0.1$ for any r^*; hence, a linearization of the curvature in Eq. (3) can be used for simplification.

The evolution of the dimensionless height of the interface apex η^*_0 as a function of D^* is shown in Fig. 3. Depending on the initial conditions employed to solve Eq. (3), we find two different positions of the apex deformation. The lower curve is a stable branch, since it corresponds to the position which provokes the minimal deformation energy, whereas the upper curve indicates an unstable branch with higher energy. When D^* decreases, η^*_0 of the stable branch grows monotonically, while that for the unstable branch decreases, until a threshold distance $D^*_{\min}$, below which the slope becomes undefined. Indeed, for separation distances shorter than the bifurcation point $D^*_{\min}$, no solution for Eq. (3) is found. This behavior is confirmed by solving the dynamic evolution of the interface [8] in which the unsteadiness arises from the viscous normal stress at the interface. For $D^* < D^*_{\min}$ the instantaneous profile diverges until the sphere surface is reached, and the final equilibrium profile corresponds to a liquid bridge wetting the tip [9], while for $D^* \geq D^*_{\min}$ the stable profile given by Eq. (3) is recovered after a relaxation time $\tau = R\mu/\gamma$, μ being the liquid viscosity.

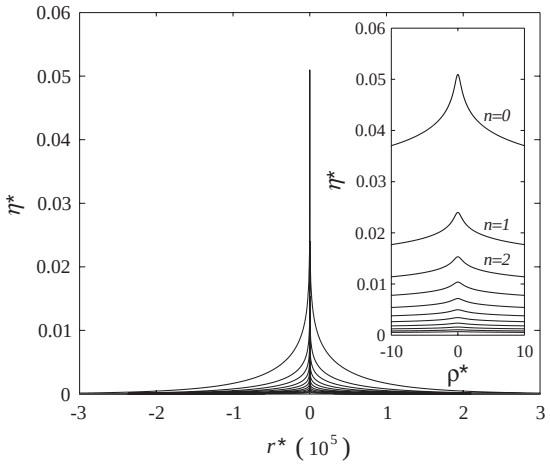


FIG. 2. Equilibrium dimensionless profiles obtained from solving Eq. (3), for $H_a = 10^{-3}$ and $B_0 = 10^{-10}$. Each curve corresponds to a profile generated with D^* equal to $(1 + n/20)D^*_{\min}$, where $n = 0, 1, 2, \ldots, 10$ and $D^*_{\min}$ is the minimum dimensionless distance at which a solution for Eq. (3) exists. Herein, $D^*_{\min} = 1.1682$ and $\eta^*_{\max} = 0.0541$.

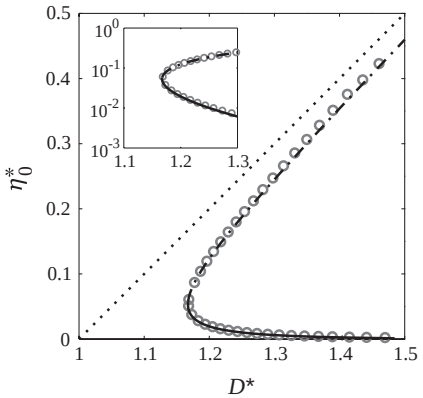


FIG. 3. Bifurcation diagram of the deformation apex for $H_a = 10^{-3}$ and $B_0 = 10^{-10}$. Solution of Eq. (3) at $r^* = 0$ (○), Eqs. (5)–(7): stable (solid line) and unstable (dash-dotted line) branches and position of the tip surface (dotted line).

For the values of B_0 considered in this study, a simple dependency of the apex curvature κ_0^* on the dimensionless height of the interface apex η_0^* is obtained empirically [8]:

$$\kappa_0^* \approx C_0 \sqrt{\frac{(\eta_0^*)^3}{H_a}}, \tag{5}$$

where $C_0 = 0.09 \pm 0.01$. Despite the complexity of the attractive potential, a very particular shape is observed at the apex. Indeed, the curvature κ_0^* is found to simply evolve as $(\eta_0^*)^{3/2}$.

From Fig. 1, we have the geometric relation

$$D^* = 1 + \eta_0^* + \epsilon_0^*, \tag{6}$$

where $\epsilon_0^* = \epsilon_0/R$ is the dimensionless gap between the sphere surface and the apex.

By considering a binomial expansion in Eq. (3) at $r^* = 0$ for the small parameter $\sqrt[3]{H_a/2\kappa_0^*}$, a second-order approximation for ϵ_0^* can be written as

$$\epsilon_0^* = \frac{1}{2}\left(\frac{H_a}{2\kappa_0^*}\right)^{1/3} - \frac{1}{8}\left(\frac{H_a}{2\kappa_0^*}\right)^{2/3}. \tag{7}$$

A good description of η_0^* as a function of D^* is obtained when combining Eqs. (5)–(7). In a bifurcation diagram (Fig. 3), the two possible stable and unstable solutions for the apex position are recovered. The minimum distance $D_{\min}^*$, at which we can approach the sphere to the interface before it ''jumps,'' corresponds to the maximum stable deformation $\eta_{\max}^*$. This point where the branches converge also marks the distance at which the attraction potential becomes so large that the restoring surface tension and gravity forces are unable to hold it anymore, and no equilibrium profile is observed. A capillary-influenced extent, where the attractive force increases without limit and leads to the irreversible wetting process of the probe, is delimited. Finally, minimizing D^* with respect to η_0^*, we obtain $D_{\min}^* = 1 + \eta_{\max}^* + \epsilon_{\min}^*$, with

$$\eta_{\max}^* = \left[\frac{\sqrt{H_a}}{4}\left(\frac{1}{2C_0}\right)^{1/3}\right]^{2/3}, \tag{8a}$$

$$\epsilon_{\min}^* = 2\eta_{\max}^*(1 - \eta_{\max}^*). \tag{8b}$$

Therefore, $D_{\min}^*$ and $\eta_{\max}^*$ grow monotonically when increasing H_a (Fig. 4).

The sphere-liquid interaction force is equal to the addition of the deformation and the gravity forces. In turn, the deformation force is given by the derivative, with respect to η_0^*, of the deformation energy, calculated from integrating the surface deformation, as follows:

$$F_\gamma = -2\pi\gamma R^2 \frac{d}{d\eta_0^*}\left[\int_0^{\lambda^*} r^* \sqrt{1 + ([\eta^*]')^2}\, dr^* - \frac{(\lambda^*)^2}{2}\right]. \tag{9}$$

In order to validate our model, AFM experiments have been conducted. Indeed, local scanning probe techniques allow us to measure liquid interface properties with high sensitivity in a geometry close to those considered in our study [10–16]. A polydimethylsiloxane puddle with a diameter of 2 mm, a thickness of around 200 μm (considering a heavy drop analysis [17]), and a surface tension of 3.1×10^{-2} N/m was deposed on a Si/SiO_2 substrate. An Agilent Technologies 5500 scanning probe microscope was employed in contact mode to obtain the force curve over the puddle. The experiment was made by using a scanning probe Nanotools® model B1-HDC (single-crystal silicon), with a tip radius of 20 nm measured from the capillary force [2], a cantilever stiffness of 0.2 N/m deduced from thermal noise [18,19], and a resonance frequency of 15 kHz. The tip was placed near the puddle, and a force curve over the substrate was obtained. Once the calibration factor and the stiffness were calculated, the probe was retracted 225 μm and then placed above the center of the puddle. Several scanning cycles, composed of an approach-withdrawal displacement of 2 μm (motion of a piezoelectric actuator) and a subsequent automatic approach of the same size (displacement with a step motor), were then executed until the interface was reached and the tip was dipped. The force curve was carried out by taking 50 samples per nanometer and a vertical scan rate of 10 nm/s. The common resolution of an AFM is limited by the thermal noise, which takes values of around 10^{-12} N [20] at 295 K. In our experiments, this force presented a greater magnitude than thermal noise.

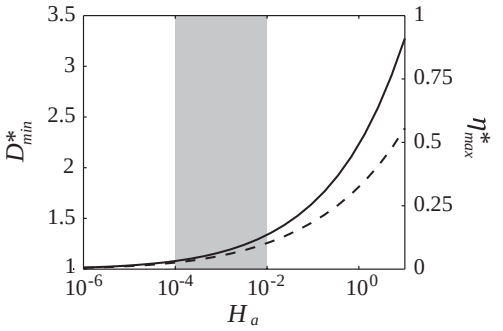


FIG. 4. Minimal dimensionless distance $D_{\min}^*$ (solid line) and apex deformation $\eta_{\max}^*$ (dashed line) as a function of H_a, corresponding to $B_0 = 1.308 \times 10^{-10}$. AFM range (shaded area).

The orders of magnitude and behaviors of theoretical and experimental force curves (Fig. 5) are in very good accordance. When the nanoscopic tip is placed far from the sample, at a distance greater than $2D_{\min}$, the deflection of the cantilever is negligible. When it approaches the interface, from $2D_{\min}$ to $D_{\min}$, the AFM measures a gradually increasing force. Within the frame of reference employed, cantilever deflections toward the interface are considered as negative values and, thus, attraction forces as well. Before reaching $D_{\min}$, the force increases abruptly, provoking a great deflection of the cantilever, which implies a magnitude of around 10^{-11} N. The gap arrives at its

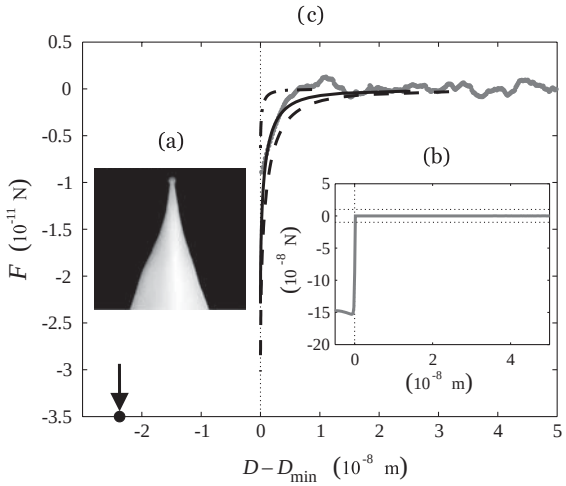


FIG. 5. (a) Tip of B1-HDC probe [23]. (b) Full view of the AFM experimental force curve for which $B_0 = 1.308 \times 10^{-10}$, corresponding to the last approach-withdrawal displacement before contact. The 0 position indicates the tip wetting. (c) Zoom of the experimental force (gray line) and the force obtained from Eq. (9) with $H = 4 \times 10^{-20}$ J (solid line), and the near values 10^{-19} (dashed line) and 10^{-21} J (dash-dotted line), corresponding to the experimental B_0. The arrow marks the position of the nondeformed liquid surface deduced from the value $D_{\min} = 24 \pm 4 \times 10^{-9}$ m calculated from Eq. (3).

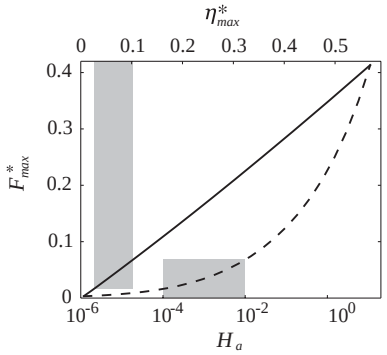


FIG. 6. Maximum dimensionless force $F^*_{\max}$ obtained from the model as a function of H_a (dashed line) and of $\eta^*_{\max}$ (solid line), corresponding to $B_0 = 1.308 \times 10^{-10}$. AFM range (shaded area).

minimum value when reaching $D_{\min}$. Hence, any separation distance smaller than $D_{\min}$ means imminent contact and the subsequent displacement of the liquid over the tip, which provokes an irreversible wetting process. The best fit is shown by the theoretical curve obtained with $H = 4 \times 10^{-20}$ J, for which $H_a = 1.4 \times 10^{-3}$, the Bond number being $B_0 = 1.308 \times 10^{-10}$. The obtained magnitude of H is very close to the value $H = 4.8 \times 10^{-20}$ J deduced from the literature [1,21,22], since the AFM measurement error is of around 20%. Consequently, a separation distance of $D_{\min} = 24 \pm 4 \times 10^{-9}$ m, at which the jump-to-contact process happens, is found. In such a way, a reference position at the nanoscopic scale is now available when scanning with an AFM probe over a liquid surface.

In Fig. 6, the maximum dimensionless force $F^*_{\max} = -F_{\max}/(R\gamma)$, as a function of H_a, shows a behavior similar to the quantities described in Fig. 4. Therefore, it exhibits a linear dependency represented by $F^*_{\max} \approx 0.7\eta^*_{\max}$, which is consistent with the fact that the surface energy follows $E \sim \gamma(R\eta^*_{\max})^2$, for small displacements of the interface.

In summary, $\eta_{\max}$, $F_{\max}$, and $D_{\min}$ increase in magnitude when increasing H. Likewise, an increase in R provokes the enlargement of $\eta_{\max}$ and $F_{\max}$; nevertheless, it causes a decrease of $D_{\min}$. For very small tips, of around $R = 1$ nm and considering $H = 10^{-20}$ J, interaction forces of the order of $F_{\max} = -3.6 \times 10^{-12}$ N are generated, which is hardly measurable with a common apparatus. In contrast, we find a significantly quantifiable $F_{\max} = -2.6 \times 10^{-11}$ N for relatively large tips of $R = 100$ nm and the same H, which strongly reduces the scanning resolution. Therefore, the resolution of AFM experiments rises when using probes with small tip radius, but their size is restricted by the minimum force measurable with an AFM. The employment of our probe-sample interaction model is suggested to obtain quantitative data from local probe measurements of liquid surfaces. Whereas a wide range of $H \in (10^{-19}, 10^{-21})$ J is commonly employed, our methodology allows us to estimate a more accurate value for a given nanoscopic tip-liquid system, when meticulous AFM measurements are performed and $F_{\max}$ is available. In addition, together with the estimation of the tip radius [2], the minimum tip-liquid distance and its corresponding deformation are obtained. Our prediction of H leads to finding the optimal distance range for scanning $D \in [D_{\min}, 2D_{\min}]$, needed to keep the interaction regime within the attractive zone before the wetting phenomenon takes control.

In this Letter, from a theoretical analysis, we have established the necessary experimental conditions to implement nanoprobe techniques when studying liquid interfaces. This work is a crucial step for imaging liquids and measuring their properties with a nanometer resolution.

[1] J. N. Israelachvili, *Intermolecular and Surface Forces* (Elsevier, New York, 2011), 3rd ed.
[2] J. Crassous, E. Charlaix, H. Gayvallet, and J. L. Loubet, Langmuir **9**, 1995 (1993).
[3] L. Bocquet and E. Charlaix, Chem. Soc. Rev. **39**, 1073 (2010).
[4] H. C. Hamaker, Physica (Utrecht) **4**, 1058 (1937).
[5] F. P.-A. Cortat and S. J. Miklavcic, Langmuir **20**, 3208 (2004).
[6] Y. Z. Wang, B. Wang, X. Xiong, and J. Zhang, Surf. Sci. **605**, 528 (2011).
[7] L. Nan, B. Yi-Long, X. Meng-Fen, and K. Fu-Jiu, Chin. Phys. Lett. **22**, 2012 (2005).

[8] See Supplemental Material at http://link.aps.org/supplemental/10.1103/PhysRevLett.108.106104 for a description of the dynamic model and the variables dependency.
[9] F. M. Orr, L. E. Scriven, and A. P. Rivas, J. Fluid Mech. **67**, 723 (1975).
[10] H. J. Butt, J. Colloid Interface Sci. **166**, 109 (1994).
[11] S. N. Magonov and D. H. Reneker, Annu. Rev. Mater. Sci. **27**, 175 (1997).
[12] A. Knoll, R. Magerle, and G. Krausch, Macromolecules **34**, 4159 (2001).
[13] F. Dutka and M. Napiorkowski, J. Phys. Condens. Matter **19**, 466104 (2007).
[14] T.-D. Li and E. Riedo, Phys. Rev. Lett. **100**, 106102 (2008).
[15] M. Delmas, M. Monthioux, and T. Ondarcuhu, Phys. Rev. Lett. **106**, 136102 (2011).
[16] J. Crassous, M. Ciccotti, and E. Charlaix, Langmuir **27**, 3468 (2011).
[17] P.-G. de Gennes, F. Brochard-Wyart, and D. Quere, *Capillarity and Wetting Phenomena: Drops, Bubbles, Pearls, Waves* (Springer, New York, 2003).
[18] B. Capella and G. Dietler, Surf. Sci. Rep. **34**, 1 (1999).
[19] J. N. Sharpe, *Handbook of Experimental Solid Mechanics* (Springer, New York, 2008).
[20] D. Smith, Rev. Sci. Instrum. **66**, 3191 (1995).
[21] K. Mougin and H. Haidara, Europhys. Lett. **61**, 660 (2003).
[22] J. Visser, Adv. Colloid Interface Sci. **3**, 331 (1972).
[23] Image provided by the manufacturer, from the Web site http://www.nanotools.com/afm-probes/ebd/general-purpose/ball-b1-b150/.

PHYSICAL REVIEW E **85**, 061602 (2012)

Multiscale deformation of a liquid surface in interaction with a nanoprobe

R. Ledesma-Alonso, P. Tordjeman, and D. Legendre
Université de Toulouse, INPT-CNRS, Institut de Mécanique des Fluides de Toulouse (IMFT), 1 Allée du Professeur Camille Soula, 31400 Toulouse, France
(Received 22 March 2012; published 7 June 2012)

The interaction between a nanoprobe and a liquid surface is studied. The surface deformation depends on physical and geometric parameters, which are depicted by employing three dimensionless parameters: Bond number B_o, modified Hamaker number H_a, and dimensionless separation distance D^*. The evolution of the deformation is described by a strongly nonlinear partial differential equation, which is solved by means of numerical methods. The dynamic analysis of the liquid profile points out the existence of a critical distance $D^*_{\min}$, below which the irreversible wetting process of the nanoprobe happens. For $D^* \geqslant D^*_{\min}$, the numerical results show the existence of two deformation profiles, one stable and another unstable from the energetic point of view. Different deformation length-scales, characterizing the stable liquid equilibrium interface, define the near- and the far-field deformation zones, where self-similar profiles are found. Finally, our results allow us to provide simple relationships between the parameters, which leads to determine the optimal conditions when performing atomic force microscope measurements over liquids.

DOI: 10.1103/PhysRevE.85.061602 PACS number(s): 68.37.Ps, 68.03.−g

I. INTRODUCTION

The study of fluids and their properties at the nanoscopic scale by means of local probe techniques is still today a big challenge. Involving molecular interaction forces, several apparatuses and techniques have been in constant development for the past four decades, mainly the surface force apparatus (SFA) and the atomic force microscope (AFM). Even though the SFA gives a vertical distance resolution of about 0.1 nm and a force sensitivity of 10 nN [1], its lateral resolution is limited by the radius of the two approaching cylinders, around 1 cm, on which the technique is based. Nevertheless, its configuration is optimum for studying rheological properties of thin films [2]. On the other hand, the AFM provides a similar vertical resolution and an augmented force sensitivity of 10 pN [3], whereas its lateral resolution is given by the size of the tip radius, commonly between 10–20 nm. Hence, AFM techniques allow the acquisition of detailed topographies and the visualization of different material phases, among other properties involving molecular interactions [4–7]. However, in spite of its advantages and possible applications, the characterization of liquid surfaces by means of AFM methods has been delayed due to the difficulties induced by the interface deformation, the jumping capillarity phenomenon, and the inherent probe wetting.

The geometry of an ordinary SFA experiment allows the employment of the Derjaguin approximation, which has been proven to be appropriate in most cases. For common AFM nanoprobes, it is not applicable because the tip radius has a smaller or similar size compared to the gap between the deformed liquid surface and the tip [8]. Previously, the basis of a theoretical model to compute the liquid surface deformation were developed [9], in which no geometric hypothesis was made, providing a valid analysis at any length-scale. Taking into account the molecular attractive interaction, represented by a modified Hamaker number, and neglecting the effect of gravity, depicted by the Bond number, the height of the deformation profile was estimated. Good agreement between AFM experiments and the deformation force computed with the model were achieved, validating the introduced methodology. Herein, we present an extensive analysis, which deepens into the parametric study and its consequences over the dynamic evolution of the interface profile, at different length-scales. The results show that the deformation extends beyond the tip radius, and as far as the capillary length, which for the case of local probes (tip radius $\sim 10^{-8}$ m) is several orders of magnitude greater (capillary length $\sim 10^{-3}$ m). Different deformation zones are portrayed and delimited by different characteristic length-scales: from the origin of an axisymmetric reference system up to a length-scale given by the Hamaker interaction force, a near-field is found; from a transition length-scale up to the capillary length, a far-field spans; and between the two previous zones, a transition or linking zone is located, which extension depends on the combined effect of the attractive interaction and capillarity parameters. Keeping in mind the different length-scales, we find that the deformation profile shows a self-similar behavior.

In addition, a particular relationship between the apex deformation and its curvature is found. The resulting fit serves to calculate the minimum distance at which the probe can approach the liquid without being wetted, as well as its corresponding maximum deformation. These quantities result to be functions of the dimensionless parameters, and can be employed to determine the optimal experimental conditions when AFM measurements are performed over liquid surfaces.

II. INTERFACE DEFORMATION

A. Model

Considering that the London–van der Waals (London–vdW) interaction force between molecules acts over a relatively short distance, only the rounded extreme of the tip generates a reaction at the interface [9]. Consequently, in order to understand the nature of the noncontact interaction between a local probe and a deformable material surface, we model the tip as a sphere of radius R. Within a cylindrical coordinate system, a perfectly rigid sphere is placed at a fixed position over a semi-infinite liquid body, which is deformed like the one shown in Fig. 1, the gap between them being filled with air.

 ©2012 American Physical Society

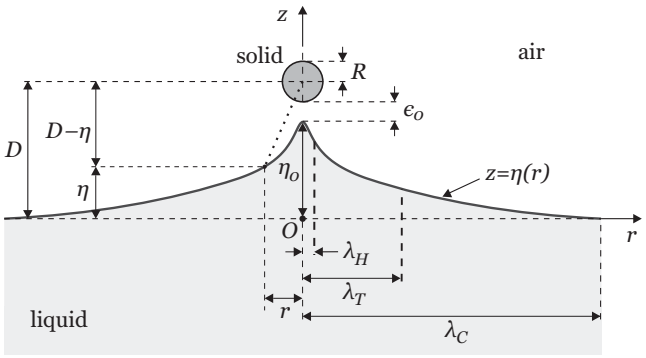


FIG. 1. Scheme of the liquid surface deformation in interaction with a probe. Parameters defined in the text.

The interface is initially flat and located at $z = 0$. Based on the Hamaker theory [10], the pressure field (or attractive potential) Π exerted by the sphere at a distance D over the bulk liquid is

$$\Pi = \frac{4HR^3}{3\pi}\frac{1}{[(D-z)^2 + r^2 - R^2]^3}, \tag{1}$$

where H is the Hamaker constant of the probe/air/liquid system, while z and r are the vertical and the radial coordinates of any point in the liquid, as shown in Fig. 1. Equation (1) is obtained from integrating the London–vdW interaction potential between the sphere atoms and a differential volume at a given distance from the sphere surface. As shown in Fig. 2, the radial extent of the pressure field is smaller than the sphere radius. As well, considering the dilated vertical axis, which allows the visualization of the corresponding equilibrium liquid surface, the depth barely

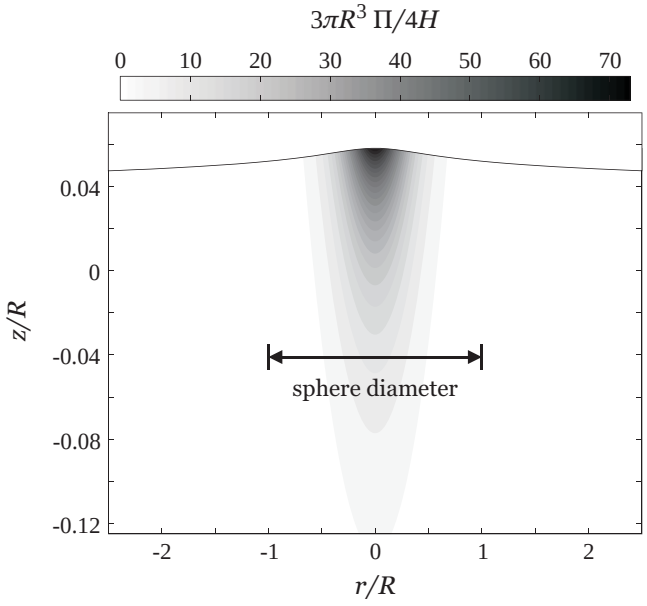


FIG. 2. Pressure field over the liquid body generated by the interaction with the spherical probe, obtained from Eq. (1), and the corresponding interface deformed position for $H = 4 \times 10^{-20}$ Nm and $R = 10^{-8}$ m. The vertical axis is magnified to facilitate the interface visual recognition.

reaches 0.1 times the sphere radius. In brief, the interaction effect is restricted to a very small zone over the liquid phase.

In turn, this attractive potential tends to deform the interface, which provokes a capillary pressure difference and a hydrostatic pressure in order to balance the system, as well as a dynamic contribution entailed by the viscous dissipation of the system. As a first approach, we have disregarded the inertial effect with respect to the viscous contribution. Thence, the generalized Young-Laplace's equation without mass transfer, which describes the interface behavior, is expressed as

$$\Pi - \Delta\rho g\eta + \underline{n}\cdot\Sigma\cdot\underline{n} = 2\kappa\gamma, \tag{2}$$

where $\Delta\rho$ is the density difference between the liquid phase and the air, g is the gravitational acceleration, $\underline{n}\cdot\Sigma\cdot\underline{n}$ is the normal viscous stress difference across the interface characterized by the unit normal vector $\underline{n}$, κ is the local interface mean curvature, γ is the surface tension, and η is the local interface position, which within an axisymmetric model is given as a function of the radial position r and the time t. Within this portrayal, inertia was disregarded with respect to viscous dissipation because, at the AFM scale, the Reynolds number is of the order of $Re \in [10^{-9}, 10^{0}]$.

Additionally, considering a general case for which large deformations are envisaged, the expression of the curvature in cylindrical coordinates is given by

$$2\kappa = -\frac{1}{r}\frac{\partial}{\partial r}\left[r\frac{\partial\eta}{\partial r}\left\{\left(\frac{\partial\eta}{\partial r}\right)^2 + 1\right\}^{-1}\right]. \tag{3}$$

As well, in the more simplistic case, the viscous stresses at the air-side are negligible with respect to those at the liquid-side. Hence, for an incompressible single-directional viscous flow, which moves mainly in the z direction, and considering that in cylindrical coordinates $\underline{n}$ is approximated by $n_r \approx -\partial\eta/\partial r$ and $n_z \approx 1$, we have

$$\underline{n}\cdot\Sigma\cdot\underline{n} \approx -\mu\frac{\partial}{\partial t}\left(\frac{\partial\eta}{\partial r}\right)^2, \tag{4}$$

where μ represents the viscosity of the liquid. We can introduce the definitions of the capillary length, $\lambda_C = \sqrt{\gamma/(\Delta\rho g)}$, and the relaxation time, $\tau = (R\mu)/\gamma$, of the system. As well, considering R as the characteristic length-scale and τ as the characteristic time-scale of the system, we find the dimensionless variables: $D^* = D/R$ the distance from the center of the sphere to the originally undeformed interface, $r^* = r/R$ and $z^* = z/R$ the horizontal and vertical coordinates, $\eta^* = \eta/R$ and $\kappa^* = \kappa R$ the deformation and curvature, $\lambda_C^* = \lambda_C/R$ the dimensionless capillary length, and $t^* = t/\tau$ the dimensionless time. Thus, matching Eqs. (1)–(4), the nonlinear partial differential equation that describes the instantaneous position of the interface is written as the following dimensionless expression:

$$-\frac{1}{r^*}\frac{\partial}{\partial r^*}\left[\frac{r^*\frac{\partial\eta^*}{\partial r^*}}{\left(\frac{\partial\eta^*}{\partial r^*}\right)^2 + 1}\right] + B_o\,\eta^* - \frac{H_a}{[(D^*-\eta^*)^2 + r^{*2} - 1]^3} = -\frac{\partial}{\partial t^*}\left(\frac{\partial\eta^*}{\partial r^*}\right)^2, \tag{5}$$

in which we find two dimensionless parameters: the Bond number $B_o = (R/\lambda_C)^2$ and the modified Hamaker number $H_a = 4H/(3\pi\gamma R^2)$.

This dimensionless analysis gives rise to an equation that is valid for a system of any length-scale. In addition, as it is clearly observed from the parameter definitions, H_a and B_o are coupled by R. Hence, their values are restricted according to the product of physical properties given by:

$$H_a B_o = \frac{4}{3\pi}\left(\frac{H\Delta\rho g}{\gamma^2}\right). \tag{6}$$

Considering real probe/air/liquid systems [1,11–13], for which $H \in [10^{-21},10^{-19}]$J, $\gamma \in [10^{-2},10^{-1}]$N/m, $\Delta\rho \in [10^{2},10^{4}]$kg/m^3, and $\mu \in [10^{-3},10^{0}]$Pa s, and common AFM probes, with $R \in [10^{-8},10^{-7}]$, the range of the dimensionless parameters remains within $H_a \in [10^{-8},10^{-1}]$ and $B_o \in [10^{-11},10^{-8}]$.

For simplicity, the deformation, and its first and second derivatives with respect to r^* are written as η_0^*, $[\eta^*]_0'$, and $[\eta^*]_0''$, respectively, when evaluated at $r^* = 0$, and as η_C^*, $[\eta^*]_C'$, and $[\eta^*]_C''$, respectively, when evaluated at $r^* = \lambda_C^*$.

At $r^* = 0$, a symmetry boundary condition, $[\eta^*]_0' = 0$, should be considered. Meanwhile, far from the axis at $\lambda_C^* \gg 0$, where the interaction potential, which decays as $(r^*)^{-6}$, is negligible ($\Pi \approx 0$), the boundary condition comes from the quasistatic asymptotic solution of Eq. (5), also considering that in this outlying region the surface is nearly flat ($[\eta^*]' \ll 1$). The exact solution, which leads to the corresponding faraway boundary condition, is

$$\eta^* = G K_0(\sqrt{B_o}\, r^*), \tag{7}$$

with the coefficient $G = \eta_C^*/K_0(1)$, and K_0 being a zero-order modified Bessel function of the second kind. Hence, the boundary condition at $r^* = \lambda_C^*$ is given by

$$[\eta^*]_C' + \sqrt{B_o}\frac{K_1(1)}{K_0(1)}\eta_C^* = 0, \tag{8}$$

where K_1 is a first-order modified Bessel function of the second kind.

We suppose that the interface is undeformed and completely flat before the dynamic process starts. Hence, the initial condition at $t = 0$, is given by $\eta^* = [\eta^*]' = \kappa^* = 0$ for all $r^* \geqslant 0$, which is equivalent to say that the sphere is suddenly set at $t = 0$.

After a time interval close to τ, a steady-state profile is expected to be obtained. Considering real probe/air/liquid systems, we find $\tau \in [10^{-6},10^{-10}]$s for AFM situations. Because of the relatively small magnitude of this characteristic time-scale compared to the common laboratory measured time-scales, as a second approach, we consider that the steady state is reached instantaneously. At equilibrium, liquid and interface are motionless, viscous stresses do not appear and the temporal derivative in Eq. (5) is omitted. Thus, Eq. (5) is transformed into a dimensionless nonlinear ordinary differential equation and, as expected, the equilibrium profile is obtained when the interaction pressure field is totally compensated by the gravity and the capillary contributions.

A posteriori, it was verified that $([\eta^*]')^2 \ll 1$, which supports the employment of the small interface displacements hypothesis in our theoretical analysis. Taking this into account, the dimensionless mean curvature κ^* is decomposed in two principal curvatures

$$2\kappa^* = \kappa_m^* + \kappa_a^* \tag{9a}$$

$$\kappa_m^* = -\frac{d^2\eta^*}{dr^{*2}} \qquad \kappa_a^* = -\frac{1}{r^*}\frac{d\eta^*}{dr^*}, \tag{9b}$$

where κ_m^* is the dimensionless meridional curvature—the axisymmetric curvature of the interface that determines the behavior of the profile at any axial plane—while κ_a^* is the dimensionless azimuthal curvature—the curvature projection of the circle describing isodeformation contour lines in the direction normal to the interface.

B. Numerical method

Due to the impossibility of solving analytically the strongly nonlinear Eq. (5), a numerical method was implemented. Firstly, taking care of the singularity present at $r^* = 0$, we consider the Taylor expansion

$$\frac{1}{r^*}\frac{d\eta^*}{dr^*} \approx [\eta^*]_0'' + O(r^*). \tag{10}$$

Additionally, employing the finite difference method to discretize the time derivative, we can write the dynamic term as

$$\frac{\partial}{\partial t^*}\left(\frac{\partial\eta^*}{\partial r^*}\right)^2 = \frac{1}{\Delta t^*}\left\{\left(\frac{\partial\eta^*}{\partial r^*}\right)^2\Big|^{n} - \left(\frac{\partial\eta^*}{\partial r^*}\right)^2\Big|^{n-1}\right\}, \tag{11}$$

where n and $n-1$ indicate two consecutive time-steps, and Δt^* is the dimensionless time-step of the simulation.

Now, writing Eq. (5) as a system of nonlinear ordinary differential equations, we have to solve

$$\left.\frac{d\eta^*}{dr^*}\right|^{n} = u \tag{12a}$$

$$\left.\frac{du}{dr^*}\right|^{n} = \begin{cases} -\frac{u[u^2+1]}{r^*} + \left[B_o\,\eta^* - \frac{H_a}{([D^*-\eta^*]^2+r^{*2}-1)^3} + \frac{u^2-A}{\Delta t^*}\right][u^2+1]^{3/2}, & \forall\, r^* > 0 \\ \left[B_o\,\eta^* - \frac{H_a}{([D^*-\eta^*]^2+r^{*2}-1)^3} + \frac{u^2-A}{\Delta t^*}\right]\frac{[u^2+1]^{3/2}}{u^2+2}, & r^* = 0, \end{cases} \tag{12b}$$

where u is the first spatial derivative of the liquid surface position, $\eta^* = \eta^*|^n$ for simplicity, and $A = (d\eta^*/dr^*)^2|^{n-1}$ is a numerical method parameter. The problem represented by Eqs. (12) must be solved to obtain the profile of the interface at any time n, with the knowledge of the profile at the previous instant $n-1$. This system is a two-point boundary value problem, which is worked out using a MATLAB routine including the function bvp4c.m, which employs the so-called Simpson's method [14]. Because of the smooth shape of the composing functions of the system expressed in Eqs. (12), the solution is easily found with the proposed method.

The boundary and initial conditions are

$$r^* = 0 \quad \Rightarrow \quad u = 0 \tag{13a}$$

$$r^* = \lambda_C^* \quad \Rightarrow \quad u = -\sqrt{B_o}\frac{K_1(1)}{K_0(1)}\eta_C^* \tag{13b}$$

$$\left.\begin{array}{c} t = 0 \\ 0 \leqslant r^* \leqslant \lambda_C^* \end{array}\right\} \Rightarrow \left\{\begin{array}{l} \eta^* = \eta_i^*\left(1 - \frac{r^*}{\lambda_C^*}\right) \\ u = -\frac{\eta_i^*}{\lambda_C^*}, \end{array}\right. \tag{13c}$$

where η_i^* is the initial guess of the interface apex position. Due to the nonlinearity of the system, two different shapes of the interface profile can be found as simultaneous solutions of Eq. (5), depending on the value of η_i^* (this point is discussed in Sec. III C). For the dynamic calculation of the profile evolution, the surface is initially placed at $\eta_i^* = 0$. For steady-state calculation, the dynamic system is transformed into the equivalent system of equations, which describes the static case. The previous and the current instants are then nullified, and we take $A = u^2$ and suppress the superindex n. For all the situations, dynamic or static, interface profiles are calculated with a relative tolerance of 10^{-4}.

III. LIQUID SURFACE DEFORMATION

A. Transient state

From the results presented in the literature [9], for a given combination of the parameters H_a and B_o, the evolution of the interface profile depends completely on the relative value of D^*. If D^* is greater than a threshold value, $D^*_{\min}$, a bumplike equilibrium profile is attained. On the other hand, if D^* is smaller than $D^*_{\min}$, the profile deformation grows until the liquid touches the sphere, developing the so-called jump-to-contact processes and the formation of a liquid capillary bridge [15].

A typical interface profile evolving and reaching an equilibrium state is shown in Fig. 3(a). As well, the different evolution paths that the interface apex can follow, depending on D^*, are shown in Fig. 3(b). For all the considered values of D^*, the instantaneous application of the attractive force at $t = 0$ directly results into an abrupt acceleration of the interface. In turn, surface tension generates a restoring force, which acts to oppose the interface deformation. As a consequence, the driving force in the next instant results from the balance between attractive and surface tension forces, both increasing along with the deformation. At the initial stage, the interface speed decreases monotonically due to the viscous dissipation within the liquid phase, which tends to damp the bulk liquid motion. If $D^* > D^*_{\min}$, the attractive force is sufficiently small to be controlled by the surface tension, and

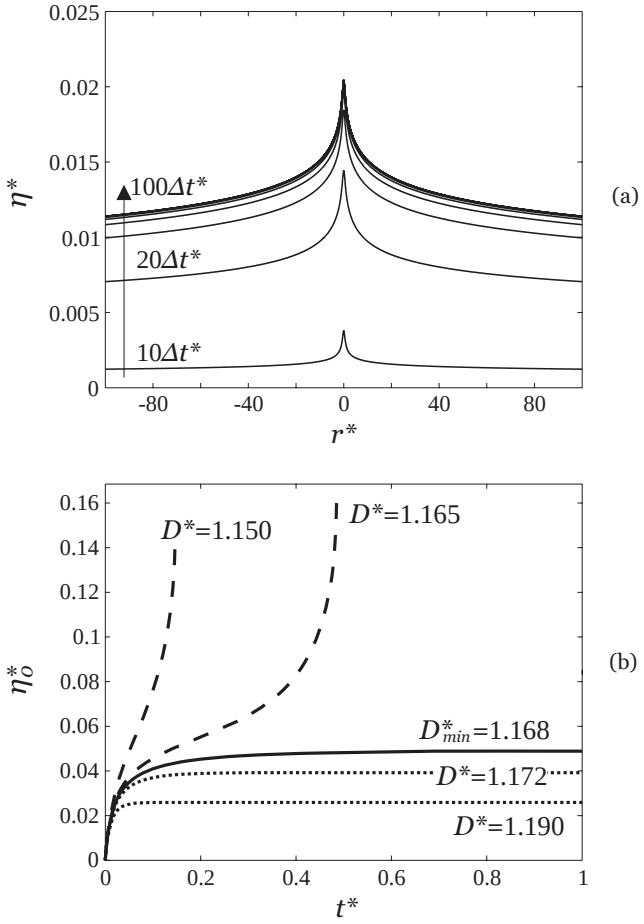


FIG. 3. Interface dynamic evolution obtained from solving Eqs. (12) for $H_a = 10^{-3}$, $B_o = 10^{-10}$, and $\Delta t^* = 10^{-3}$. (a) Instantaneous dimensionless profiles for $D^* = 1.2 > D^*_{\min}$, corresponding to increments of $10\Delta t^*$ (from bottom to top). (b) Time-dependent dimensionless apex position for: [- -] $D^* < D^*_{\min}$, [—] $D^* = D^*_{\min}$, and [$\cdots$] $D^* > D^*_{\min}$.

the interface motion slows down until a steady-state profile is achieved, as represented by the dotted curves in Fig. 3(b). The solid curve indicates the critical dynamic evolution, for which $D^* = D^*_{\min}$ and the profile converges slowly toward an equilibrium state, attained near $t^* \approx 1$. In contrast, when $D^* < D^*_{\min}$, the attractive force is large enough to go beyond the tension force, and the motion grows without a regulating mechanism, leading to the sphere-liquid contact. The profile begins normally its deformation and the speed decreases until it reaches a temporary shrinkage, followed by a rise of the speed, the profile divergence, and the subsequent wetting process. Also in Fig. 3(b), the dashed curves describe this behavior, characterized by the so-called jump-to-contact process.

B. Steady-state equilibrium profile

The interface profile converges toward a final steady-state solution only if $D^* \geqslant D^*_{\min}$. An example of the typical equilibrium deformation profiles are shown in Fig. 4, for fixed values of H_a and B_o, and an initially flat surface placed at $\eta_i^* = 0$, but for different values of D^*. The corresponding curvatures, κ_m^* and κ^* [see Eq. (9)], are displayed in Fig. 5. As it

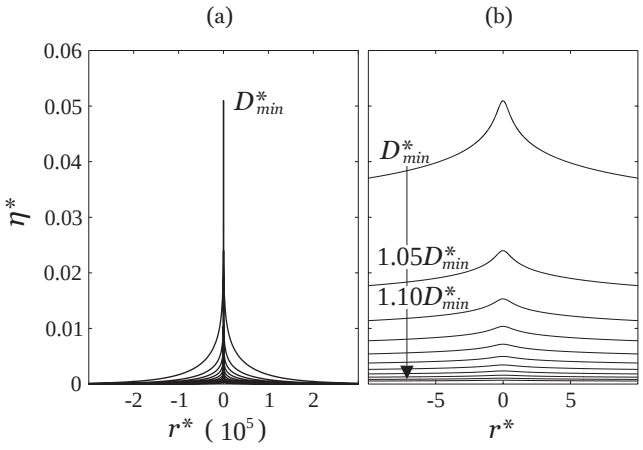


FIG. 4. (a) Steady-state dimensionless equilibrium profiles and (b) zoom of the central region obtained from solving the steady-state Eq. (5), for $H_a = 10^{-3}$, $B_o = 10^{-10}$, an initial guess with $\eta_i^* = 0$, and D^* with increments of $0.05D^*_{\min}$ (from top to bottom). In this case, it was found that $D^*_{\min} = 1.168$.

is clearly depicted in the deformation profile shown in Fig. 4(a), the sphere pulls the interface towards itself only at a very reduced zone near the symmetry axis, as shown in Fig. 4(b), which is a central region zoom. From $r^* \approx 10^2 - 10^3$ and beyond, the asymptotic solution expressed in Eq. (7) perfectly describes the declining capillary behavior of the deformation. In addition, the meridional and mean curvatures are shown in Figs. 5(a) and 5(b), respectively. There is a passage from a negative to a positive value of κ_m^*, near $r^* = 0.37$, which indicates a change in the sense of the surface tension force in the axial plane. On the contrary, κ^* remains always within positive values, showing a narrow logisticlike behavior, barely covering a projected radius. In short, from the curves in Figs. 4 and 5, reducing D^* provokes an increment in the magnitude of the attractive force, leading to greater deformation and curvature states, as well as a slight variation of the radial extension of both.

C. Bifurcation diagrams

In fact, for each combination of the parameters H_a, B_o, and D^*, two solutions for the deformation profile arise from the initial value chosen for η_i^*. By taking D^* and the two corresponding values of η_0^* as coordinate pairs, we obtain a bifurcation curve. Examples are shown in Fig. 6(a) for a fixed value $B_o = 10^{-10}$. When $D^* = D^*_{\min}$, there is only one solution profile, corresponding to the maximum apex deformation $\eta^*_{\max}$ and the minimum gap $\epsilon^*_{\min}$ between the liquid surface and the sphere. There is no solution for the deformation profile further to the left than this critical point $(D^*_{\min}, \eta^*_{\max})$, from which the two branches emerge.

As observed from Fig. 6(a), the curve showing the highest apex deformation is thus an unstable branch from the energetic point of view. As well, the curve reporting the lowest apex position, associated to the minimum deformation energy, is a stable branch and thus describes the only possible interface profile. For the stable apex position, the dependency of η_0^* on D^* seems to take the form of a rectangular hyperbola:

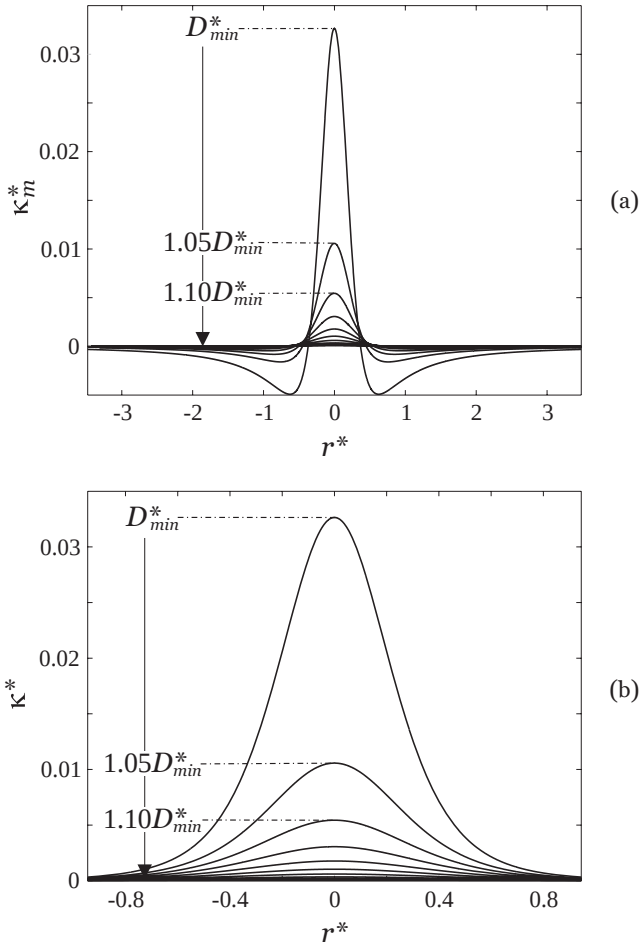


FIG. 5. Steady-state dimensionless equilibrium (a) meridional curvatures and (b) local mean curvatures obtained from solving the steady-state Eq. (5), with the same parameter values and variables as in Fig. 4.

the shorter the gap between the probe and the undeformed surface, the larger the deformation becomes. In Figs. 6(b) and 6(c), the derivative of η_0^* with respect to D^* and the curvature of the stable branch are shown, respectively. In both cases, $D^*_{\min}$ marks the location of a vertical asymptote, at which the stable branches are completely halted.

An increase of H_a generates a displacement of the bifurcation curve to larger values of D^*, as well as a proportional scaling. Conversely, an increase of B_o provokes a very small decrease of D^*, which is negligible in comparison with those provoked by H_a. In general, the impact of H_a is significant, while the effects of a change in B_o are negligible within the range of common liquids, as it is summarized in Fig. 7. Increasing H_a provokes an enlargement of $\eta^*_{\max}$ and $D^*_{\min}$; while, if B_o increases, both $\eta^*_{\max}$ and $D^*_{\min}$ show slightly smaller values.

D. Geometric relations

Noncontact AFM experiments require to control the tip/liquid distance, which is a function of their physical properties. This can be done by considering the geometric relations that are presented below. When analyzing the apex

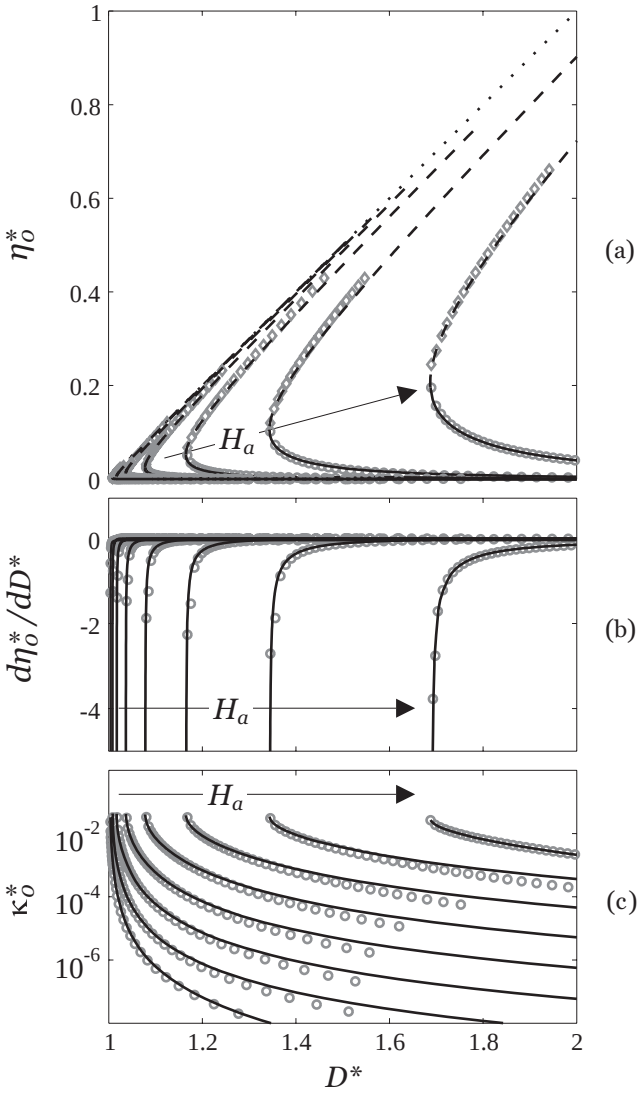


FIG. 6. Bifurcation diagrams: (a) apex deformation of the interface, (b) its derivative with respect to the separation distance, and (c) its mean curvature, as functions of D^*, for $H_a \in [10^{-8},10^{-1}]$ and $B_o = 10^{-10}$. Numerical solution of the steady-state Eq. (5) for [○] the stable and [◇] the unstable branches, and the analytical solution for [—] the stable and [- -] the unstable branches given by Eqs. (14) and (15). In (a) the position of the sphere surface [·] is shown.

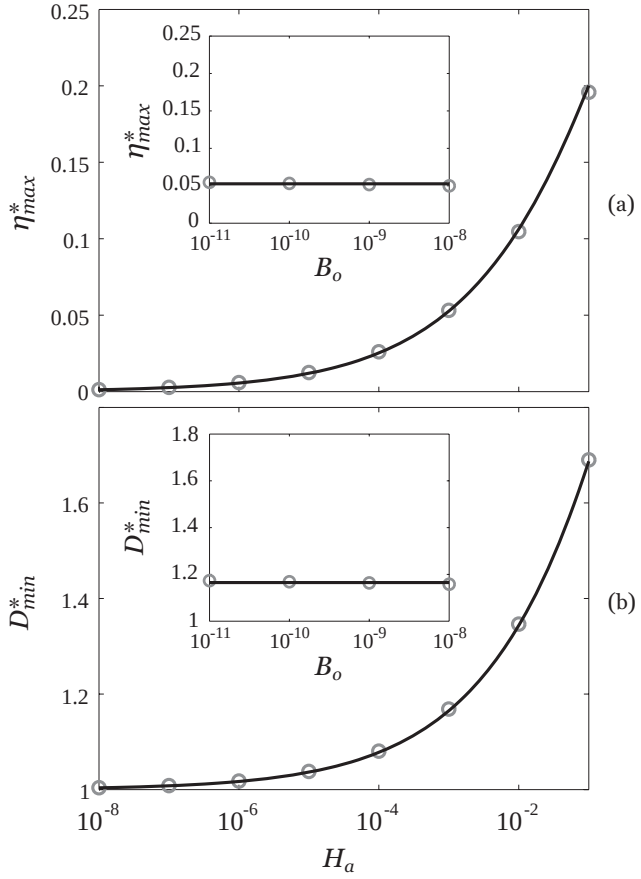


FIG. 7. (a) Maximum apex deformation and (b) minimal dimensionless distance as functions of H_a for a fixed $B_o = 10^{-10}$, and (insets) as functions of B_o for a fixed $H_a = 10^{-3}$. [○] solution of the steady-state Eq. (5), and [—] tendency curve from the combination of Eqs. (16), (18), and (19).

behavior for a given combination of H_a and B_o, it is found that κ_0^* grows along with η_0^*, which in turn becomes larger when D^* decreases, as observed in Fig. 8. The curvature κ_0^* shows a remarkable simple dependency on η_0^*, given by

$$\kappa_0^* = C(\eta_0^*)^{3/2}, \tag{14}$$

in which the prefactor $C \approx 0.4(B_o^{0.06}/H_a^{0.5})$ is obtained from fitting the solutions of Eq. (5) for the range of parameters considered. From Fig. 8, a horizontal logarithmic displacement is produced when modifying the dimensionless numbers: significantly toward larger values of η_0^* when H_a increases; barely noticeable to smaller values of η_0^* when B_o grows. While η_0^* moves towards $\eta_{\max}^*$, κ_0^* reaches its maximum value $\kappa_{\max}^* \approx 3.3 \times 10^{-2}$, which stays nearly constant for any H_a and B_o. $\eta_{\max}^*$ and $\kappa_{\max}^*$ indicate the limits of validity of Eq. (14).

For the case of local probes, R is always much smaller than λ_C, and as a consequence $B_o \ll 1$. Thence, the effect of the capillarity is negligible compared to that of the attractive term at the symmetry axis, which corresponds to say that η_0^* is fully controlled by the London–vdW potential. Following this statement, disregarding the hydrostatic term in the steady-state Eq. (5), and analytically solving for D^* at $r^* = 0$, we obtain

$$D^* = \eta_0^* + \sqrt{1 + \left(\frac{H_a}{2\kappa_0^*}\right)^{1/3}}, \tag{15}$$

which, when substituting Eq. (14), gives the dependency of D^* on η_0^*, leading to the bifurcation diagram's construction. The resulting relationship supplies the two physically possible solutions of Eq. (5), both stable and unstable branches. Bifurcation curves obtained using Eqs. (15) and (14) are also shown in Fig. 6(a), corresponding to a fixed $B_o = 10^{-10}$ and a range $H_a \in [10^{-8},10^{-1}]$. Furthermore, the derivative of η_0^* with respect to D^*, as well as κ_0^*, are compared to the stable branch results in Figs. 6(b) and 6(c), respectively. In all cases, a very good accordance with the numerical solution is observed.

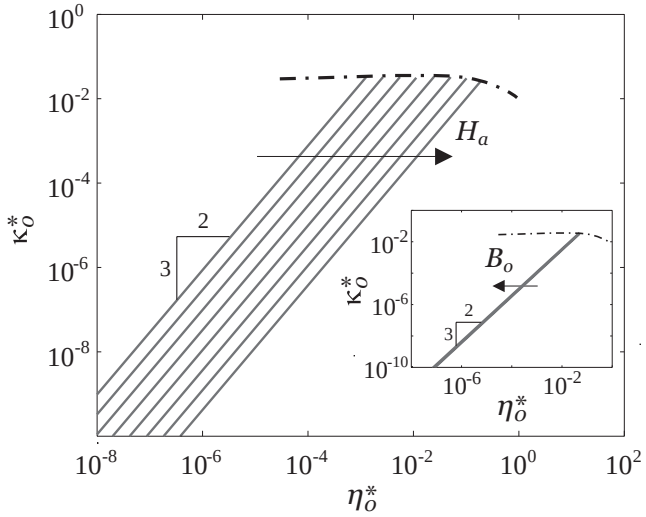


FIG. 8. Apex mean curvature κ_0^* as a function of η_0^* obtained for different modified Hamaker numbers in the range $H_a \in [10^{-8},10^{-1}]$ and a fixed Bond number of $B_o = 10^{-10}$ and (inset) for different Bond numbers in the range $B_o \in [10^{-11},10^{-8}]$ and a fixed $H_a = 10^{-3}$. [- · -] indicates $\eta^*_{\max}$ obtained from the evaluation in Eq. (14) of $\eta^*_{\max}$, in turn obtained when solving Eq. (18). Arrows indicate the growth of the corresponding parameter.

From Fig. 1, the separation distance D between the liquid surface and the probe center, and the height of the interface apex η_0 are related by an evident geometric relation

$$D^* = 1 + \eta_0^* + \epsilon_0^*, \tag{16}$$

where $\epsilon_0^* = \epsilon_0/R$ is the dimensionless gap between the deformed interface and the sphere surface. Combining Eq. (16) with Eq. (15) gives the exact expression of the dimensionless gap

$$\epsilon_0^* = \sqrt{1 + \left(\frac{H_a}{2\kappa_0^*}\right)^{1/3}} - 1, \tag{17}$$

which, once more with the employment of Eq. (14), also relates ϵ_0^* and η_0^*. Considering that the apex position diverges at $D^*_{\min}$, thus $d\eta_0^*/dD^* \to \infty$, we obtain $D^*_{\min}$ by calculating analytically the minimum of Eq. (15). Combining the latter with Eq. (14), the acquired polynomial

$$(\eta^*_{\max})^3 + \left(\frac{Ha}{2C}\right)^{1/3} (\eta^*_{\max})^{5/2} - \frac{1}{16}\left(\frac{Ha}{2C}\right)^{2/3} = 0, \tag{18}$$

is meant to be solved in order to find the maximum deformation, and used to determine the minimum separation distance and the corresponding gap. The minimum gap is now given by

$$\epsilon^*_{\min} = \sqrt{1 + \left(\frac{H_a}{2C}\right)^{1/3} \frac{1}{\sqrt{\eta^*_{\max}}}} - 1, \tag{19}$$

while $D^*_{\min}$ is obtained when substituting $\eta^*_{\max}$ and $\epsilon^*_{\min}$ in Eq. (16).

In conclusion, the employment of Eq. (14) leads to find expressions, with which we can easily determine $\eta^*_{\max}$, $\epsilon^*_{\min}$, and $D^*_{\min}$. Together with the knowledge of H_a and B_o, which are determined using data from the literature [1,11,12] or experiments [9], the optimal AFM scanning separation distance range $]D_{\min},2R]$ is found. Such information is important for imaging liquid topographies and material properties at the nanoscale.

IV. DEFORMATION SCALING

A. Characteristic length-scales

Taking $\Pi^* = 3\pi R^3\Pi/4H$, we write the steady-state Eq. (5) as follows:

$$2\kappa^* + B_o\eta^* - H_a\Pi^* = 0. \tag{20}$$

The absolute value of the terms appearing in Eq. (20) and the curvature decomposition terms in Eq. (9), which contribute to achieve an equilibrium steady state, are depicted in Fig. 9. The existence of three important length-scales, already introduced in Fig. 1, is emphasized.

Firstly, corresponding to the position for which $\kappa_m^* = 0$ (inflection point of the meridional profile), λ_H^* indicates the boundary of a near-field zone, and the beginning of a transition zone, where all the variables contribute to the deformation. At $r^* \in [0,\lambda_H^*[$, the attractive term $H_a\Pi^*$ (positive) is mostly opposed by $2\kappa^*$ (positive), whereas the hydrostatic term $B_o\eta^*$ (positive) is negligible. Characterized by H_a, the equilibrium profile in this near-field range is directly controlled by the balance between attractive potential and capillary pressure, both showing constant magnitudes that slowly decay when $r^* \to \lambda_H^*$.

Then, at the radial extent for which $2\kappa^* = 0$ (zero-curvature), λ_T^* marks the end of the transition region and

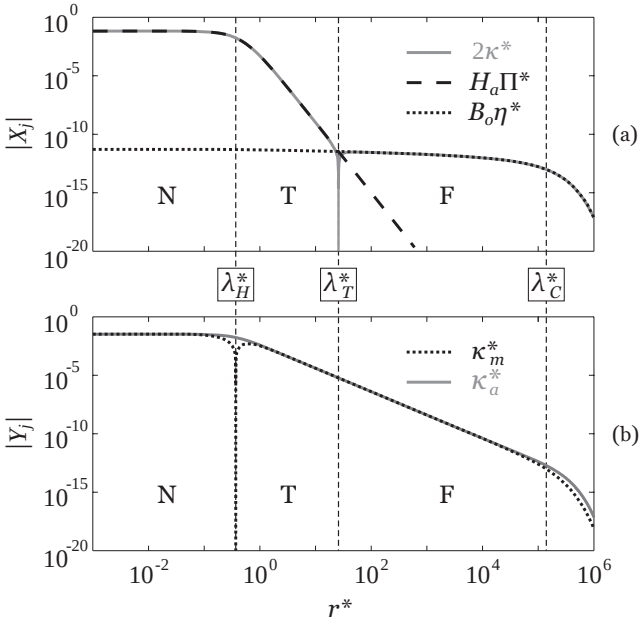


FIG. 9. Characteristic length-scales determination. Different terms (a) X_j from Eq. (20), for which $\sum X_j = 0$, and (b) Y_j from Eq. (9), for which $\sum Y_j = 2\kappa^*$, as functions of r^*, for $H_a = 10^{-3}$, $B_o = 10^{-10}$, and $D^* = D^*_{\min} = 1.168$. The uppercase letters N, T, and F designate the near-field, transition, and far-field zones, respectively, which extents are bounded by the characteristic length-scales λ_H^*, λ_T^*, and λ_C^*.

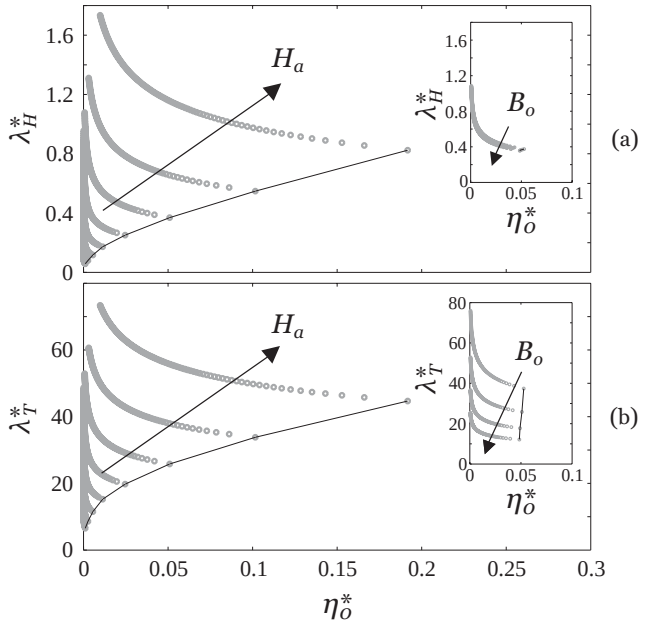


FIG. 10. (a) Radial position of the inflection point of the profile λ_H^* and (b) radial position of zero-curvature λ_T^*, as functions of η_0^*, with the same parameter values and variables as in Fig. 8, as well as the same considerations for the insets. Arrows indicate the growth of the corresponding parameter.

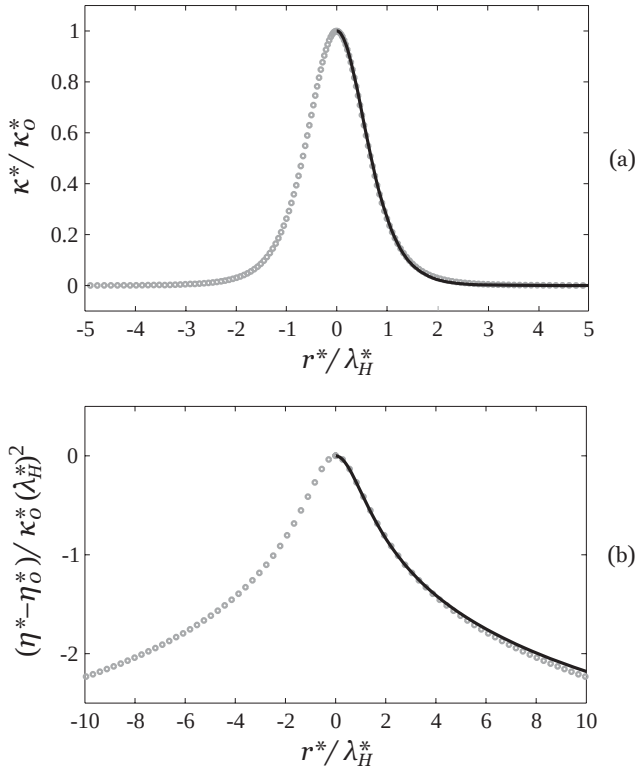


FIG. 11. Near-field self-similar dimensionless (a) curvature and (b) interface profile for $H_a \in [10^{-8},10^{-1}]$ and $B_o \in [10^{-11},10^{-8}]$. [○] numerical solution of the steady-state Eq. (5) and [—] approximations obtained from Eqs. (21) and (23), for the curvature and the interface profile, respectively.

the beginning of the far-field zone, which corresponds to a capillarity dominated decay. When $r^* \in]\lambda_H^*,\lambda_T^*[$, κ_a^* withstands both $H_a\Pi^*$, which quickly loses its intensity, and κ_m^*, which has adopted a negative value. In this region, κ_m^* and κ_a^*, the latter always showing a positive value, are antagonists. $B_o\eta^*$ remains nearly constant as it slowly gains weight while both $H_a\Pi^*$ and $2\kappa^*$ decrease at the same rate.

Finally, the dimensionless capillary length λ_C^* shows the extension at which the effect of all terms tend to disappear. Within $r^* \in]\lambda_T^*,\lambda_C^*]$, $H_a\Pi^*$ has become negligible whereas $2\kappa^*$, which has become negative, attains the order of magnitude of $B_o\eta^*$. In this zone, $B_o\eta^*$, which diminishes gradually, is opposed by $2\kappa^*$, while κ_m^* and κ_a^* are still contending. The shape of the interface profile in this far-field zone is completely given by B_o. Beyond $r^* = \lambda_C^*$, the interface returns to its unperturbed flat state.

In Fig. 10, λ_H^* and λ_T^* are shown as functions of η_0^* for different H_a and B_o. For a given combinations of parameters, λ_H^* and λ_T^* decline as functions of η_0^*, following rectangular hyperbolalike behaviors. This tendency continues until the values of $D_{\min}^*$ and $\eta_{\max}^*$ are reached, for which the limiting equilibrium profile and the minimum radial positions of λ_H^* and λ_T^* are attained. The numerical results indicate that λ_H^* shifts toward higher values when H_a increases in the range $H_a \in [10^{-8},10^{-1}]$. On the other hand, the impact of B_o on λ_H^*, within $B_o \in [10^{-11},10^{-8}]$, is not significant. Likewise, λ_T^* follows the same tendency when H_a augments; however, we observe an important decrease of λ_T^* when B_o grows.

The curves in Fig. 10 can also be analyzed as follows. For a given H_a, a decrease of D^* provokes the growth of Π^* and η_0^*, leading to a decrease in both λ_H^* and λ_T^*, which is the action of the capillary pressure to restrain the radial extent of the deformation. From another viewpoint, an increase of H_a generates a given η_0^* at a larger D^*, and both λ_H^* and λ_T^* are subsequently increased, which indicates that the attractive potential spans over a larger zone. Because D^* and its induced η_0^* are not significantly affected by B_o, a change in this parameter has a faint effect over λ_H^*. On the other hand, an increase of B_o directly provokes a decrease of λ_T^*, which corresponds to enlarging the heaviness of the interface.

B. Self-similarity

Taking into account the length-scales, λ_H^* and λ_C^*, we find master curves that display the self-similarity of the deformation profile in the near- and far-field zones, respectively. For $r^* \in [0,\lambda_H^*[$, the reduced variables κ^*/κ_0^* and r^*/λ_H^* allow us to find the dimensionless curvature presented in Fig. 11(a). This curve exhibits a logisticlike probability function shape

$$\frac{\kappa^*}{\kappa_0^*} = \frac{4\exp\left(-\frac{r^*}{b\,\lambda_H^*}\right)}{\left[1+\exp\left(-\frac{r^*}{b\,\lambda_H^*}\right)\right]^2}, \tag{21}$$

where b is a fitting parameter, which is determined below. The relative error between the numerical solution of κ^*/κ_0^* and Eq. (21) is 10^{-3}, for a radial position up to $r^* \leqslant 5\lambda_H^*$.

In addition, the reduced curvature κ^*/κ_0^* can be taken as negligible for radial positions beyond $r^* \approx 10b\,\lambda_H^*$.

Matching Eq. (21) with Eq. (3), for small displacements of the liquid surface, and integrating we find

$$\frac{1}{r^*}\frac{d\eta^*}{dr^*} = 8\kappa_0^*\left(\frac{b\,\lambda_H^*}{r^*}\right)\left\{\frac{\exp\left(-\frac{r^*}{b\,\lambda_H^*}\right)}{1+\exp\left(-\frac{r^*}{b\,\lambda_H^*}\right)} + \left(\frac{b\,\lambda_H^*}{r^*}\right)\left(\ln\left[1+\exp\left(-\frac{r^*}{b\,\lambda_H^*}\right)\right] - \ln B\right)\right\}, \tag{22}$$

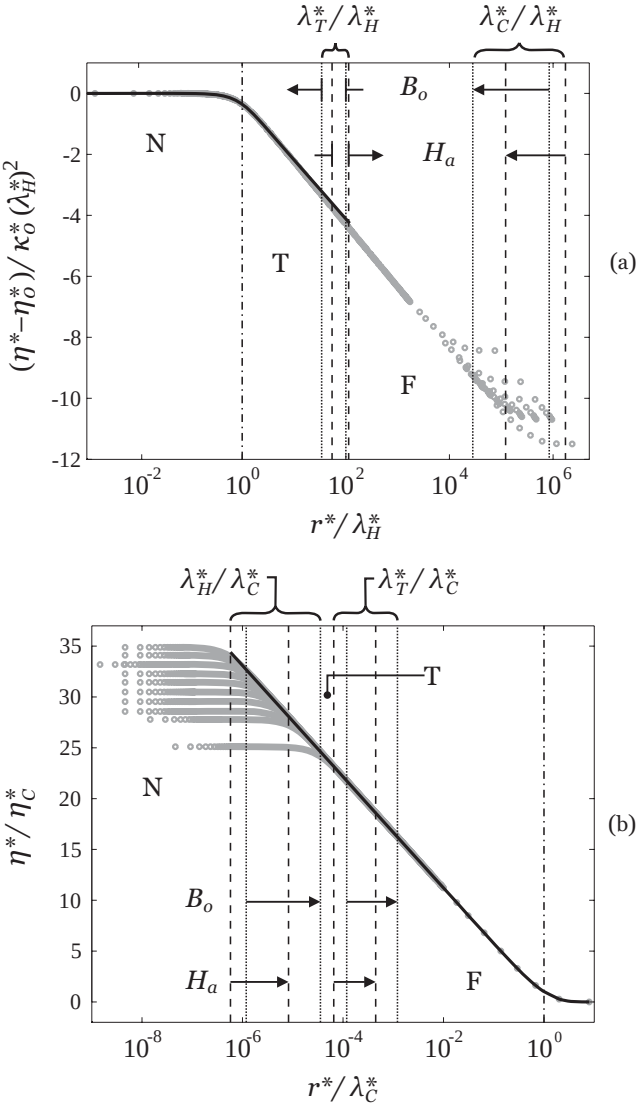


FIG. 12. Self-similar deformation profile obtained with the dimensionless variables in (a) Eq. (23) and (b) Eq. (24). [○] numerical solution of the steady-state Eq. (5) and [—] approximations obtained from Eqs. (23) and (24). The uppercase letters N, T, and F designate the near-field, transition, and far-field zones, respectively. Vertical lines indicate the positions of the reduced characteristic length-scales, while the sense of the arrows shows its displacement when the corresponding dimensionless parameter grows: shifting $H_a \in [10^{-8},10^{-1}]$ for a fixed $B_o = 10^{-10}$, and varying $B_o \in [10^{-11},10^{-8}]$ for $H_a = 10^{-3}$.

where B is an integration constant. From the boundary conditions $[\eta^*]_0' = 0$ and the corresponding Taylor expansion of the logarithmic term, we find $B = 2$. As well, evaluating Eq. (22) and (21) at $r^* = \lambda_H^*$, where $2\kappa^* = \kappa_a^*$, we deduce the value of $b = 3.89 \times 10^{-1}$. Afterward, performing a second integration of Eq. (22), we obtain the expression of the dimensionless deformation profile

$$\frac{\eta^*-\eta_0^*}{\kappa_0^*(\lambda_H^*)^2} = 8b^2\left\{-\ln\frac{1}{2}\left[1+\exp\left(-\frac{r^*}{b\,\lambda_H^*}\right)\right] + \int_0^{r^*/(b\,\lambda_H^*)}\ln\frac{1}{2}[1+\exp(-x)]\frac{dx}{x}\right\}, \tag{23}$$

where x is an integration variable. Once more, the relative error between the numerical solution and Eq. (23) is also 10^{-3}, for a radial position up to $r^* \leqslant 5\lambda_H^*$. In Fig. 11(b), the self-similar profile given by Eq. (23) is compared to the numerical results, showing a very good agreement within $0 \leqslant r^* \leqslant \lambda_H^*$, for $H_a \in [10^{-8},10^{-1}]$ and $B_o \in [10^{-11},10^{-8}]$. Therefore, it is proven that $(\eta^*-\eta_0^*)/\kappa_0^*(\lambda_H^*)^2$ and r^*/λ_H^* are the dimensionless variables that characterize the self-similar behavior of the deformation in the near-field zone. The logarithmic plot of these parameters, depicted in Fig. 12(a), exposes that this self-similarity spans largely over the transition zone.

For $r^* \in]\lambda_T^*,\lambda_C^*]$, the couple of reduced variables η^*/η_C^* and r^*/λ_C^*, where $\eta_C^* = \eta^*(r^* = \lambda_C^*)$, leads us to find the far-field self-similar deformation profile

$$\frac{\eta^*}{\eta_C^*} = \frac{K_0\left(\frac{r^*}{\lambda_C^*}\right)}{K_0(1)}, \tag{24}$$

As shown in Fig. 12(b), Eq. (24) gives a quite good description of the far-field results within $\lambda_T^* < r^* \leqslant \lambda_C^*$, and even spanning over the whole transition zone. The decaying behavior, described by the far-field self-similarity, is observed for $r^* \in]\lambda_H^*,\infty[$.

V. CONCLUDING REMARKS

An extensive analysis of the deformation of a liquid surface, due to its interaction with a nanoprobe, was presented. The phenomenon was portrayed by a strongly nonlinear equation, and the effects of physical and geometric parameters over the system were considered. Mainly when the interaction within a nanoscale system is considered, our model generates a more accurate description of the interface deformation than previous works [16,17], which employ the Derjaguin approximation. Furthermore, the application of our results is possible at any scale, considering realistic situations, due to the performed dimensionless approach.

The interface profile evolution, whether the system attains equilibrium or not, depends on the relative magnitude of D^* with respect to the threshold distance $D_{\min}^*$, which in turn is given by the combination of the remaining parameters, B_o and H_a. Bifurcation diagrams relating η_0^* and D^* are established, in which a zone with nonexistent equilibrium is uncovered and explained, when $D^* < D_{\min}^*$. On the other hand, steady-state stable and unstable equilibrium profiles are obtained when $D^* \geqslant D_{\min}^*$, thus the attractive force is thwarted mostly by the capillary pressure.

Three different length-scales were obtained from the analysis of the steady-state equilibrium profiles, all of them being function of H_a and/or B_o. They determine the existence of: a near-field zone, $r^* \in [0,\lambda_H^*[$, controlled by the attractive interaction/surface tension balance; a far-field zone, $r^* \in]\lambda_T^*,\lambda_C^*]$, dominated by the gravity/surface tension interplay; and a transition zone, $r^* \in]\lambda_H^*,\lambda_T^*[$, where all the variables take an important role. It was found that the two interior length-scales are affected by the size of the probe: $\lambda_H \lesssim R$ and $\lambda_T \gtrsim 10R$, while the capillary length remains fixed $\lambda_C \sim 10^{-3}$. These length-scales are responsible for the liquid surface self-similar deformation profile.

The curvature of the stable profile is found to take a remarkable shape at its apex, $\kappa_0^* \propto (\eta_0^*)^{3/2}$. This fact and the problem geometry give rise to accurate simple formulas for computing the minimum separation distance $D_{\min}^*$, its corresponding maximum deformation $\eta_{\max}$ and minimum gap $\epsilon_{\min}^*$, when H_a and B_o are previously known [1,11,12] or experimentally obtained [9]. The knowledge of $D_{\min}^*$ is fundamental when searching the optimal scanning noncontact AFM conditions, in order to avoid undesired capillarity effects. Nevertheless, the power-law relationship between κ_0^* and η_0^* remains a factual but empiric result, which is a topic for future studies.

[1] J. N. Israelachvili, *Intermolecular and Surface Forces*, 3rd ed. (Elsevier, Amsterdam, 2011).

[2] E. Pelletier, J. P. Montfort, and F. Lapique, J. Rheol. **38**, 18 (1994).

[3] J. N. Sharpe, *Handbook of Experimental Solid Mechanics* (Springer, Berlin, 2008).

[4] A. Knoll, R. Magerle, and G. Krausch, Macromolecules **34**, 4159 (2001).

[5] H. J. Butt, B. Cappella, and M. Kappl, Surf. Sci. Rep. **59**, 1 (2005).

[6] T.-D. Li and E. Riedo, Phys. Rev. Lett. **100**, 106102 (2008).

[7] M. Delmas, M. Monthioux, and T. Ondarcuhu, Phys. Rev. Lett. **106**, 136102 (2011).

[8] B. A. Todd and S. J. Eppell, Langmuir **20**, 4892 (2004).

[9] R. Ledesma-Alonso, D. Legendre, and P. Tordjeman, Phys. Rev. Lett. **108**, 106104 (2012).

[10] H. C. Hamaker, Physica **4**, 1058 (1937).

[11] L. Bergstrom, Adv. Colloid Interface Sci. **70**, 125 (1997).

[12] J. Visser, Adv. Colloid Interface Sci. **3**, 331 (1972).

[13] K. Mougin and H. Haidara, Europhys. Lett. **61**, 660 (2003).

[14] L. F. Shampine, I. Gladwell, and S. Thompson, *Solving ODEs with MATLAB* (Cambridge University Press, Cambridge, 2003).

[15] F. M. Orr, L. E. Scriven, and A. P. Rivas, J. Fluid Mech. **67**, 723 (1975).

[16] F. P.-A. Cortat and S. J. Miklavcic, Langmuir **20**, 3208 (2004).

[17] Y. Z. Wang, D. Wu, X. M. Xiong, and J. X. Zhang, Langmuir **23**, 12119 (2007).

Langmuir

Article

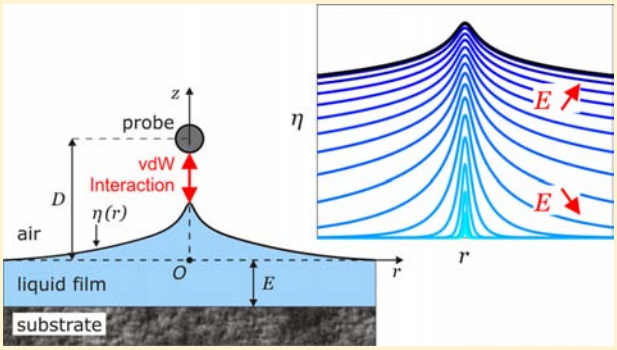
pubs.acs.org/Langmuir

AFM Tip Effect on a Thin Liquid Film

R. Ledesma-Alonso, D. Legendre,* and Ph. Tordjeman*

Institut de Mécanique des Fluides de Toulouse (IMFT), INPT-CNRS, Université de Toulouse, Allée du Professeur Camille Soula, 31400 Toulouse, France

ABSTRACT: We study the interaction between an AFM probe and a liquid film deposited over a flat substrate. We investigate the effects of the physical and geometrical parameters, with a special focus on the film thickness E, the probe radius R, and the distance D between the probe and the free surface. Deformation profiles have been calculated from the numerical simulations of the Young−Laplace equation by taking into account the probe/liquid and the liquid/substrate interactions, characterized by the Hamaker constants, H_{pl} and H_{ls}. We demonstrate that the deformation of a shallow film is determined by a particular characteristic length $\lambda_F = (2\pi\gamma E^4/H_{ls})^{1/2}$, resulting from the balance between the capillary force (γ is the surface tension) and the van der Waals liquid/substrate attraction. For the case of a bulk liquid, the extent of the interface deformation is simply controlled by the capillary length $\lambda_C = (\gamma/\Delta\rho g)^{1/2}$. These trends point out two asymptotic regimes, which in turn are bounded by two characteristic film thicknesses $E_g = (H_{ls}/2\pi\Delta\rho g)^{1/4}$ and $E_\gamma = (R^2H_{ls}/2\pi\gamma)^{1/4}$. For $E > E_g$, the bulk behavior is recovered, and for $E < E_\gamma$, we show the existence of a particular shallow film regime in which a localized tip effect is observed. This tip effect is characterized by the small magnitude of the deformation and an important restriction of its radial extent λ_F localized below the probe. In addition, we have found that the film thickness has a significant effect on the threshold separation distance D_{min} below which the irreversible jump-to-contact process occurs: D_{min} is probe radius-dependent for the bulk whereas it is film-thickness-dependent for shallow films. These results have an important impact on the optimal AFM scanning conditions.



1. INTRODUCTION

The current development of nanotechnology is responsible for the emergence of micro- and nanofluidic systems.[1] A large number of these systems are based on the flow of very thin liquid films in confined geometries.[2] Under these conditions, capillary and van der Waals forces are dominant, and as a consequence, the behavior of liquids is strongly dependent on the film thickness. For instance, the flow relaxation time,[3,4] the slip length,[5] and the glass-transition temperature,[6,7] among other properties, are controlled by the characteristic length of confinement.

The properties of a liquid film as function of its thickness, from the molecular to the macroscopic scale, can be studied by means of atomic force microscopy (AFM) as a result of the recent progress of this technique.[8,9] Indeed, noncontact AFM is a useful method for quantifying the local properties of liquid films,[10] identifying the local positions of interfaces, and detecting liquid-phase domains and studying their rheology. In such experiments, the study of the probe/liquid film interaction is fundamental to understanding the behavior of liquids of different thicknesses. With respect to the extensive work done by means of the surface force apparatus (SFA), we recall that the thickness has been shown to be a fundamental parameter in determining the stability of the film.[11] In addition, it has been proposed, for a liquid nanofilm,[12] that the film thickness should have a significant effect on AFM measurements and also promising applications.

In our previous studies,[13,14] the surface deformation of a bulk liquid in interaction with an AFM tip has been modeled, solved numerically, and validated with experiments. We have shown that the magnitude of the bulk liquid surface deformation and its curvature are functions of the probe/liquid separation distance. When a probe is approached towards the liquid surface below a threshold separation distance, we have found that the liquid undergoes a jump-to-contact phenomenon, which triggers probe wetting. Knowledge of this critical distance, called D_{min}, is essential to determining the experimental optimal conditions for noncontact AFM measurements over liquids. We have demonstrated that a combined approach, based on theory and experiments, leads to a better understanding of the whole phenomenon. In particular, a fine prediction of the Hamaker interaction constant has been deduced from AFM force/distance curves.[13]

The aim of this Article is to analyze the effect of the film thickness on the surface deformation. For this purpose, the Young−Laplace equation has been generalized to include the interaction between the liquid film and the underlaying

Received: February 15, 2013
Revised: May 28, 2013
Published: May 30, 2013

ACS Publications © 2013 American Chemical Society

dx.doi.org/10.1021/la4006086 | Langmuir 2013, 29, 7749−7757

substrate. The present communication is organized as follows: in section 2, we describe briefly the system configuration, together with the corresponding theoretical model, in which molecular interactions and capillarity are included. Section 3 discusses the general surface deformation and the jump-to-contact phenomenon and their dependency on the involved dimensionless parameters in which some of them are thickness-dependent. Several characteristic length scales, naturally arising in the model, are introduced and employed to describe the surface shape. The theoretical analysis allows us to define two critical film thicknesses, marking the boundaries of a shallow film regime and the bulk behavior, which are presented in section 4 and discussed in section 5. Finally, in section 6 the effects of the probe radius and the film thickness are studied quantitatively in order to apply the results when performing AFM measurements.

2. PROBLEM FORMULATION

Consider a stable liquid film of thickness E deposited over a flat substrate, as shown in Figure 1. When a spherical probe of

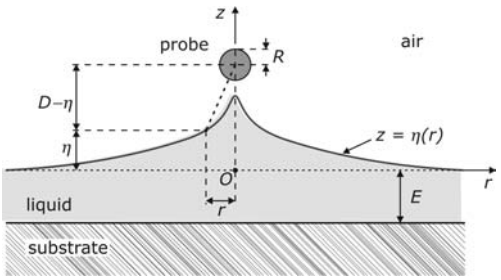


Figure 1. Surface deformation of the liquid film interacting with a spherical probe.

radius R is placed at a distance D from the liquid free surface, a bump-like shape is observed. Because of the system geometry, the deformation is described by an axisymmetric profile $z = \eta(r)$, where r and z are the radial and axial coordinates.

On the basis of the Hamaker theory,[15] the attractive interaction potential or pressure field Π_{pl} exerted by the probe over the liquid film is

$$\Pi_{pl} = \frac{4H_{pl}R^3}{3\pi}\frac{1}{[(D-z)^2 + r^2 - R^2]^3} \tag{1}$$

where H_{pl} is the Hamaker constant of the probe/air/liquid system. Equation 1 is obtained from integrating the London–van der Waals interaction potential of the spherical probe over a differential volume of liquid, anywhere outside the probe. Only the nonretarded interactions are considered in view of the dimensions of common AFM setups.

The presence of the substrate provokes, over the liquid film, the potential field Π_{ls} given by

$$\Pi_{ls} = -\frac{H_{ls}}{6\pi}\left[\frac{1}{(E+z)^3} - \frac{1}{(E)^3}\right] \tag{2}$$

where H_{ls} is the Hamaker constant of the air/liquid/substrate system. This potential is the difference between the so-called disjoining pressure[16] of the initial state and that of the perturbed state (by the approach of the probe). Furthermore, the capillary pressure difference and the hydrostatic pressure appear in the pressure balance so that the surface shape of the film is described by the generalized Young–Laplace equation

$$\Pi_{pl} - \Delta\rho g\eta = 2\kappa\gamma + \Pi_{ls} \tag{3}$$

where $\Delta\rho$ is the liquid/air density difference, g is the gravitational acceleration, γ is the liquid surface tension, η is the local surface position, and κ is the local mean curvature, which, expressed in axisymmetric cylindrical coordinates, takes the form

$$2\kappa = -\frac{1}{r}\frac{d}{dr}\left[r\frac{d\eta}{dr}\left\{\left(\frac{d\eta}{dr}\right)^2 + 1\right\}^{-1/2}\right] \tag{4}$$

Using R as the characteristic length scale, we introduce dimensionless variables: $D^* = {}^{D}/_{R}$ the distance from the center of the probe to the originally undeformed free surface, $E^* = {}^{E}/_{R}$ the film relative thickness, $r^* = {}^{r}/_{R}$ and $z^* = {}^{z}/_{R}$ the horizontal and vertical coordinates; and $\eta^* = {}^{\eta}/_{R}$ and $\kappa^* = \kappa R$, the interface position and mean curvature. From eqs 1–4, the dimensionless nonlinear ordinary differential equation describing the free surface position results in

$$2\kappa^* - \frac{AH_a}{8}\Pi_{ls}^* + B_o\eta^* - H_a\Pi_{pl}^* = 0 \tag{5}$$

where

$$\Pi_{ls}^* = \frac{1}{(E^*+\eta^*)^3} - \frac{1}{(E^*)^3} \tag{6a}$$

$$\Pi_{pl}^* = \frac{1}{[(D^*-\eta^*)^2 + r^{*2} - 1]^3} \tag{6b}$$

Three dimensionless parameters are present in eq 5: the Hamaker constant ratio $A = H_{ls}/H_{pl}$, the modified Hamaker number $H_a = 4H_{pl}/(3\pi\gamma R^2)$, and the Bond number $B_o = \Delta\rho g R^2/\gamma$.

In AFM setups, the probe radius R is within the range $[10^{-9}, 10^{-7}]$ m, and the probe/liquid and liquid/substrate interactions are characterized by Hamaker constants H_{pl} and H_{ls} within $[10^{-21}, 10^{-19}]$ J.[17−20] For air/liquid interfaces, one usually has $\gamma \in [10^{-2}, 10^{-1}]$ N/m and $\Delta\rho \in [10^2, 10^4]$ kg/m^3. Consequently, for a film thickness E spanning $[10^{-10}, \infty]$ m, the dimensionless parameters are normally found to satisfy $A \in [10^{-2}, 10^2]$, $H_a \in [10^{-7}, 10^0]$, and $B_o \in [10^{-13}, 10^{-8}]$.

In particular, considering a PDMS film deposited over a silicon wafer and in interaction with an $R = 1 \times 10^{-8}$ m silicon AFM probe, the system is characterized by $\gamma = 3.1 \times 10^{-2}$ N/m, $\Delta\rho = 9.7 \times 10^2$ kg/m^3, and $H_{ls} = H_{pl} = 4 \times 10^{-20}$ J.[13] The nondimensional numbers are then $A = 1$, $H_a = 5.48 \times 10^{-3}$, and $B_o = 3.07 \times 10^{-11}$, and the film relative thickness should span $E^* \in [10^{-2}, \infty]$.

Equation 5 was solved numerically following a previously developed method[14] in which the supplementary term given by eq 6a, arising from the liquid/substrate interaction, has been introduced. The symmetry condition $[\eta^*]' = 0$ at $r^* = 0$, a nearly flat surface profile $[\eta^*]' \ll 1$, and a negligible probe/liquid interaction potential $\Pi_{pl}^* \approx 0$ far from the symmetry axis were maintained as boundary conditions.

To calculate the film deformation analytically, we can write the separation distance D^* as a function of the apex position η_0^* and the curvature κ_0^* at $r^* = 0$ as follows

$$D^* = \eta_0^* + \sqrt{1 + [f(\eta_0^*, \kappa_0^*)]^{-1/3}} \tag{7}$$

dx.doi.org/10.1021/la4006086 | Langmuir 2013, 29, 7749−7757

where the function $f(\eta_0^*, \kappa_0^*)$ is defined as

$$f(\eta_0^*, \kappa_0^*) = \frac{2\kappa_0^*}{H_a} + \frac{A}{8(E^*)^3}\left[1 - \left(1 + \frac{\eta_0^*}{E^*}\right)^{-3}\right] + \frac{B_o}{H_a}\eta_0^* \tag{8}$$

D^* can also be expressed by introducing ε_0^*, the dimensionless gap between the probe surface and the deformed liquid interface inferred from Figure 1:

$$D^* = 1 + \eta_0^* + \varepsilon_0^* \tag{9}$$

In dimensional terms, $D - R$ represents the gap between the probe and the nondeformed film surface. Comparing eq 9 with an expansion of eq 7 gives

$$\varepsilon_0^* = \frac{1}{2}[f(\eta_0^*, \kappa_0^*)]^{-1/3} - \frac{1}{8}[f(\eta_0^*, \kappa_0^*)]^{-2/3} + O\{[f(\eta_0^*, \kappa_0^*)]^{-1}\} \tag{10}$$

which allows us to calculate the magnitude of the gap if $f(\eta_0^*, \kappa_0^*)$ is known.

In previous studies,[12−14,21] it has been stated that no solution of the problem can be found for distances below the threshold distance D_{min}^* because the jump-to-contact phenomenon takes place. This minimum separation distance also marks the critical point at which the maximum apex deformation $\eta_{0,max}^*$ and the maximum curvature $\kappa_{0,max}^*$ occur. D_{min}^* is obtained directly when $dD^*/d\eta_0^* = 0$, which applied to eq 7 gives

$$\frac{1}{36}\{f'(\eta_{0,max}^*)\}^2 = [f(\eta_{0,max}^*)]^{8/3}\{1 + [f(\eta_{0,max}^*)]^{-1/3}\} \tag{11}$$

An expression $f(\eta_0^*)$, which must be used in eq 11 to obtain $\eta_{0,max}^*$, exists when it is possible to express the curvature in terms of the apex deformation, $\kappa_0^*(\eta_0^*)$. Afterward, once $\eta_{0,max}^*$ is known, D_{min}^* is determined using eq 7.

In the following section, this approach is applied to generate analytical expressions of the maximum deformation $\eta_{0,max}^*$ and the minimum distance D_{min}^* in the asymptotic cases corresponding to $E^* \to 0$ (shallow-film limit) and $E^* \to \infty$ (thick-film limit).

3. SURFACE SHAPE

3.1. General Description. Some typical surface profiles obtained numerically are shown in Figure 2 for a radial extension of about 10 times the probe radius. Note that the presented window is much smaller than the capillary length so that the entire interface deformation is not shown. The profiles are reported for a single separation distance of $D^* = 1.29$ and for $H_a = 5.48 \times 10^{-3}$, $B_o = 3.07 \times 10^{-11}$, and $A = 1$. The relative thickness E^* varies over several orders of magnitude in the range of $[10^{-10}, \infty]$. We observe that all of the profiles exhibit a bump-like shape that is roughly parabolic around $r^* = 0$, followed by an exponential-like decay. The profiles obtained for $E^* > 10^2$ are overlapped, indicating the existence of an asymptotic bulk regime. The vertical displacement of the surface weakens in magnitude, and the deformation seems to be confined to a shorter radial extent as E^* is reduced. In addition, the curvature of the surface at $r^* = 0$ lowers with decreasing E^*.

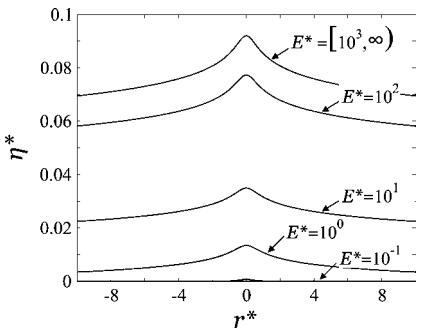


Figure 2. Surface profiles of the film η^* obtained from solving eq 5, at a constant $D^* = 1.29$, for different values of E^* and for $H_a = 5.48 \times 10^{-3}$, $B_o = 3.07 \times 10^{-11}$, and $A = 1$.

The corresponding behavior of apex deformation η_0^* at $r^* = 0$ is shown in Figure 3 as a function of the separation distance D^*. As observed for infinite film thickness,[14,22] we found a stable and an unstable position of the interface for any film thickness. In Figure 3, we present the stable deformation, corresponding to the minimal free energy of the system, that is present when experiments are performed. Similar hyperbolic evolutions for η_0^* are observed for the different values of E^*. When sweeping from right to left, as the curve approaches the threshold distance D_{min}^*, the slope increases dramatically until a vertical asymptote is reached. At D_{min}^*, the maximum possible apex position $\eta_{0,max}^*$ is attained. For shorter separation distances, the probe/liquid attraction becomes unconstrained and the so-called jump to contact is observed, which provokes the wetting of the probe in a real situation. Consistent with expectations on physical grounds, a decrease in E^* leads to a decrease of D_{min}^* along with a shrinkage of $\eta_{0,max}^*$ as the attractive liquid/substrate potential pulls the liquid film uniformly downward, therefore inhibiting its upward displacement. In other words, when the film thickness is decreased, the jump to contact is shifted to separation distances shorter than that observed for a bulk liquid. Additionally, it is relevant to remark that a reduction of E^* provokes a similar effect to that induced by a diminution of H_a for the bulk.[14]

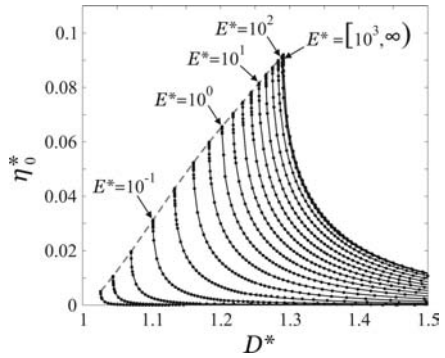


Figure 3. Apex position η_0^* of the air/liquid interface as a function of D^* for different values of E^* and for $H_a = 5.48 \times 10^{-3}$, $B_o = 3.07 \times 10^{-11}$, and $A = 1$. (•) Numerical solutions of eq 5 and (---) extreme values D_{min}^* and $\eta_{0,max}^*$.

The corresponding evolution of the apex curvature κ_0^* as a function of the surface deformation η_0^* is shown in Figure 4 for different values of the relative thickness E^*. As a general trend, for a given E^*, the apex curvature increases along with the associated deformation, showing a nearly constant slope on the presented logarithmic scale. Nevertheless, mainly observed for the curves belonging to $E^* \leq 10^{-1}$, the slope gradually becomes

dx.doi.org/10.1021/la4006086 | Langmuir 2013, 29, 7749−7757

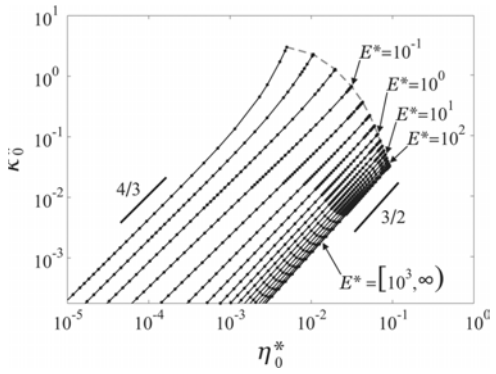


Figure 4. Apex mean curvature κ_0^* as a function of η_0^* obtained for different values of E^* and for $H_a = 5.48 \times 10^{-3}$, $B_o = 3.07 \times 10^{-11}$, and $A = 1$. (●) Numerical solution of eq 5 and (---) extreme values $\kappa_{0,max}^*$ and $\eta_{0,max}^*$.

steeper as η_0^* increases and approaches the value of $\eta_{0,max}^*$. In most cases, the behavior of each curve seems to be properly described by a power law. For relatively thick films, an exponent of $^3/_2$ has been found,[12,13] whereas for shallow films and small deformations an exponent of $^4/_3$ is discerned. The theoretical analysis of these two particular power laws is given in section 4.

3.2. Jump to Contact. Now the effect of the film thickness on the jump-to-contact condition is discussed. Figure 5 reports the evolution of the maximum apex position $\eta_{0,max}^*$ and the minimum separation distance D_{min}^* as function of the film relative thickness. Both D_{min}^* and $\eta_{0,max}^*$ show analogous trends. The bulk behavior is characterized by a plateau, which in the presented case takes the values $D_{min}^* \approx 1.29$ and $\eta_{0,max}^* \approx 0.09$ for thicknesses $E^* > 10^2$. However, $D_{min}^* \to 1$ and $\eta_{0,max}^* \to 0$ when the limit of $E^* \to 0$ is approached. These two asymptotic behaviors are associated with two characteristic film thicknesses that will be discussed in more detail in the following section. For intermediate thicknesses typically varying from 10^{-1} to 10^2, D_{min}^* and $\eta_{0,max}^*$ go through a transition regime associated with noticeable variations due to the film thickness. It is interesting that for the nondimensional parameters considered here $\eta_{0,max}^*$ never takes larger values than the film relative thickness E^*. In other words, $\eta_{0,max}^*/E^* < 1$.

In Figure 6, interface shape η^* at $D^* = D_{min}^*$ is shown as a function of the radial position r^* for different values of E^*. As

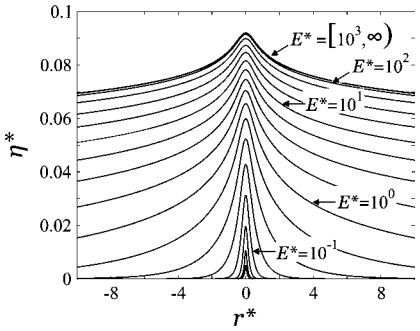


Figure 6. Surface profiles of the film η^* obtained from solving eq 5 at $D^* = D_{min}^*$ for different values of E^* and for $H_a = 5.48 \times 10^{-3}$, $B_o = 3.07 \times 10^{-11}$, and $A = 1$.

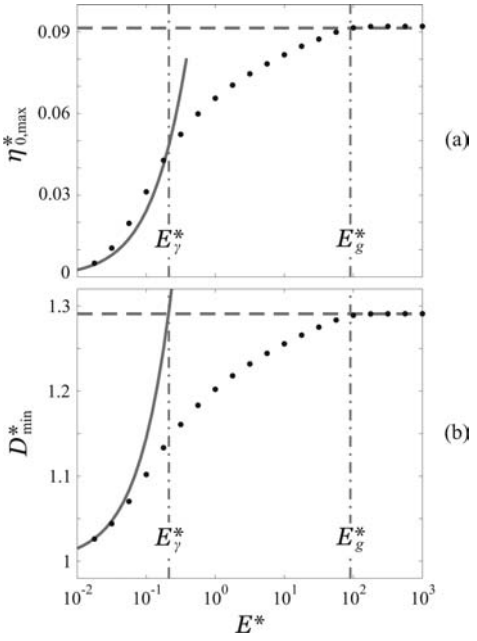


Figure 5. (a) $\eta_{0,max}^*$ and (b) D_{min}^*, as functions of E^*, for $H_a = 5.48 \times 10^{-3}$, $B_o = 3.07 \times 10^{-11}$, and $A = 1$. (●) Numerical solution of eq 5 and asymptotic approximations for (---) $E^* > E_g^*$ and (−) $E^* < E_\gamma^*$, with $E_g^* = 9.05 \times 10^1$ and $E_\gamma^* = 2.13 \times 10^{-1}$. The approximations are obtained by applying eqs 19 and 20 for thick films and eq 23 for shallow films to eqs 11 and 7 in sequence. The characteristic thicknesses, E_g^* and E_γ^*, are defined in eqs 14 and 15, respectively.

previously discussed, the maximum apex position $\eta_{0,max}^*$ and the radial extent of the deformation diminish when E^* is reduced. As a consequence, the surface profile sharpens, which provokes a dilatation of the curvature at the surface apex. Indeed, as observed in Figure 4, for a fixed value of η_0^*, the apex curvature κ_0^* grows significantly by orders of magnitude when the film relative thickness E^* decreases.

On the basis of these results, we can define two behaviors depending on the film thickness. For thin films, the amplitude of the surface deformation is small and restricted to a length scale significantly shorter than the capillary length, clearly indicating the appearance of a localized tip effect. This phenomenon is characterized by a deformation profile of confined radial extent, specifically restricted to the near-field underneath the probe. In contrast, for thick films, the surface deformation of large magnitude is observed up to the capillary length. Hence, the tip effect is not observed for thicknesses above a characteristic value, which is found within $E^* \in [10^2, 10^3]$, and as a consequence, the deformation corresponds to that of the bulk.[14]

3.3. Deformation Length Scales. To understand the localized tip effect and to identify the different length scales arising in this problem, we linearize normalized eq 5 for small surface deformations. Far from the axis, where $r^* \to \infty$, the surface is nearly flat, $[\eta^*]' \ll 1$, the probe/liquid interaction potential is negligible, $\Pi_{pl}^* \approx 0$, and the liquid/substrate interaction potential, Π_{ls}^*, is approximated by the first-order term in eq 6a for $[\eta^*] \ll E^*$. Therefore, the surface profile in this region is obtained from

$$\frac{d^2\eta^*}{dr^{*2}} + \frac{1}{r^*}\frac{d\eta^*}{dr^*} - [(\lambda_C^*)^{-2} + (\lambda_F^*)^{-2}]\eta^* = 0 \qquad (12)$$

dx.doi.org/10.1021/la4006086 | Langmuir 2013, 29, 7749−7757

where the dimensionless capillary length $\lambda_C^* = \lambda_C/R = (\gamma/\Delta\rho g R^2)^{1/2}$ and a dimensionless film characteristic length $\lambda_F^* = \lambda_F/R = (8(E^*)^4/(3AH_a))^{1/2}$ appear. $\lambda_F = (2\pi\gamma E^4/H_{ls})^{1/2}$ corresponds to the radial distance beyond which the liquid/substrate interaction contributes to the flattening of the liquid surface. A condition for observing the localized tip effect is thus given by $\lambda_F \ll \lambda_C$, which is satisfied in the shallow film limit $E \to 0$. As clearly revealed in eq 12, these two length scales are compared through an effective capillary length, $\lambda_{CF}^* = 1/((\lambda_C^*)^{-2} + (\lambda_F^*)^{-2})^{1/2}$, that indicates which one of the two mechanisms, gravity or the liquid/substrate interaction, prevails and controls the radial extent of the deformation. In the literature,[12] the inverse of λ_{CF}^* has been introduced as an effective Bond number, which indicates when the effect of the substrate is negligible. Indeed, the exact solution of eq 12 is given by

$$\eta^* = GK_0\left(\frac{r^*}{\lambda_{CF}^*}\right) \tag{13}$$

where K_0 is a zeroth-order modified Bessel function of the second kind and $G = \eta_{CF}^*/K_0(1)$, with η_{CF}^* being the surface deformation at $r^* = \eta_{CF}^*$. For the studied range of parameters, $G \lesssim 10^{-2}$ and $K_0(1) \approx 0.42$. Thus, for $r^* \geq \eta_{CF}^*$, $\eta^* \lesssim 10^{-2}$ and $[\eta^*]' \lesssim 10^{-3}$, demonstrating the validity of the small deformation hypothesis.

In the particular case of an $R = 1 \times 10^{-8}$ m silicon AFM probe interacting with a PDMS film of thickness $E \approx R$ deposited over a silicon wafer, the film characteristic length $\lambda_F \approx 2.2 \times 10^1 R$ is much smaller than the corresponding capillary length $\lambda_C \approx 1.8 \times 10^5 R$.

4. CHARACTERISTIC FILM THICKNESSES

The characteristic radial length scales are now used to highlight the existence of two characteristic film thicknesses. When the capillary length λ_C and the film characteristic length λ_F are of the same order of magnitude, film thickness effects are expected to be observed. The first critical film thickness E_g is obtained from $\lambda_F^* \approx \lambda_C^*$

$$E_g \simeq \left(\frac{H_{ls}}{2\pi\Delta\rho g}\right)^{1/4}, \quad E_g^* \simeq \left(\frac{3AH_a}{8B_o}\right)^{1/4} \tag{14}$$

E_g is a constant of the system, independent of the probe radius R, and $E_g^* = E_g/R$ depends on dimensionless parameters A, H_a, and B_o. The value of this critical thickness in common AFM setups is $E_g \in [10^{-7}, 10^{-6}]$ m, corresponding to $E_g^* \in [10^0, 10^3]$.

When the film characteristic length λ_F is on the order of the probe radius, the probe/liquid attraction is opposed only by the liquid/substrate attraction. Hence, from $\lambda_F^* \approx 1$, we find a second critical film thickness E_γ that is given by

$$E_\gamma \simeq \left(\frac{R^2 H_{ls}}{2\pi\gamma}\right)^{1/4}, \quad E_\gamma^* \simeq \left(\frac{3}{8}AH_a\right)^{1/4} \tag{15}$$

E_γ is a function of the probe radius, scaling as $R^{1/2}$, and $E_\gamma^* = E_\gamma/R$ changes with the product of H_a and A. Within common AFM setups, this critical thickness is on the order of $E_\gamma \in [10^{-10}, 10^{-8}]$ m, corresponding to $E_\gamma^* \in [10^{-2}, 10^0]$.

We expect to observe different behaviors depending on the film thickness, relative to the aforementioned critical values. They might be useful for marking the boundaries of the arising regimes in which the involved mechanisms alternate their contributions.

In Figure 7, the terms in eq 5 are shown as function of the film thickness E^* under the jump-to-contact condition. The

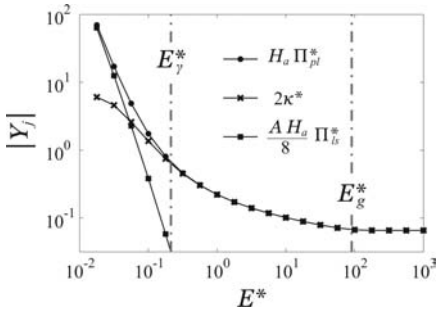


Figure 7. Absolute value of the different terms Y_j from eq 5 for which $\sum Y_j = 0$ as functions of E^* at $D^* = D_{min}^*$ and for $A = 1$, $H_a = 5.48 \times 10^{-3}$, and $B_o = 3.07 \times 10^{-11}$. The hydrostatic term $B_o\eta^*$, which is not represented herein, remains on the order of 10^{-11}. The critical film thicknesses are $E_\gamma^* = 2.13 \times 10^{-1}$ and $E_g^* = 9.05 \times 10^1$.

presented curves correspond to our reference case for which $A = 1$, $H_a = 5.48 \times 10^{-3}$, and $B_o = 3.07 \times 10^{-11}$. In addition, hydrostatic term $B_o\eta^*$ is not shown because its magnitude is very small compared to that of the other terms.

As can be seen on the right-hand side of Figure 7, where $E^* > E_g^*$, the curvature and the probe/liquid interaction terms are nearly constant. The presence of the substrate can be disregarded because the liquid/substrate interaction term in eq 5 is negligible. Consequently, the deformation of the liquid surface results from the equilibrium between the surface tension and the probe/liquid interaction, and in dimensionless terms, it is determined only by the values of H_a and B_o, as described in previous studies.[14] Moreover, the minimum separation distance D_{min}^* and the maximum apex position $\eta_{0,max}^*$ do not vary with the film relative thickness E^*, as depicted in Figure 5. The surface deformation spreads to the effective capillary length, which is essentially given by the usual capillary length $\lambda_{CF}^* \approx \lambda_C^*$, because in this case $\lambda_F^* \gg \lambda_C^*$. We shall name this regime the asymptotic "thick-film" behavior.

For a film with an intermediate thickness $E_\gamma^* < E^* < E_g^*$, though the liquid/substrate term continues to be negligible, the curvature term and the probe/liquid interaction are not constant anymore. These two terms increase slowly and simultaneously, remaining in balance, when reducing the film relative thickness E^*, as can be discerned from Figure 7. In this case, the deformed surface shape stretches out to the effective capillary length λ_{CF}^*, which takes values between the capillary length λ_C^* and the film characteristic length λ_F^*. This constraint forces the surface to recover from its deformation, getting back to a flat profile at a radial distance shorter than the capillary length. The resulting restrained interface shape shows a curvature that is greater than that of the deformed bulk. Hence, the surface position results from the interplay of the three involved physical mechanisms: surface tension and probe/liquid interaction forces act directly, whereas liquid/substrate interaction force appears by means of an implicit modification of the curvature.

On the left-hand side of Figure 7, where $E^* < E_\gamma^*$, the curvature term seems to reach a saturated state. Meanwhile, the probe/liquid and the liquid/substrate attraction terms increase

dx.doi.org/10.1021/la4006086 | Langmuir 2013, 29, 7749−7757

monotonically, approaching each other in magnitude as E^* decreases from E_γ^* toward smaller values. Hence, the effect of the proximity of the substrate dominates over that of the surface tension, and the position of the film free surface is retrieved from the equilibrium of the probe/liquid and the liquid/substrate attractive interactions. D_{min}^* and $\eta_{0,max}^*$ change significantly with the film relative thickness E^*, as shown in Figure 5. A direct effect of the substrate attraction is observed on the radial span of the surface deformation λ_{CF}^*. In this case, $\lambda_F^* \ll \lambda_C^*$; therefore, the effective capillary length is mainly given by the film characteristic length $\lambda_{CF}^* \approx \lambda_F^*$. Hence, the deformation profiles are sharp, and they are restrained to a very narrow zone around $r^* = 0$. We name this regime the asymptotic "shallow-film" behavior, where the localized tip effect is observed.

5. FILM THICKNESS ASYMPTOTIC BEHAVIORS

5.1. Thick Film. Considering the limit of a thick film $E^* > E_g^*$, the surface deformation is controlled by the capillary force and the probe/liquid interaction. The force due to the surface deformation can be taken as

$$F_\gamma \approx \pi\gamma R\eta_0^* \tag{16}$$

Also, the force mutually exerted between the probe and the liquid surface can also be approximated by the force between a sphere and a flat surface:[17]

$$F_{pl} \approx \frac{H_{pl}}{6R(\varepsilon_0^*)^2} \tag{17}$$

Therefore, when the equilibrium between these two forces is attained, the surface deformation is described by

$$\eta_0^* \approx \frac{H_a}{8(\varepsilon_0^*)^2} \tag{18}$$

In the limit $E^* \to \infty$, with the dominant term in eq 8 being the one containing the curvature, the function $f(\eta_0^*, \kappa_0^*)$ is given by

$$f(\eta_0^*, \kappa_0^*) \simeq \frac{2\kappa_0^*}{H_a} \tag{19}$$

which, combined with the first-order approximation of eq 10, results in an expression for ε_0^* in terms of κ_0^*. Taking this within eq 18, one obtains the power law relation of the curvature in terms of the apex deformation

$$\kappa_0 \simeq C\sqrt{\frac{3\pi\gamma}{2H_{pl}}}\left(\frac{\eta_0}{R}\right)^{3/2}, \quad \kappa_0^* \simeq C\sqrt{\frac{2}{H_a}}(\eta_0^*)^{3/2} \tag{20}$$

which is in agreement with that observed in Figure 4 for large values of E^* and has been previously found for the bulk.[12,13] For this case, where $H_a = 5.48 \times 10^{-3}$ and $B_o = 3.07 \times 10^{-11}$, coefficient C takes a value of 6.37×10^{-2}. The employment of eqs 19 and 20 in eqs 11 and 7 allows us to forecast the asymptotic bulk behavior shown in Figure 5.

5.2. Shallow Film. We now focus on the particular evolution observed in Figure 4 for shallow films, $E^* < E_\gamma^*$, and small deformations. Consequently, according to the relative contributions shown in Figure 7, the first-order surface deformation results from the balance between the probe/liquid and the liquid/substrate interactions. The force due to the liquid/substrate interaction can be taken as

$$F_{ls} \approx \frac{H_{ls}\eta_0^*}{R(E^*)^4} \tag{21}$$

Equilibrium between this expression and the probe/liquid interaction force, given by eq 17, yields

$$\eta_0^* \approx \frac{(E^*)^4}{6A(\varepsilon_0^*)^2} \tag{22}$$

Now, the dominant term in eq 8 comes from the liquid/substrate interaction, and the function $f(\eta_0^*, \kappa_0^*)$ for $\eta_0^*/E^* \to 0$ is given by

$$f(\eta_0^*, \kappa_0^*) \simeq \frac{\eta_0^*}{H_a(\lambda_F^*)^2} \tag{23}$$

The asymptotic shallow film behavior is obtained when combining eq 23 with eqs 11 and 7, which is a good approximation of the numerical results displayed in Figure 5. From the first-order approximation of eq 10, we find an expression for ε_0^* in terms of η_0^*, which when substituted into eq 22 gives

$$\eta_0^* \approx \frac{(E^*)^4}{24A} \tag{24}$$

Moreover, from the balance between the two interaction terms in eq 5

$$-\frac{1}{8}AH_a\Pi_{ls}^* = H_a\Pi_{pl}^* \tag{25}$$

the free surface shape of the thin film is given by

$$\eta^*[(D^* - \eta^*)^2 + r^{*2} - 1]^3 = \frac{8(E^*)^4}{3A} \tag{26}$$

from which, at $r^* = 0$ and considering $D^* \gg \eta_0^*$, we obtain

$$\eta_0^* \simeq \frac{8(E^*)^4}{3A(D^{*2} - 1)^3} \tag{27}$$

Differentiating eq 26 and evaluating at $r^* = 0$ gives

$$\kappa_0^* \simeq \frac{16(E^*)^4}{A(D^{*2} - 1)^4} \tag{28}$$

Finally, by combining the last two relations in order to eliminate D^*, we find that

$$\kappa_0 \simeq \sqrt[3]{\frac{H_{ls}}{H_{pl}}}\left(3\frac{\eta_0}{E}\right)^{4/3}\left(\frac{1}{R}\right), \quad \kappa_0^* \simeq \sqrt[3]{A}\left(3\frac{\eta_0^*}{E^*}\right)^{4/3} \tag{29}$$

which is in agreement with the trend observed in Figure 4 for shallow films and small deformations. Within this regime, the minimum separation distance D_{min}^* and the maximum apex position $\eta_{0,max}^*$ are significantly modified by the film relative thickness E^*, in contrast to the thick-film case. Note also that the deformation is dependent on the Hamaker constant ratio, A, but not on the modified Hamaker and Bond numbers.

6. PROBE SIZE EFFECT

With the purpose of determining the experimental parameters for AFM measurements, the probe size and the film thickness effects are quantitatively studied. Therefore, the dimensional jump-to-contact threshold is analyzed, considering the constant physical properties of the system. The combined effect of H_a

dx.doi.org/10.1021/la4006086 | Langmuir 2013, 29, 7749−7757

and E^* on the deformation for a given value of $H_{ls} = H_{pl}$ is equivalent to studying the effects of R and E on the free surface displacement. The dimensionless representation depicted in Figure 5a corresponds to the evolution of $\eta^*_{0,max}$ in terms of E^* for a single value $H_a = 5.48 \times 10^{-3}$. As a consequence, it is possible to reconstruct the dimensional dependency of the maximum apex displacement $\eta_{0,max}$ on the film thickness E, but only for $R = R_3 = 10^{-8}$ m with parameters $\gamma = 3.1 \times 10^{-2}$ N/m and $H_{pl} = 4 \times 10^{-20}$ J. Additionally, considering the same physical parameters, we solved eq 5 numerically for different values of E and for $R_2 = 10^{-6}$ m and $R_1 = 10^{-4}$ m. In Figure 8,

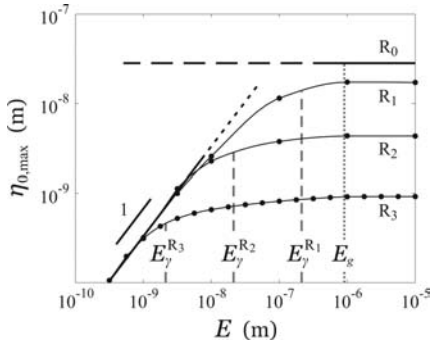


Figure 8. Maximum apex displacement $\eta_{0,max}$ as a function of the film thickness E for $H_{ls} = H_{pl} = 4 \times 10^{-20}$ J and different values of the probe radius R ($R_1 = 10^{-4}$ m, $R_2 = 10^{-6}$ m, and $R_3 = 10^{-8}$ m). The values of E_γ, corresponding to the different values of R, are summarized in Table 1, as is the value of E_g. The horizontal line (---) is the solution of eq 11, considering the thick-film approximation given by eqs 19 and 20 for $R_0 \gtrsim \lambda_C \approx 10^{-3}$ m.

the maximum apex displacement $\eta_{0,max}$ is displayed as a function of the film thickness E for the three probe radii. One notes that the evolution of $\eta_{0,max}(E)$ follows similar tendencies: for $E < E_\gamma$, $\eta_{0,max}$ increases linearly with E; for $E_\gamma < E < E_g$, $\eta_{0,max}$ grows monotonically as E increases with a slowly declining slope; and finally for $E > E_g$, $\eta_{0,max}$ reaches a plateau.

Figure 8 points out that for a shallow film $E < E_\gamma$ the maximum apex displacement $\eta_{0,max}$ is independent of the probe radius R. A linear dependency of the displacement on the thickness, $\eta_{0,max} = \alpha_0 E$ with $\alpha_0 \simeq 0.33$, is found. Because E_γ grows as $R^{1/2}$, the linear regime is extended to a larger range of E. Furthermore, the value of $\eta_{0,max}$ at the plateau, characteristic of bulk behavior $E > E_g$, increases with the value of R. As depicted in eq 14, E_g is constant for a given set of physical parameters, whatever the value of R. In Figure 8, the free surface displacement of a bulk liquid due to its interaction with a probe of millimetric size, $R_0 = 10^{-3}$ m $\approx \lambda_C$, is also represented. In the theoretical case in which $R = \lambda_C$, the two critical film thicknesses collapse into a single value, $E_g = E_\gamma$. As a consequence, the value of $\eta_{0,max}$ obtained with $R = R_0$ in the bulk regime corresponds to the maximum displacement that the liquid surface can attain by increasing the probe radius, even for $R > \lambda_C$. Hence, for probes of larger radius, the system can be modeled as a film interacting with a flat, solid surface for which the maximum apex displacement is approximately the same as for $R \approx \lambda_C$ and completely independent of R. Table 1 reports the characteristic parameters computed for the different values of R.

The combined analysis of Figures 6 and 8 shows that the localized tip effect is observed only for shallow films for which $E < E_\gamma$. As a consequence, when R increases, the localized tip effect is observed at larger thicknesses as a result of the relation between E_γ and R. Within this regime, the linear dependency of $\eta_{0,max}$ on E can be understood by considering that the confined liquid behaves as a linearly elastic solid. This is in agreement with the linear relationship observed between the displacement and the thickness of confined materials undergoing a constant force test.[23] In conclusion, the localized tip effect is characterized by a constant deformation $\eta_{0,max}/E = \alpha_0$. In the particular case of $A = 1$, the value $\alpha_0 \approx 0.33$ is found.

A film with a very small thickness compared to the size of the probe ($R \gg E$) corresponds to $E < E_\gamma$, so the surface deformation at the jump-to-contact results from the balance between the probe/liquid and the liquid/substrate interactions. Considering the geometric decomposition, $D_{min} = R + \eta_{0,max} + \varepsilon_{0,min}$, we can deduce from Figure 5 that the surface displacement and the gap are comparable in magnitude, $\eta_{0,max} \approx \varepsilon_{0,max}$. Thus, taking into account the dependency $\eta_{0,max} = \alpha_0 E$, we find that the gap is much smaller than the probe radius, $\varepsilon_{0,min} \ll R$. Therefore, eq 1 can be condensed to

$$\Pi_{pl} \simeq \frac{H_{pl}}{6\pi(\varepsilon_{0,min})^3} \tag{30}$$

In addition, eq 2 is also reduced to

$$\Pi_{ls} \simeq \frac{\alpha_1 H_{ls}}{6\pi(E)^3} \tag{31}$$

where $\alpha_1 = 1 - (1 + \alpha_0)^{-3}$. The balance between these two simplified potentials gives

$$\varepsilon_{0,min} \simeq [\alpha_1 A]^{-1/3} E \tag{32}$$

Using this result, a linear evolution of the gap between the probe surface and the originally flat surface is yielded:

$$D_{min} - R \simeq \{\alpha_0 + [\alpha_1 A]^{-1/3}\} E \tag{33}$$

In Figure 9, $D_{min} - R$ is shown as a function of E for different values of R. $D_{min} - R$ behaves essentially the same way as $\eta_{0,max}$, shown in Figure 8. The only difference is that the magnitude of $D_{min} - R$ is slightly superior to that of $\eta_{0,max}$, for the same value

Table 1. Values of the Dimensionless Parameters, the Characteristic Film Thicknesses, and the Bulk Apex Displacement for the Different Probe Radii and for the Given Physical Properties[a]

R	[m]	$R_0 \approx \lambda_C$ (10^{-3})	R_1 (10^{-4})	R_2 (10^{-6})	R_3 (10^{-8})
H_a	[1]	5.48×10^{-13}	5.48×10^{-11}	5.48×10^{-7}	5.48×10^{-3}
B_o	[1]	3.07×10^{1}	3.07×10^{3}	3.07×10^{7}	3.07×10^{11}
E_g	[m]		9.05×10^{-7}		
E_γ^R	[m]	6.73×10^{-7}	2.13×10^{-7}	2.13×10^{-8}	2.13×10^{-9}
$\eta_{0,max}$ (bulk)	[m]	2.83×10^{-8}	1.72×10^{-8}	4.31×10^{-9}	9.18×10^{-10}

[a] $\gamma = 3.1 \times 10^{-2}$ N/m, $\Delta\rho = 9.7 \times 10^{2}$ kg/m^3, and $H_{pl} = H_{ls} = 4 \times 10^{-20}$ J.

dx.doi.org/10.1021/la4006086 | Langmuir 2013, 29, 7749−7757

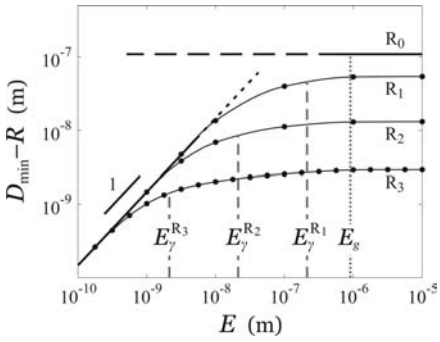


Figure 9. $D_{min} - R$ as a function of the film thickness E for $H_{ls} = H_{pl} = 4 \times 10^{-20}$ J and different values of the probe radius R ($R_1 = 10^{-4}$ m, $R_2 = 10^{-6}$ m, and $R_3 = 10^{-8}$ m). The values of E_γ corresponding to the different values of R are summarized in Table 1, as well as the value of E_g. The horizontal line (---) is the solution of eq 7 for $D_{min} - R$, considering the thick-film approximation already described in Figure 8 for $R_0 \gtrsim \lambda_C \approx 10^{-3}$ m.

of E. The linear dependency described by eq 33 is verified in Figure 9 for small values of E.

The value of gap $D_{min} - R$ should be respected when performing AFM measurements because it indicates the experimental set point needed to avoid the jump to contact and the wetting of the probe. For example, colloidal AFM probes, with a radius of $R = R_2 = 10^{-6}$ m, must be used at a distance of $D_{min} - R \gtrsim 10^{-8}$ m when scanning, whereas for common AFM probes with $R = R_3 = 10^{-8}$ m, we should use $D_{min} - R \gtrsim 10^{-9}$ m, which is 1 order of magnitude closer to the interface.

7. CONCLUSIONS

We have studied the interaction between an AFM probe and a liquid film deposited over a flat substrate. The competition between probe/liquid and liquid/substrate attraction determines the equilibrium position of the liquid surface. The radial extent of the deformation reaches the effective capillary length λ_{CF}, which takes values between the capillary length λ_C and the film characteristic length λ_F. When the deformation extends up to $\lambda_{CF} \approx \lambda_C$, gravity is responsible for the flattening of the surface. However, when $\lambda_{CF} \approx \lambda_F$, the liquid/substrate attraction is the mechanism that restrains the deformation.

From these two characteristic length scales, the existence of two characteristic film thicknesses, E_γ and E_g, is pointed out. E_γ depends on the liquid/substrate interaction constant and the liquid surface tension, also scaling as $R^{1/2}$. In contrast, E_g is independent of the probe radius R, taking a constant value for a given set of physical properties of the system.

For shallow films (i.e., $E < E_\gamma$), the maximum apex displacement varies linearly with the film thickness $\eta_{0,max} = \alpha_0(A)E$ and is independent of R. In addition, a localized tip effect is revealed, which is characterized by a deformation of localized radial extent $\lambda_{CF} \approx \lambda_F$ and small amplitude. For thick films (i.e., $E > E_g$), no tip effect is observed, and $\eta_{0,max}$ takes a fixed value independent of the film thickness E but given by the probe radius R.

From a practical point of view with the aim of performing AFM experiments, E_γ emerges as the relevant characteristic thickness, which can be used to separate two regimes: a linear regime for $E < E_\gamma$ where $\eta_{0,max}$ and D_{min} are controlled by film thickness E and a plateau regime for $E > E_\gamma$ where $\eta_{0,max}$ and D_{min} are mainly determined by probe radius R.

AUTHOR INFORMATION

Corresponding Author

*E-mail: dominique.legendre@imft.fr; philippe.tordjeman@imft.fr. Phone: +(33)0534322858. Fax: +(33)0534322991.

Notes

The authors declare no competing financial interest.

REFERENCES

(1) Bhushan, B., Ed. *Springer Handbook of Nanotechnology*; Springer: New York, 2004.

(2) Bocquet, L.; Charlaix, E. Nanofluidics: from bulk to interfaces. *Chem. Soc. Rev.* **2010**, *39*, 1073−1095.

(3) Li, T.-D.; Riedo, E. Nonlinear viscoelastic dynamics of nanoconfined wetting liquids. *Phys. Rev. Lett.* **2008**, *100*, 106102.

(4) Riedel, C.; Sweeney, R.; Israeloff, N.; Arinero, R.; Schwartz, G.; A., A.; Tordjeman, P.; Colmenero, J. Imagining dielectric relaxation in nanostructured polymers by frequency modulation electrostatic force microscopy. *Appl. Phys. Lett.* **2010**, *96*, 213110.

(5) Maali, A.; Bhushan, B. Measurement of slip length on superhydrophobic surfaces. *Philos. Trans. R. Soc. A* **2012**, *39*, 2304−2320.

(6) Kim, J.; Jang, J.; Zin, W. Estimation of the thickness dependence of the glass transition temperature in various thin polymer films. *Langmuir* **2000**, *16*, 4064−4067.

(7) Grohens, Y.; Hamon, L.; Reiter, G.; Soldera, A.; Holl, Y. Some relevant parameters affecting the glass transition of supported ultra-thin polymer films. *Eur. Phys. J. E* **2002**, *8*, 217−224.

(8) Butt, H. J.; Cappella, B.; Kappl, M. Force measurements with the atomic force microscope: technique, interpretation and applications. *Surf. Sci. Rep.* **2005**, *59*, 1−152.

(9) Yaccot, A.; Koenders, L. Aspects of scanning force microscope probes and their effects on dimensional measurements. *J. Phys. D: Appl. Phys.* **2008**, *41*, 103001.

(10) Ondarcuhu, T.; Aime, J.-P. *Nanoscale Liquid Interfaces: Wetting, Patterning and Force Microscopy at the Molecular Scale*; Pan Stanford Publishing: Singapore, 2013.

(11) Christenson, H. Capillary condensation due to van der Waals attraction in wet slits. *Phys. Rev. Lett.* **1994**, *73*, 1821−1824.

(12) Quinn, D.; Feng, J.; Stone, H. Analytical model for the deformation of a fluid-fluid interface beneath an AFM probe. *Langmuir* **2013**, *29*, 1427−1434.

(13) Ledesma-Alonso, R.; Legendre, D.; Tordjeman, P. Nanoscale deformation of a liquid surface. *Phys. Rev. Lett.* **2012**, *108*, 106104.

(14) Ledesma-Alonso, R.; Tordjeman, P.; Legendre, D. Multiscale deformation of a liquid surface in interaction with a nanoprobe. *Phys. Rev. E* **2012**, *85*, 061602.

(15) Hamaker, H. C. The London-Van der Waals attraction between spherical particles. *Physica* **1937**, *4*, 1058−1072.

(16) de Gennes, P.-G.; Brochard-Wyart, F.; Quere, D. *Capillarity and Wetting Phenomena: Drops, Bubbles, Pearls, Waves*; Springer: New York, 2004.

(17) Israelachvili, J. N. *Intermolecular and Surface Forces*, 3rd ed.; Academic Press: Burlington, MA, 2011.

(18) Bergstrom, L. Hamaker constants of inorganic materials. *Adv. Colloid Interface Sci.* **1997**, *70*, 125−169.

(19) Visser, J. On Hamaker constants: a comparison between Hamaker constants and Lifshitz-van der Waals constants. *Adv. Colloid Interface Sci.* **1972**, *3*, 331−363.

(20) Mougin, K.; H., H. Wetting of liquid films at nanoscale heterogeneous surfaces. *Europhys. Lett.* **2003**, *61*, 660−666.

(21) Cortat, F. P.; Miklavcic, S. J. How closely can a solid approach an air-water surface without becoming wet? *Phys. Rev. E* **2003**, *68*, 052601.

(22) Wang, Y. Z.; Wang, B.; Xiong, X.; Zhang, J. Spherical solid model system: exact evaluation of the van der Waals interaction between a microscopic or submacroscopic spherical solid and a deformable fluid interface. *Surf. Sci.* **2011**, *605*, 528−538.

(23) Tordjeman, P.; Papon, E.; Villenave, J. Squeeze elastic deformation and contact area of a rubber adhesive. *J. Chem. Phys.* **2000**, *113*, 712−716.